DESIGN, ANALYSIS AND SIMULATION IN INJECTION IN-MOLD LABELING

WERKZEUGAUSLEGUNG, ANALYSE UND SIMULATION DES IN-MOLD LABELING SPRITZGIEßENS

Von der Fakultät Energie-, Verfahrens-, und Biotechnik der Universität Stuttgart
zur Erlangung der Würde eines Doktor-Ingenieurs (Dr.-Ing.)
genehmigte Abhandlung

Vorgelegt von

M.Sc. Patcharee Larpsuriyakul
aus Bangkok, Thailand

Hauptberichter:	Prof. Dr.-Ing. H.-G. Fritz
Mitberichter:	Prof. Dr.-Ing. C. Merten
Tag der mündlichen Prüfung:	26. März 2009

Institut für Kunststofftechnik
der Universität Stuttgart

2009

Acknowledgements

Stuttgart, March 2009   Patcharee Larpsuriyakul

Content

List of Figures

List of Tables

List of Symbols and Abbreviations

Latin Alphabets

a_T	[-]	temperature shift factor
A	[mm^2]	cross-section area
A	[mm^2]	surface area
A_C	[mm^2]	surface of the cooling channel
A_P	[mm^2]	surface of the molding
AS	[%]	after-shrinkage
b	[mm]	distance between channels
c_p	[J/mol K]	specific heat capacity of the polymer melt at constant pressure
d	[mm]	diameter of the cooling channel
D, DA	[mm]	diameter
DC	[kV]	direct current
E	[V/m]	magnitude of an electric field
E	[MPa]	modulus of elasticity
E_0	[J/mol]	fluid activation energy
F	[N]	force
h	[mm]	height of the cavity
I	[mm]	distance between surfaces
j	[%]	cooling error
K	[-]	consistency index
L	[mm]	flow length
L	[mm]	unguided length of the ejector pin
L	[-]	flow efficiency of the melt through a runner
n	[-]	power law index
p	[bar]	pressure, injection pressure
p	[mm]	perimeter

PS	[%]	processing shrinkage
q	[m]	point of charge
$\dot{Q}_{AD}$	[W/m^2]	additional heat flux
$\dot{Q}_C$	[J]	heat exchange with coolant
$\dot{Q}_E$	[J]	heat exchange with environment
$\dot{Q}_{KS}$	[W/m^2]	heat flux from molding
R	[mm]	radius
R	[J/mol K]	universal gas constant
Rc	[Rockwell]	hardness unit
Re	[-]	Reynolds number
s	[mm]	part thickness
s	[mm]	critical length of buckling
S	[-]	fluidity
SD	[%]	shrinkage after demolding
t	[s]	time
T	[^{o}C]	temperature
Tc	[^{o}C]	crystallization temperature
T$_C$	[^{o}C]	coolant center temperature
T$_{CW}$	[^{o}C]	cooling channel wall temperature
TS	[%]	total shrinkage
T$_W$	[^{o}C]	mold wall temperature
u	[m/s]	average velocity of the coolant
$\dot{V}$	[cm^3/s]	volume throughput
w	[mm]	part width
W	[g]	part weight
z	[mm]	thickness

Greek Alphabets

α	[^{o}]	tunnel gate angle
α	[1/K]	linear expansion coefficient
β	[^{o}]	tunnel gate angle
$\dot{\gamma}$	[1/s]	shear rate
η	[Pas]	dynamic viscosity
η_0	[Pas]	zero shear viscosity
λ	[W/m K]	thermal conductivity of the polymer
ϑ_A	[^{o}C]	quenching temperature
ϑ_E	[^{o}C]	freezing temperature
ρ	[g/cm^3]	density, density of the coolant
σ	[MPa]	stress
τ	[Pa]	shear stress
τ^{*}	[Pa]	critical shear stress
υ_x	[m/s]	velocity in x direction
υ_y	[m/s]	velocity in y direction
υ_z	[m/s]	velocity in z direction
$\overline{\upsilon}_x$	[m/s]	average velocity in x direction
$\overline{\upsilon}_y$	[m/s]	average velocity in y direction
$\overline{\upsilon}_z$	[m/s]	average velocity in z direction

Abbreviations

2.5D	2.5 dimensional
3D	3 dimensional
ABS	acrylonitrile butadiene styrene

AISI	American Iron and Steel Institute
BEM	boundary element method
CAD	computer-aided design
DIN	Deutsches Institut für Normung
EOAT	end-of-arm tool
FEM	finite element method
FDM	finite difference method
FVM	finite volume method
GF-PA	glass-reinforced polyamide
GNF	Generalized Newtonian Fluid
HDPE	high density polyethylene
IML	in-mold labeling
IR	infrared
PA	polyamide
PC	polycarbonate
PDE	partial differential equation
PE	polyethylene
PMMA	polymethylmethacrylate
POM	polyoxymethylene
PP	polypropylene
PS	polystyrene
S1, S2	sensor node 1 and 2
SEM	scanning electron microscope
WLF	William-Landel-Ferry

Abstract

Years ago, the production of packaging with the injection-IML has been established. This procedure concept ranks nowadays among the most modern technologies in the area of the plastic packaging. With this manufacturing technique, label and packaging, both are of the same polymer materials, become inseparably connected during the injection molding process. Since thermal conductivity of the polymeric label material is clearly smaller than that of the metal mold wall, thermal induced warpage of injected IML part or part surface deformation could be occurred. The objective of this work is to analyze and simulate the filling, holding, and cooling phases of the injection IML process by means of the simulation program Moldex3D$^{®}$ and to study the effect of inserted label on the warpage behavior and modulus of elasticity of injected parts. For this study, the injection mold for injection IML equipped with vacuum ports for holding the label was designed and constructed. For the automation of the injection IML process, a linear pneumatic robot was employed.

As a preliminary examination, the experimental study and numerical simulation of the melt front advancement, course of the pressure and melt temperature profile during the injection molding of double-plated parts with non-uniform part thickness were done in order to acquire better understanding of the simulation program Moldex3D$^{®}$ prior to its application later on to the injection IML simulation calculations. The molded part composes of two thin plates joined together with a cold runner. One fan gate is connected to the thick side of the first plate and the other connected to the thin side of the second plate. Comparisons between the experiment and simulation performed with the same molding parameters were carried out. From the results, 2.5D simulation was verified to be more reliable than 3D simulation particularly in terms of predicting the melt front advancement as well as the melt pressure development during the molding. Owing to the complex flow and unbalance of the pressure within two cavities of the part, 3D simulation based on non-isothermal computation failed to predict course of the pressure and hence the melt front advancement within both cavities. However, with the 3D isothermal computation, improvement in accuracy was achieved. This phenomenon resulted from the instability of the 3D simulation program. By molding the double-plated part separately, both 2.5D and 3D simulation results agreed well with those from the experiments.

After the preliminary examination has been done, analysis and 3D simulation on filling, holding, and cooling phases of the injection IML process and warpage behavior of injected IML parts were investigated, since the presence of label can significantly affect the molding process. From the study, good agreement of the mold filling, holding, and cooling results between 3D simulation and experiment was acquired. Structure and warpage behavior of IML parts were also investigated. In order to cope with part warpage problem, variations in mold temperature on the stationary and moving mold halves were carried out. With the higher mold temperature setting on the label side, part warpage was reduced. Furthermore, study of the effect of the mold temperature combination settings on the modulus of elasticity of the IML part was conducted. The results revealed that despite a slight reduction in the modulus of elasticity of the IML part owing to the different mold temperature settings on two mold halves, modulus of elasticity of the IML part was still found to be satisfactory.

Kurzfassung

Seit geraumer Zeit, hat sich die Herstellung von Verpackungskomponenten nach dem In-Mold-Labeling-Spritzgießverfahren (IML) etabliert. Bei dieser Technologie werden das Etikett und die Verpackung, die i.a. aus demselben Material bestehen, im Zuge des Formgebungsschrittes unlösbar miteinander verbunden. Beim Einspritzvorgang des Plastifikats in die mit dem Etikett bestückte Kavität kann es dazu kommen, dass das Etikett aus seiner Ursprungslage verschoben oder gefaltet wird. Außerdem ist die Wärmeleitfähigkeit des Label-Materials deutlich niedriger als die der metallischen Werkzeugwandung, so dass es zu Strukturfehlern auf der Formteiloberfläche und/oder zu einem Verzug des Spritzgießteils kommen kann. Im Rahmen dieser Arbeit werden deshalb die Formfüll- und Bauteil-Abkühlvorgänge beim IML-Spritzgießen analysiert, wobei das Simulationsprogramm Moldex3D® zum Einsatz kommt. Die dabei gewonnenen Ergebnisse werden mit denen des realen Prozesses verglichen. Des Weiteren werden die generierten Produkte im Bezug auf ihren Verzug und ihren E-Modul bewertet. Für diese Studie wurde ein spezielles Spritzgießwerkzeug, welches mit Vakuumanschlüssen für die Positionierung und Fixierung des In-Mold-Etiketts ausgerüstet ist, konstruiert und gebaut. Für die Automatisierung des IML-Spritzgießprozesses wurde ein linearer, pneumatisch betätigter Roboter eingesetzt.

Um ein besseres Verständnis für das Simulationsprogramm bezüglich seiner Funktionsweise vor der Anwendung auf das In-Mold-Labeling-Spritzgießen zu erwerben, wurden vorab simulative und experimentelle Voruntersuchungen bezüglich der Fließfrontenverläufe, der Druckverläufe und der Temperaturprofile beim Spritzgießen von Doppelplatten mit Dickensprung durchgeführt. Dieses Formteil besteht aus zwei plattenförmigen Kavitäten, die jeweils über einen Filmanschnitt an der dicken und der dünnen Seite der Kavität angespritzt werden. Ein Vergleich von Versuchs- und Simulationsergebnissen wurde durchgeführt. Dabei zeigte sich, dass eine 2.5D-Simulation hinsichtlich der Voraussagen der Fließfrontenverläufe in den Kavitäten sowie der Schmelzedruckverteilungen während des Spritzgießens zu einer zufrieden stellenden Übereinstimmung führte. Infolge des komplexen Füllvorgangs und der „Druckumkehr" innerhalb der beiden Kavitäten konnte die nicht-isotherme 3D-Simulation den Druck und somit die Fließfrontenverläufe nicht richtig wiedergeben. Mit der isothermen 3D-Simulation konnte hingegen eine deutliche Verbesserung in der Genauigkeit erzielt werden. Des Weiteren wurde die Doppelplatte in zwei Einzelplatten zerlegt, die separat gespritzt werden. Mit diesen Platten konnten sowohl 2.5D- als auch 3D- Füllbildsimulationen erfolgreich durchgeführt und die Fließfrontenverläufe in der Kavität richtig beschrieben werden.

Da das Etikett auf den Formteil-Herstellungsprozess zurückwirken kann, wurden nach diesen Voruntersuchungen die Einflüsse des Etiketts unter Durchführung von 3D-Simulationen bezüglich der Füll-, Nachdruck-, und Kühlphase sowie hinsichtlich des Verzugsverhaltens beim In-Mold-Labeling-Spritzgießen studiert. Dabei wurde eine gute Übereinstimmung von Versuchs- und Simulationsergebnissen festgestellt. Weiterführend wurden die Struktur und das Verzugsverhalten des IML-Formteils analysiert. Um den Verzug des IML-Formteils zu reduzieren wurden die Spritzgießversuche mit verschiedenen Werkzeugtemperatur-Kombinationen durchgeführt. Dabei zeigte sich, dass mit einer höheren Werkzeugtemperatur auf der Labelseite der Verzug verringert werden kann. Zusätzlich wurde der Einfluss der Werkzeugtemperatur-Kombination auf die Steifigkeit des IML-Formteils untersucht. Es zeigte sich, dass trotz einer geringfügigen Verringerung des Elastizitätsmoduls des IML-

Formteils infolge der unterschiedlichen Werkzeugtemperaturen der beiden Werkzeughälften der Elastizitätsmodul des IML-Formteils noch in einem akzeptablen Bereich bleibt.

1   Introduction and Objectives

Numerous new polymer grades have been developed over the last few years for specific applications. Some of these materials may require different production methods to accomplish the articles required, such as compression and injection molding, blow molding, extrusion, and thermoforming. In most cases, a mold is required to give the product the desired shape. At the present time, injection molding seems to be the most common and economical method to produce plastic products, especially when large quantities are required. Therefore, it is very important that a mold must be carefully designed and precisely constructed. This may be performed by experience or with the help of CAD/CAM and simulation programs. By using special programs, many calculations can be performed rapidly and accurately, and newly created mold designs can be easily checked for efficiency of melt flow, cooling, strength of materials, etc. Various programs can be used to check for physical strength and to check with other programs the expected efficiency of filling the mold cavities, gate location and sizes, runner sizes, the cooling layout, and so on. Note that all the simulation results depend on the accuracy of the data provided, such as reasonable assumptions as to temperatures, pressures, and times. In this study, the injection mold which was used in the injection in-mold labeling of the flat part has been designed and constructed. Details of this IML mold inclusively the mold components as well as their geometries and dimensions are described in Chapter 4.

In conventional injection molding, mold filling can be successfully predicted for thin parts using the Hele-Shaw model. It assumes that the flow profiles are the same at all gapwise positions. Conventional algorithm extracts mid-plane surface of the part to represent the 3D geometry. These simulation codes are usually referred to as 2.5D. It simplifies the 3D geometry model into 2.5D mid-plane and proceeds to the simulation [1]. This technology has been successfully applied to simulate the molding process of most thin shell plastic parts. In the past decade 3D simulation programs have become widely available. However, 2.5D programs cannot take advantage of these models. Especially for thick parts, the 3D effects are absolutely obvious and can no longer be precisely analyzed by the conventional 2.5D methods. Moreover, the effort required to generate 2.5D models from 3D models is sometimes equivalent to generating 3D information from the beginning [2]. Another solution is to avoid the use of the Hele-Shaw equations and solve the governing equations in their full generality [3] that means it provides a true 3D solution.

Nowadays, numerous commercial simulation programs for injection molding are available. Usually, users are told that 3D simulation has advantages over 2.5D one. Also, there are many studies conducted in the last years in order to compare the efficiency and accuracy of 2.5D to 3D simulation concepts. In spite of this, it is still worth performing such a comparison of one's own simulation program, whether it would be able to deal with more complex problem. For this reason, flow analysis and simulation by means of the double-plated part with non-uniform part thickness were carried out as a preliminary examination which is shown in Chapter 3. By doing this, a better understanding of the simulation program regarding how it works, its strength and weakness can be obtained. In this study, Moldex3D simulation program which is capable of the true 3D (Solid models) CAE analysis was used. Simulations were carried out based on 2.5D mid-plane (Hele-Shaw) and 3D analyses and later their results were evaluated and compared with each other and with those from the real molding process.

More than 25 years ago the production of packaging articles with the injection in-mold labeling (IML) technology has been established. This molding concept ranks nowadays among the most modern technologies in the area of plastic packaging. In-mold labeling is a pre-decorating technique used worldwide for blow molded bottles as well as for injection molded and thermoformed containers or other plastic objects. Injection in-mold labeling is an injection molding technique, in which the film, label or decorating material is back injected. In the in-mold labeling process, a label is placed in the open mold and held in the desired position by vacuum ports, electrostatic attraction or other appropriate means. The mold closes and molten plastic resin is injected into the mold where it conforms to the shape of the object. The plastic melt envelopes the label, making it an integral part of the molded part. With this manufacturing technique, the label and packaging, both are of the same polymeric material, become inseparably adhered during the injection molding process. Besides the injection molding machine, process parameters, and the quality of the labels used, the quality of injected IML parts is significantly affected by the injection mold, which must be deliberately designed and carefully constructed. Main advantage of injection in-mold labeling is the integration of a follow-up step into the injection molding process. The heat transport reduction owing to the label and the associated slightly higher molding cycle time are some unfavorable aspects of this molding technique. By back injection of the plastic melt into the cavity preloaded with the label, it can occasionally come to the situation that the label is folded, slipped or shifted from its starting position, whereby the injected IML part becomes useless. In addition, the thermal conductivity of the label material is significantly smaller than that of the metal mold wall, so that the thermally induced warpage of the injected IML part or surface deformation could occur.

Since the label has different thermal properties relative to the polymer melt and mold, the presence of the label as an insert can significantly affect the filling, holding, cooling and warpage behaviors of the injection molding process. To fully consider the complex insert effects, especially warpage of the IML part, a true three-dimensional finite element solution [4, 5] is a better choice than the traditional 2.5-dimensional finite element solution [6 and 7]. Warpage is caused by variations in shrinkage throughout the part. For injection molded part, the part is constrained in the mold. During the solidification of an injection molded part, shrinkage of the solidified layer is prevented by two mechanisms. Firstly, adhesion to the mold walls restrains (at least the outer skin of) the solid layers from moving, and secondly, the newly formed solid surface will be kept fixed by the stretching forces of melt pressure. In-cavity residual stresses are then built up during solidifications. Due to the nature of constrained quenching, the residual stress distribution is largely determined by the varying pressure history coupled with the frozen layer growth. Once the part is ejected from the mold, these residual stresses will be released in the form of shrinkage deformation. If the initial strains, which are equivalent to the in-cavity residual stresses, are symmetric, the part will shrink uniformly without any warpage and post-mold residual stresses.

The objective of this work can be subdivided into two subtasks. Firstly, the experimental study and numerical simulations of the melt front advancement, course of the pressure and melt temperature profile during the injection molding of double-plated parts with non-uniform part thickness will be carried out. This will be done by means of the injection simulation program Moldex3D®. Furthermore, simulation results from 2.5D and 3D simulation calculations will be verified. Secondly, analysis and simulation on filling, holding, and cooling phases of the injection IML process and warpage behavior of injected IML parts will be investigated, in order to study the effect of in-mold labels on the injection molding and warpage behaviors of injected IML parts. In this stage, only 3D simulation calculation

will be conducted and its results will then be compared with those of the experiments. In addition, the injected part quality particularly in terms of degree of part warpage and modulus of elasticity will be evaluated.

2   Fundamentals

2.1   Injection Mold Design

One basic requirement must be met by every mold that is intended to run on an automatic injection molding machine is that the molded parts must be ejected automatically without the need for secondary finishing operations (degating, machining to final dimensions, etc.). From a practical standpoint, the classification of injection molds should be accomplished on the basis of the major features of the design and operation [8, 9, 10, and 11]. These include:

- the type of gating, i.e. runner system and means of separation,

- the type of ejection used for the molded parts,

- the presence or absence of external or internal undercuts on the part to be molded, and

- the manner in which the molded part is released.

The DIN ISO standard 12165 "Components for Compression, Injection, and Compression-Injection Molds" classifies molds on the basis of the following criteria:

- standard molds (two-plate molds),

- split-cavity molds (split-follower molds),

- stripper plate molds,

- three-plate molds,

- stack molds,

- hot runner molds.

Standard components of an injection mold are shown in Appendix 1. There are also cold runner molds for runnerless processing of thermosetting resins in analogy to the hot runner molds used for processing thermoplastic compounds and elastomers.

Figure 2.1 shows a procedure to plan and design injection molds methodically. The Finite Element Method (FEM) along with the computational methods is being used increasingly to design and dimension parts and the associated injection molds. The final mold design can be prepared only after the part design has been specified and all requirements affecting the design of the mold have been clarified.
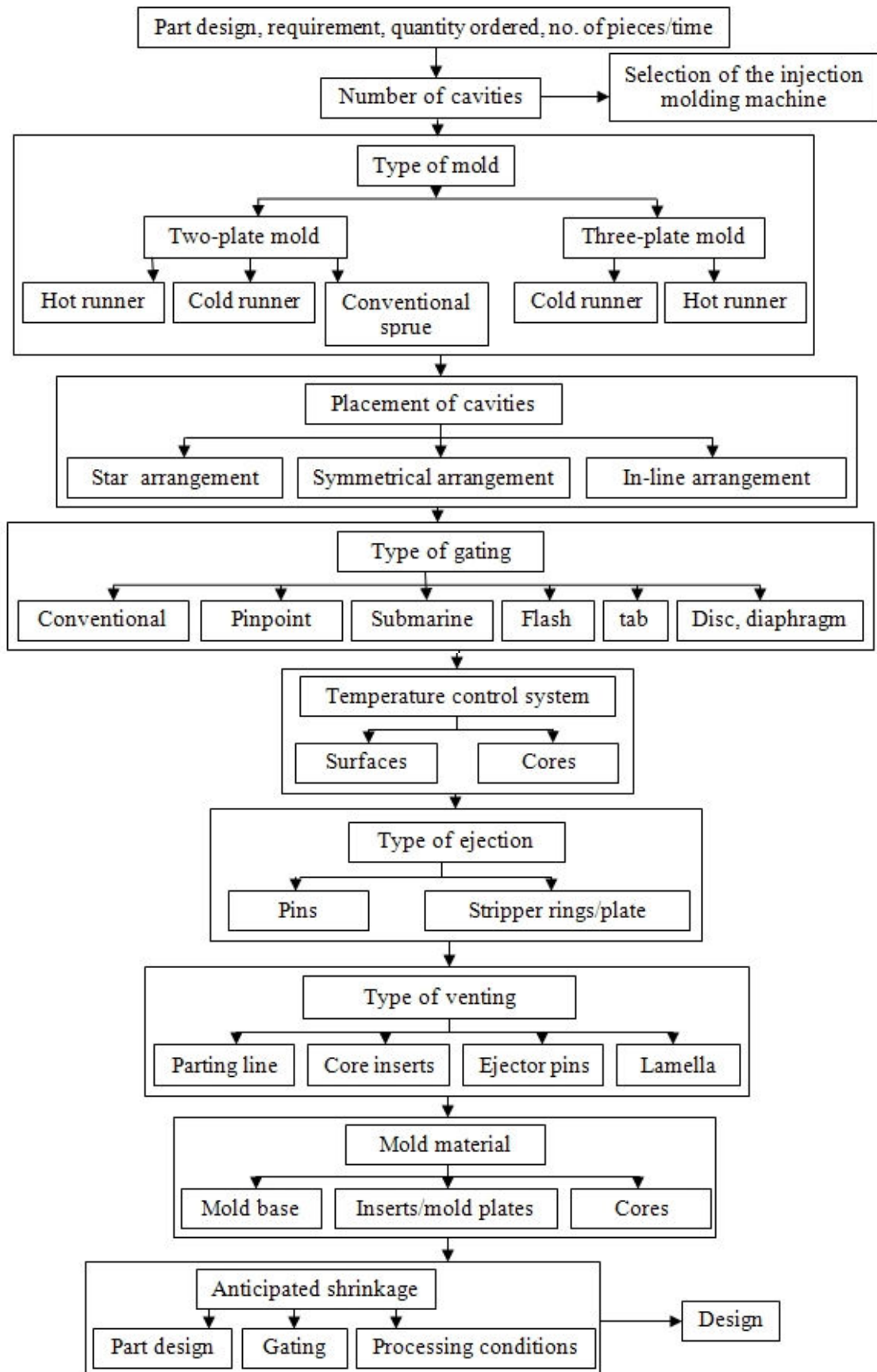
Figure 2.1: Flow chart for methodical designing of injection molds [9]

2.1.1 Runner System Design

A runner system directs the melt flow from the sprue to the mold cavities. Additional pressure is required to push the melt through the runner system. Frictional heat generated within the melt while the material is flowing through the runner raises the melt temperature and also facilitates the flow. While large runners facilitate the flow of material at relatively low pressure requirements, they require a longer cooling time, more material consumption and scrap, and high clamping forces. Designing the smallest adequate runner system will maximize efficiency in both raw material use and energy consumption in molding. At the same time, however, runner size reduction is constrained by the molding machine's injection pressure capability.

There are three basic runner system layouts typically used for a multi-cavity system [12]. These concepts are illustrated in the Figure 2.2.

The standard (herringbone) runner system

The "H" (branching) runner system

The radial (star) runner system

(Poor Design)　　　(Better Design)
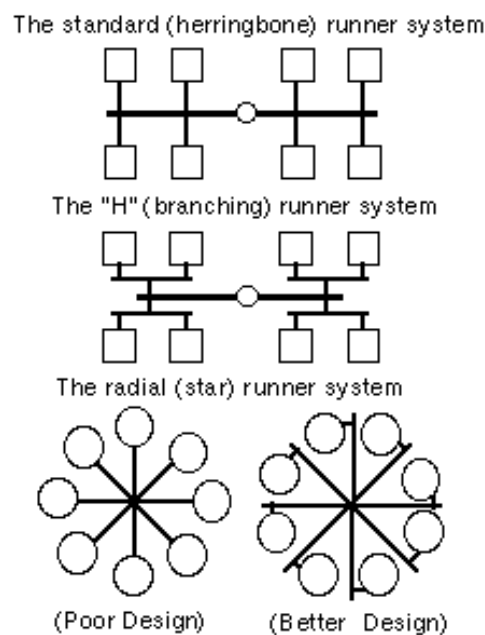
Figure 2.2: Basic runner system layouts

The "H" (branching) and radial (star) systems are considered to be naturally balanced. The naturally balanced runner provides equal distance and runner size from the sprue to all the cavities, so that each cavity is filled under the same conditions. Although the herringbone is naturally unbalanced, it can accommodate more cavities than its naturally balanced counterparts, with minimum runner volume and less tooling cost. An unbalanced runner system can be artificially balanced by changing the diameter and the length of the runner segments.

The number of cavities in a mold plays a crucial role not only for the efficiency of the molding process but also for the quality of the injection molded parts. Because of the artificial balancing of the standard (herringbone or in-line) runner system, an employment of a symmetrical runner system with H- or T- branching is recommended.

Inevitable, the possible number of cavities resulted from the symmetrical runner alignment are 2, 4, 8, 16, 32, 64 etc. Note that, despite artificial balancing, molds with 10, 14 and 20

cavities, which are aligned in one or two rolls, cannot provide the uniform filling and hence are not recommended for the production of precise parts [13].

Balanced flow into the cavities is a prerequisite for a quality part production. This can be achieved by changing the runner size and length. Changing the gate dimension may give a seemingly balanced filling. However, it affects the gate freeze-off time greatly, which is detrimental to part uniformity. Whenever possible, a naturally balanced runner system should be used to balance the flow of material into the cavities. If a naturally balanced runner is not possible, then the runner system should be artificially balanced [14, 15].

To balance a runner system, melt flow is encouraged to the cavities farthest from the sprue by reducing the diameter of runners feeding the other cavities. Note that decreasing the runner diameter excessively may cause it to freeze prematurely, causing a short shot. On the other hand, increased frictional shear heating may actually reduce the resin's viscosity, and thus, resistance to flow and fill the cavity even faster [16]. Keep in mind that non-standard runner diameters will increase mold manufacturing and maintenance costs. An artificially balanced runner system designed for one material may not work for others. Further, an artificially balanced runner system requires tighter process controls. A small variation in the process control will alter filling pattern of the mold, leading to consistently unbalanced filling.

For example, if a standard (in-line) runner system with various injection rates is used, various filling patterns will occur. Generally speaking, a slow injection rate will first fill parts further out onto the runner, while a faster injection rate will first fill the parts closest to the sprue. This is because at a slower injection rate, the melt tends to hesitate at the restricted gate it first encounters. It moves out to fill the remaining runner system. By the time all the runner branches are filled, the melt at the first, upstream gates may have already become more resistant than the downstream gates, due to solidification. Varied injection speed will result in filling patterns between these two extremes, as illustrated in Figure 2.3.
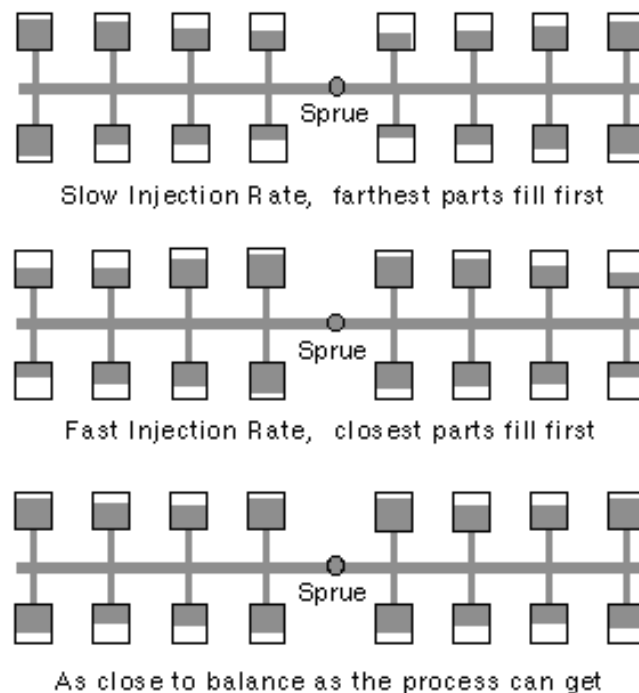
Figure 2.3: Filling patterns resulting from various injection rates in an unbalanced runner system

Figure 2.4 shows commonly used runner cross section shapes. The full-round runner is the best in terms of a maximum volume-to-surface ratio, which minimizes pressure drop and heat loss. However, the tooling cost is generally higher because both halves of the mold must be machined so that the two semi-circular sections are aligned when the mold is closed.

The trapezoidal runner also works well and permits the runner to be designed and cut on one side of the mold. It is commonly used in three-plate molds, where the full-round runner may not be released properly, and at the parting line in molds, where the full-round runner interferes with mold sliding action [17].
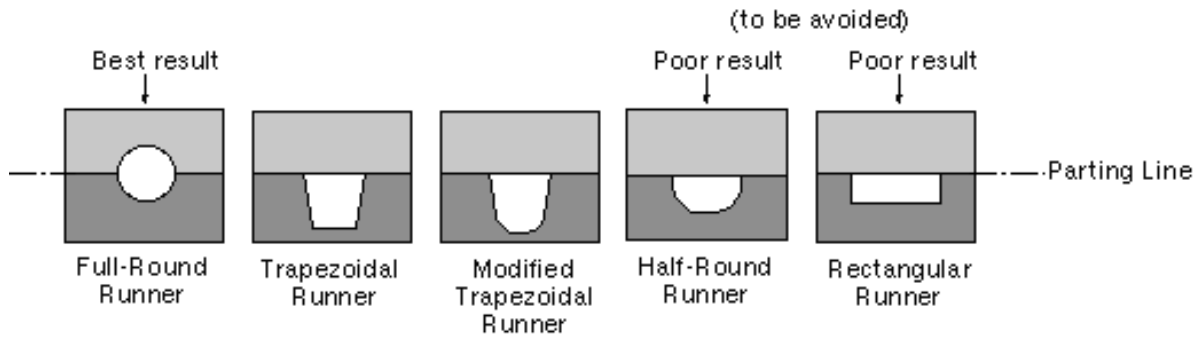
Figure 2.4: Commonly used runner cross sections

Figure 2.5 illustrates how to use the flow efficiency to compare different runner shapes.

Figure 2.5: Comparison of the flow efficiency of different runner shapes

To compare runners of different shapes, the flow efficiency L of the melt through a runner, which is an index of flow resistance, is employed. The higher the flow efficiency of the melt through the runner, the lower the flow resistance is. Flow efficiency can be defined as [18]:

$$L = \frac{A}{P} \qquad (2\text{-}1)$$

where L = flow efficiency of the melt through a runner,

A = cross section area,

P = perimeter.

The diameter and length of runners influence the flow resistance [19]. The higher the flow resistance in the runner, the higher the pressure drop will be. Reducing flow resistance in runners by increasing the diameter will use more resin material and cause longer cycle time if the runner has to cool down before ejection. One may first design the runner diameter by using empirical data or the equation (2-2). Then fine-tune the runner diameter using computational analysis to optimize the delivery system. Figure 2.6 shows the definition of the flow length L used for calculating the runner diameter. Following is the formula for runner diameter determination [18]:
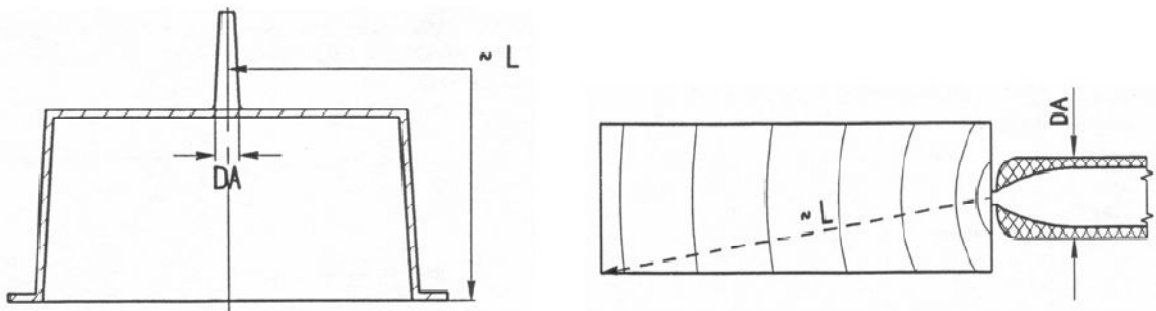
Figure 2.6: Runner diameter and flow length determination

$$DA = \frac{\sqrt{W} \cdot \sqrt[4]{L}}{4} \qquad (2\text{-}2)$$

where DA = runner diameter (mm),

W = part weight (g),

L = flow length (mm).

2.1.2 Gate Design

A gate is a small opening through which the polymer melt enters the cavity. Gate design for a particular application includes selection of the gate type, dimensions, and location. It is dictated by the part and mold design, the part specifications (e.g., appearance, tolerance, concentricity), the type of material being molded, the fillers, the type of mold plates, and economic factors (e.g., tooling cost, cycle time, allowable scrap volume). Gate design is of great importance to part quality and productivity.

The following provides an overview of the most commonly encountered types of gates:

- Pinpoint gate (automatically trimmed),

- Diaphragm gate,

- Disk gate,

- Film gate and,

- Submarine gate (automatically trimmed).

The gate location should be at the thickest area of the part, preferably at a spot where the function and appearance of the part are not impaired. This leads the material to flow from the thickest areas through thinner areas to the thinnest areas, and helps maintain the flow and holding paths. Gate location should be central so that flow lengths are equal to each extremity of the part.

Symmetrical parts should be gated symmetrically, to maintain that symmetry. Asymmetric flow paths will allow some areas to be filled, packed, and frozen before other areas are filled. This will result in differential shrinkage and probable warpage of the parts. Gate length should be as short as possible to reduce an excessive pressure drop across the gate. Gates should always be small at the beginning of the design process so they can be enlarged, if necessary. The freeze-off time at the gate is the maximum effective cavity holding time. However, if the gate is too large, freeze off might be in the part, rather than in the gate, or if the gate freezes after the holding pressure is released, flow could reverse from the part back into the runner system. A well-designed gate freeze-off time will also prevent back flow of the injected material. Fiber-filled materials require larger gates to minimize breakage of the fibers when they pass through the gate [11].
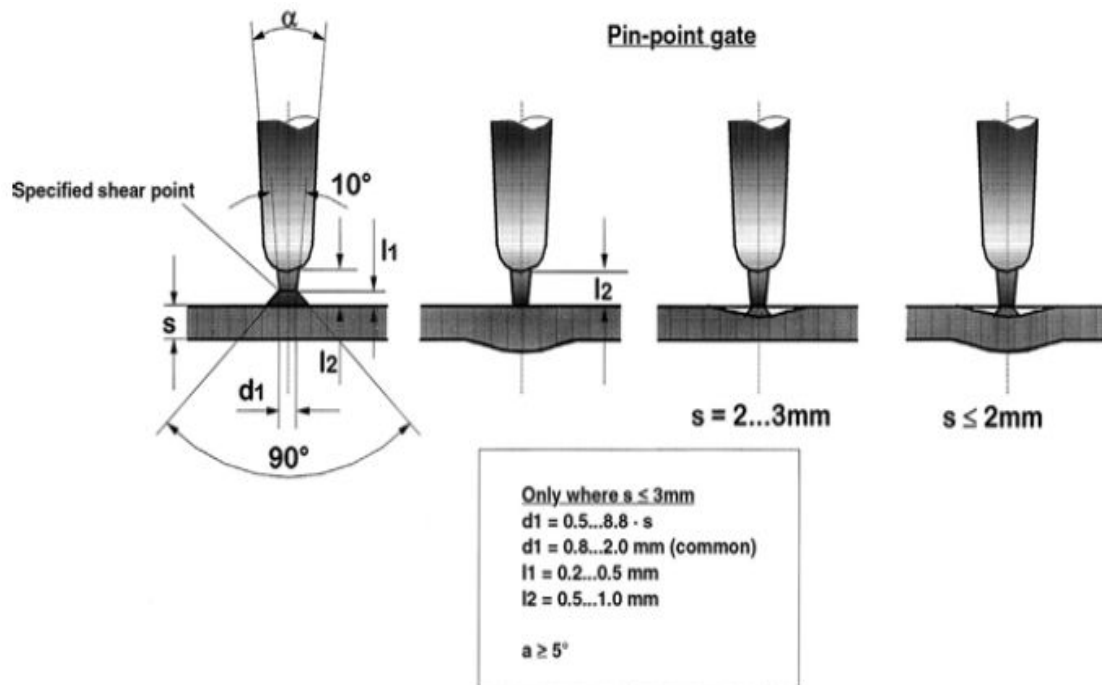
Figure 2.7: Pin-point gate design [9]

Figure 2.7 illustrates the design of the pin-point gate. Pin-point gate is generally separated from the molded part automatically. Pin-point gating has been especially successful in application for small and thin-walled molded parts. At separation, however, drool has been a

problem with certain polymers and premature solidification of the pin gate may make it difficult to optimize holding time.

The diaphragm gate (see Fig. 2.8 (a)) is useful for producing cylindrical parts with the highest possible degree of concentricity and avoidance of weld lines. On the other hand, the diaphragm encourages jetting which, however, can be controlled by varying the injection rate so as to create a swelling material flow. Having to remove the gate by means of subsequent machining is a disadvantage of this gate type. Disk gate (Fig. 2.8 (b)) is used preferably for internal gating of cylindrical parts in order to eliminate disturbing weld lines. With fibrous reinforcements, for instance, the disk gate can aggravate the tendency for distortion. The disk gate must also be removed subsequent to the part ejection.

Diaphragm gate   **Disk gate**

$$s \leq 4 : d_1 = 1.5 \cdot s + K. \; K = 0...3mm$$
$$s \geq 4 : d_1 = s + 1...2mm$$
$$l_1 = 1...3mm \text{ (common)}$$
$$t_1 = 0.5...0.8 \cdot s \qquad \alpha \leq 90°$$
$$t_2 \approx s \qquad R \leq 0.5mm$$
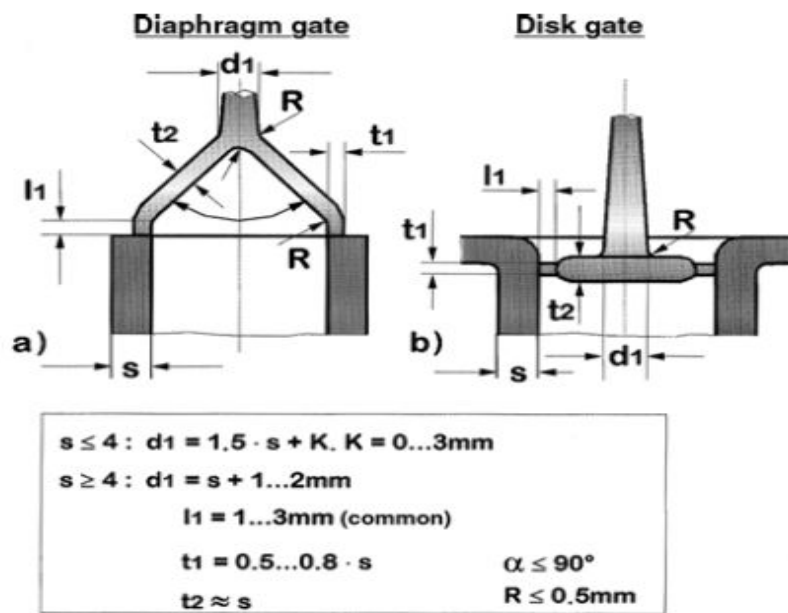
Figure 2.8: Diaphragm (a) and disk (b) gate designs

Flash (film) gate

Common only when $s \leq 4mm$

$$d_1 = 1.5 \cdot s + K. \; K = 0...3mm$$
$$l_1 = 0.5...2.0mm$$
$$l_2 = 0.5...3mm$$
$$t_1 = 0.5...0.8 \cdot s$$
$$t_1 = 0.5...2.0mm$$
$$t_1 \leq t_2 \leq s$$
$$t_1 \leq l_3 \leq s$$
$$b_1 \leq 50mm$$
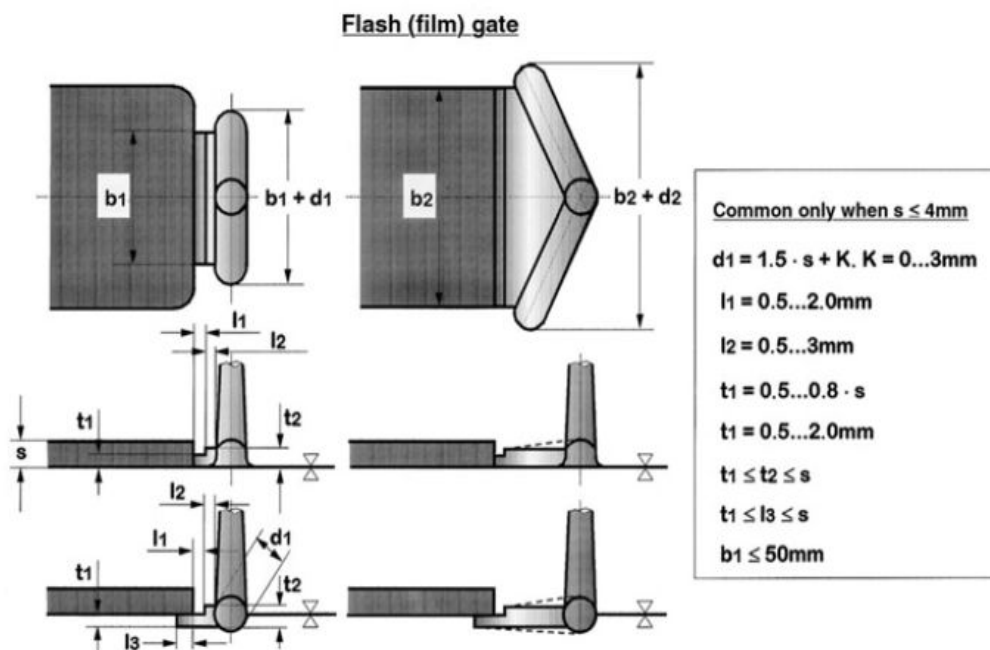
Figure 2.9: Film gate design

Figure 2.9 illustrates the recommended dimension of a film gate. The film gate is used when a uniform flow front especially in flat molded parts is desired. This kind of flow leads to few internal stresses and little tendency to warp of the part. A certain tendency of the melt to advance faster in the vicinity of the sprue can be offset by correcting the cross-section of the film gate. The film gate is usually trimmed off the part after ejection.

Figure 2.10 depicts the dimensional design of the submarine (tunnel) gate. As same as the pin-point gate, this type of gate is trimmed off the molded part during mold opening or directly on ejection at a specified cutting edge.
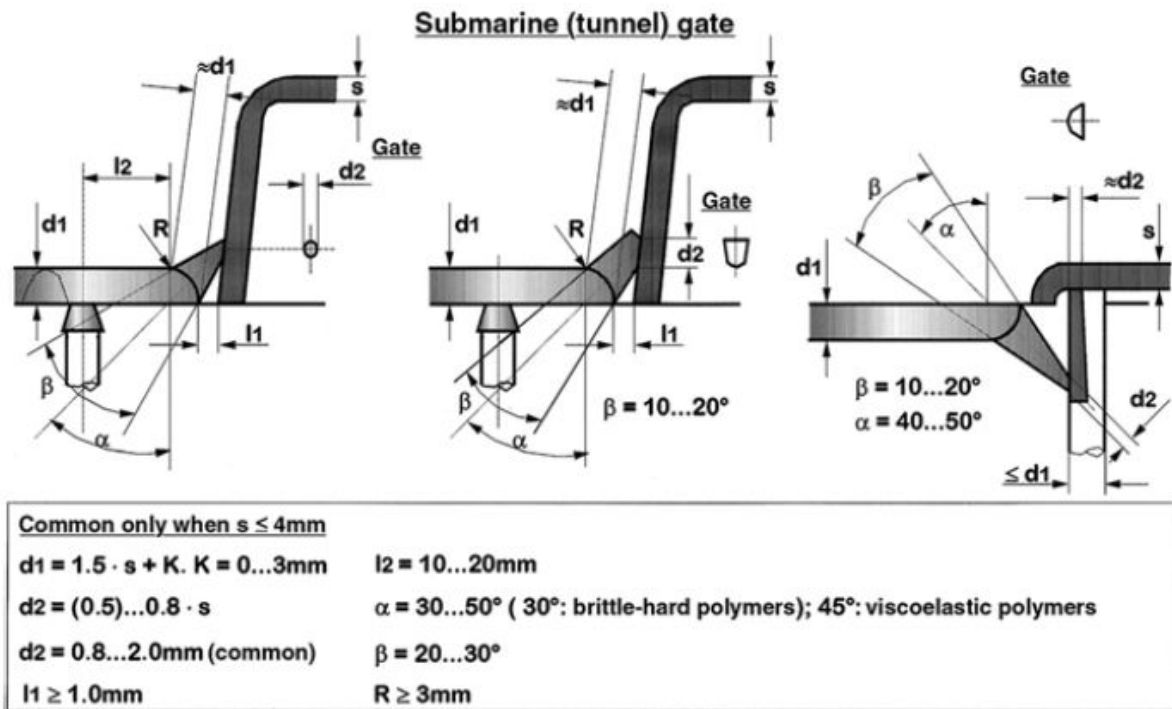
Figure 2.10: Submarine gate design

2.1.3 Cooling System Design

Generally, heat from the melt injected into the cavity has to be rapidly and uniformly extracted until the injected part possesses a sufficient rigidity and then can be demolded without a risk to warp. To calculate the heat flux and design the heat exchange-system of a mold, the total amount of heat carried into the mold has to be first determined. In the range of quasi-steady operation, heat flux applied to the mold (positive value) and heat flux to be removed from the mold (negative value) have to be in equilibrium. Heat flux balance can be described in the following form [20]:

$$\dot{Q}_{KS} + \dot{Q}_E + \dot{Q}_{AD} + \dot{Q}_C = 0 \qquad (2\text{-}3)$$

where $\dot{Q}_{KS}$ = Heat flux from molding,

$\dot{Q}_E$ = Heat exchange with environment,

$\dot{Q}_{AD}$ = Additional heat flux (e.g. from hot runner),

$\dot{Q}_C$ = Heat exchange with coolant.

Figure 2.11 illustrates the heat flux balance in an injection mold. With the equation (2-3), the necessary heat exchange with the coolant can be calculated after the heat exchange with the environment and any additional heat flux have been estimated.
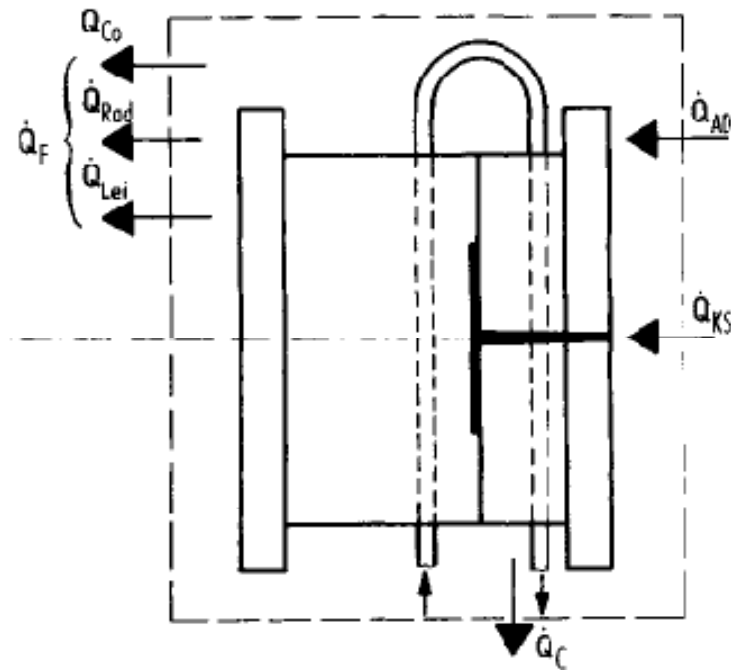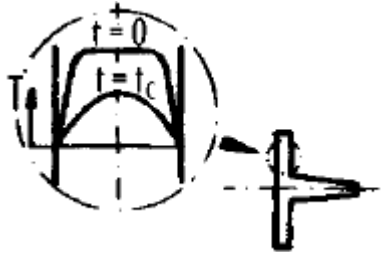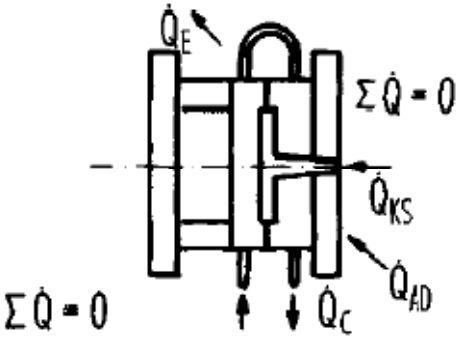
Figure 2.11: Heat flow assessment in an injection mold [21]

Instead of relying on experience, a simple analytical calculation can be employed as a first approximate value for thermal design of the cooling system. Nevertheless, this calculation is based on a two-dimensional viewpoint. Its simplification can, therefore, lead to errors of the outer edges and corners of the mold, if for instance no insulation is inserted at high temperature operations.

Design steps		Criteria
1. Computation of cooling time		Minimum cooling time down to demolding temperature
2. Balance of heat flow		Required heat flow through coolant
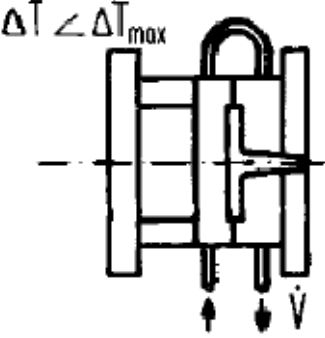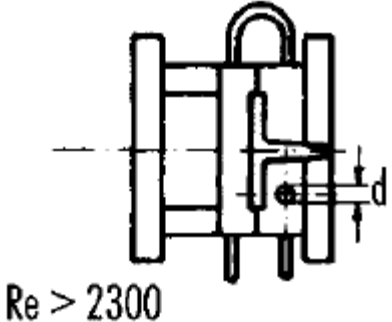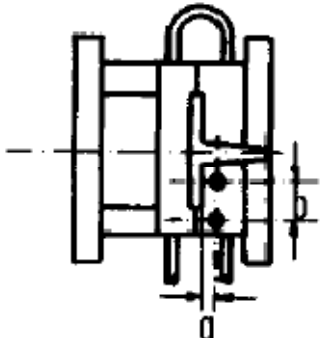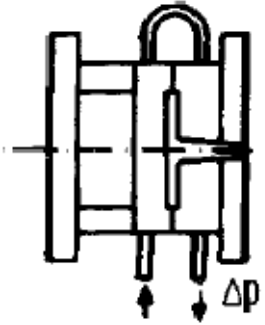
3. Flow rate of coolant		Uniform temperature along cooling line
4. Diameter of cooling line		Turbulent flow
5. Position of cooling line		Heat flow uniformity
6. Computation of pressure drop		Selection of heat exchanger modification of diameter or flow rate

Figure 2.12: Analytical computation of the cooling system [21]

The analytical thermal calculation can be subdivided into separate steps (Fig. 2.12). The heat flux balance not only provides information about the operating range of the heat-exchange system, but also indicates design problems along the cooling path. High heat flux, which has to be subtracted by the coolant and which occurs particularly with thin, large moldings of semi-crystalline material, requires a high flow rate of the coolant and results in a high pressure drop in the cooling system. Then the use of several cooling circuits can offer an advantage. A low heat flux, on the other hand, may result in a small flow rate of the coolant

in channels with common diameter and this encourages the laminar flow. For this reason, a higher flow rate should be accomplished than that resulting from the criterion of temperature difference between coolant entrance and exit. After the flow rate of the coolant has been calculated, the requirement of a turbulent flow sets an upper limit for the diameter.
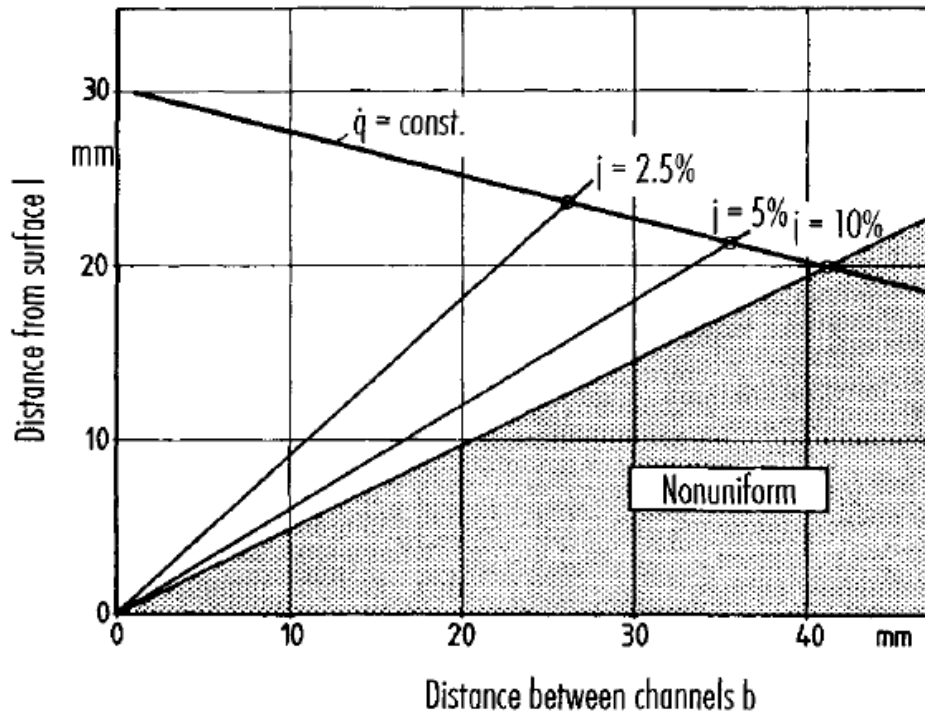
Figure 2.13: Position of cooling channel and temperature uniformity [21]

The position of one cooling channel to another as well as their distance from the cavity wall results from the calculated heat flux including compliance with the limits of homogeneity (Fig. 2.13). Homogeneity can be measured in form of cooling error j as follows:

$$j\,[\%] = \frac{\dot{Q}_{max} - \dot{Q}_{min}}{\dot{\bar{Q}}}\;.$$
(2-4)

For semi-crystalline polymers, the maximum value of cooling error should lie between 2.5-5 % and 5-10 % for amorphous polymers.

For analytical calculation, the configuration of the molding is simplified by a plate with the same volume and surface as the molding. This allows segmenting the internal area of the mold with each segment having a width equal to the calculated distance between the cooling channels.

Alternatively, the distance between two cooling channels in a mold can be calculated based on the relationship given in Figure 2.14, where *Ap* is the surface of molding, and *Ac* refers to the surface of cooling channel.

With the position of the cooling channels defined, the whole length of the cooling system, the number of corners, elbows and connectors can be determined. This information allows the computation of the pressure drop and the necessary capacity of heat exchangers. Eventually,

the minimum diameter of the cooling channel or the maximum flow rate of the coolant for a given permissible pressure drop can be calculated.

$$\dot{j} = \frac{k}{L} \cdot \Delta T_1 = \frac{A_C}{A_M} \cdot \alpha \cdot \Delta T_2$$

$$A_C \approx \pi d_{CW} \qquad A_M \approx b$$

$$\Delta T_1 = T_W - T_{CW} \qquad \Delta T_2 = T_{CW} - T_C$$
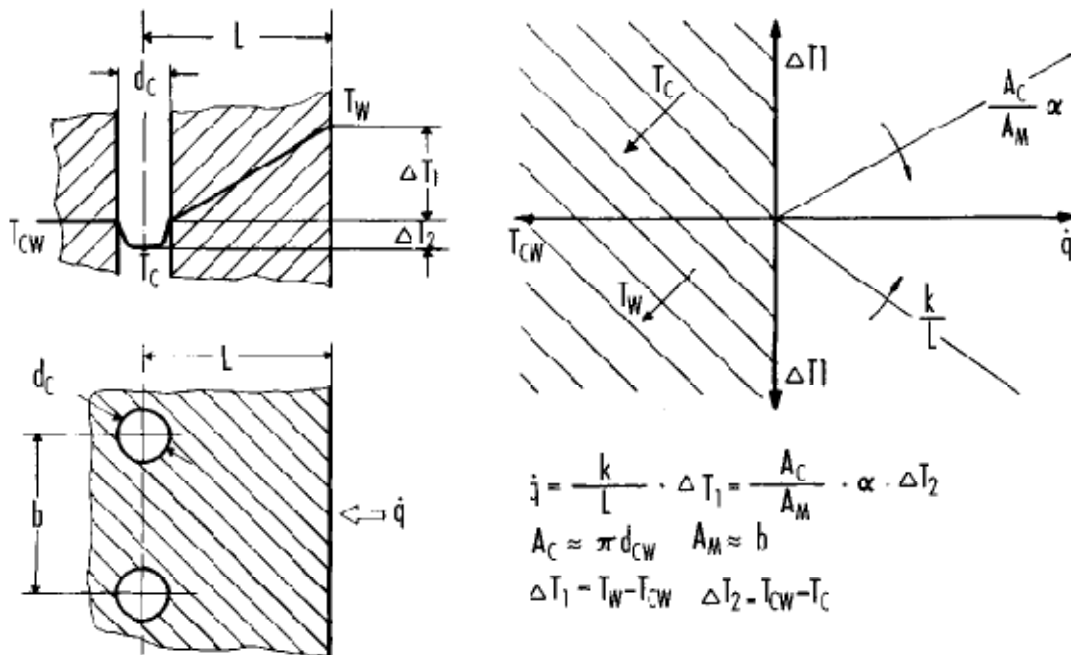
Figure 2.14: Thermal reactions during a steady conduction [21, 22]

Controlled cooling channels are essential in a mold and require special attention in mold design. The cooling medium must be in turbulent flow, rather than laminar flow, in order to transfer heat out of the molded part at an adequate rate [23]. The Reynolds number is used to determine whether the coolant will be turbulent. It is the dimensionless number that is significant in the design of any system in which the effect of viscosity is important in controlling the velocity or the flow pattern of a fluid. Following is the equation for calculating the Reynolds number:

$$\mathrm{Re} = \frac{\rho U d}{\eta} \qquad (2\text{-}5)$$

where ρ = density of the coolant,

U = average velocity of the coolant,

d = diameter of the cooling channel,

η = dynamic viscosity of the coolant.

The transition between laminar and turbulent flow is often indicated by a critical Reynolds number, which depends on the exact flow configuration and must be determined experimentally. Within circular channels the critical Reynolds number is generally accepted to be 2300, where the Reynolds number is based on the channel diameter and the average velocity U within the channel. Anyhow, to ensure the turbulent flow in the cooling channel, the Reynolds number should be at least 10,000 [24].

2.1.4 Design of Ejection

Ejection of a molded article is normally accomplished mechanically by the opening stroke of the molding machine. If this simple ejection effected by the movement of the clamping unit is not sufficient, ejection can be performed pneumatically or hydraulically [25].

As a consequence of the processing shrinkage, molded parts tend to be retained on mold cores. Following are various types of ejectors commonly used to release molded parts:

- Ejector pins,

- Ejector sleeves,

- Stripper plates, stripper bars, stripper rings,

- Slides and lifters,

- Air ejectors,

- Disc or valve ejectors, etc.
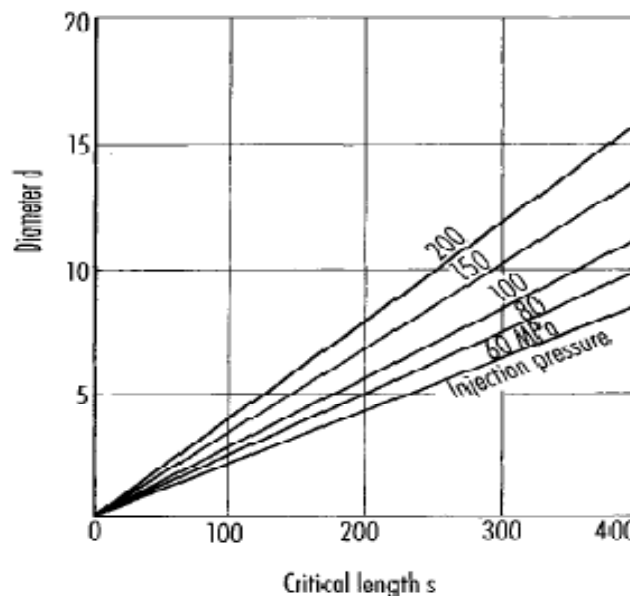
Figure 2.15: Suggested diameter of ejector pins depending on critical length of buckling and injection pressure

For larger molded parts, demolding is usually accomplished by pushing them out, instead of ejecting. They are removed manually or by robot after being loosened. Type of ejector depends on the shape of the molded part. The force acting on the surface area of the molded part to be ejected should be as low as possible in order to avoid deformation. To release undercuts, slides are generally needed. Internal undercuts can be released by collapsible cores or internal slides. Threads may be released by slides, removable inserts, collapsible cores, unscrewing cores, and etc. To demold a molding, ejector pins are the most frequently employed elements. Ejector pins are mostly made of hotwork die steel (AISI H-13 type) and hardened or gas nitrided to achieve a high surface hardness of about 70 Rc. When dimensioning ejector pins, eventual instability problems should be considered due to the slenderness of the pins. The diameter is therefore:

$$d \geq 0.000836 \cdot L \cdot \sqrt{P} \qquad\qquad (2\text{-}6)$$

For steel P is nearly 100 MPa, and the equation above becomes

$$d \geq 0.028 \cdot L \tag{2-7}$$

where L is the unguided length of the pin.

The diameter of an ejector pin dependent on critical length of buckling and injection pressure can be taken directly from the Figure 2.15 [21, 26, 27], which is derived from the equation (2-6).

2.1.5 Design of Venting

During mold filling the melt has to displace the air which is contained in the cavity. If this cannot be done, the air can prevent a complete filling of the cavity. Beside this the air may become so hot from compression that it burns the surrounding material. The molding compounds may decompose, outgas or form a corrosive residue on cavity walls.

Most molds do not need special design features for venting because air has sufficient possibilities to escape along ejector pins or at the parting line. This is called passive venting. In case of a rib, an additional joint for venting is obtained by dividing the mold inserts into two pieces. With the passive venting, it was assumed that the air can escape through joining faces, but this is feasible only if the faces have sufficient roughness and the injection process is adequately slow to allow the air to escape. This solution fails, however, for molding thin-walled parts with relatively short injection times. Here, special venting channels become necessary.

An annular channel situated on the parting line around the round-shaped part is another reasonable venting method (Fig. 2.16). The annular gap is not interrupted by flanges but it is continuous in form. Melt penetration into the venting channel can be prevented by adjusting the gap width so as to just prevent entrance of the melt. Usual gap widths vary from 20 μm in accordance with the polymer employed.
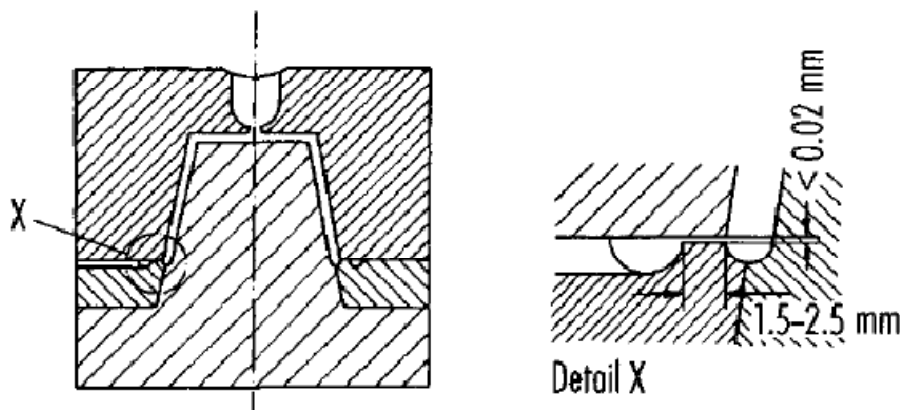
Figure 2.16: Cup mold with annular channel for venting [28]

Porous sintered metals that open out into free space, have not proved suitable for venting because they tend to clog rapidly. But if the sintered metals open into a cooling channel, completely new perspectives open up for the use of sintered metal mold inserts, since an existing cooling water circuit can provide active venting to the cavity. The water from the circuit draws the air out of the cavity via the sintered metal insert, without water entering the cavity.

If ejector pins are located in an area where the air may be trapped, they can also function as a venting. Frequently, the so-called venting pins are employed. They can be grooved or kept 0.02 to 0.05 mm smaller in diameter than the receiving hole. To avoid flashing, a certain gap width, which is polymer-specific, cannot be exceeded after mold clamping. The critical gap width for specific polymers is as follows [29]:

- Polycrystalline thermoplastics: 0.015 mm

    (PP, PA, GF-PA, POM, PE)

- Amorphous thermoplastics: 0.03 mm

    (PS, ABS, PC, PMMA)

- Extremely low viscous materials: 0.003 mm

Apart from active venting by means of the cooling water circuit, which was already mentioned above, partial or complete evacuation of the cavity prior to the injection process is possible. This type of venting is used in the injection molding of microstructures, since conventional venting gaps are too large for the extremely low-viscosity plastic melts [30]. In thermoset and elastomer processing, there are applications that require evacuation of the cavity, primarily to improve the accuracy of reproduction and the molded part quality [31]. Evacuation of the molds is only sufficient, if the whole mold structure is sealed off. Due to many moving parts on the mold, such as slides, ejectors, etc., this is extremely complicated and virtually impossible to achieve. The mold is instead surrounded with a closed jacket or box that has only one parting line. This type of construction for a microinjection mold is schematically shown in Figure 2.17.
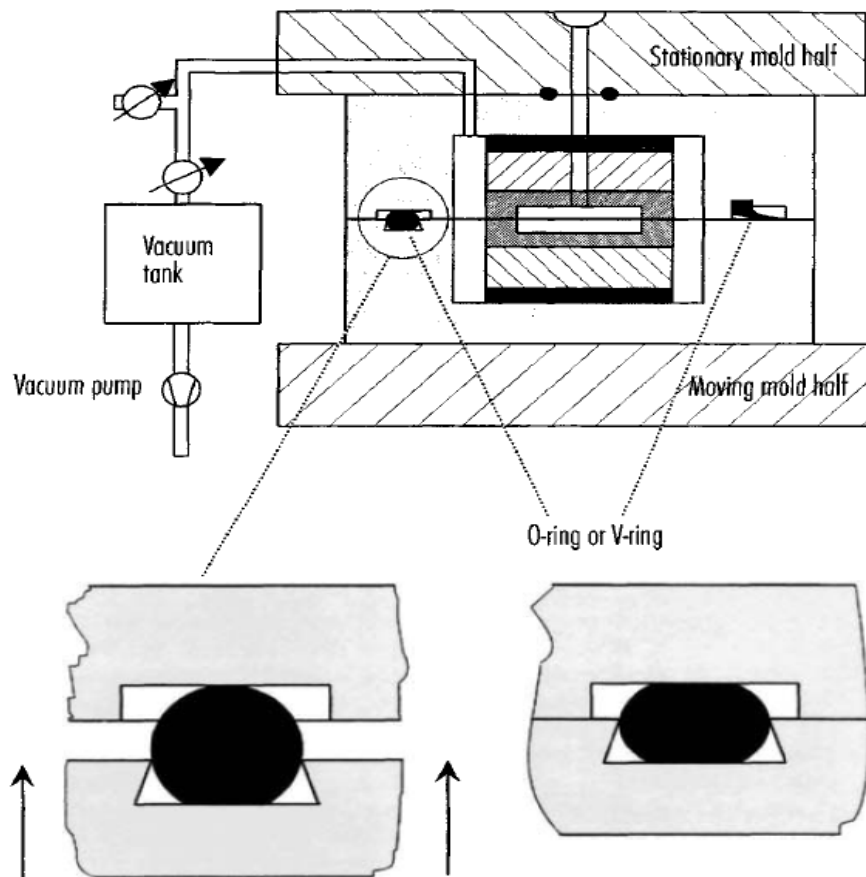
Figure 2.17: Evacuation of the microinjection mold [32]

2.1.6 Selection of Mold Materials

The requirements to be met while selecting mold material are machinability, ability to harden, ability to take a polish, corrosion resistance, etc.

There is a long list of factors to be considered in selecting materials for plastic molds. The primary factors are:

- Type of polymer to be molded,

- Method of forming cavities,

- Mold wear and mold life,

- Physical or chemical properties,

- Quantity of parts to be made,

- Mold fabrication,

- Cost.

Mold wear is one of the most troublesome problems to handle. Primary factors influencing mold wear and mold life are the case depth (for the case hardening steels), surface hardness of the mold, and the abrasive characteristics of the material being molded.

A mold hardened to less than Rockwell C 50 is likely to fail in compression before it wears excessively. Mold life increases as the hardness increases to about Rockwell C 60. Further gains from increased hardness above C 60 are unpredictable because of increased brittleness at sharp corners. With the same surface hardness, mold life is much shorter with thinner cases. Resistance to parting-line indentation of pressure or flash lands is a function of steel surface hardness and internal compressive strength.

The forces involved in the injection molding operation are compressive. They are exerted by the clamping ram and internal melt pressure. Most mold platens are made of cast steel with yield strength of about 386 MPa. Allowing a safety factor of 7, a permissible load of 54 MPa is defined [23]. Molds that are built for long life and high activity are heat-treated either initially or whenever the intermediate hardness of the cavities begins to affect the quality of the product unfavorably.

Mold life is a term used to define the number of acceptable piece parts produced from a single mold. Some of the material choices made by the mold designer to increase mold life include:

- Short Run: Possible choices might be aluminum and low carbon steel.

- Medium Run: Possible choices would be P20, P21, and medium carbon steels.

- Long Run: Possible choices would be chrome plated or nitrated P20, stainless steel, inserted tool steels of H13, D2, S7 or other air and oil hardening steel choices.

2.1.7 Part Shrinkage

By shrinkage or tolerance is meant the dimensions to which a cavity and core should be fabricated in order to produce a product of desired shape and size. Shrinkage is a function of mold temperature, part thickness, injection pressure, and melt temperature [35]. Moreover,

shrinkage is influenced by cavity pressure to a very large degree. Depending on the pressure in the cavity alone, the shrinkage may vary as much as 100 %.

Part thickness will cause a change in shrinkage. The thicker the part, the higher shrinkage value resulted. The mold and melt temperature also influence shrinkage. A cooler mold will result in less shrinkage, whereas a hotter melt will cause more shrinkage. The longer the time in the cavity, the closer the part comes to mold dimensions, which means less in shrinkage [23, 33, and 34].

In the injection molding process, shrinkage is the difference between an arbitrary dimension in the cavity and the corresponding dimension in the injected part with reference to the cavity dimension.
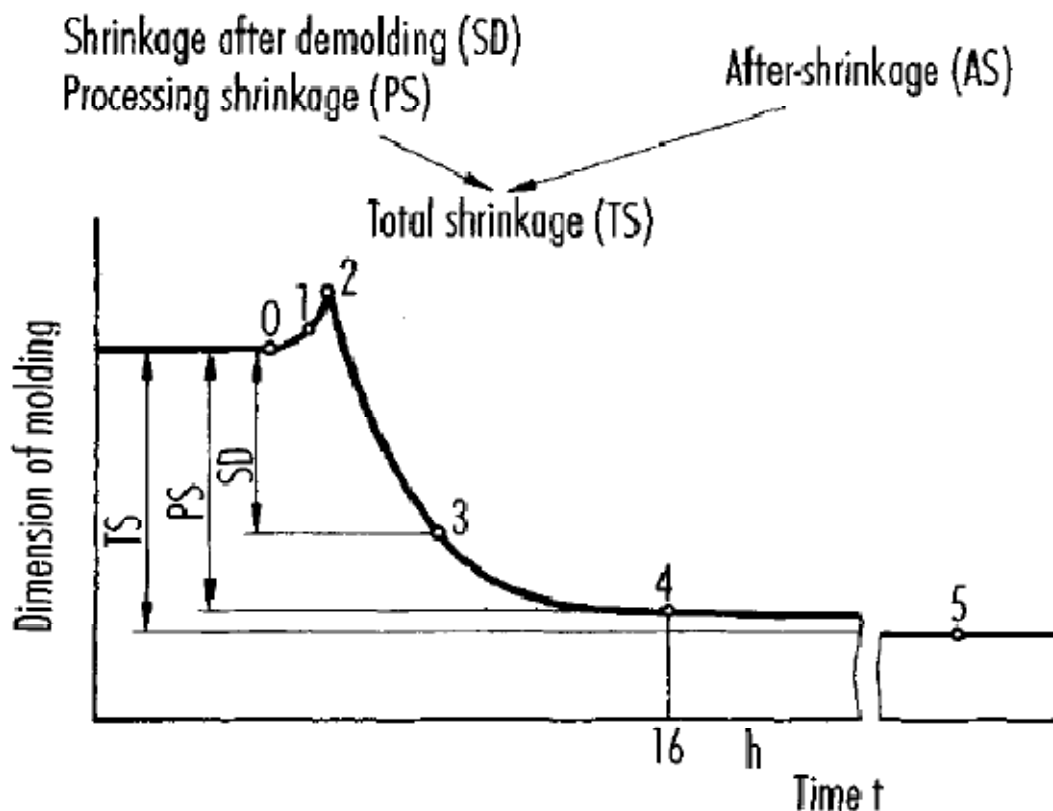
Figure 2.18: Dimensional changes as a function of time [36]

Figure 2.18 shows the dimensional changes as a function of time, where 0 is the dimension in cold mold, 1 is the dimension in hot mold, 2 is dimension in mold under clamping force and holding pressure, 3 is dimension of part after demolding, 4 is measurement of processing shrinkage (DIN 16901), and 5 is dimension after storage. Usually the dimensions of the cavity change from thermal expansion (0→1) and mechanical loading during operation (1→2). Anyway, the effect of time on the dimensions of the molding has to be taken into account (2→5). The demolding shrinkage (point 3), which is measured immediately after the part has been ejected, and the processing shrinkage (point 4) have to be differentiated. The processing shrinkage is measured after storing the injected part in a standard climate for 16 hours [37]. In this context the cavity dimension has to be determined at an ambient temperature of 23°C ± 2°C. After extended storage, another dimension change may occur from the effect of temperature changes and especially from post-conditioning, this is called post-shrinkage (4→5). This change is caused by relaxation of residual stresses, re-orientation,

and post-crystallization in semi-crystalline materials. The sum of processing shrinkage and post-shrinkage is called total shrinkage.

The simplest way to estimate shrinkage for dimensioning a mold is to consult tables. These data are provided by the raw-material suppliers in the data sheets for their respective materials. However, these data neither allow a sufficiently accurate prediction of shrinkage nor are pertinent to the process parameters known or configurations of moldings from which the shrinkage was obtained. Transfer to other configurations is, therefore, difficult. Another and increasingly more accurate estimate of shrinkage behavior is provided by FE simulation [38]. Exact dimensioning of parts with the aid of this method is not yet possible. However, the process and the part can be optimized in respect to shrinkage and distortion behavior. Since several physical parameters such as crystallization behavior cannot as yet be determined, some material data cannot be determined with sufficient accuracy and hence it is still not possible to make an exact predictive simulation of part dimensions.

2.2 Injection In-Mold Labeling

2.2.1 A Brief History of IML

Pioneered in Europe in the late 1970's, injection in-mold labeling (injection-IML) has experienced rapid adoption and high annual growth rates. IML application began with paper labels on PS substrates. IML in Europe is a mainstream process used extensively, but not exclusively, for food packaging. Until recently, low cavitation molds and relatively slow cycle times adequately served the demands of the European Market [39]. An estimated 85 % to 95 % of rigid food packaging there now uses IML, as do some durable goods such as returnable beer crates.

IML reportedly started in the U.S. in the early 1980s. Shape Inc. in Biddeford, Me., was one of the first to get into injection IML, taking a license in 1982 from Cerbo in Sweden, which held patents on a technique to inject the melt through the label. In 1983, Shape applied the process, using Cerbo's automation, to production of video cassette sleeves in a two-cavity mold [40]. By Procter & Gamble and Owens-Illinois Packaging (now part of Graham Packaging), the first applications were blow molded HDPE bottles with paper labels coated with a heat-activated adhesive. Problems with label quality, feeding, and handling kept IML activity low-key in the U.S. until the mid-1990s, when it was rekindled by molders' attempts to eliminate secondary operations, reduce the scrap rate from post-mold labeling, and to produce a "no-label" look similar to that of blow molded articles.

2.2.2 Injection IML Process

The use of IML (In-Mold Labeling) in the injection molding technology provides significant advantages for the manufacturer or marketer of the product as well as the end user. It eliminates secondary steps in the manufacturing process and the end result is permanent.

Injection in-mold labeling is an injection molding process, in which a flat, even film surface, is back injected. In-Mold-Labeling is often used in the packaging industry as an alternative to printing when design requirements call for a high degree of flexibility or else when the impression cannot be directly molded on the part. The labels are usually a printed polypropylene film with a thickness of 50-100 μm. The advantages of In-Mold-Labeling are listed below [41]:

- One step process (integration of the downstream process directly with the injection molding process),

- Highly attractive print quality,

- Increased surface coverage- multi language product descriptions,

- No stopping production for changeover to new print pattern,

- Short print runs can be produced cost-effectively,

- Absolute bonding between label and container,

- Reduce in wall thickness, less material used, and hence material cost reduction,

- Ease of recycling.

The disadvantages, on the other hand, are for instance a heat transport reduction caused by the label, the slightly increased cycle times owing to the insertion of the label into the mold cavity and the part warpage possibly occurred from the existence of the label, which leads to the non-uniform cooling of the part [42].

Figure 2.19 illustrates the sequence of the injection IML process. In the in-mold labeling process, a label is first placed in the open mold and held in the desired position by vacuum nozzles, electrostatic attraction, or other appropriate means. The mold closes and then molten plastic resin is injected into the mold where it conforms to the shape of the object. The hot plastic envelopes the label and makes it an integral part of the molded object. As soon as the melt cools down to the ejection temperature, the injected IML-part is ready to be demolded, usually with the help of a robot.

The difference between glue applied labels and in-mold labels is that a glue applied label is "on" the surface of the plastic object; the in-mold label is "in" the wall of the object. In-Mold-Labeling makes no more demands on the machine than those made by thin-walled molding. Table 2.1 shows the requirements for the injection molding machine and mold for the injection IML. To produce packaging with 5-sided label integrated, inside gating (patented) must be employed. This procedure offers an uninterrupted decoration of the injected part.
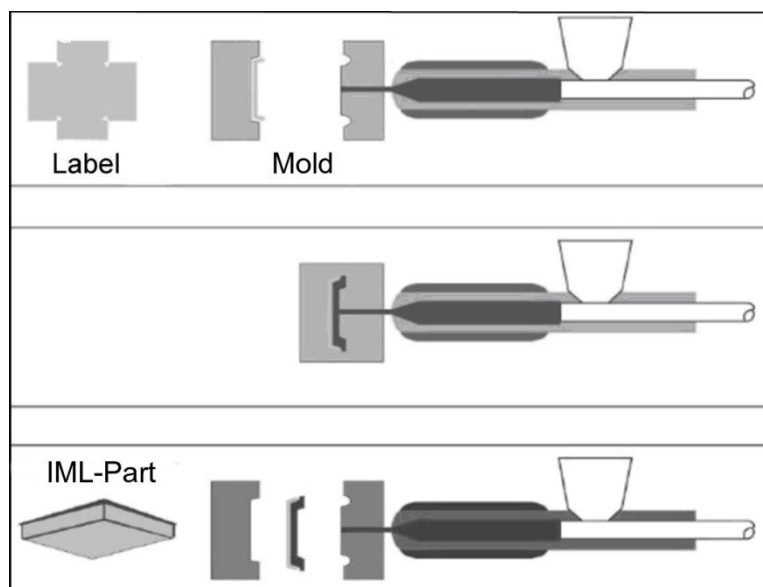
Figure 2.19: Injection in-mold labeling sequencing [43]

Injection molding machine requirements	Injection mold requirements
• High injection speed • Accurate shot weight control • High quality melt • Accurate clamp open position	• Rugged design for fast cycles • Good cooling • Vacuum system for label retention • Single face or stack molds

Table 2.1: Machine and mold requirements for injection IML

Table 2.2 shows the comparison between inside and outside gating.

Inside gating	Outside gating
• Uninterrupted decoration of bottom • No gate mark on part outside • Smaller dome is required • Mold manufacturing cost approximately 15 % higher	• Less cooling time required • Mechanical tripping off core by machine ejector is possible • No restrictions by IML for multi-stage stripping systems

Table 2.2: Comparison between inside and outside gating for injection IML

In-mold labeled containers offer the following advantages:

- Lower costs than other pre-decorating methods
- No extra labeling step or equipment
- In-case product filling and capping
- Increased packaging line speeds
- Reduces in-house container inventory
- Reduced container weight
- Improved appearance
- Better stain resistance
- Improved sidewall strength
- Better squeeze resistance

2.2.3 Key Label Properties

Labels printed on paper substrate cannot be recycled together with the container. Besides, paper will cause pin holes that will results in leak if the recycled polymer will be used to produce new bottles [44]. One problem dealing with the printing of paper labels is the paper waste, which is not recyclable compared with the plastic film. Also during labeling of self adhesive labels, a huge amount of release paper is left. Labels for injection molded IML, on the other hand, do not require an adhesive on the back side. IML labels printed on the plastic substrate are the most compatible with the container, since the label is printed on the same

polymer (mainly PP and PE) and this gives total recycling possibility. Furthermore, during printing, scrap can be easily recycled. The IML process eliminates the labeling step and all associated equipment and labor. Other types of labels used in packaging are shown in Appendix 7.

The physical and electrical characteristics of the label are extremely important to the reliability of using static charges to adhere the label to the mold. The surface of the label that is to contact the mold cavity must be a good insulator to accept and maintain the static charge. Ideally, this surface should have a resistivity of 1,012 ohms/m^2 or greater [45]. The higher the resistivity, the better the label will accept the charge without bleeding the charge to the ground when it contacts the metal mold cavity. If the charge is not maintained when in contact with the mold, adhesion is lost and the label slips from the intended position. Measurement of the label's resistivity can be performed using a commercially available surface resistivity meter.

If conductive inks, coatings, or foil laminations are used, they must be on the back side of the label, opposite the surface that is to contact the mold. In such a case, the best method for charging the label is with the charging applicator external to the press (Fig. 2.21) and the conductive surface of the label against the vacuum nozzles on the end-of-arm tool (EOAT). If the charging applicator is mounted on the EOAT behind the label, the high-voltage field cannot penetrate the conductive layer and sufficient charge will not be applied to the surface that is to contact the mold cavity. A charged foil or conductive layer will most likely discharge in the form of an arc as it approaches the mold surface. A result of this arcing is RFI, which may cause problems with microprocessor controls, especially if unshielded sensors or cables are nearby. Ongoing arcing over a long period of time may also produce pits on the mold cavity.

Label properties such as thickness, curl, and surface texture also affect adhesion. For example, a relatively thick label that may have some curl due to an asymmetrical laminated structure or improper storage may break loose from a flat mold surface if the electrostatic forces are unable to overcome the physical forces causing the label to curl. Similarly, preformed labels may be required for compatibility with contoured mold surfaces. A textured label or mold surface can also result in poor adhesion due to the reduction in intimate surface contact between the label and mold surface. A relatively thin, non-textured label with good dielectric properties on a non-textured mold surface will produce the best adhesion. However, there are still other important adhesion factors to consider, such as molding temperature, polymer compatibility with the label, gate location, and material flow when the mold is injected.

2.2.4 Automation in IML

Although there are numerous know-hows of IML technology, one of the most important considerations is how the label is held in place in the injection mold. In many applications, electrostatic charging device offers a reliable and cost-effective alternative to the use of vacuum for holding the label in its proper position in the cavity. This approach can provide distinct benefits to the molder as well as the molder's customer and the end user. Mostly used label holding methods in the injection IML are described as follows:

Holding with Vacuum

The most obvious is to incorporate vacuum channels and nozzles into the mold. Designing and machining the mold to incorporate vacuum can add significant cost to the tooling. This results in high manufacturing costs and hence increases in product costs. Furthermore, the label must be substantial enough to prevent it from being sucked into the vacuum nozzles, causing a deformed image or "pimples" on the surface of the finished product. In addition, it is very important that the robot does not miss the label. Injecting the mold without a label in place can result in very time-consuming and costly downtime to remove the mold and clean out all the vacuum nozzles and channels. Also, should the label shift or rupture during molding, molten plastic may be drawn into the vacuum nozzles, which results in the process interruption. To prevent this, a device of detecting the vacuum and stopping injection of the polymer into the mold is required. Another main drawback of this holding method is that the vacuum channels in the mold halves may also result in non-uniform mold temperatures. A label to be back injected can be held in the desired location in the mold by means of the specially designed and machined vacuum channels with sintered metals (Fig. 2.20). The sequence is as follows: A robot picks up the label from a label magazine, places it in the desired position in the mold cavity, the vacuum is turned on, and the melt is finally injected into the pre-loaded cavity.
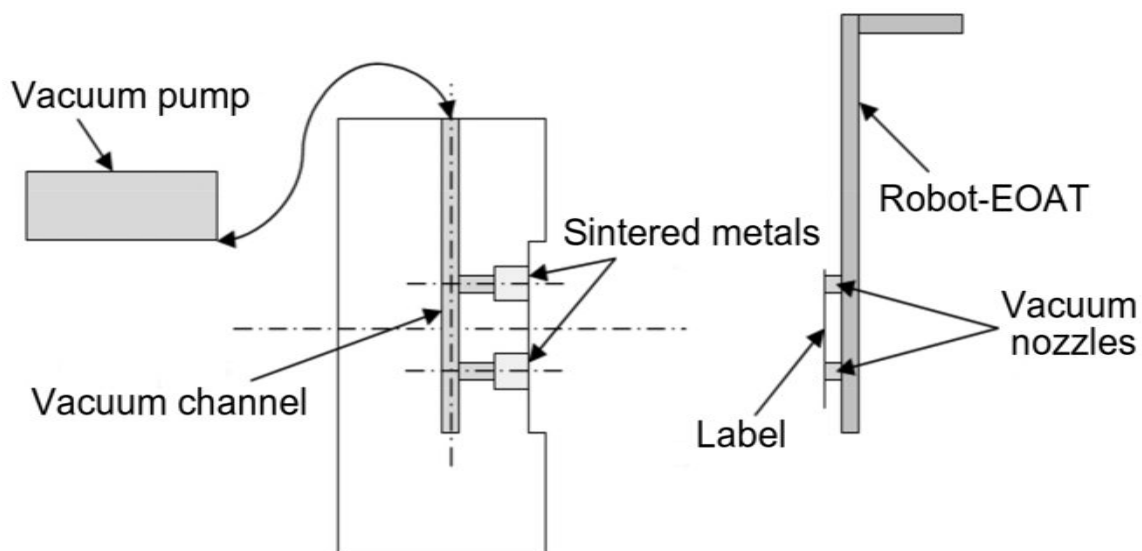
Figure 2.20: Label holding with vacuum

The use of vacuum appears to be most advantageous when the shape of the molded product requires complex preformed labels or when thick labels are to be injected as well as when the molded part and/or label are required to have a textured surface. Dealing with relatively thin labels, antistatic additives will make process easier and prevent static charges to create "block" of labels.

Holding with Electrostatics

Applying a static charge to hold the label in the injection mold eliminates the need for vacuum nozzles that are responsible for the higher cost of making and maintaining the mold [45]. In in-mold labeling with the use of a mold equipped with vacuum channels, static charge in the label stack may be considered to be an unwanted problem. To the contrary, considering the technique of pinning the label into the mold by an electrostatic attractive

force, it is necessary to control static charges to be able to feed, pick and deliver the labels and in the mold to make the label adhere long enough to have the melt injected and the label remains in the intended position.

Static electricity is an imbalance in the charge of a material, which means that there are a larger number of positive and/or negative charges than at equilibrium. A negatively charged surface has an excess of electrons and a positive surface is lacking electrons. A charged surface will produce an electrostatic field which is directed perpendicularly from any point of the surface. Static electricity does not flow across a surface or rather it moves very slowly which means that there will be a charge buildup with time when running a process. The strength of an electric field is defined in terms of the force that an imaginary test charge would experience if it was placed in the field. The magnitude, E, of an electric field at a particular location in an electrostatic system is the force acting upon a unit positive charge placed at that point. Thus, the force experienced by a point charge, q, in a field E is:

$$F = qE \qquad\qquad (2\text{-}8)$$

Units will be 1 Newton/C = 1 Nm/As = 1 V/m. In practical work kV/m is used rather than V/m. A practical way of representing the electrostatic field is by the use of field lines. At every point on a field line the direction of the field line is determined by the tangent to the field line at that point and the density of the field lines is a measure of the field strength.

In the electrostatic process, the robot picks up the label from the magazine with suction. A high static charge is placed on the label as the end-of-arm tool (EOAT) with the label approaches the mold surface. Then, the robot positions the label, releases the vacuum, and the label is transferred to the surface of the mold cavity. Neither vacuum in the mold nor adhesive on the label is needed (Fig. 2.21). When a static charge is placed on a label of suitable material and construction, the label will be attracted electrostatically to the grounded metal surface of the mold and may stick with excellent adhesion for up to several minutes. One caution to be taken when charging the label is that the label must contain no ink or coating with antistatic properties. Generally, labels should have good dielectric properties and should be a good insulator.

Using electrostatics to their full advantage requires the following components:

- A robot with a suitably designed end-of-arm tool (EOAT),

- A label magazine,

- A high-voltage DC charging power supply with adjustable output capability,

- A label of proper material and construction to accept and maintain a static charge.

Figure 2.21 illustrates the simplified electrostatic charging method used for round-shaped products. Use of a remote-mounted charging applicator is a simplified way to apply a charge. It requires little modification of the EOAT, is relatively easy to set up, and can satisfy the requirements of many different sizes and shapes of labels with the same charging applicator.

In this charging process, the robot picks up the label at the magazine, orients the label, and passes it by the charging bar. The surface is charged by a high voltage corona discharge (3-10 kV) from the tips of a small conical cluster of fine wires mounted on the underside of a light moveable plate. This plate is moved between the field meter sensing aperture and the material surface exposed through the instrument base plate. Corona is usually generated as a brief

pulse (20 ms) immediately before the plate is moved away. The plate moves fully away within 20 ms. The moving plate and instrument construction shield the field meter from high voltage connections so reliable measurements can be made down to even quite low surface voltages. The ground reference surface behind the label attracts the electric field from the charging bar and the label becomes charged. The robot places the label in position against the surface of the cavity, releases the vacuum to the suction cups, and the label stays in place on the surface of the mold.
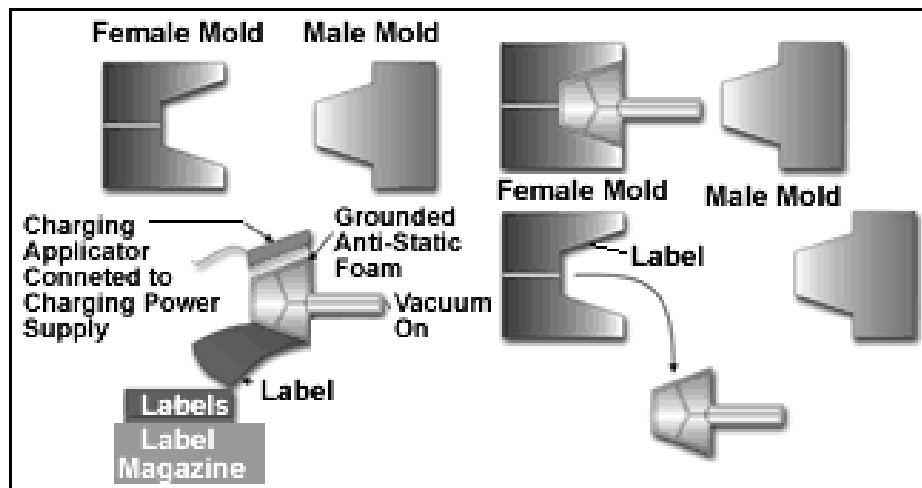
Figure 2.21: Simplified electrostatic charging for round-shaped products [46]

The fixture on the EOAT requires a grounded conductor such as a metal plate. The conductive surface should be at least as large as the label and mounted 6.35 to 12.7 mm directly behind the label [46]. The suction cups should have the minimum diameter necessary to provide sufficient holding power to prevent the label from slipping and attracting to the grounded conductive surface of the fixture.

All conductive components of the robot fixture must be grounded and should have rounded edges and corners. There should be no sharp edges or corners within 1 in. of the label [47].

2.3   Injection Molding Simulation

For 30 years, the CAE software for mold filling has been developed based on Hele-Shaw model. The calculation algorithms use finite element method for pressure and finite difference method for temperature, such as introduced by Hieber and Shen [1]. During the development of injection molding, plastic simulation tools are used to predict mold filling and the subsequent cooling process. Conventional algorithm extract mid-plane surface of the part to represent the 3D geometry. These simulation codes are usually referred to as 2.5D. It simplifies the 3D geometry model into 2.5D mid-plane and proceeds to the simulation [1]. This technology has been successfully applied to simulate the molding process of most thin shell plastic parts. In the past decade, 3D CAD systems have become widely available. However, 2.5D programs can't take advantage of these models. The effort required to generate 2.5D models from 3D models is sometimes equivalent to generating 3D information from scratch [2]. The preparation of such a mesh can take a considerable amount of time. Indeed model preparation now represents the greatest share of time of a filling analysis [48].

The widespread used simulation programs today take a basis of computation model, with which the three-dimensional, thin-walled geometry in two-dimensional shell elements is

illustrated. With the Hele-Shaw model, the momentum equation and mass equation can be described in a simplified form, in which the pressure loss is the only unknown quantity (so-called pressure loss equation). The interrelation between the volume throughput, the pressure loss and the position of the flow front can then be computed with the finite element method. Shear thinning behavior of the plastic melt are usually modeled with empirical approaches like e.g. Carreau, power law and Cross models. Temperature and shear rate dependent viscosity couples the pressure loss equation with the energy equation, which takes into account the three-dimensional thermal effects and is solved by means of the finite difference method. Since the computation consists of a two-dimensional flow and a three-dimensional temperature calculation, it can also be called as a 2.5D formulation. For thin-walled parts, 2.5D approaches provide good results in good agreement with the real process. However, technical plastic parts today have become thicker and more complex in their geometry. Therefore, the assumptions of the Hele-Shaw model are no longer valid for such a complex part. This effect led to the development of algorithms for the computation of three-dimensional mold filling processes. Only with the three-dimensional computation, it is possible to perform a realistic simulation of the critical features in the mold for example at the flow front, area with thickness jump and weld lines.

2.3.1 Concept of the Hele-Shaw Model (2.5D Analysis)

Since the thickness of most plastic products is far beyond the planar directions, their molding features can be described by shell model shown in the Figure 2.22.
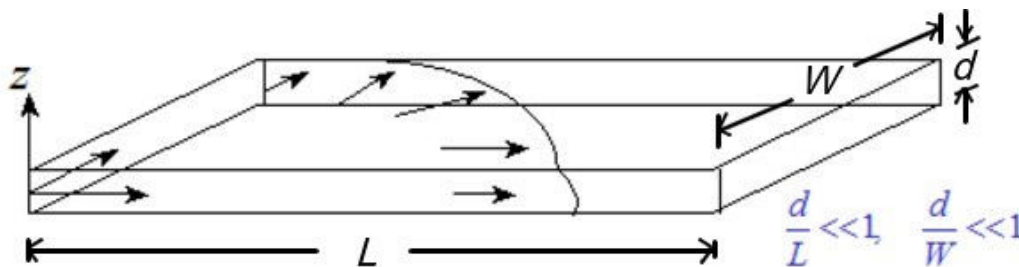
Figure 2.22: Definition of shell analysis

The general characteristics in shell model are listed as follows:

- When the thickness of the part is far beyond the planar direction (thickness/dimension ratio < 0.1), the gap-wise flow can be ignored.

- The combination of geometry approaching and thickness definition is called Thin Shell assumption, which features the shell model.

- To model a solid part, the geometry of the solid part is simplified into mid-plane model. At the same time, the corresponding thickness in gap-wise direction is specified as well to complete the geometrical modeling.

The key point is that the construction of mid-plane in the geometry (Fig. 2.23) requires familiarity with CAD tools, and so it is somehow not easy to generate shell model automatically. Besides, from physical solid model to shell model, users have to define the thickness of the mesh in form of an attribute by themselves (Fig. 2.24). The transition of the thickness (thickness jump) can be categorized into three forms as shown in Figure 2.24 (bottom). However, these types of the thickness jump will be considered the same during the analysis.
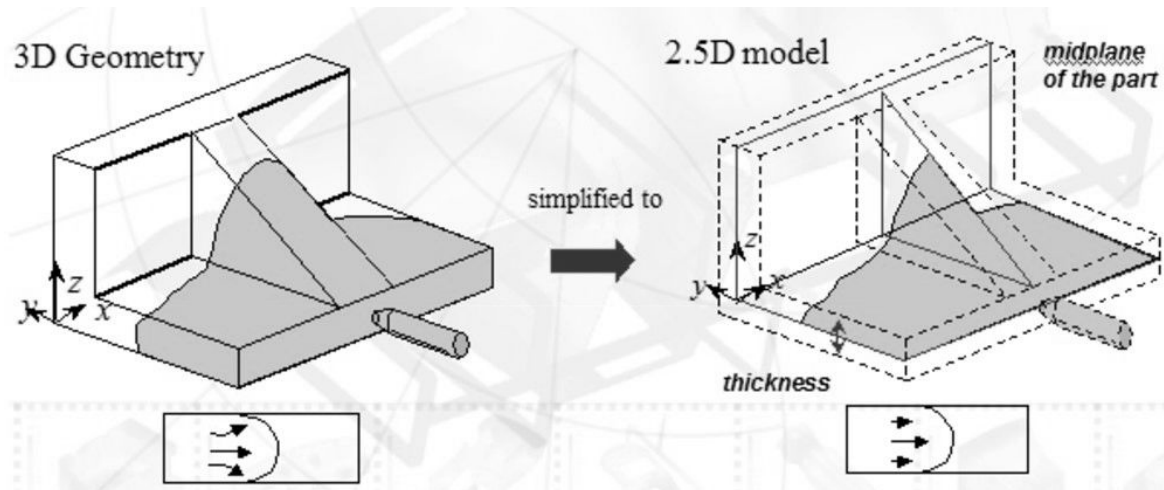
Figure 2.23: Modeling of shell model [49]
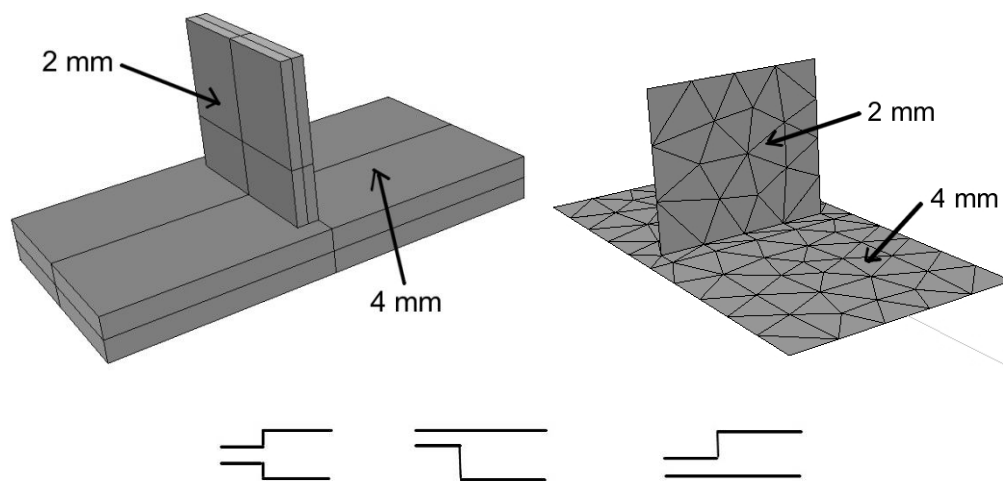
Figure 2.24: Thickness assignment in shell modeling

Governing Equations and Assumptions

Theoretically, the injection molding process is a three-dimensional, transient problem with moving melt front. Non-Newtonian fluid flow and coupled heat transfer problems are involved in this complicated process. The mathematical models for shell flow are governed by Hele-Shaw flow model under non-isothermal condition. In figure 2.23, x and y are the planar coordinates while z is the gapwise coordinate. Incompressibility of the fluid is assumed to be filled into a thin cavity and the gapwise velocity can be hence ignored. For general injected flows, it is reasonable to assume the viscous fluids with inertia effect neglected. In addition, heat convection in gapwise direction and the heat conduction in the flow direction could be ignored. The flow component in the thickness direction and thus the fountain flow are neglected. Moreover, normal stresses in the xy-plane are negligible compared to the high shear stresses in the xz-plane. Under these conditions, the momentum equation is reduced to

$$\frac{\partial p}{\partial x} = \frac{\partial}{\partial z}\left(\eta\frac{\partial \upsilon_x}{\partial z}\right); \quad \frac{\partial p}{\partial y} = \frac{\partial}{\partial z}\left(\eta\frac{\partial \upsilon_y}{\partial z}\right); \quad \frac{\partial p}{\partial z} = 0. \tag{2-9}$$

As a result of double integration of the equation (2-9) on the assumption that at the cavity surface the adhesion condition of the melt applies, the velocity distributions over the thickness of the cavity can be described as

$$v_x(z) = \left(\frac{\partial p}{\partial x}\right)\int_0^h \frac{z-z_0}{\eta(z)}dz; \quad v_y(z) = \left(\frac{\partial p}{\partial y}\right)\int_0^h \frac{z-z_0}{\eta(z)}dz. \tag{2-10}$$

With the introduction of fluidity S:

$$S = \int_0^h \frac{z^2}{\eta(\dot\gamma,T)}dz, \tag{2-11}$$

the average velocities $\bar{v}_x$ and $\bar{v}_y$ can be presented in form of the following relationships with the pressure loss:

$$\bar{v}_x = -\frac{S}{h}\left(\frac{\partial p}{\partial x}\right); \quad \bar{v}_y = -\frac{S}{h}\left(\frac{\partial p}{\partial y}\right). \tag{2-12}$$

Inserting these equations into the conservation of mass

$$\frac{\partial(h\cdot\bar{v}_x)}{\partial x} + \frac{\partial(h\cdot\bar{v}_y)}{\partial y} = 0, \tag{2-13}$$

results in

$$\frac{\partial}{\partial x}\left(S\frac{\partial p}{\partial x}\right) + \frac{\partial}{\partial y}\left(S\frac{\partial p}{\partial y}\right) = 0. \tag{2-14}$$

This equation represents a combination of conservation of momentum and mass and is designated as pressure loss equation. The pressure loss equation is coupled with the energy equation by the temperature-dependent viscosity contained in fluidity S. With the help of a dimensional analysis, terms of the smallest order can be eliminated. Thus, only terms for the heat convection in the xy-plane, the heat conduction in thickness direction as well as the heat dissipation remain in the energy equation:

$$\rho c_p\left(\frac{\partial T}{\partial t} + v_x\frac{\partial T}{\partial x} + v_y\frac{\partial T}{\partial y}\right) = \eta\dot\gamma^2 + \frac{\partial}{\partial z}\left(\lambda\frac{\partial T}{\partial z}\right). \tag{2-15}$$

The necessary boundary conditions have usually resulted from a coupling with the computation of the thermal conduction in the mold. In addition, to model the injection molding process, a viscosity function is required. A number of well-known models are available and they will be particularly described in the section 2.3.3.

2.3.2 Concept of Solid Modeling (3D Analysis)

The model of traditional shell analysis needs to be translated into mid-plane model. However, this translation is very difficult and time-consuming for complicated models, especially those

with significantly different thicknesses. Besides, the features of some parts are usually ignored such as round corners and regions in thickness jump. In solid or 3D analysis, users can decide whether to take them into considerations. The result of solid analysis provides information i.e. over fountain flow, corner effect, fiber-induced warpage etc. which cannot be derived from those of traditional shell analysis.
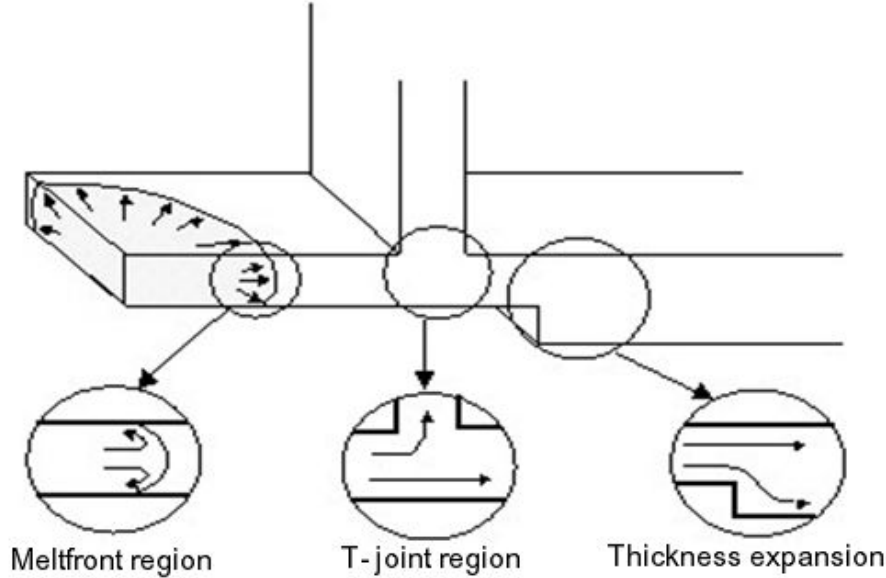
Figure 2.25: True 3D flow pattern

Figure 2.25 illustrates some 3D flow phenomena. These will be lost by using 2.5D model to simulate, such as flow passes expansion and contraction area, flow passes spheres, flow passes a small dimension-to-thickness ratio area, and flow of material containing fibers. In the injection molding process, filling of cavity is the first key step. Basically, it is a three-dimensional, transient problem with moving melt front. Non-Newtonian fluid flow and coupled heat transfer problems are involved in this complicated process.

Governing Equations and Assumptions

The mathematical models for solid flow (3D flow) are also governed by conservation of mass, the conservation of momentum, and the conservation of energy. For general injected flows, it is reasonable to assume them as the viscous fluids. At filling stage, both polymer and air are assumed incompressible. The polymer melt is assumed to behave as Generalized Newtonian Fluid (GNF). Hence the 3D flow motion can be mathematically described by the following equations:

Conservation of mass:

$$\frac{\partial \upsilon_x}{\partial x} + \frac{\partial \upsilon_y}{\partial y} + \frac{\partial \upsilon_z}{\partial z} = 0 \tag{2-16}$$

Conservation of energy:

$$\rho c_P \frac{\partial T}{\partial t} = \rho c_P \left(\upsilon_x \frac{\partial T}{\partial x} + \upsilon_y \frac{\partial T}{\partial y} + \upsilon_z \frac{\partial T}{\partial z} \right) + \frac{\partial}{\partial x}\left(\lambda \frac{\partial T}{\partial x} \right) + \frac{\partial}{\partial y}\left(\lambda \frac{\partial T}{\partial y} \right) + \frac{\partial}{\partial z}\left(\lambda \frac{\partial T}{\partial z} \right) + \eta \dot{\gamma}^2 \tag{2-17}$$

Conservation of momentum:

$$\frac{\partial}{\partial x}\left(2\eta\frac{\partial v_x}{\partial x}\right)+\frac{\partial}{\partial y}\left[\eta\left(\frac{\partial v_y}{\partial x}+\frac{\partial v_x}{\partial y}\right)\right]+\frac{\partial}{\partial z}\left[\eta\left(\frac{\partial v_z}{\partial x}+\frac{\partial v_x}{\partial z}\right)\right]-\frac{\partial p}{\partial x}=0$$

$$\frac{\partial}{\partial x}\left[\eta\left(\frac{\partial v_y}{\partial x}+\frac{\partial v_x}{\partial y}\right)\right]+\frac{\partial}{\partial y}\left(2\eta\frac{\partial v_y}{\partial y}\right)+\frac{\partial}{\partial z}\left[\eta\left(\frac{\partial v_z}{\partial y}+\frac{\partial v_y}{\partial z}\right)\right]-\frac{\partial p}{\partial y}=0 \qquad (2\text{-}18)$$

$$\frac{\partial}{\partial x}\left[\eta\left(\frac{\partial v_z}{\partial x}+\frac{\partial v_x}{\partial z}\right)\right]+\frac{\partial}{\partial y}\left[\eta\left(\frac{\partial v_y}{\partial z}+\frac{\partial v_z}{\partial y}\right)\right]+\frac{\partial}{\partial z}\left(2\eta\frac{\partial v_z}{\partial z}\right)-\frac{\partial p}{\partial z}=0$$

Generally, the density of the melt is assumed to be constant during filling phase (ρ=const.). In the holding phase, however, the compressibility of the melt must be taken into account, in which the reduction of the flow rate as a result of change of the pressure and temperature is computed.

The ignorance of the compressibility in the conservation of mass is permissible only during filling phase.

2.3.3 Viscosity Models for Thermoplastics

Viscosity is an index of the resistance of fluid to flow. The viscosity of simple fluids, for example water, is usually a constant value at constant temperature. These fluids are generally referred to as Newtonian fluids. The viscosity of thermoplastics is, however, very complicated and very nonlinear. Unlike simple fluids, the viscosity of thermoplastic depends on its chemical structure, composition and processing conditions. With a given chemical structure and formulation, viscosity of thermoplastics depends primarily on the temperature, shear rate and pressure. To understand the viscosity nature of thermoplastics, shear stress, shear rate and viscosity must be first defined.

The viscosity of thermoplastics shows strong dependence on temperature. Typically, viscosity drops dramatically when temperature increases. Two temperature dependence of the viscosity that are widely accepted, namely Arrhenius (Exponential) model and William-Landel-Ferry (WLF) model will be described later. Many different mathematical models used for describing the steady shear viscosity behavior of thermoplastics have been proposed. But the most acceptable viscosity models for one dimensional flow are described below.

Power-Law Model:

$$\eta = K\left(\dot{\gamma}\right)^{n-1} \qquad (2\text{-}19)$$

where η is the viscosity, $\dot{\gamma}$ is shear rate, n is the Power Law Index, and K is the consistency index. For a Newtonian fluid, Power Law Index = 1; for a shear-thinning fluid, this value lies between 0 and 1 and for a shear-thickening fluid, it is greater than 1.

The Power-Law model has the weak point in determining the viscosity of the melt in the upper Newtonian region that is the region with low shear rate. Using this model in filling simulation may cause the over-estimation of the viscosity at low shear rate region.

Carreau Model:

$$\eta = \frac{\eta_0}{\left[1 + \left(\frac{\eta_0}{\tau^*}\dot{\gamma}\right)\right]^{1-n}}$$ (2-20)

where η_0 is the zero shear (Newtonian) viscosity, τ^* represents the critical shear stress roughly characterizing transition shear stress from the Newtonian range to the pseudo plastic region, and n represents the shear rate sensitivity, $0 < n < 1$, where 1-n roughly characterizes the slope of the line over the pseudo plastic region in the logarithmic plot.

Modified Cross Model:

$$\eta = \frac{\eta_0}{1 + \left(\frac{\eta_0}{\tau^*}\dot{\gamma}\right)^{1-n}}$$ (2-21)

A general form of the constitutive equation for incompressible non-Newtonian fluid can be written as follows:

$$\underline{\sigma} = -p\underline{E} + \underline{\tau} = -p\underline{E} + 2\eta(I_i)\underline{D}$$ (2-22)

The apparent viscosity η in the above equation is a function of the first (I_1), second (I_2) and third (I_3) invariants of the rate of deformation tensor. For incompressible fluids, the first invariant becomes identically equal to zero. The third invariant vanishes for simple shear flows and is normally neglected in non-viscometric flows as well. The apparent viscosity then is a function of the second invariant alone. Hence the second invariant can be written as:

$$I_2 = \sum_i \sum_j \dot{\gamma}_{ij} \cdot \dot{\gamma}_{ji}$$ (2-23)

Viscosity is a decreasing function of temperature. The temperature-time superposition principle of viscoelasticity describes the dependence of viscosity on temperature as follows. It states that a change in the temperature from T_1 to T_2 does not affect the functional dependence of η on $\dot{\gamma}$, but merely alters the zero shear viscosity and the shear rate at which transition from Newtonian to pseudoplastic behavior occurs. As temperature increases, the viscosity curve at T_1, in the log (η) versus log ($\dot{\gamma}$) plot, is shifted by a "shift factor" log(a_T) given by:

$$a_T = \frac{\eta_0(T_1) \cdot T_2 \cdot \rho_2}{\eta_0(T_2) \cdot T_1 \cdot \rho_1}$$ (2-24)

Where ρ_1 and ρ_2 denote the densities at the temperature values T_1 and T_2, respectively. The temperature effect on the viscosity function η is described in many references [50, 51, and 52] by the Arrhenius equation. This law states that for thermorheologically simple fluids the shift factor a_T is given by

$$\log a_T = \frac{E_0}{R}\left(\frac{1}{T_1} - \frac{1}{T_2}\right), \tag{2-25}$$

where E_0 is the fluid activation energy in J/mol and R = 8.314 J/molK is the universal gas constant. Equation (2-22) describes temperature dependence well for thermorheologically simple, (partially crystalline) polymers. This is because glass transition region for such materials lies well below their fluid state. For amorphous thermoplastic materials, on the other hand, the glass transition region is close to their fluid state. Free volume effects predominate and the Arrhenius-WLF equation

$$\log a_T = \frac{E_0}{R}\left(\frac{1}{T_1} - \frac{1}{T_2}\right) - b_1\left(\frac{T_1 - T_2}{b_2 + T_2 - T_1}\right) \tag{2-26}$$

should be used instead of equation (2-25), where b_1 and b_2 are parameters to be determined.

2.3.4 Thermal Equation of State

When numerical simulations are involved, a mathematical representation of the specific volume is necessary. With the help of a thermal equation of state like the Tait equation [53] and the Spencer and Gilmore equation [54], the dependence of the density on pressure and temperature (pvT-data) can be described. Tait equation assumes that the specific volume only depends on pressure and temperature. Modifying the Tait equation for amorphous polymers was done by Chang [55] in order to include the cooling rate effect. Zoller [56] showed that the Tait equation yields a good representation only of semi-crystalline polymer melts, while the description of the compressibility behavior of solid semi-crystalline polymers is quite unsatisfactory.

The Spencer and Gilmore equation is derived from the ideal gas law by adding a pressure and temperature correction term to the specific volume:

$$\left(v - b^*\right)\cdot\left(p + p^*\right) = \frac{R \cdot T}{W} \tag{2-27}$$

$$v = \frac{R \cdot T}{W\left(p + p^*\right)} + b^* = \frac{1}{\rho} \tag{2-28}$$

$$\rho = \frac{1}{v} = \frac{W \cdot \left(p + p^*\right)}{b^* \cdot W \cdot \left(p + p^*\right) + RT} \tag{2-29}$$

where $b^*\left[\dfrac{cm^3}{g}\right]$ = specific individual volume of the macromolecule,

$p^*\left[bar\right]$ = cohesion pressure,

$W\left[g/mol\right]$ = molecular weight of the monomer,

$$R \left[\frac{energie}{mol \cdot K} \right] = \text{universal gas constant.}$$

However, the Spencer and Gilmore equation is not valid in the temperature range below the melting point.

For the simulations in this thesis, a modified Tait model (Eq. 3-3) is used. This model can predict the abrupt volumetric change for semi-crystalline polymers and it is also suitable for amorphous polymers.

Because the melt is assumed to be incompressible, the thermal equation of state will be disregarded for the conservation of mass and momentum. However, for the holding simulation, compressibility of the melt must be regarded and the thermal equation of state must be taken into account to both equations.

2.3.5 Numerical Discretization Methods

In the design of engineering structures, numerical simulation plays an increasingly important role. This can be attributed to the high costs or practical difficulties related to experiments, which have to confront rapid advances in the computational power and the resulting decrease in the costs for computer simulations. However, in order to supplement or even replace experiments, simulation approaches have to fulfill strong requirements. An essential demand is that the simulation calculations are efficient and lead to accurate and reliable results (Fig. 2.26). This in turn will depend upon the mathematical model of the physical problem which must be solved with a specific simulation tool by applying assumptions about the loading situation, initial and boundary conditions.

The mathematical model of a physical problem is described using partial differential equations, which comprise different physical parameters. An analytical solution of these equations as a system is not always possible because of their complexity and non-linearity. Because of this, a numerical method is necessary for solving the problem. The numerical method requires a discretization of the equation system and a reformulation of the differential equations into an algebraic form. The discretization is usually a compromise between coarse and fine meshing. With a relatively coarse discretization, the solutions of the problem will be attained with fewer resolutions. With extremely fine discretization, almost unlimited simulation time results. Generally for the solution of complex flow in injection molding, four numeric discretization methods are used:

- Finite difference method (FDM),
- Finite element method (FEM),
- Boundary element method (BEM),
- Finite volume method (FVM).

The **finite difference method** is widespread since the 1930s and used to solve partial-differential equations. Because of its simplicity, this discretization method is applied to many models with simple geometry. A finite difference is a mathematical expression of the form $f(x + b) - f(x + a)$. If a finite difference is divided by $b - a$, one gets a difference quotient. The approximation of derivatives by finite differences plays a central role in finite difference methods for the numerical solution of differential equations, especially boundary value problems [57, 58, 59, and 60]. FDM shows a disadvantage when meshing a complex

geometry. In injection molding simulation, FDM is used to calculate the melt temperature development during molding.

The **Finite element method** is well known since the 1960s with the beginning of the computer age and used for finding approximate solutions of partial differential equations (PDE) as well as integral equations such as the heat transport equation. The solution approach is based either on eliminating the differential equation completely (steady state problems), or rendering the PDE into an approximating system of ordinary differential equations, which are then solved using standard techniques such as finite differences, Runge-Kutta, etc [61, 62, and 63]. In solving partial differential equations, the primary challenge is to create an equation that approximates the equation to be studied, but is numerically stable, meaning that errors in the input data and intermediate calculations do not accumulate and cause the resulting output to be meaningless. The Finite Element Method is a good choice for solving partial differential equations over complex domains (like cars and oil pipelines), when the domain changes (as during a solid state reaction with a moving boundary), when the desired precision varies over the entire domain, or when the solution lacks smoothness.

Comparison to the finite difference method

The finite difference method (FDM) is an alternative way for solving PDEs. The differences between FEM and FDM are the following [64]:

- The finite difference method is an approximation to the differential equation; the finite element method is an approximation to its solution.

- The most attractive feature of the FEM is its ability to handle complex geometries (and boundaries) with relative ease. While FDM in its basic form is restricted to handle rectangular shapes and simple alterations thereof, the handling of geometries in FEM is theoretically straightforward.

- The most attractive feature of finite differences is that it can be very easy to implement.

- There are reasons to consider the mathematical foundation of the finite element approximation more sound, for instance, because the quality of the approximation between grid points is poor in FDM.

- The quality of a FEM approximation is often higher than in the corresponding FDM approach, but this is extremely problem dependent and several examples to the contrary can be provided.

The **boundary element method** is a numerical computational method of solving linear partial differential equations which have been formulated as integral equations (i.e. in boundary integral form). It can be applied in many areas of engineering and science including fluid mechanics, acoustics, electromagnetics, and fracture mechanics [65, 66, 67, 68, 69 and 70]. The boundary element method attempts to use the given boundary conditions to fit boundary values into the integral equation, rather than values throughout the space defined by a partial differential equation. Once this is done, in the post-processing stage, the integral equation can then be used again to calculate numerically the solution directly at any desired point in the interior of the solution domain. The boundary element method is often more efficient than other methods, including finite elements, in terms of computational resources for problems where there is a small surface/volume ratio. Conceptually, it works by constructing a "mesh" over the modeled surface. However, for many problems boundary

38

element methods are significantly less efficient than volume-discretization methods (Finite element method, Finite difference method, Finite volume method).
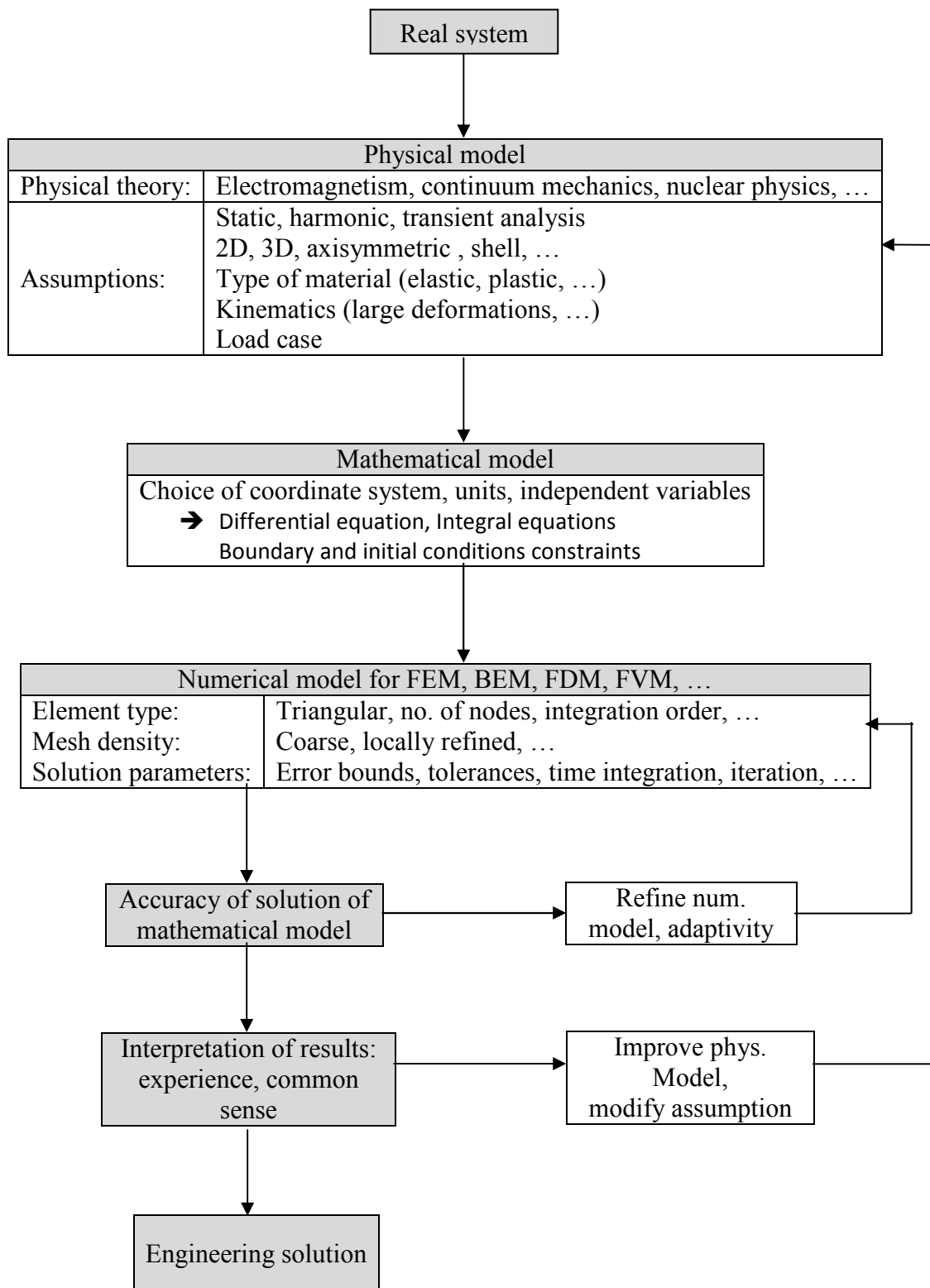
Figure 2.26: Physical and mathematical modeling [71]

The most noticeable difference between FEM and BEM and one of the important advantages of the latter concerns the discretization. While in FEM the complete domain has to be discretized, the BEM discretization is restricted to the boundary, as depicted in Figure 2.27-2.28. Depending on the complexity of geometry and load case, this can lead to important time saving in the creation and modification of the mesh. Apart from this, Boundary Element Methods usually possess advantages when dealing with stress concentration problems or with problems involving infinite or semi-infinite domains, e.g., acoustics, soil-structure interaction etc [71]. A basic feature of all Boundary Element Methods is their use of fundamental solutions, which are analytically free space solutions of the governing differential equation under the action of point source. The fact that they are exact solutions accounts for some of the advantages of the BEM for example the improved accuracy in the calculation of stresses and exterior problems.
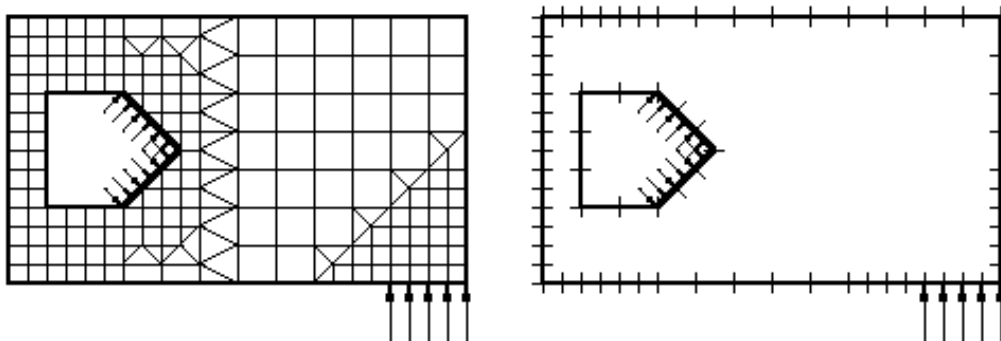
Figure 2.27: Discretization of a FEM model (left) and a BEM model (right)
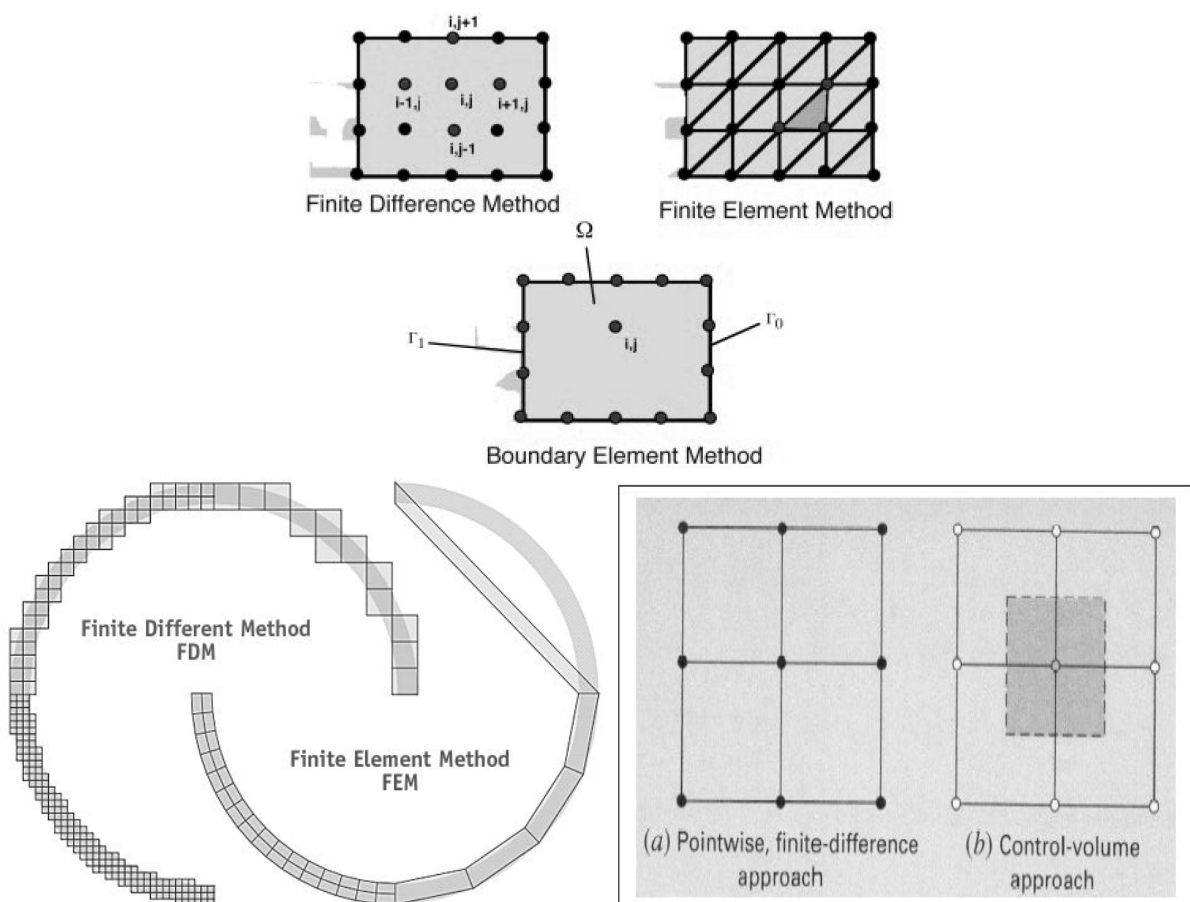
Figure 2.28: Comparison between the discretization methods

The **finite volume method** is a method for representing and evaluating partial differential equations as algebraic equations. Similar to the finite difference method, values are calculated at discrete places on a meshed geometry. "Finite volume" refers to the small volume surrounding each node point on a mesh. In the finite volume method, volume integrals in a partial differential equation that contain a divergence term are converted to surface integrals, using the divergence theorem. These terms are then evaluated as fluxes at the surfaces of each finite volume. Because the flux entering a given volume is identical to that leaving the adjacent volume, these methods are conservative. Another advantage of the finite volume method is that it is easily formulated to allow for unstructured meshes. The method is used in many computational fluid dynamics packages. The most compelling feature of the FVM is that the resulting solution satisfies the conservation of quantities such as mass, momentum, energy, and species. This is exactly satisfied for any control volume as well as for the whole computational domain and for any number of control volumes. Even a coarse grid solution exhibits exact integral balances. FVM is the ideal method for computing discontinuous solutions arising in compressible flows. FVM is also preferred while solving partial differential equations containing discontinuous coefficients [71].

3 Flow Analysis and Simulation in Injection Molding based on the Double-Plated Part with Non-Uniform Part Thickness

A number of simulation packages are nowadays commercially available for the simulation of the injection molding process, one of these is Moldex3D®. The objective of the flow analysis of the injection mold is to observe flow behavior of polymer melt during the mold filling, holding, and cooling. By means of simulation, it is possible to anticipate the way the mold cavity is filled. However, with an increase in the complexity of the molded parts or in case of non-uniform part thicknesses, 2.5D simulation loses its precision of predicting the flow of polymer melt within the cavity. With 3D simulation, on the other hand, better agreement between the real injection molding process and the simulation is generally provided. According to this, experiments on the mold filling of the double-plated part with non-uniform part thickness were conducted. As a preliminary examination, this study was done in order to acquire better understanding of the simulation program Moldex3D prior to its application in the injection in-mold labeling. The experimental results were then compared to those from 2.5D and 3D simulations.

The investigation of the injection molding simulation based on the double-plated part with non-uniform part thickness can be subdivided into three subtasks:

1. Simulation on a basis of surface mesh (2.5D simulation)

2. Simulation on a basis of volume mesh (3D simulation)

3. Comparison of all simulation results with the real process

3.1 Design of Experiments

3.1.1 Part Geometry

In order to examine the efficiency and accuracy of 2.5D and 3D simulation in terms of predicting the mold filling behavior of the polymer melt, a special double-plated part with non-uniform part thickness was modeled (Fig. 3.1).
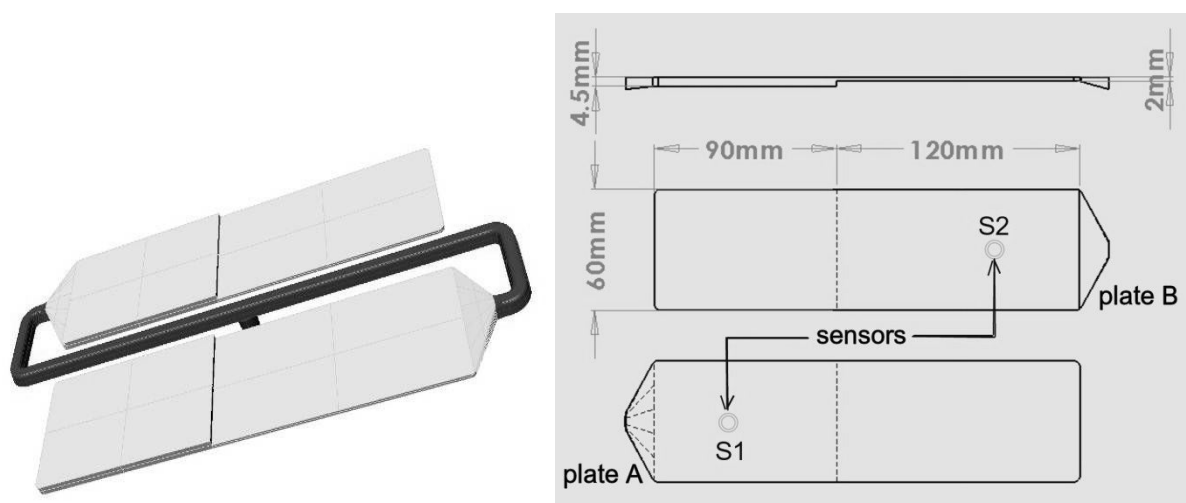
Figure 3.1: Geometry of the model

Figure 3.1 shows the part model and its dimensions used for all simulations and the injection molding processes. This molded part has the dimensions of 60x210 mm with the thickness of

2 mm on the thin side of the part and 4.5 mm on the thick side. During filling phase, polymer melt flows through the cold runner with the trapezoidal-shaped cross-section and the fan gates into the cavities.

3.1.2 Material Properties

The resin used was a polypropylene of the type Novolen 3200 MC supplied by BASF AG., Germany. A constitutive model that provides a good fit of the viscosity data and has been shown to provide an accurate prediction of mold filling is the Cross model [16]

$$\eta = \eta_0 \left[1 + \left(\frac{\eta_0 \dot{\gamma}}{\tau^*} \right)^{1-n} \right]^{-1}, \qquad (3\text{-}1)$$

where η_0 denotes the zero shear viscosity and n and τ^* are material constants. The temperature and pressure dependence of the viscosity is captured through η_0 with a simple exponential function [49]:

$$\eta_0 = C_1 \exp\left(\frac{C_2}{T} \right) \qquad (3\text{-}2)$$

Where C_1 and C_2 are material constants and T is the temperature. The numerical computations presented in this study are performed based on the viscosity data and thermal properties provided by the Moldex3D's material databank, which are shown in Figure 3.2.
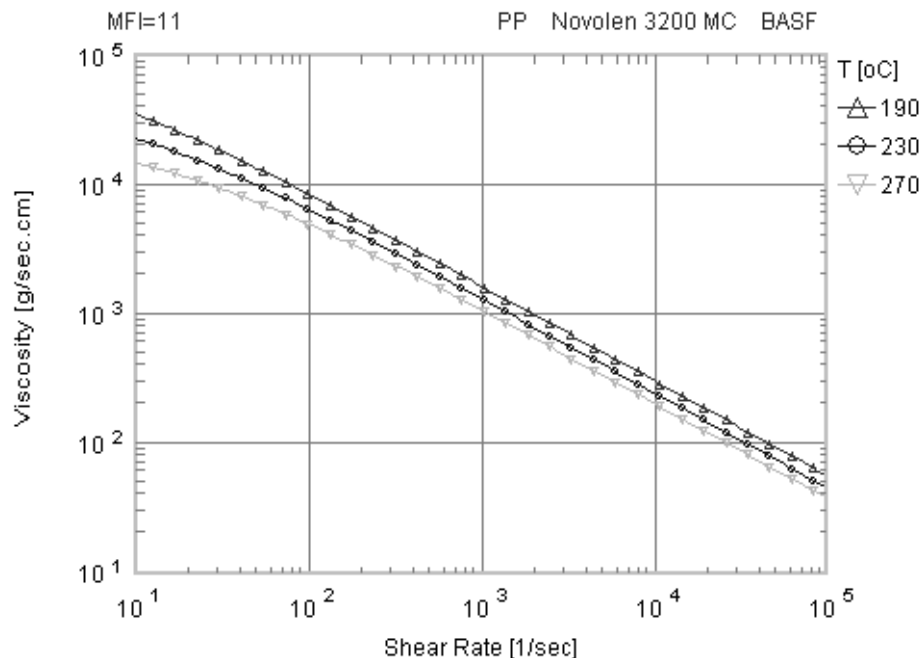
a)
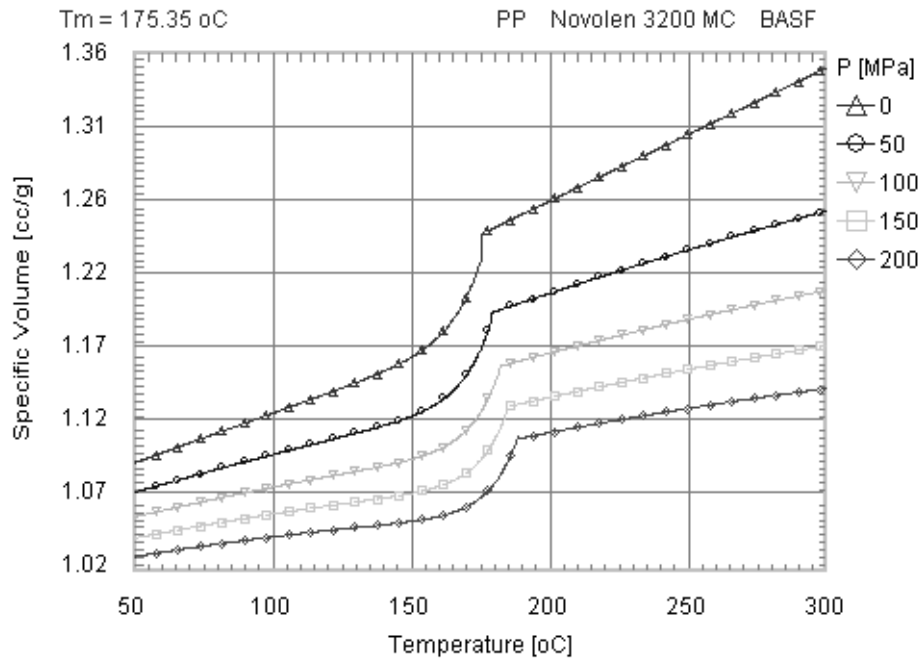
Figure 3.2: Viscosity (a) and pVT-diagram (b) of Novolen 3200 MC from Moldex3D databank

Modified Tait equation (Eq. 3-3) is used to model the pVT behavior of the plastic material during the end-of-filling/holding phase.

$$V(p,T) = V(0,T)\left[1 - C \cdot \ln\left(1 + \frac{p}{B(T)}\right)\right] + V_t(p,T) \tag{3-3}$$

where

$$V_0(T) = \begin{cases} b_{1m} + b_{2m}T, T > T_t, melt\ state \\ b_{1s} + b_{2s}T, T < T_t, solid\ state \end{cases}$$

$$B(T) = \begin{cases} b_{3m}\exp(-b_{4m}T), T > T_t, melt\ state \\ b_{3s}\exp(-b_{4s}T), T > T_t, solid\ state \end{cases}$$

$$V_t(p,T) = \begin{cases} 0, T > T_t, melt\ state \\ b_7\exp(b_8T - b_9p), T > T_t, solid\ state \end{cases}$$

$$T \equiv T - b_5$$

transition temperature: $T_t \equiv b_5 + b_6 p$

for amorphous polymers: $b_{1m} = b_{1s}$

for crystalline polymers: $b_{1m} > b_{1s}$

C = 0.0894 (universal constant)

Modified Tait equation describes the variation of density (specific volume) with temperature and pressure in the melt and the solid states, between room and processing temperature over a wide pressure range.

3.1.3 Machine Setting

A Krauss Maffei 150-ton injection molding machine with a stroke volume storage capacity of 377 cm^3 and a 50 mm screw diameter was employed in the experimental study. The machine is capable of screw velocities up to 91.6 mm/s and injection pressure up to 1,638 bars.

Specification	Value
Model	Krauss Maffei Injection molding machine (KM 150-620 B2)
Max. clamping force [t]	150
Screw diameter [mm]	50
Max. stroke volume [cm^3]	377
Max. injection speed [mm/s]	91.6
Max. volume throughput [cm^3/s]	180
Max. screw speed [min^{-1}]	326
Max. injection pressure [bar]	1638

Table 3.1: Specification of the injection molding machine

Machine parameter	Experiment
Cylinder temperature [^{o}C]	195
Mold temperature [^{o}C]	40
Max. Injection pressure [bar]	1,200
Holding time [s]	30
Cooling time [s]	20
Injection speed [%]	50
Holding pressure [bar]	500

Table 3.2: Machine settings for the injection molding

Table 3.1 shows the specification of the injection molding machine used. Experiments were performed with the machine setting as listed in the table 3.2. Only in the short-shot study, the injection velocity was set at 50 % of the maximum injection velocity and with no holding

pressure applied. Holding time, however, was set for 30 s, in order to accomplish the sufficient part stiffness to be ejected. The stroke volume was then reduced stepwise by increasing holding switch. After the cavity is approximately 98 % filled, the injection machine will switch from filling phase to holding phase with the holding pressure and duration defined. In this study, the holding pressure of the machine was kept constant for all the experiments.

3.1.4 Melt Pressure and Melt Temperature Detection by means of a Combined Pressure and Temperature Transducer

In order to measure course of the pressure and melt temperature during the injection molding process, so-called "combined pressure and temperature sensor" type MTPS 408-IR (Fig 3.3) supplied from FOS-Messtechnik GmbH. were used in this work. Two of such transducers with the sensor front diameter of 4 mm were mounted into the injection mold. The sensor was embedded into the mold by which its front absolutely lies on the cavity wall. This ensures the direct melt temperature measurement, compared with the conventional contact temperature sensor like thermocouple that measures the mold temperature instead. In addition, an IR temperature sensor has the advantage over the thermocouple in the measurement accuracy in that the shear heating of the melt is ignored. Furthermore, the emissivity of materials does not tend to change very much with temperature when using a thermometer which operates over a narrow waveband.

Figure 3.3: Combined pressure and temperature sensor for plastic injection molding [72]

The combined sensors offer the possibility of detecting the melt temperature and the melt pressure in the mold cavity time-dependently. The IR melt thermometer measures the actual melt temperature in a temperature range between 30 $^{\circ}$C and 400 $^{\circ}$C, while the pressure sensor serves for the measurement of the melt pressure in the cavity within a range between 0 and 2000 bars. The combined sensors used were positioned into the stationary mold half of the injection mold at 42 mm away from the fan gate of each cavity (Fig. 3.1).

Infrared (IR) sensors (see Appendix 8) allow a fast response, non-intrusive measurement of melt temperature [73, 74] by measuring heat radiated as infrared energy through a sapphire window. Measured temperatures are highly dependent upon the emissivity of the polymer being measured which depends on the polymer type and the presence of additives. The absorption of the polymer determines the effective depth of penetration of the measurement which, then again, depends upon the filler content if exists [75]. Quoted penetration depths for these sensors are 2-7 mm, although experimentally [73] these have been found to range from 0.033 to 7 mm.

Piezoelectric transducers measure the charge generated on a piezoelectric crystal under an applied stress or load. Piezoelectric pressure sensors measure dynamic and quasi-static pressures, and are not apt at measuring nearly static loads (e.g. extrusion) due to leakage of the charge over time [76]. The common voltage mode uses an amplifier to convert the high impedance charge into a low-impedance output voltage. Continued improvements in piezoelectric sensors have yielded sensors that are robust with respect to structural design and signal conditioning. Given that piezoelectric sensors have very high stiffness and provide for direct charge generation under applied load, these sensors provide for very fast dynamic response, typically on the order of microseconds.

3.2   Simulation on a Basis of Surface Mesh (2.5D Simulation)

3.2.1 Discretization of the Model

Firstly, the geometry of the model created in SolidWorks® was imported into Rhinoceros®, a plug-in for Moldex3D®, where the actual discretization was conducted. In Moldex3D® no CAD-model can directly created, since it is really a pure simulation program for the injection molding.

In Rhinoceros®, the imported CAD-model can be meshed by different meshing tools, for example tetrahedral meshing for the surface mesh and hexahedral, prism, or voxel meshing for 3D or volume mesh. After defining the required mesh size, the discretization of the model can now be started. Description of the simulation program Moldex3D® is shown in Appendix 2.

Discretization in the thickness direction of each surface mesh section must be defined separately as attributes after surface meshes have been successfully generated. Figure 3.4 and 3.5 illustrate tetrahedral derivative surface mesh and voxel derivative surface mesh of the model, respectively. They are surface meshes derived from the 3D tetrahedral and voxel discretizations. Square-shaped voxel derivative surface mesh extracted from the shell of 3D voxel mesh generation was automatically re-discretized into regular triangle meshes of the same size, since 2.5D simulation process can only be performed with the triangle mesh geometry. Tetrahedral derivative mesh can be trouble-freely taken over to the surface mesh of the triangle form. The cold runner of the two mesh models was meshed automatically with rod elements.

Apart from the discretization of the model comprising two plates connected by the cold runner, models of an individual plate with non-uniform part thickness were also created and meshed in the same manner as the double-plated model. These individual mesh models were used to compare the melt front advancement with that from the double-plated mesh model.

Course of the melt pressure and melt temperature can also be determined by the simulation. By placing two sensor nodes (at the comparable positions where the combined sensors are mounted in the mold) onto the mesh model, computed melt pressure and temperature can be revealed in form of the x-y plots.
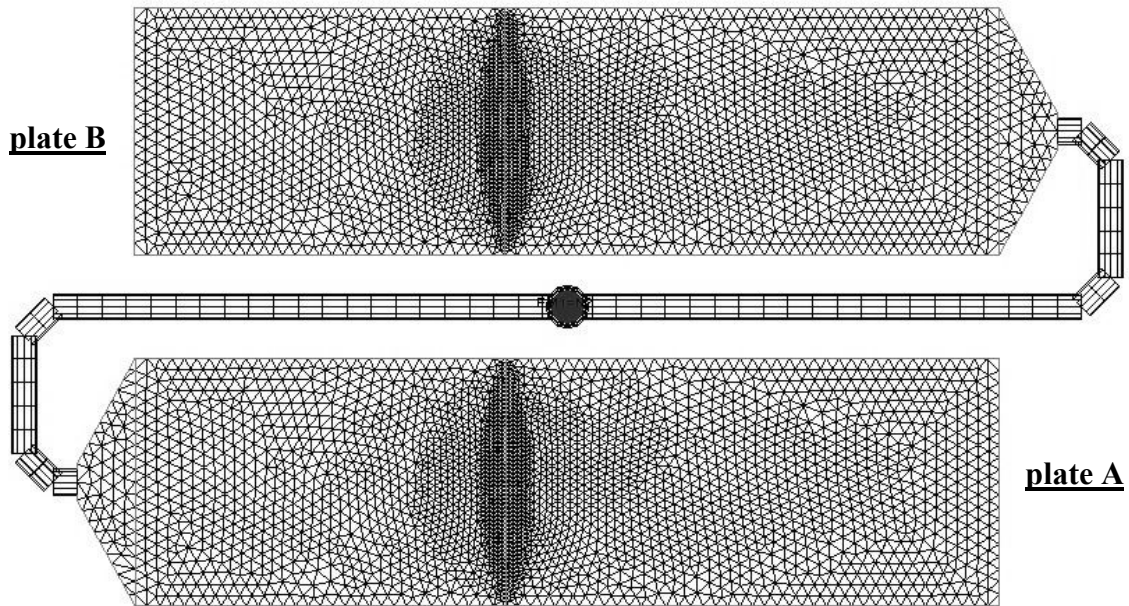
Figure 3.4: Tetrahedral derivative surface mesh (global mesh size 3 mm, 1 mm at the transition)
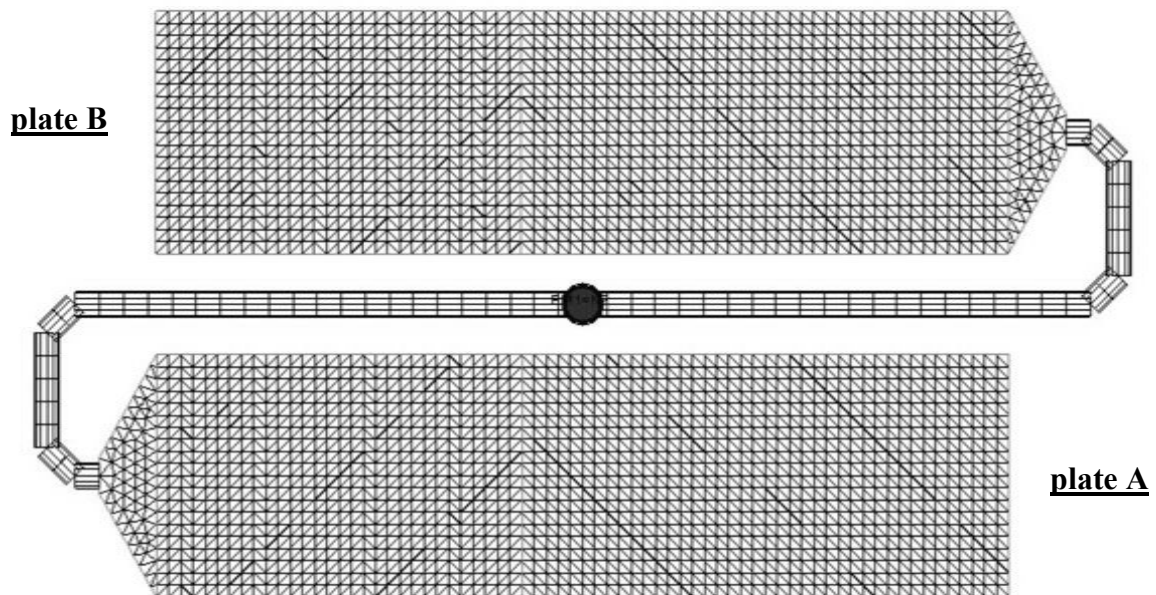
Figure 3.5: Voxel derivative surface mesh (global mesh size 3 mm)

Table 3.3 shows the number of part elements of the two surface mesh types.

Element type	Number of part element		
	Double plate	**Plate A**	**Plate B**
Tetrahedral derivative surface mesh	10,658	5,329	5,333
Voxel derivative surface mesh	5,896	2,951	2,949

Table 3.3: Number of part element of the surface mesh

_____

3.3 Simulation on the Basis of Volume Mesh (3D Simulation)

3.3.1 Discretization of the Model

Figure 3.6 illustrates the 3D discretization of the double-plated model. The double-plated model was discretized by means of the FEM-method. The discretization of the model was performed by three different mesh types: tetrahedral, voxel and prism meshes, respectively. In order to compare the effect of the mesh types as well as the number of mesh layers over the part thickness on the accuracy of the simulation results compared with the real molding process, part model was meshed with these mesh types and each with the different number of mesh layers over the thick and the thin section of each plate. By this concept, mesh models fall into two main categories: mesh with one-two layers and three-six layers in the thin-thick section of the plates (Fig. 3.7).
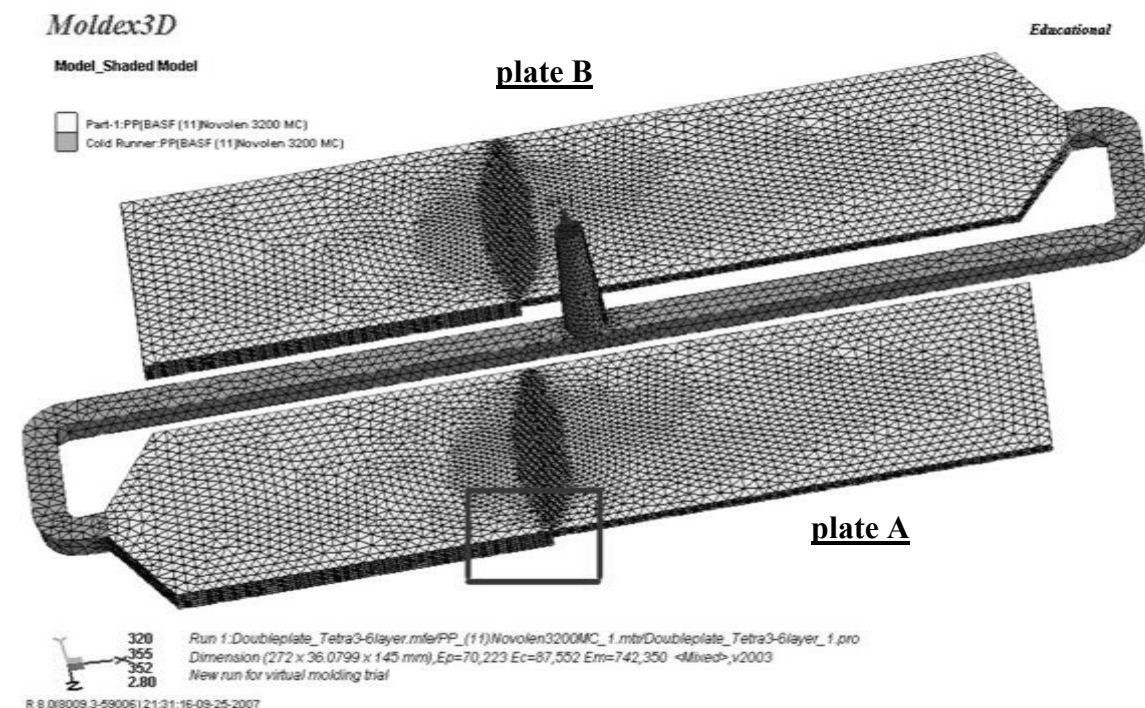
Figure 3.6: Volume mesh of the double-plated model

Like 2.5D simulation, two sensor nodes which function as the combined pressure and temperature sensors are placed onto the surface of the volume mesh at the comparable position where the combined sensors are mounted in the mold, in order to detect course of the melt pressure and melt temperature and to compare them with those from the real molding process.

In a same way as the 2.5D discretization, two individual plate models were separated from the double-plated part, which had been first connected to each other by the S-shaped cold runner. These separated plates were then discretized with tetrahedral, prism, and voxel mesh types with one or three mesh layer counts in the thin side and three or six mesh layer counts in the thick side of each plate, respectively.

Auto tetrahedral meshing method is the easiest method for three-dimensional solid mesh creation. The advantage of the auto tetrahedral method is its convenience. The disadvantages of this method are that there are too many elements and it is hard to control the mesh quality.

Users are usually not able to control the element layer count of the whole part. In this study, however, there was an attempt to create the tetrahedral mesh with the desired element layer count. By splitting the side walls of the part into as many sections as the number of the layer count required (Fig. 3.7, top), two, three or six element layer counts could be manually generated.
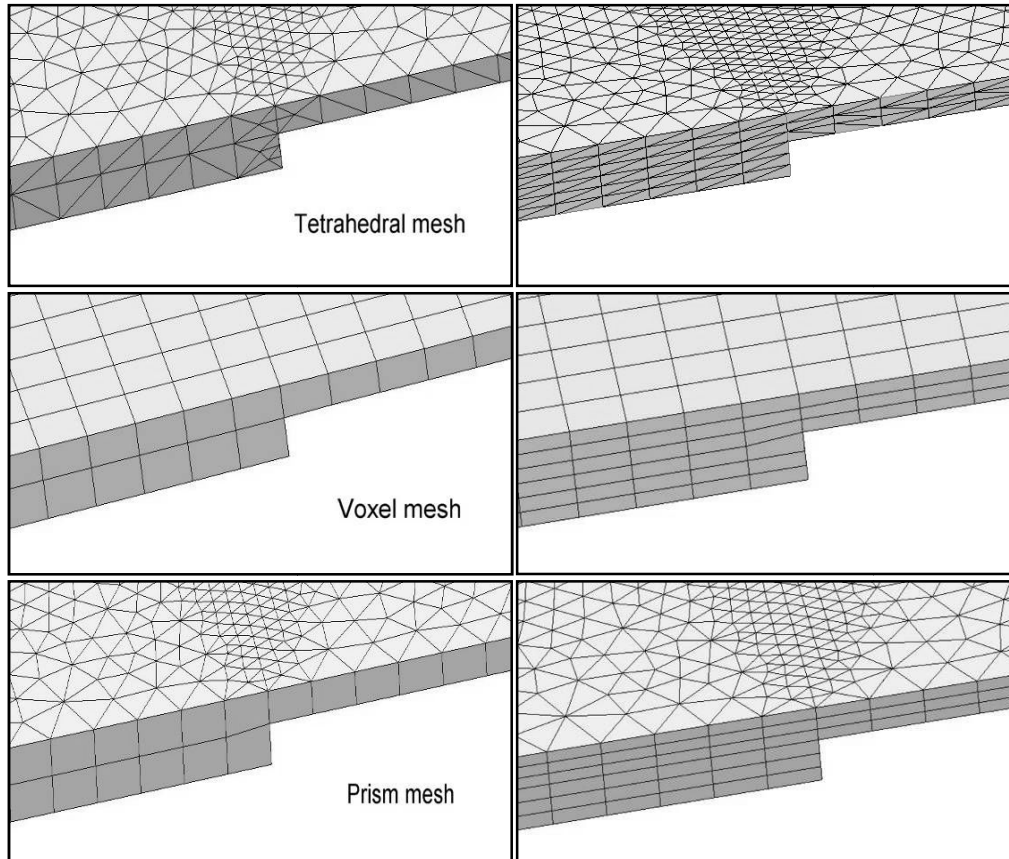
Figure 3.7: Close-up view of the 3D mesh models

Recently, the voxel method (also known as hexahedral meshing) has been applied to design systems in the various fields. In the voxel method, the mesh can be generated automatically and directly from a three dimensional model. It is possible to make the mesh of the very complicated boundary form [77]. Mesh generation by the voxel method is shown in Figure 3.7 middle. The calculation domain was divided into thousands of meshes, all of which are cubical in form. The size of each mesh could be kept uniform across the whole domain. In this study, the generation of a voxel mesh was performed automatically in Rhinoceros®. Two voxel meshes with one-two and three-six mesh layers across the part thickness were generated. In order to study the effect of the number of mesh layer counts on the accuracy of the simulation results.

Table 3.4 shows the number of part elements generated by different types of mesh. Note that, during the number of element of voxel and prism meshes with 3-6 layer counts has almost doubled in value compared to that of their 1-2 layer counts, the number of elements of tetrahedral mesh with 3-6 layer counts rose only slightly compared to its 1-2 layer counts. This resulted from the limitation that the part model must be subdivided into three or six sections over the part thickness prior to the discretization. However, the inside of the part remains unpartitioned, since it is only a hollow space and there are no concrete surfaces in it. After partitioning of the part surface, the definition of the mesh size can be done on each

surface partition. It is possible to create surfaces within the hollow part in order to achieve the concrete surfaces which can be partitioned and meshed later. Nevertheless, it was so time-consuming and arduous that creating surfaces within the hollow part was abstained.

Element type	Number of part element					
	1-2 layers			3-6 layers		
	Double	Plate A	Plate B	Double	Plate A	Plate B
Tetrahedral volume mesh	65,956	34,660	34,469	70,223	36,910	36,488
Voxel volume mesh	11,275	7,275	7,156	20,348	11,999	11,533
Prism volume mesh	22,211	12,739	12,631	53,071	28,356	27,903

Table 3.4: Number of the part element from different volume meshes

3.4 Simulation Parameters

All 2.5D and 3D simulations were conducted using the same machine setting parameters as in the real molding process (Table 3.2). With Moldex3D's 2.5D simulation, it is necessary to define the number of mesh layers across the part thickness self-reliantly. In this study, 2.5D simulations were conducted with the mesh layer count of 10, 20, and 30 layers in order to evaluate the effect thereof on the accuracy of the simulation results. Mesh layer count is one of the simulation parameters that affects the accuracy of the simulation results and can be varied independently during the simulation. Usually, the higher the number of mesh layers, the higher the accuracy and the longer the simulation time result.

3.5 Simulation Results and Its Comparison with the Real Injection Molding Process

In order to trace the progression of the melt in mold cavities, mold-filling simulations were performed on double-plated part with non-uniform part thickness. The validity of the filling analysis was confirmed by comparison of flow front predictions, pressure, and temperature developments with full-shot and short-shot experiments on the double-plated geometry as shown in Figure 3.1. Two-dimensional and three-dimensional mold filling simulations were also compared with each other in order to acquire the best results.

Element type	Calculation time [s]		
	Double plate	Plate A	Plate B
Tetrahedral derivative surface mesh	1,516	635	581
Voxel derivative surface mesh	662	228	252

Table 3.5: Calculation time as a function of the surface mesh type

Element type	Calculation time [s]					
	1-2 layers			3-6 layers		
	Double	Plate A	Plate B	Double	Plate A	Plate B
Tetrahedral volume mesh	6,515	3,169	3,249	6,966	3,325	3,233
Voxel volume mesh	877	511	570	1,997	947	903
Prism volume mesh	2,061	1,038	1,025	5,396	2,628	2,526

Table 3.6: Calculation time as a function of the volume mesh type

Table 3.5 and 3.6 display the calculation times of filling and holding simulations as a function of surface and volume mesh types, respectively. Concerning the time used to compute filling and holding simulations, it is clear that owing to smaller amounts of elements of the surface mesh of the comparable model, less calculation time is required. 2.5D simulation is also advantageous over 3D simulation regarding the reliability and simulation time when molded parts are simple in form.
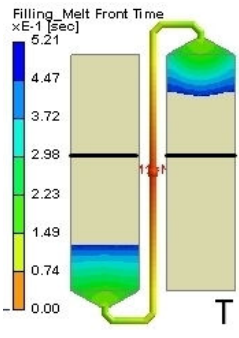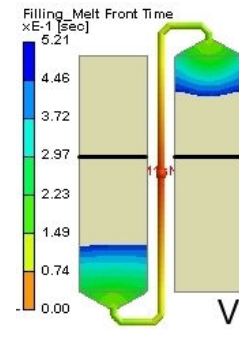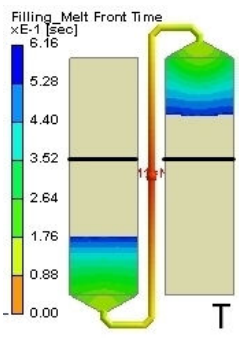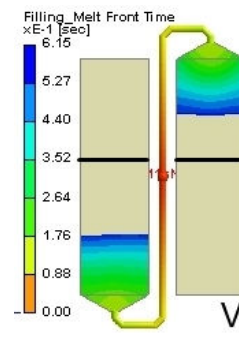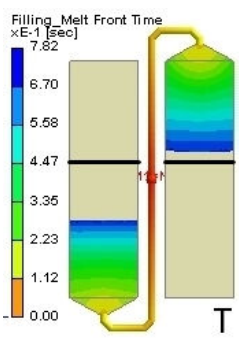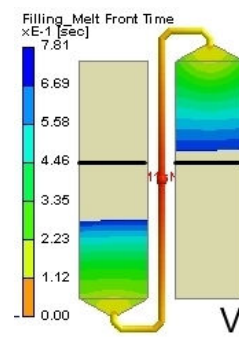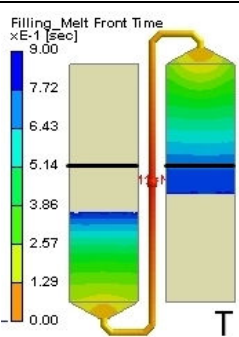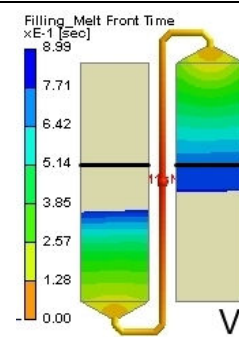
3.5.1 Filling Analysis (Short-Shot Study)

The advancement of the melt front at different filling times is displayed by different color bands. From the melt front advancement one can

- Examine filling/holding pattern of the molding,
- Check potential incomplete filling (short shot) process,
- Check unbalanced flow/over-pack-induced flashing problems,
- Identify weld line locations,
- Identify air trap locations,
- Check flow contribution from each gate for runner balance,
- Check proper gate location to balance flow and eliminate weld lines.

Figure 3.8 shows the comparison of the melt front progression in filling phase between the experiment and 2.5D simulations. Simulations were performed with the standard solver and based on non-isothermal computation using 20 mesh layer counts over the part thickness defined. Standard solver is a fast and easy solid solution of Moldex3D which requires moderate mesh resolution in computing. From the figure, the simulation results agree well with the real injection molding process. As already described, in the real injection molding process, the right cavity of the part was completely filled prior to the left cavity at the filled volume of around 78 %. Then holding followed and the changeover of the holding direction within the two cavities resulted after holding had ended. The simulation results derived from the tetrahedral derivative and the voxel derivative meshes are nearly identical in quality and when compared with the melt advancement from the real process this proves the higher accuracy of 2.5D simulation over 3D simulation (Fig. 3.9), particularly in predicting the filling progression of this specific double-plated part. Both computed melt front times were comparable, step by step, to those in the real molding process. At 78 % filled volume, the

computed melt fronts of the two derivative meshes had reached the end of the right cavity, while the melt front in the left cavity was computed somewhat further than that in the real molding process. However, this is the only deviation being found by 2.5D simulations.

	Short-shot study	Tetrahedral derivative mesh	Voxel derivative mesh
32 % filled			
38 % filled			
49 % filled			
56 % filled			
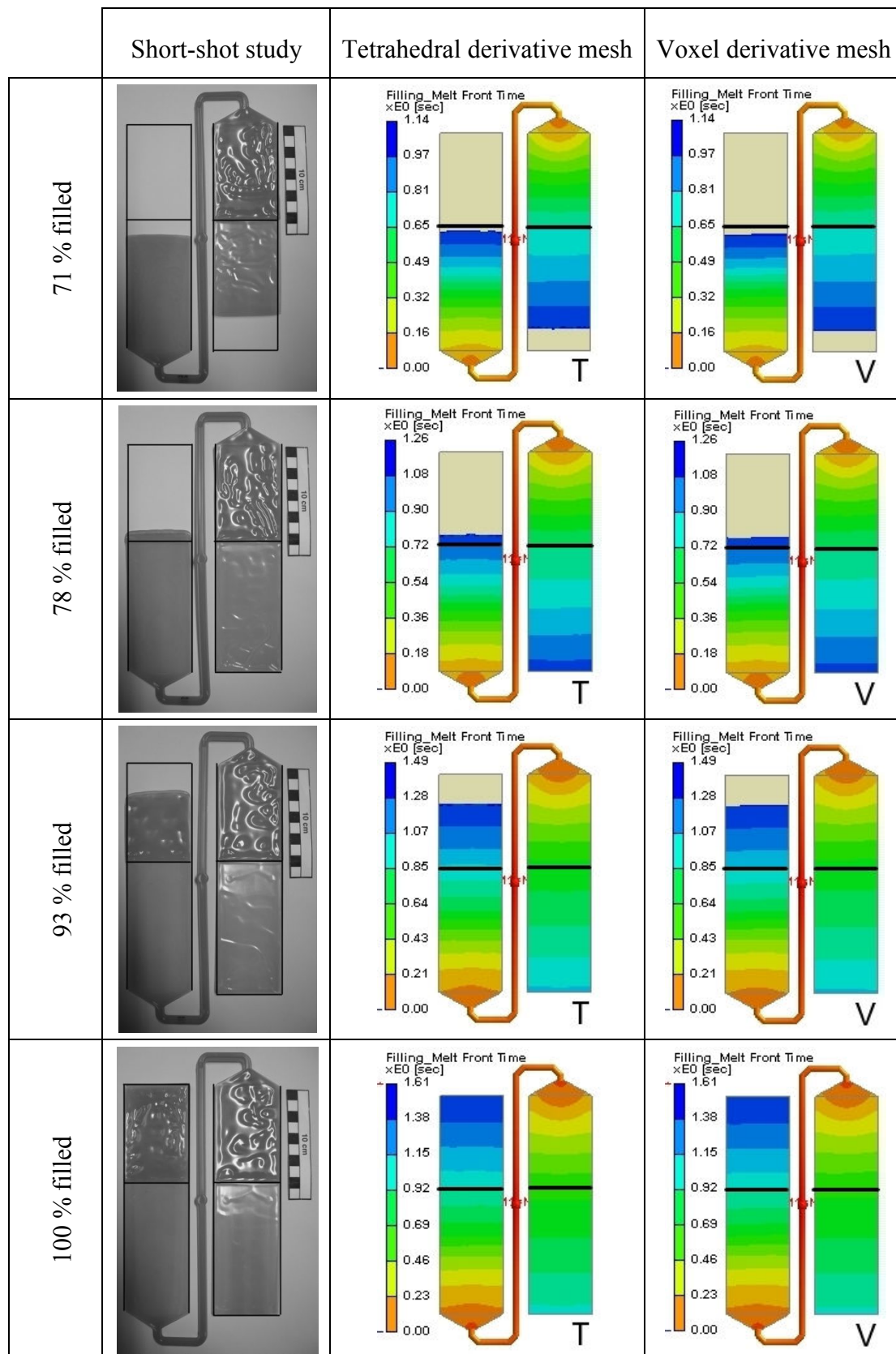
Figure 3.8: Short-shot study from the experiment and 2.5D simulations (with 20 layers defined)

54

	32 % filled	38 % filled	49 % filled
Prism mesh 3-6 layers	P3-6	P3-6	P3-6
Prism mesh 1-2 layers	P1-2	P1-2	P1-2
Voxel mesh 3-6 layers	V3-6	V3-6	V3-6
Voxel mesh 1-2 layers	V1-2	V1-2	V1-2
Tetrahedral mesh 3-6 layers	T3-6	T3-6	T3-6
Tetrahedral mesh 1-2 layers	T1-2	T1-2	T1-2
Short-shot study			

	56 % filled	71 % filled	78 % filled
Prism mesh 3-6 layers			
Prism mesh 1-2 layers			
Voxel mesh 3-6 layers			
Voxel mesh 1-2 layers			
Tetrahedral mesh 3-6 layers			
Tetrahedral mesh 1-2 layers			
Short-shot study			

Figure 3.9: Comparison of the melt front progression between the experimental study and 3D non-isothermal simulations

Figure 3.9 shows the melt front advancement derived from the short-shot study (left) of the real molding process and 3D simulation results using different mesh types. Usually in a short-shot study, the injection molding of the part is carried out without the holding pressure, which results in a high degree of part shrinkage. By doing this, the real melt front progression will be obtained without any manipulation of the flow front from the holding pressure. In this study, 3D simulations were performed with standard solver and based on non-isothermal computation. In the real molding process, flow deceleration phenomena have been involved in the filling phase. The melt spread from the fan gates into the cavities until 35 % filled volume where the melt advancement in both cavities was almost the same. At the filled volume of about 38 %, melt front gradually expanded and changed its shape from the fan-shaped nearly to the parallel one. At the 49 % filled volume, melt front in the thick section of the right cavity advanced further than in the thin section of the left cavity. At this stage, because of less flow resistance in the thick section of the right cavity, flow deceleration in the thin section of the left cavity developed and the melt in thick section can therefore advance a little bit more quickly than in the other section. As time went by, the melt in the thick section of the right cavity that had experienced less flow resistance spread faster than in the thin section of the left cavity. As the melt front in the thick section of the right cavity had crossed the transition where the part thickness suddenly changes, the flow velocity increased. Despite the increasing flow resistance as a result of the smaller cross-section area in the thin section of the right cavity, the melt front velocity in this section increased, since the injection velocity was set constant. While the right cavity was completely filled at around 78 % filled volume, the melt front in the left cavity was just found at slightly behind its transition. Right after the first cavity has been completely filled, holding of this cavity took place. At the same time, the left cavity was further filled with the holding pressure until this cavity was totally filled and almost no melt flow deceleration existed at this time. Although the thick section of the left cavity was merely filled with the holding pressure, melt front velocity in this section increased compared to the thin section of the same cavity as it passed through the transition. This is because of the lower flow resistance as well as the fact that the holding pressure, which also drives the melt to flow, dedicates to the filling only in this section of the left cavity.

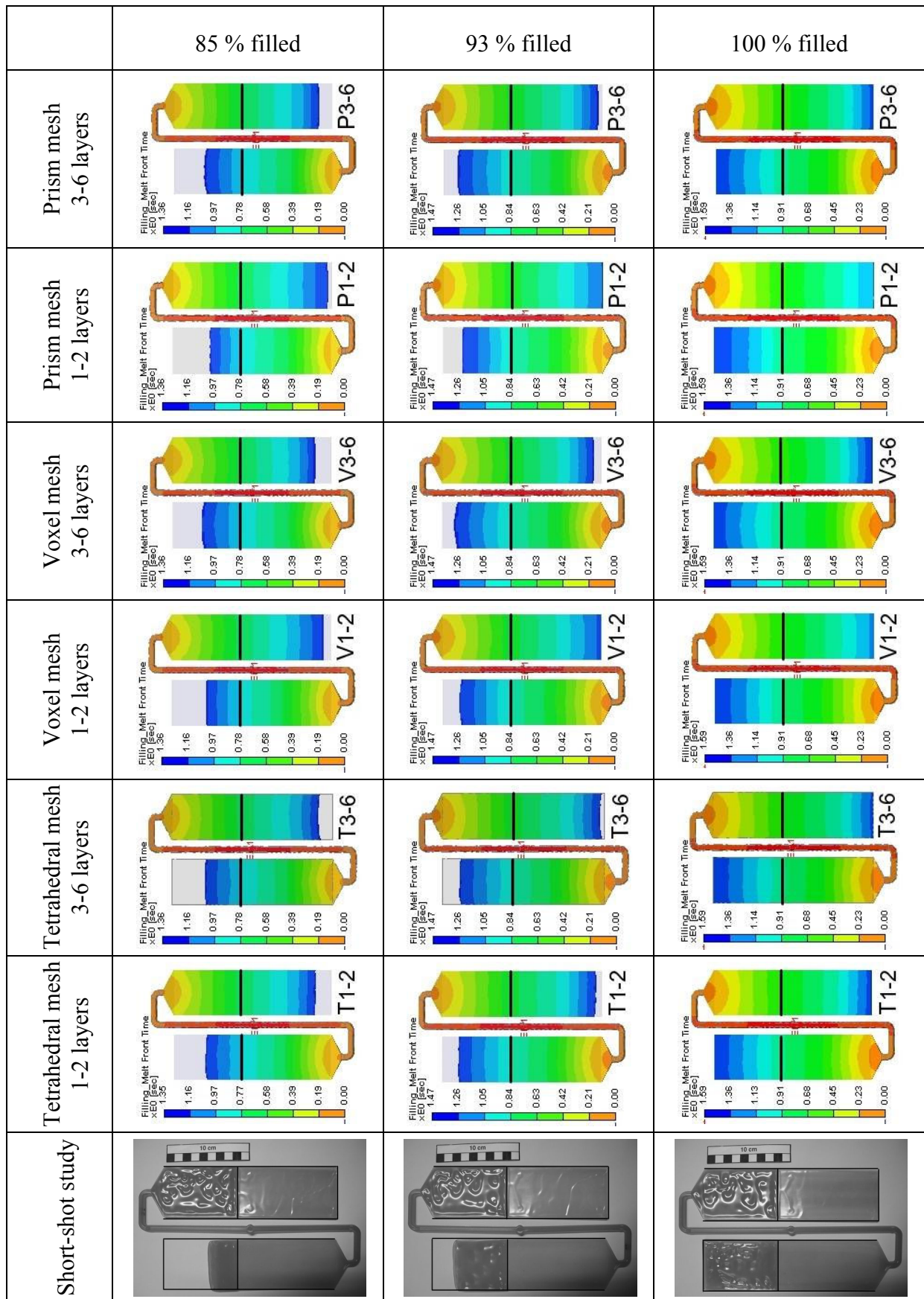Usually, the accuracy of the simulation results depends highly upon the mesh quality and the mesh resolution. Moreover, to compute the molding properties which differentiate over the part thickness e.g. melt temperature effectively, part in the thickness direction must be meshed generally suggested with 3 mesh layer counts. Considering 3D simulations with different mesh types and numbers of mesh layers (Fig 3.9), at the beginning of the molding process, the results from the mold filling simulations are nearly identical in filling pattern up until the shape of the melt front. Some simulation results show the melt front in convex form, the others in concave form. But these are not important in predicting the flow behavior of the melt in the cavity. Much more important is the so-called melt front time (term used in Moldex3D®), which is the position of the melt front in the cavity as a function of the filling time. With the melt front time, occurrence of weld line and air trap, for example, can also be predicted.

According to Figure 3.9, differences in filling can already be seen at 78 % filled volume. With the voxel mesh with 1-2 layer counts (1 mesh layer in the thin section and 2 mesh layers in the thick section of the part) and the prism mesh with 1-2 layer counts, the melt front in the right cavity advances somewhat faster and thus farther than the other meshing types. Compared to the real molding process, however, all the computed melt front advancements deviate from that of the real molding process, which has already reached the end of the right

cavity. At this point, filling phase has terminated. In the left cavity, the melt advancement of all the simulations slightly exceeds the real molding situation. At 85 % filled volume, the melt fronts in the right cavity of the voxel mesh with 1-2 layer counts and the prism mesh with 1-2 layer counts nearly approach the end of the cavity, while these of the other meshing types remain farther away from the end of the cavity. In the left cavity, all the computed melt fronts advance farther than the melt front of the real process. Not until the 93 % filled volume have the melt fronts of the voxel mesh with 1-2 layer counts and the prism mesh with 1-2 layer counts reached the end of the right cavity. In the left cavity, the computed melt fronts are at the position comparable to that of the real molding process.

The effect of the number of mesh layers over the part thickness on the accuracy of the simulation results were not clearly confirmed by this study. Usually, with more mesh layers, the accuracy and calculation time increase. Instead, no distinct improvement in the accuracy of predicting the melt front advancement was acquired.

Tetrahedral meshing compared to prism and voxel meshing was verified to be the worst method concerning the accuracy of the simulation results and calculation time (see Table 3.6), since its mesh quality is poor and the number of elements created by tetrahedral meshing in one part is markedly high compared to the uniform elements generated by prism or voxel meshing. Surprisingly, the 3D simulation results, independent of the mesh types and the number of mesh layers over the part thickness, deviated much from the actual molding situation. This resulted mainly from the numerical instability of the 3D-filling simulation of Moldex3D®. This double-plated part is a highly complex part regarding the flow and pressure imbalance between the two plates with non-uniform part thickness. Flow deceleration has also been involved in filling because of the different flow resistances in the cavities. Since the source code of this simulation program is unknown, no further statement can be made by now.

Based on simulations of the double-plated part proposed in this study, all the simulation results has shown that 2.5D numerical computation of Moldex3D® is more stable and more reliable than its 3D numerical computation. This is evidence that 3D simulation does not always function correctly and if a complex flow system involved as can be seen in the molding of the double-plated part, limitations of the simulation program become conspicuous. Since it is possible to set the simulation parameters in Moldex3D® freely, another 3D simulation process based on the isothermal computation with the standard solver was carried out in order to examine the effect of the computational mode setting on the accuracy of the simulation results. The result of mold filling simulation based on the isothermal computation is introduced in Figure 3.10. From this figure, melt front progression in each filling step of the isothermal based computation of 3D simulation agrees well with that from the real molding process. Compared to the results of 3D simulation based on non-isothermal computation shown in the Figure 3.9, obvious improvement in predicting the melt front advancement and the proximity of the results of the isothermal based computation of 3D simulation to the real process were astonishingly provided. At the beginning of filling, however, outrunning of the computed melt front remained unsolved. In addition, the simulation results show that at every filling step the right cavity always has higher degree of filled volume than the other. The tendency of the right cavity to be filled prior to the other was thus given by isothermal based 3D simulation. At 78 % filled volume, the simulation shows that the right cavity was completely filled and began to be packed by the holding pressure, while the melt front in the left cavity had already passed its transition. The rest of the cavity filling from the simulation did not substantially differentiate from the real process.

The reason why the isothermal simulation results better agree with the real process, which is not usual, is based on the assumption that with the complex flow balance induced from the flow resistance differentials and the pressure changeover between the two cavities, non-isothermal numerical computation of the filling pressure as a function of the flow velocities and temperature became instable which resulted in the wrong prediction in pressure level and pressure balancing between the two cavities (Fig. 3.17) and thus the melt advancement was foretold in the incorrect way.
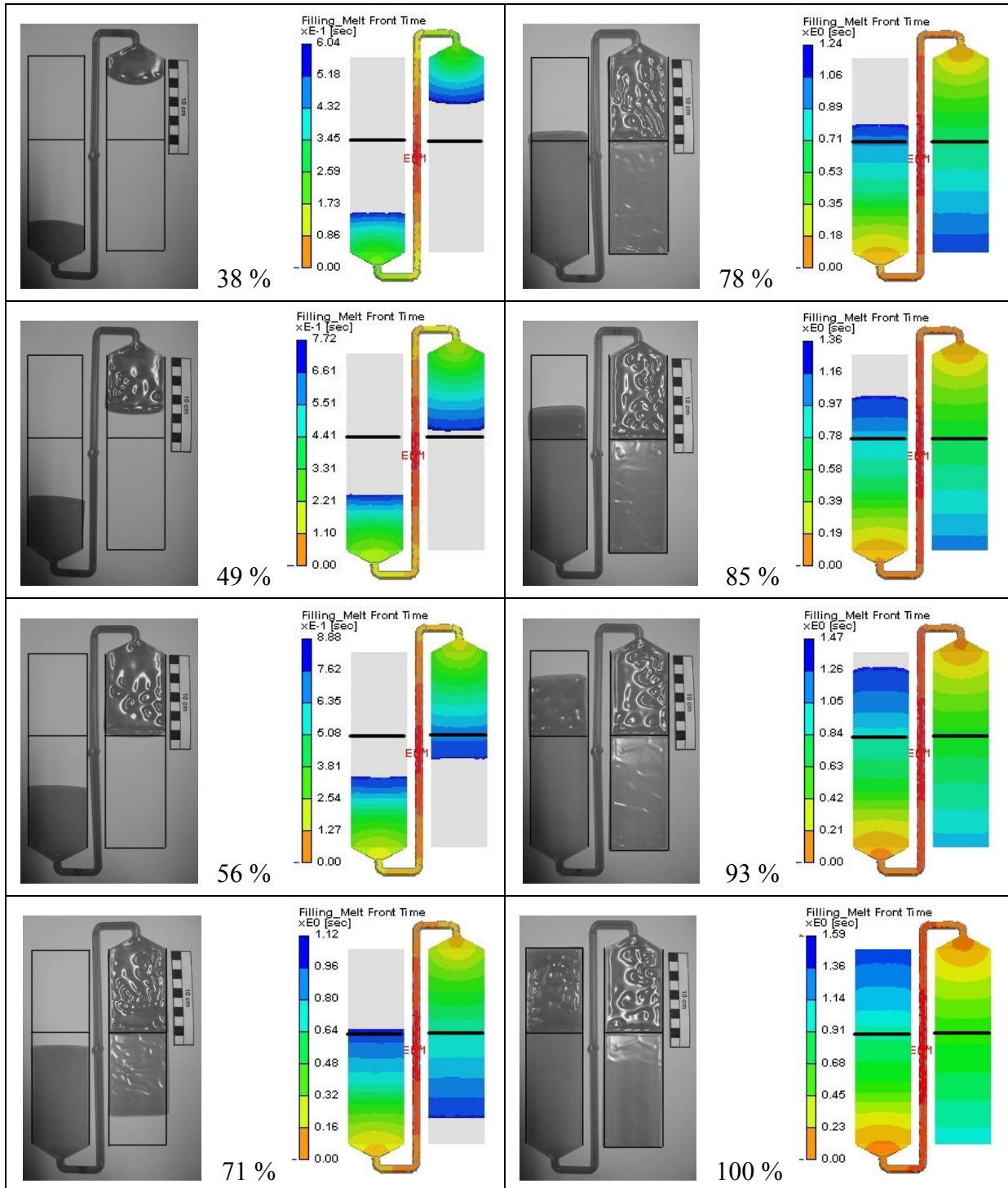
Figure 3.10: Comparison of the melt front progression between the experimental study and 3D simulation with prism mesh 3-6 layers based on the isothermal computation

	Short-shot study	Tetrahedral derivative mesh	Voxel derivative mesh
100 % filled			
87 % filled			
73 % filled			
60 % filled			
46 % filled			
32 % filled			

Figure 3.11: Comparison of the melt front progression of the left cavity (plate B) between the experimental study and 2.5D simulations

	32 % filled	46 % filled	60 % filled
Prism mesh 3-6 layers	P3-6	P3-6	P3-6
Prism mesh 1-2 layers	P1-2	P1-2	P1-2
Voxel mesh 3-6 layers	V3-6	V3-6	V3-6
Voxel mesh 1-2 layers	V1-2	V1-2	V1-2
Tetrahedral mesh 3-6 layers	T3-6	T3-6	T3-6
Tetrahedral mesh 1-2 layers	T1-2	T1-2	T1-2
Short-shot study			

	73 % filled	87 % filled	100 % filled
Prism mesh 3-6 layers	P3-6	P3-6	P3-6
Prism mesh 1-2 layers	P1-2	P1-2	P1-2
Voxel mesh 3-6 layers	V3-6	V3-6	V3-6
Voxel mesh 1-2 layers	V1-2	V1-2	V1-2
Tetrahedral mesh 3-6 layers	T3-6	T3-6	T3-6
Tetrahedral mesh 1-2 layers	T1-2	T1-2	T1-2
Short-shot study			

Figure 3.12: Comparison of the melt front progression of the left cavity (plate B) between the experimental study and 3D simulations

Since 3D simulation of the double-plated part failed to predict the melt front progression, further simulations using a single cavity with the same dimensions should also be performed in order to prove the capability of the 3D-subroutine of Molex3D. By closing one side of the cold runner in the moving mold half, an individual injected part instead of double-plated part will be acquired. During molding, the polymer melt can only flow through the opening side of the cold runner into the cavity. By this way, molding conditions can be constantly controlled and the complexity of the molding is significantly reduced.

Figure 3.11 shows the comparison of the melt front advancement of the left cavity between the experimental study and 2.5D simulation performed with the stan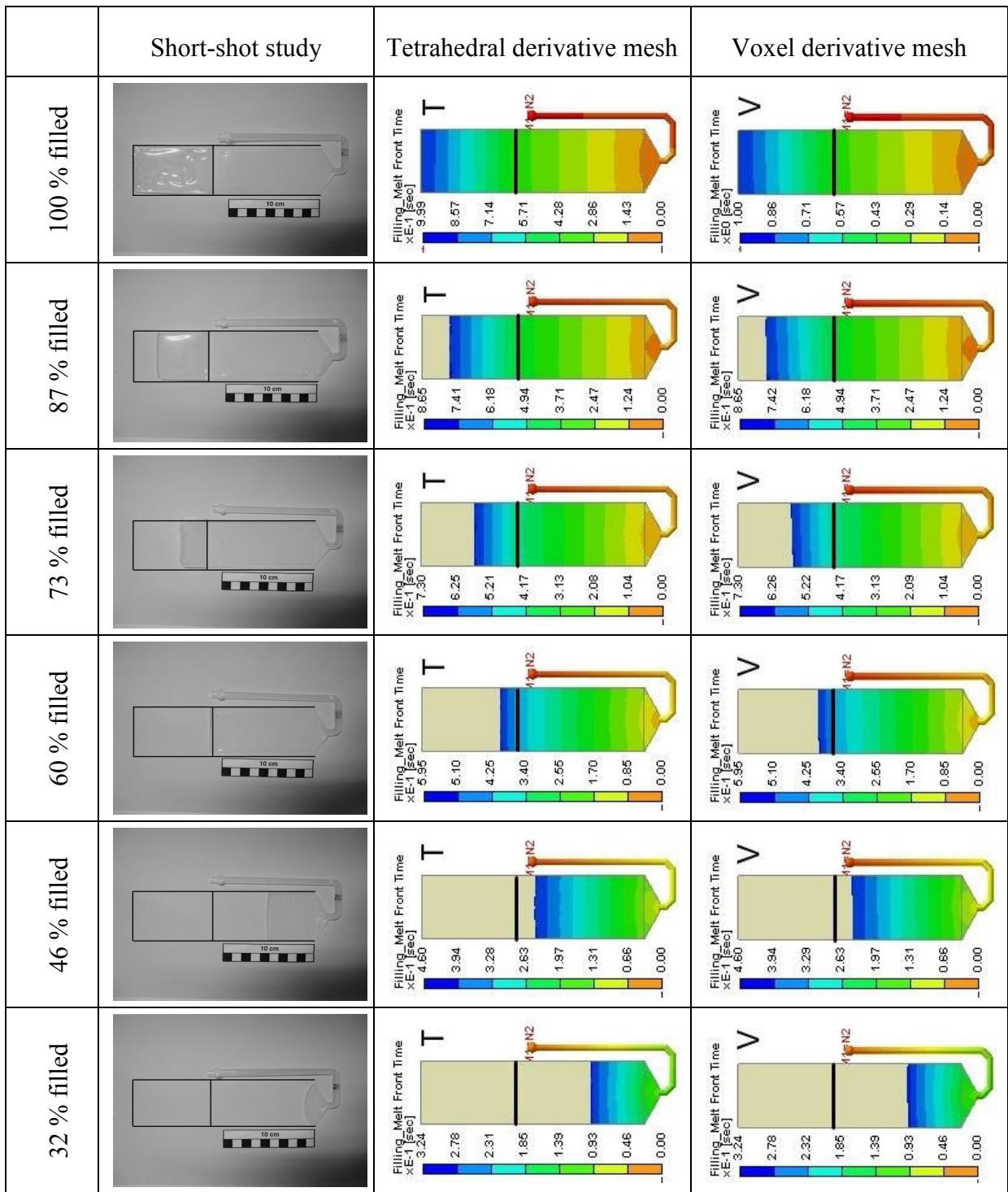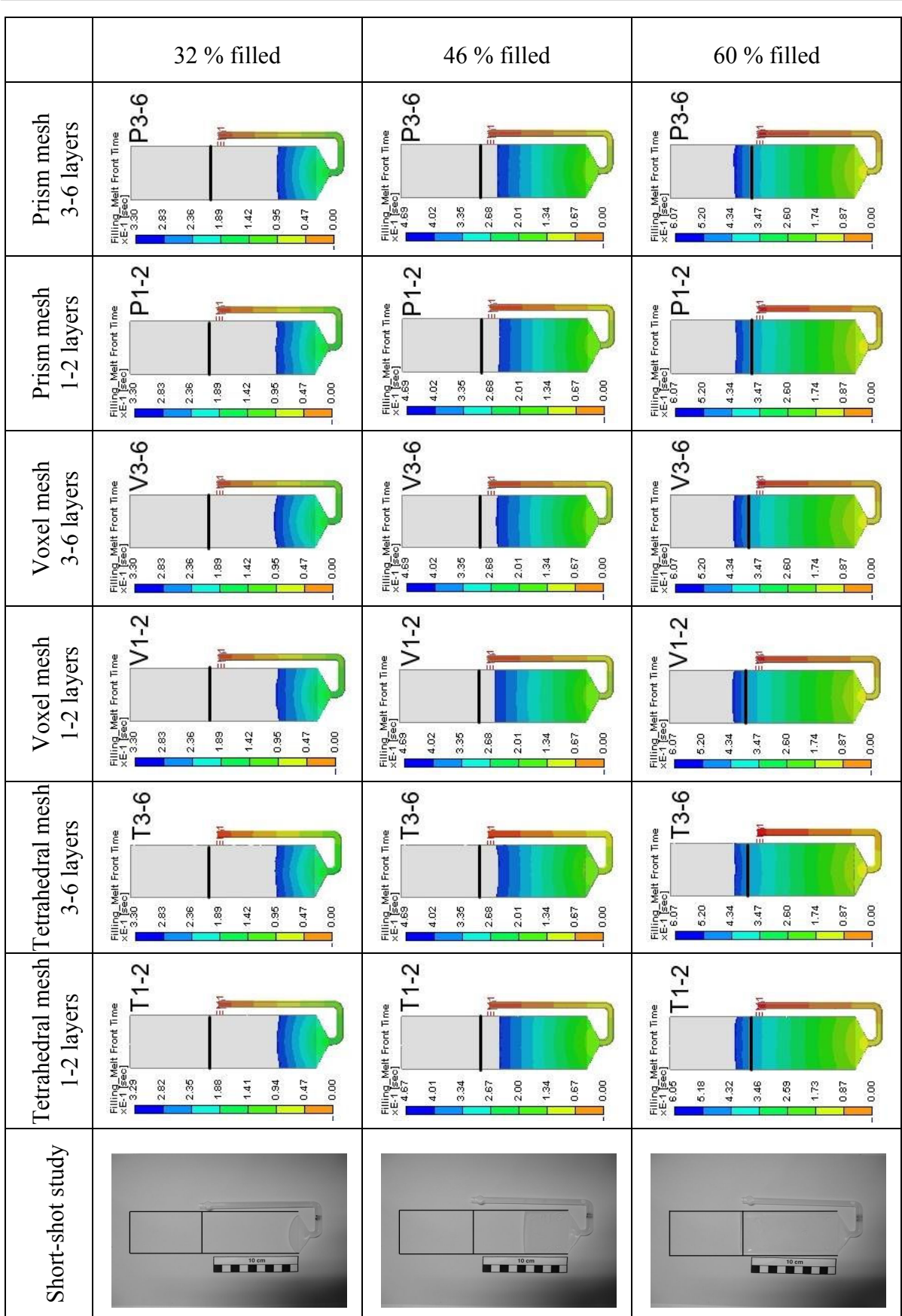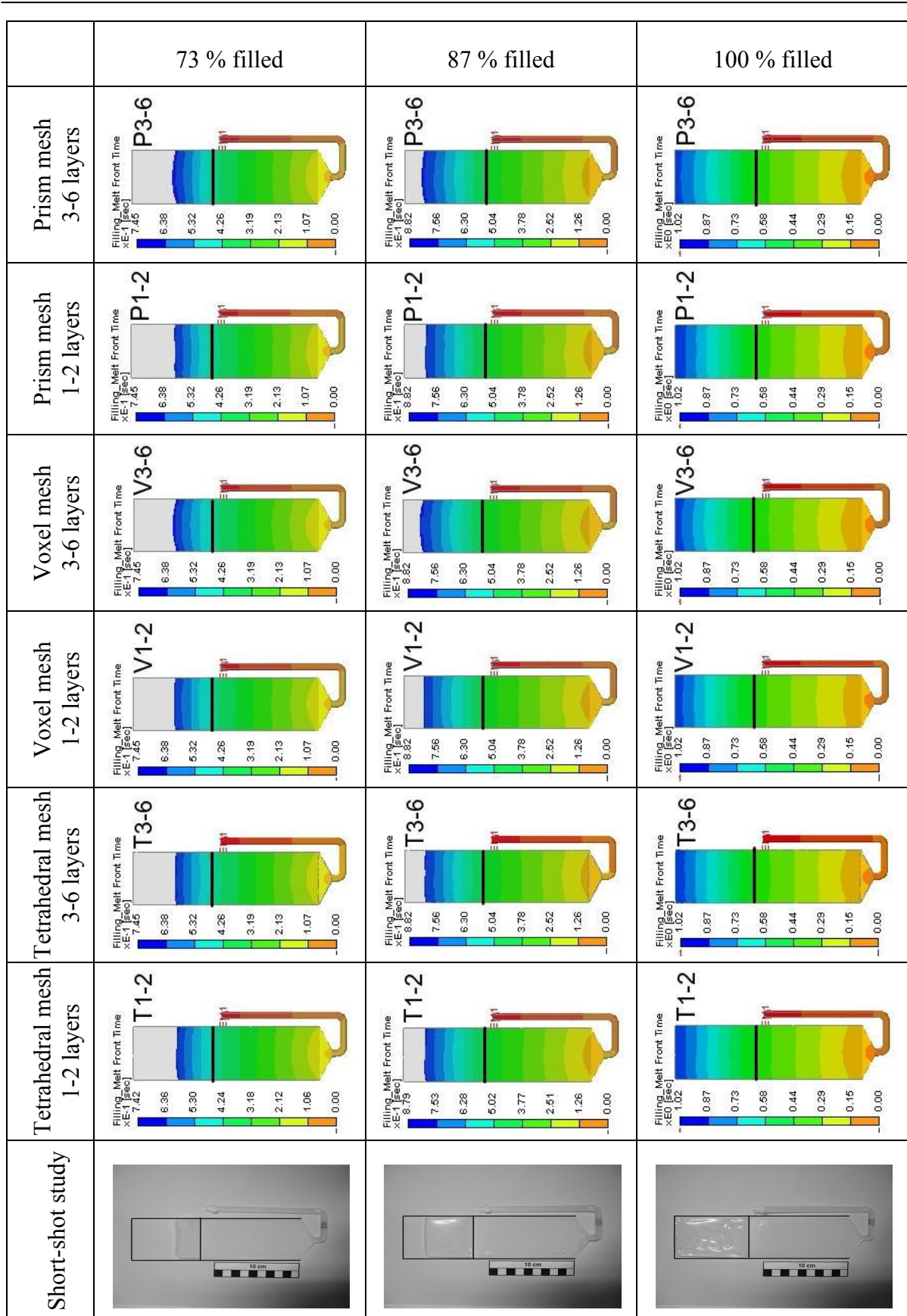dard solver and based on non-isothermal computation and with 20 mesh layer counts over the part thickness defined. 2.5D simulation results show the comparable melt front advancement to that of 3D simulation. The outrunning of the melt front in every filling step also arose from 2.5D simulation. From 32 % to 73 % filled volume, both 3D and 2.5D simulations show the qualitatively comparable melt front advancements. From 73 % filled volume on, a slight outrunning of the 3D-computed melt front advancement compared with that of the 2.5D occurred. Particularly the slight outrunning of the melt front makes the 3D simulation results more reliable, since they even approximate the real molding process.

Figure 3.12 displays the comparison of the melt front advancement of the left cavity between the experimental study and 3D simulations performed with standard solver and based on non-isothermal computation. From the beginning, the 3D computed melt front advancement in each filling step fairly outran the melt front of the real molding process. Apart from this, no obvious deviation in the melt front advancement between the mesh types and the number of mesh layers over the part thickness was noticed.

Comparison of the melt front progression of the right cavity between the experimental study, 2.5D simulations, and 3D simulations was also performed. Similar to the left cavity, the outrunning of the melt advancement from the beginning of filling up to 74 % filled volume computed by 2.5D and the 3D simulation is viewable. This is shown in Appendix 3 and 4.

As a whole image, no decisive accuracy deviation in predicting the melt front advancement between 3D simulation and 2.5D simulation was manifested when molding the plates separately, since the complexity of the flow and unbalancing of the pressure within the two cavities as a system were dismantled. In addition, no extensive disagreement among the simulation results of the molding of these individual plates was proved. Furthermore, the advantage of the higher regularity of the voxel derivative mesh over the tetrahedral derivative mesh cannot be observed. For 2.5D mold filling simulation, higher number of the mesh layer count over the part thickness dedicated mainly to the computation of the temperature distribution within the molded part rather than to the prediction of the melt front advancement (Appendix 5 and 6).

3.5.2 Course of the pressure

The moment at which the changeover or holding switch is activated, determines when the alteration of the velocity-controlled filling phase into the pressure-controlled holding phase is realized. The point of switching should agree, if possible, with the volumetric filling of the cavity, since the cavity is to be filled with a defined velocity. Shrinkage arising in holding phase must be compensated by a given holding pressure. Pressure fluctuations and pressure peaks must be avoided at the point of switching, so that a constant and harmonious transition

between injecting phase and holding phase results and no negative influences can impair the quality of the molded part.
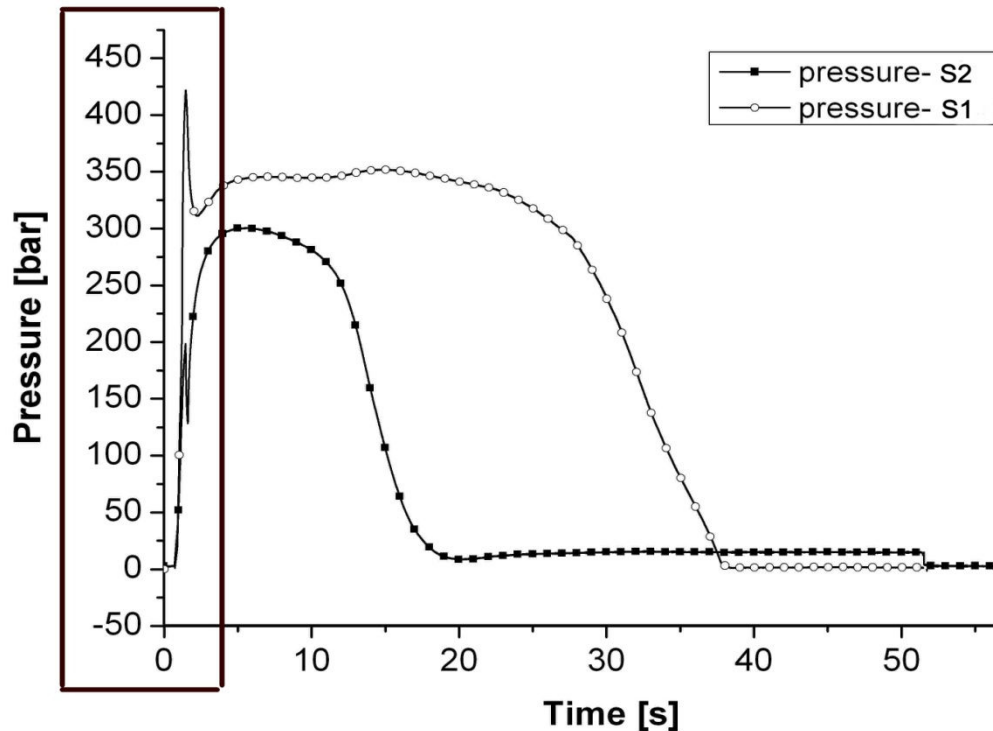

Figure 3.13: Measured course of the pressure during a molding cycle of the double-plated part with non-uniform part thickness

Figure 3.13 illustrates course of the pressure developed during an injection molding cycle of the double-plated part with non uniform part thickness. Courses of the pressure were measured by two of the combined pressure and temperature sensors built into each cavity at the position approximately 42 mm near the gates. A peak and a spontaneous pressure drop can be seen on the pressure-S1 and pressure-S2 curves, which represent a too early holding switch and a too late holding switch, respectively. The proper holding switch is suggested to be at 98 % of filled volume for molding with a hydraulic injection molding machine, since this type of injection molding machine reacts relatively slowly to the changes in machine settings. Normally, this kind of peak or spontaneous pressure drop within a pressure gradient is undesirable. If holding was implemented too early, the cavity will be completely filled by holding instead of filling and an incomplete mold filling or high shrinkage of the molded part has to be expected. If, to the contrary, holding switch was done too late, the cavity will be overpacked or flashes may be developed.

As can be seen from the Figure 3.13, the maximum pressure measured during holding phase of the plate A which has the gate connected to the thick section is 350 bars, whereas the maximum pressure during holding of the second cavity with the gate connected to the thin section is only 300 bars. This is because the melt can be rapidly transported into the thicker section of the first plate as a result of the lower flow resistance. The lower the resistance of the cavity, the lower the pressure level will be contributed. In the first cavity, this pressure level remained by this value almost throughout holding phase. Shortly before the end of holding phase, the pressure measured by this point began to gradually drop and sloped down to the ambient pressure. In a comparable manner, the pressure maximum plateau during

holding of the second cavity ended up with the steep pressure drop to the ambient pressure. However, this occurred much earlier than in the first cavity. This is because of the smaller thickness of the thin section of the second cavity which allows faster cooling of the melt. As soon as the melt at the wall cooled down, the frozen surface lifted off the mold cavity. Consequently, the pressure level in this cavity was lower right from the time that the melt had reached the sensor fronts (Fig 3.14). By the end of the cooling, some extents of the pressure in the thin section of the second cavity can still be detected, whereas in the thick section of the first cavity, ambient pressure was measured at this point. This resulted from the overpacking of the melt especially in the thin section of the second cavity during holding. After the thin section of the second cavity had solidified, holding pressure can no longer take an effect on this, even if the holding pressure was still loaded. But the melt in this section of the part had experienced an excessive stress load during holding, which lastly resulted in the expansion of this side against the sensor front after being unloaded and hence the pressure detected increased.
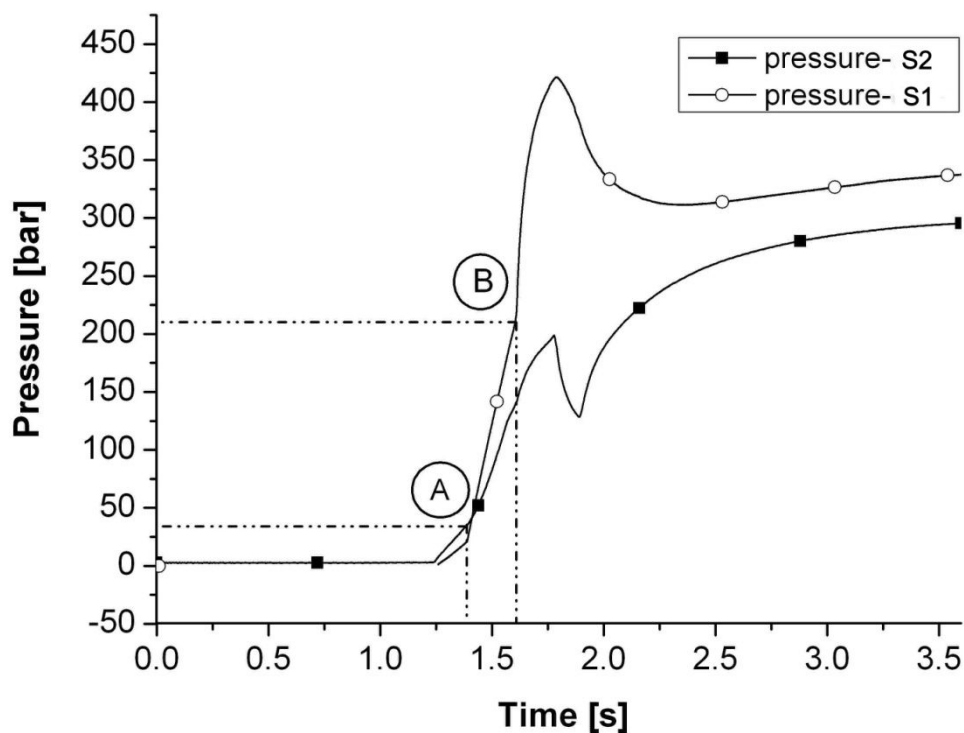

Figure 3.14: Course of the pressure during mold filling (filling time 1.59 s)

Figure 3.14 exhibits course of the pressure during mold filling of the double-plated part with non-uniform part thickness (zoom section of Fig. 3.13). Filling time was defined by 1.59 s at the given injection velocity of 50 %. It can be implied from the figure that flow deceleration of the melt involved in filling phase of this part. Firstly, the melt was symmetrically injected into both cavities via the cold runner of the same size and length. Then the melt entered each cavity through the fan gates. From this point on, the melt encountered the different circumstances that were non-uniform flow resistances within the cavity due to the cross section area differentials between the two cavities. As soon as the melt reaches the sensor front, a continuous voltage signal will be collected, sent to an amplifier and finally converted to the pressure gradient. From Figure 3.14 the melt pressure at the beginning of filling in the thin section of the second plate (pressure-S2 curve) is somewhat higher than that in the thick section of the first plate (pressure-S1) with higher slope. At the point A (time at 1.4 s), the

first buckling of the two curves is defined. This is the point where the melt front in the thick section of the first plate reached the transition to the thin section of the same plate.

After the point A, the melt in the first plate flowed into the thin section with the higher melt front velocity because of the constant injection velocity, despite the increasing flow resistance as a result of the decrease in the cross section area. Whereas the melt front in the second plate was still being found in the thin section (Fig. 3.9). With an increase in the flow length in the first plate as well as the higher flow resistance in the thin section of the first plate, much higher filling pressure was necessary compared to the thin section of the second plate and hence a steep pressure gradient resulted. The increase in filling pressure in the first plate also influences filling in the second plate, since they are connected to each other by the cold runner of the same size. If higher pressure is supplied in one branch of the runner, the same amount of the pressure must be provided to the other, except for the hot runner system with valve gate control. And this is the reason why the pressure in the second plate also increases, but with gentler gradient.

Point B (the second buckling, filling time at 1.59 s) is the point where the plate A was completely filled with the melt following with the melt compression whereas the melt front in the plate B had already crossed its transition. This results in the highly steep pressure gradient of the pressure-S1 curve. This point is counted as the actual filling time obtained from the molding machine. From the figure, the maximum melt pressure in the plate A is at approximately 215 bars, while the maximum melt pressure in the plate B is approximately 150 bars high. As already mentioned above, the pressure supplied to one cavity is also taking an effect on the other, since they are connected to each other by the cold runner. While the melt in the plate A was being packed, the plate B was being topped off, not by the effect of the filling velocity but actually by the effect of holding pressure, and the melt front in this plate, which was found at this time in its thick section, continued to move toward the end of the cavity. So the melt pressure in the plate B after point B kept rising but with the gentler gradient compared with the steep gradient (compression) of the plate A. Because the plate A was filled first, the melt in this plate was excessively packed by the holding pressure. Under this molding situation, the plate A will generally suffer from overpacking, which results in a deterioration of this part under some mechanical loads. In the same way, the plate B, especially the thick section, which was filled with the holding pressure instead of the filling velocity, will also suffer from excessive shrinkage and warpage. Apart from the molding situation, gate should be positioned at the thickest section of the part in order that holding can bring about the highest and longest efficiency, since the thick section will solidify last. Considering the plate B, the fan gate is connected to the thin section of this part. During holding phase, this thin section will solidify prior to the thick section. Consequently, the thick section will be insufficiently packed and non-uniform shrinkage and warpage result.

As already mentioned a peak and a spontaneous pressure drop can be seen on the pressure-S1 and pressure-S2 curves, which represent a too early holding switch and a too late holding switch, respectively. Although this peak and spontaneous pressure drop in course of the pressure are not optimum, they cannot be avoided, since filling of this molding system is not symmetrical as usual. Flow deceleration, unbalance and direction changeover of holding involved in the filling and holding phases and they make this molding process almost impossible to be repeated and more difficult to be controlled. In industry, molding of such a part is seldom performed, since the mold maker and part designer will always avoid positioning gate and arranging the cavities into the mold in the manner they know that quality and repeatability of molded parts will hardly be guaranteed.
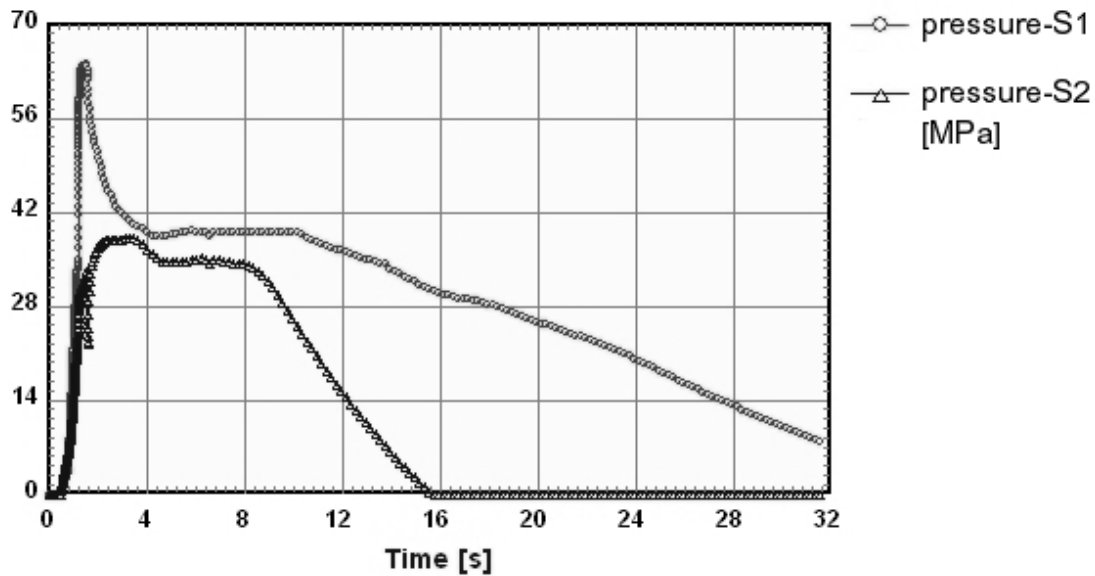
Figure 3.15: 2.5D computed course of the pressure during filling and holding phase of the double-plated part with non-uniform part thickness

Figure 3.15 and 3.16 illustrate course of the pressure derived from 2.5D simulation during mold filling and holding of the double-plated part with non-uniform part thickness. The maximum computed pressure during holding phase in the plate A is 384 bars, whereas the maximum computed pressure in the plate B is approximately 350 bars. Compared with course of the pressure from the real injection molding process, these values lie relatively near together, despite a little excess of the computed values. A peak and a spontaneous pressure drop can also be seen in course of the pressure computed by 2.5D simulation.
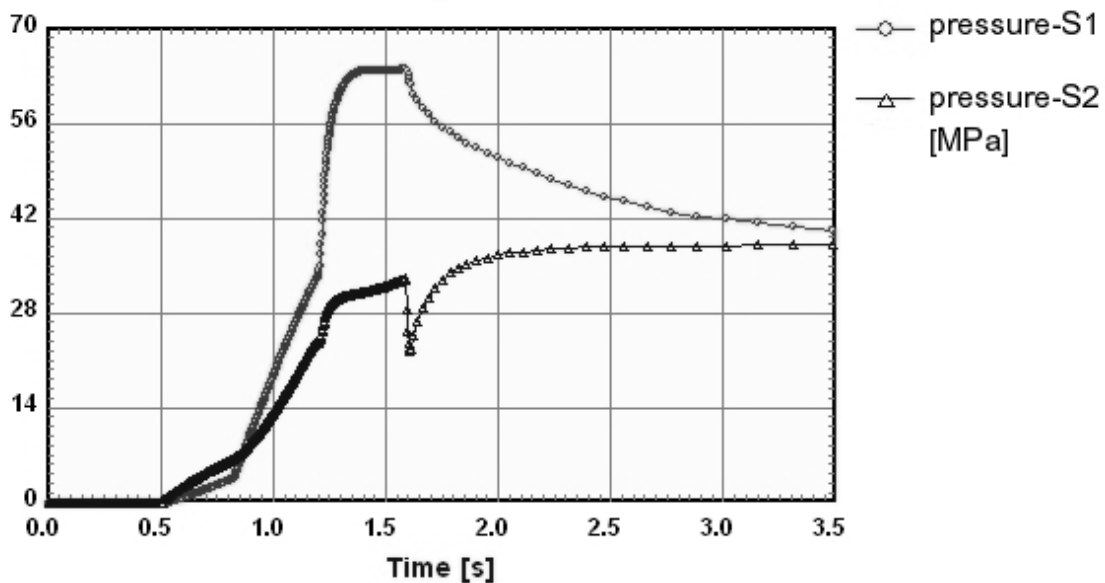
Figure 3.16: 2.5D computed course of the pressure during filling phase (expanded view)

Regarding the pressure-S1 and pressure-S2 curve in the Figure 3.16, crossing of the two curves is apparent which indicates changes in the part thickness. Courses of the pressure in the two cavities were predicted correctly, however with a slight shift in filling time. In the real molding process, filling time determined by the molding machine was 1.59 s (Point B in

Fig. 3.14), right after this time, the melt compression occurred, whereas at this comparable point in the Figure 3.16, filling time can be read at 1.20 s. In 2.5D simulation, however, filling time which was set at 1.59 s is where the melt compression in the first plate had ended and holding phase started. At this point the maximum melt pressure shown in figure 3.16 is 640 bars in the plate A and 340 bars in the plate B. Compared with the melt pressure at the end of filling from the real process, these values are much higher. This is the reason for the melt front outrunning of the simulation compared to the real molding.

At this moment, it can be concluded that 2.5D simulation has met the correct conditions indispensable to the prediction of course of the pressure which, then again, is the decisive condition in predicting the melt front advancement within the mold cavity particularly of this specially molded part.

Figure 3.17: 3D computed course of the pressure based on non-isothermal computation during filling (top) and holding (bottom) phase of the double-plated part with non-uniform part thickness

Figure 3.17 and 3.18 exhibit pressure profiles during filling and holding phase derived from 3D simulation based on non-isothermal and isothermal computation, respectively. From the Figure 3.17, the maximum computed pressure at the end of filling phase of the plate A is

approximately 100 bars, whereas the maximum computed pressure in the plate B is 115 bars. According to the results, it is apparent that 3D simulation based on non-isothermal computation has computed course of the pressure defectively. The pressure levels in the two cavities were shown in the shuffle way and the pressure values at the end of filling were highly underestimated compared to the real molding process. In addition, the pressure-S2 curve lies over the pressure-S1 one which is clearly incorrect. This is responsible for an error in predicting the melt front advancement of the double-plated part with non-uniform part thickness by 3D simulation (Fig. 3.9).

There are some limitations in showing the pressure computed by 3D filling and holding simulation and thereby an unpleasant experience was made. It is not able to attach the holding pressure curve to the pressure curve of filling phase. According to this, two separate figures containing course of the pressure must be made (Fig. 3.17). And this leads to the absolutely unreliable prediction of course of the pressure during holding as can be seen in the Figure 3.17 (bottom).

To the contrary, with the 3D isothermal computation, the pressure curves shown in Figure 3.18 resemble the measured pressure curves shown in the Figure 3.13 and 3.14. The maximum pressure at the end of filling can be read at 665 bars in the plate A and at approximately 500 bars in the plate B. These values were however highly overestimated.

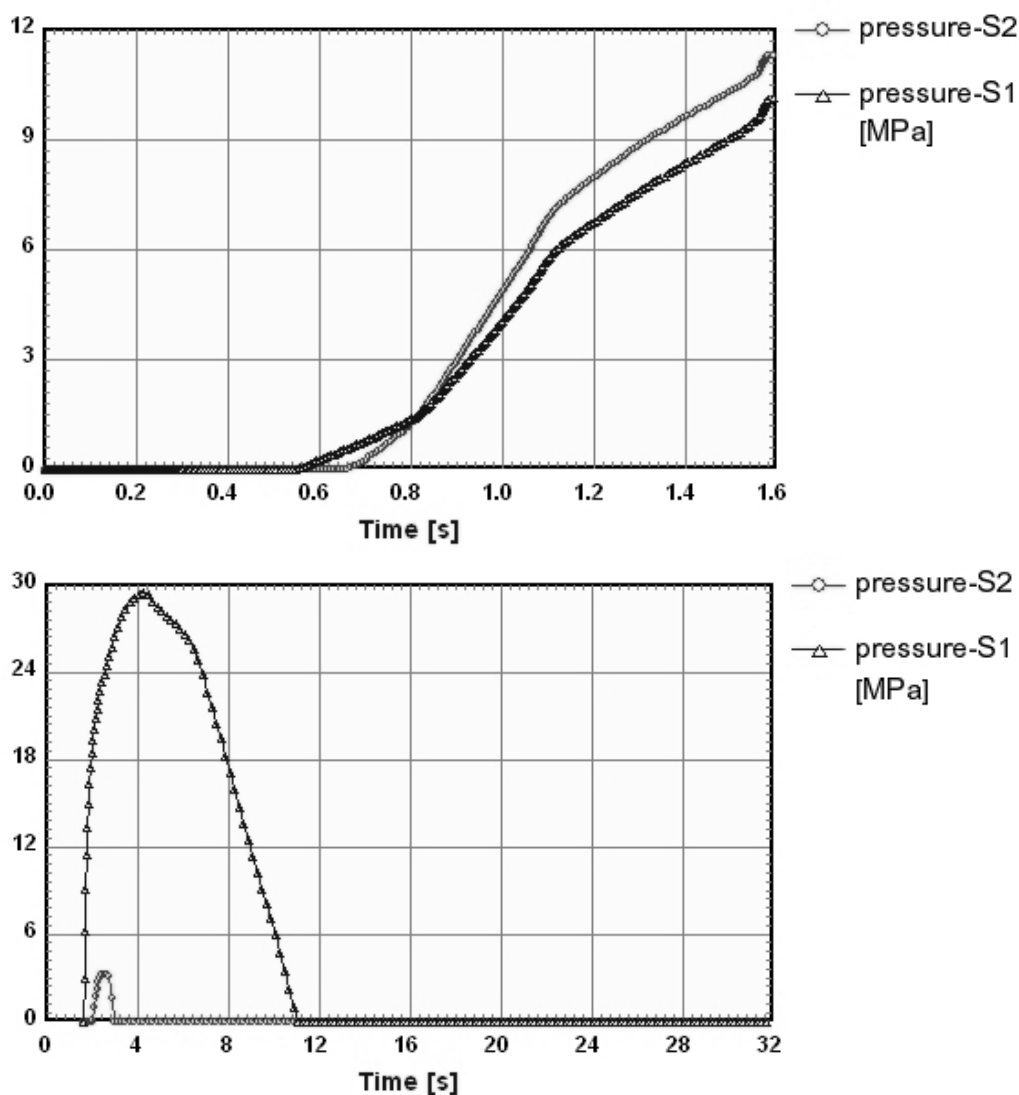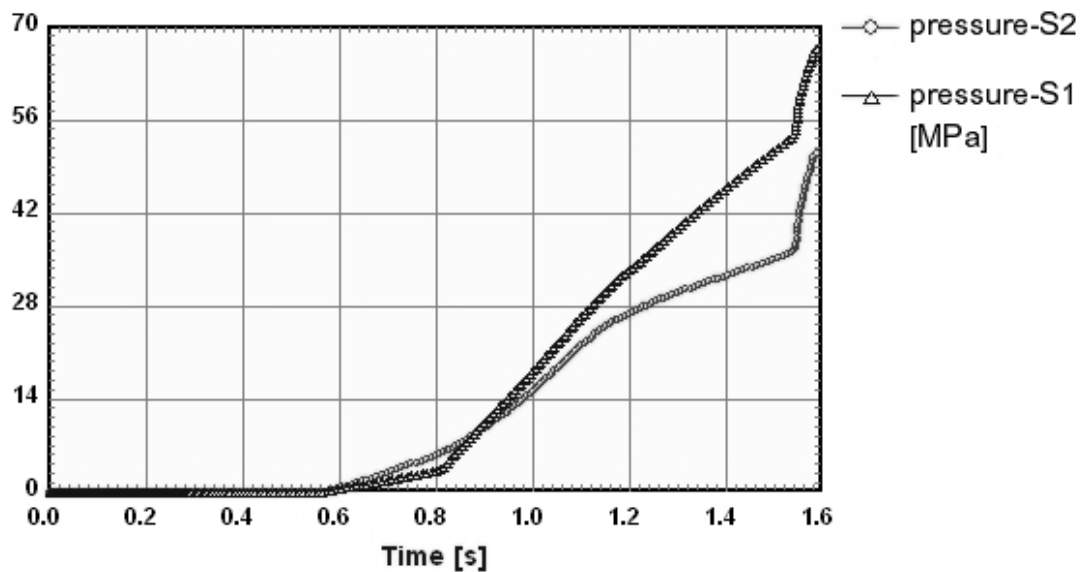**Figure 3.18**: 3D computed course of the pressure based on isothermal computation during filling phase of the double-plated part with non-uniform part thickness

3.5.3 Time/temperature Profiles

For injection molding analysis, the element layer count across the part thickness is very important. This is because the element layer count determines the resolution of the analysis results. Take the temperature distribution across the thickness direction, for example, the temperature usually rises steeply because of the shear heating phenomena near the cavity wall. Then the temperature lowers down slowly around the middle of the part. To obtain the temperature distribution from the analysis result, the element resolution is the key point. The more the element layer count, the better the element resolution is.

Figure 3.19 shows temperature profiles during an injection molding cycle of a double-plated part with non-uniform part thickness measured by two IR-temperature sensors mounted near the gate of each cavity. The injection molding of the part was carried out by the cylinder temperature set at 195 $^{\circ}$C and the mold temperature of 40 $^{\circ}$C. The temperature-S1 and temperature-S2 curves show the temperature levels developed in the plate A and the plate B, respectively. At the beginning of mold filling, no signal can be detected. Until the melt reached the sensor front, a sudden rise in the temperature can then be measured. The maximum melt temperature of the plate A and plate B were detected by 205 $^{\circ}$C and 220 $^{\circ}$C, respectively. Owing to higher shear heating which contributes to an additional rise in the melt temperature during mold filling of the thin section of the plate B, the higher maximum temperature in this section resulted. As soon as the melt contacts the cold mold wall, melt cooling takes place and a steady decline in the melt temperature results. Since the IR-sensors are positioned in the thick and thin section of each cavity, two different rates of the melt cooling are observed. Of course, the melt in the thin section of the plate B solidifies more rapidly than the melt in the thick section of the plate A. At the end of the cooling, the melt temperature in the thick section of the plate A can still be detected at approximately 75 $^{\circ}$C while the melt in the thin section of the plate B already cooled down to the ambient temperature (25 $^{\circ}$C).
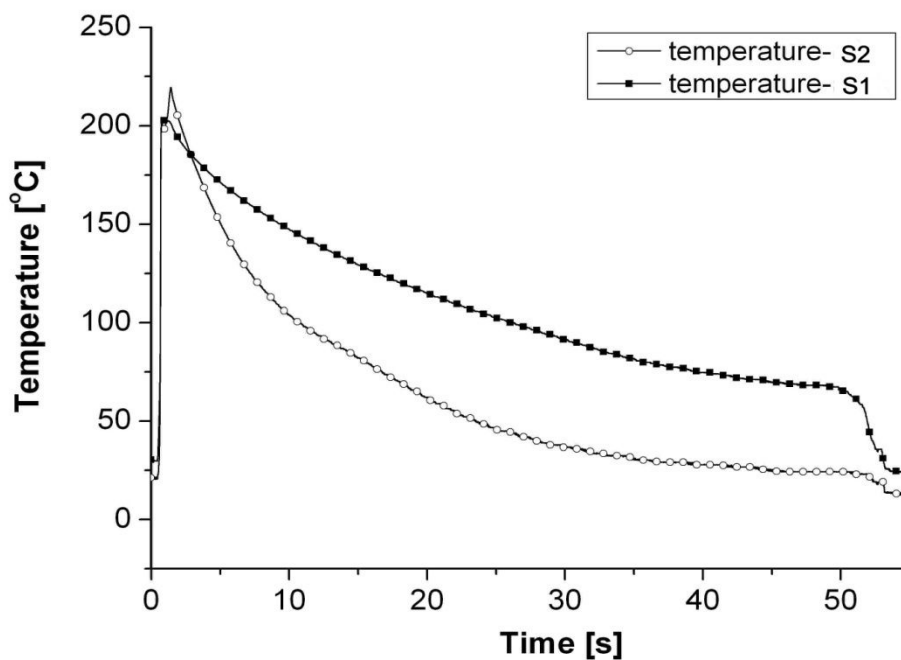

Figure 3.19: Melt temperature profiles during the injection molding of the double-plated part with non-uniform part thickness

Figure 3.20 and 3.21 display melt temperature profile during filling and holding phase from 2.5D simulation. From the figures, the computed average melt temperatures in the plate A and plate B are 198 $^{\circ}$C and 202 $^{\circ}$C, respectively. Despite the slightly underestimated melt temperatures compared with the real molding process, the temperature values lie relatively near together. Nevertheless, the comparison between the measured and the computed melt temperature must be made with caution because the depth of penetration of the IR-temperature sensor is still unknown.
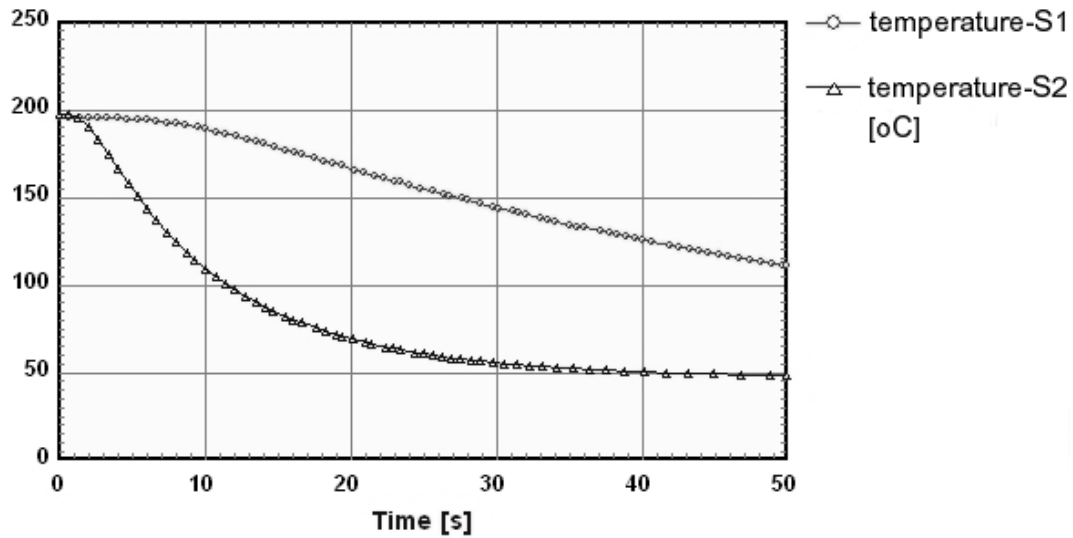
Figure 3.20: 2.5D computed melt temperature profiles during the molding of the double-plated part with non-uniform part thickness (with 20 layer counts defined)
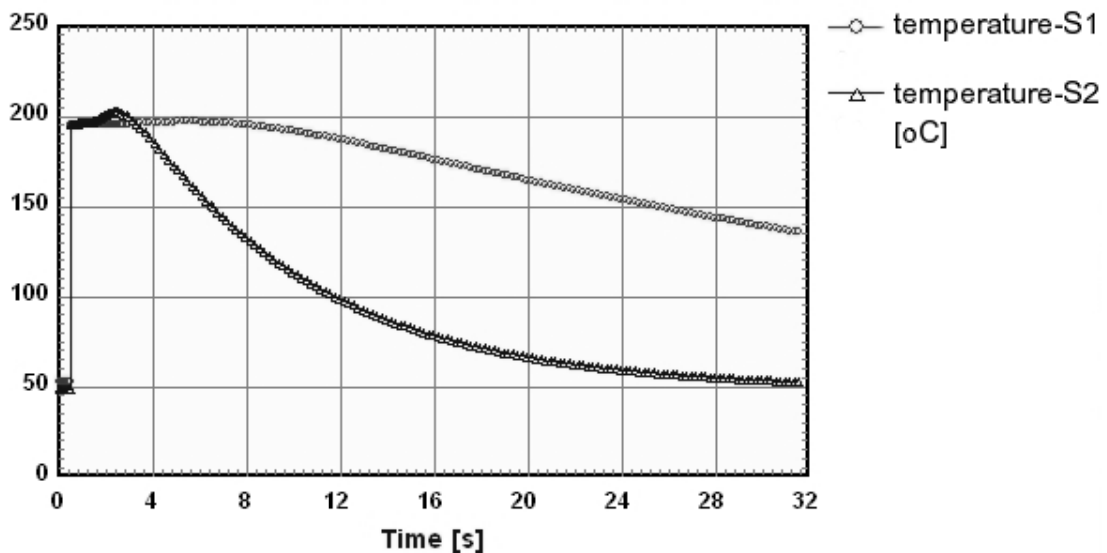

Figure 3.21: 2.5D computed melt temperature profiles during filling and holding phase of the double-plated part with non-uniform part thickness (with 20 layers defined)

Figure 3.22 and 3.23 show temperature profiles during filling phase and holding phase of the double-plated part with non-uniform part thickness from 3D simulations. Course of the melt temperature derived from 3D simulation is not really meaningful since the sensor nodes used in simulation are not comparable with the real IR-temperature sensors. The sensor nodes were position on the surface of the volume mesh, therefore the melt temperature computed by them are only the melt surface temperature, which of course rapidly falls down to the mold temperature level as soon as the melt contacts the mold wall. Unlike the sensor nodes used in 2.5D simulation, with which the average or center melt temperature over the part thickness was computed, gradual change in the melt temperature underneath the part surface during filling and holding phase cannot be reported based on these sensor nodes used in 3D simulation. The comparison of melt temperature profile between the real molding process and 3D simulation is thereby foregone.
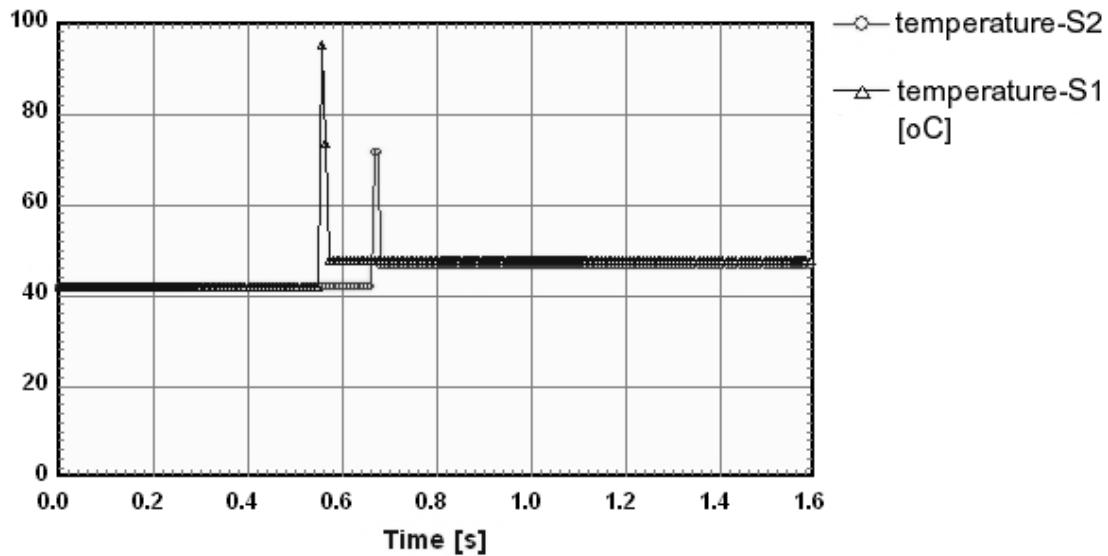
Figure 3.22: 3D computed melt temperature profiles during filling phase of the double-plated part with non-uniform part thickness
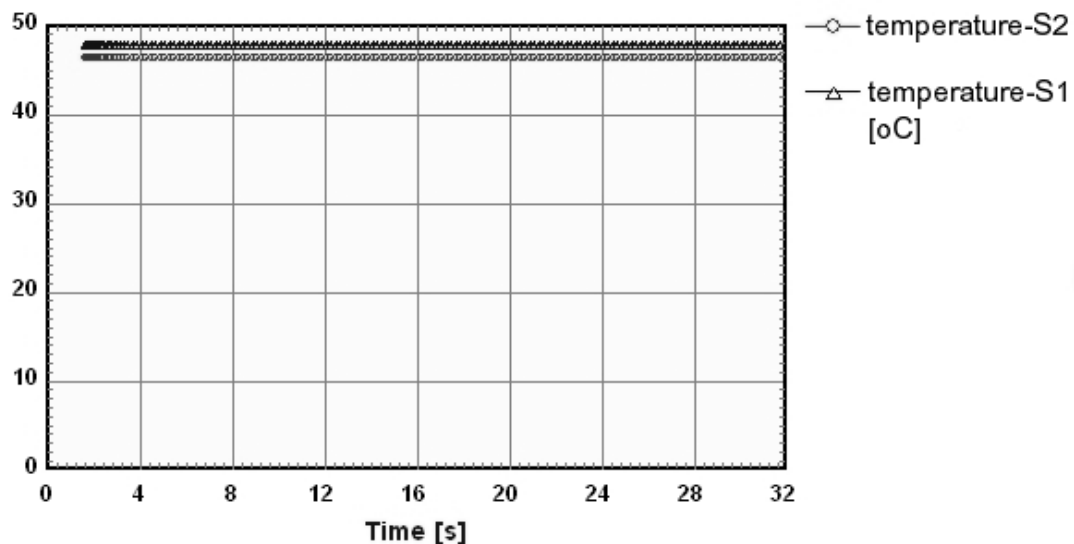

Figure 3.23: 3D computed temperature profiles during holding phase of the double-plated part with non-uniform part thickness

Figure 3.24 shows the temperature distribution over the part thickness during filling phase resulted from 3D simulations based on the prism meshing with different element layer counts over the part thickness. With one element layer count in the thin section and two layer counts in the thick section of the part (Fig. 3.24, top), the temperature gradient within the thin section is not visible. On the other hand, with three element layer counts in the thin section and six layer counts in the thick section of the part (Fig. 3.24, bottom), more distinct and more reliable temperature distribution over the part thickness is descriptively and effectively shown. This is a simple example showing how important the element layer count over the part thickness is to the accuracy and quality of the simulation results. Basically, when the computation is not convergent, the higher the resolution of the meshes, the more accurate the result is. During filling phase, the physical phenomena happen dramatically across the thickness direction. When there is only one mesh layer across the thickness direction, the temperature distribution, for example, will be shown in a uniform pattern. On the other hand,

when the part is meshed into many layers across the thickness direction, the temperature distribution will be shown with high value portion in the middle of the layers. That means more physical phenomena will be taken into account during the process. Therefore, setting up the suitable mesh resolution for numerical simulation is one of the most crucial factors.
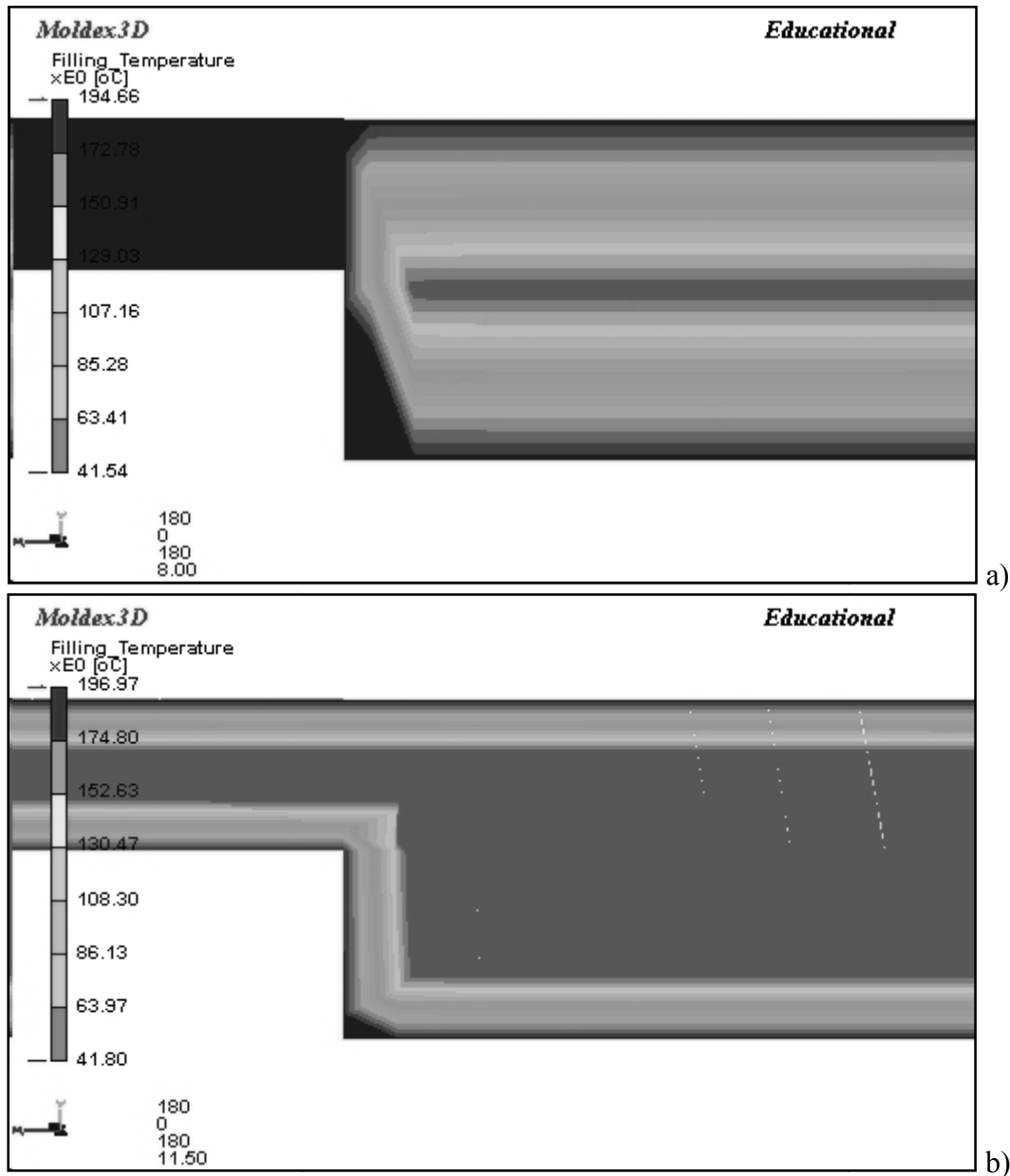

Figure 3.24: Temperature distribution during filling phase with prism mesh a): 1-2 and b): 3-6 layers

In conclusion, it is well-known from the former studies that better agreement between 3D simulation and experimental result can be generally expected [78]. If the part to be molded is simple in form and relatively uniform in thickness, reasonable solutions are also achievable by 2.5D simulation, which is proved in this study to be sufficient for predicting such a simple flow. Contrary to 2.5D simulation, with the double-plated part with non-uniform part thickness introduced in this study, 3D simulation based on non-isothermal computation has failed to predict course of the pressure during filling and hence malfunctioned to foretell the flow pattern within the cavities. This is probably due to some assumptions required to be

made in the governing equations as well as numerical difficulties and inaccuracies that are likely to appear when the real molding conditions deviate much from the assumptions made or when the molded part is highly complex. With the separated parts with non-uniform part thickness, however, non-isothermal based 3D computation of Moldex3D® has been proved to be reliable in predicting the flow behavior of the polymer melt in injection molding process and particularly in predicting the temperature distribution across the part thickness when the number of mesh layer count is chosen properly. Credible melt temperature prediction is one of the utmost conditions especially when the back injection of a film is to be handled. By these reasons, non-isothermal based 3D computation of Moldex3D® will be used for the simulation on the injection in-mold labeling which will be discussed later in Chapter 5 and 6.

4   Design of an Injection Mold for Injection In-Mold Labeling

Other than extrusion, injection molding runs discontinuously and therefore the stages involved in this process are time-dependent [79]. Similar to the extrusion die, injection mold is one of the most important components needed for injection molding of the polymer products. The purpose of this chapter is to apply the basic knowledge necessary for designing of an injection mold to the design of the injection mold particularly used later in the experimental study on the injection in-mold labeling. The design of the injection mold for the production of IML parts is conducted according to Figure 2.1.

4.1   IML Part Geometry

In this study, a flat IML part of polypropylene with the dimensions 100 x 50 x 2 mm shown in the Figure 4.1 was designed. On the upper side, two polypropylene in-mold labels with dimensions 90 x 40 mm are inseparable attached to the substrate during molding.
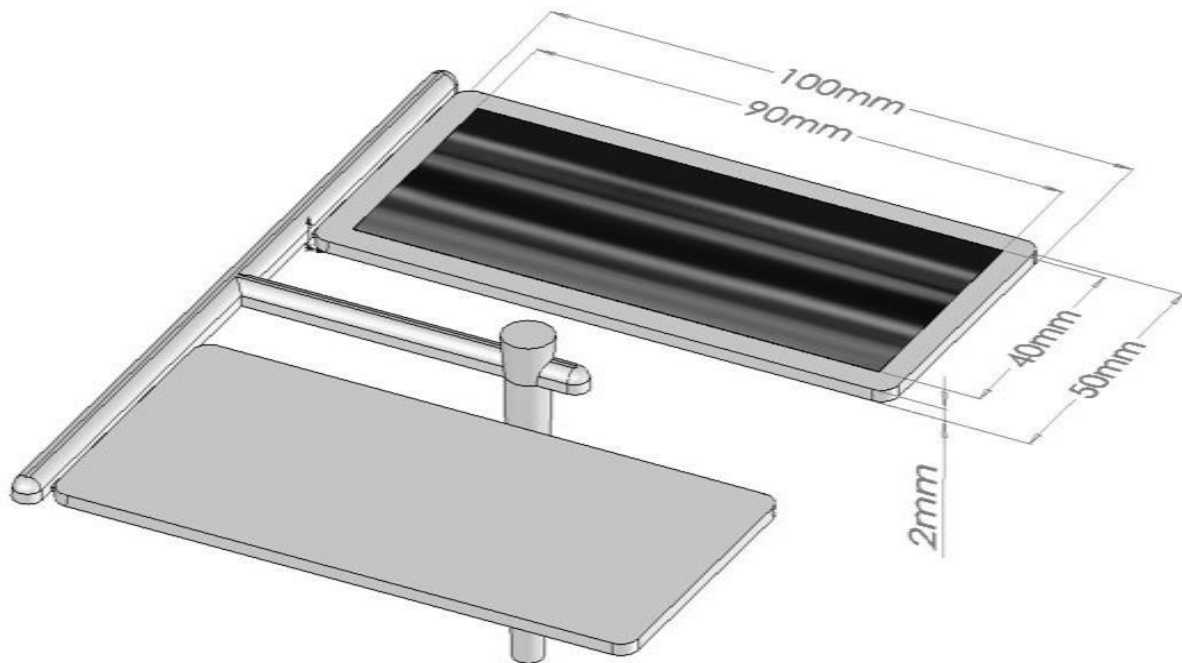

Figure 4.1: IML part geometry

4.2   Type of Mold

The mold is based on the use of standard mold components. For this flat IML part, the conventional two-plate mold consisting of the cavity mold half, stationary mold half, sprue bushing, cold runner, and an ejector mechanism actuated by a helical spring was chosen. The cavity mold half of the twin-cavity consists of the cavity plate (246 x 190 x 36 mm), the support plate, the pillar support, the ejector plate including ejector pins and four return pins, and the clamping plate, while the stationary mold half consists essentially of the mold plate, the clamping plate, and the sprue bushing (Fig. 4.2).

No accurate alignment of the two mold halves is required in this case, since the part to be formed is situated only in the cavity plate and the mold plate is merely a plane. The mold opens at the parting line between the cavity plate and the mold plate. The molded part is

retained on the cavity as the mold opens by the cold slug well at the end of the sprue. As the ejector rod is pushed forward, the ejector plate is actuated and the ejector pins move forward to strip the molded part off the cavity. Then the helical spring triggers the ejector plate to move backward, the mold can now be closed for the new molding cycle.
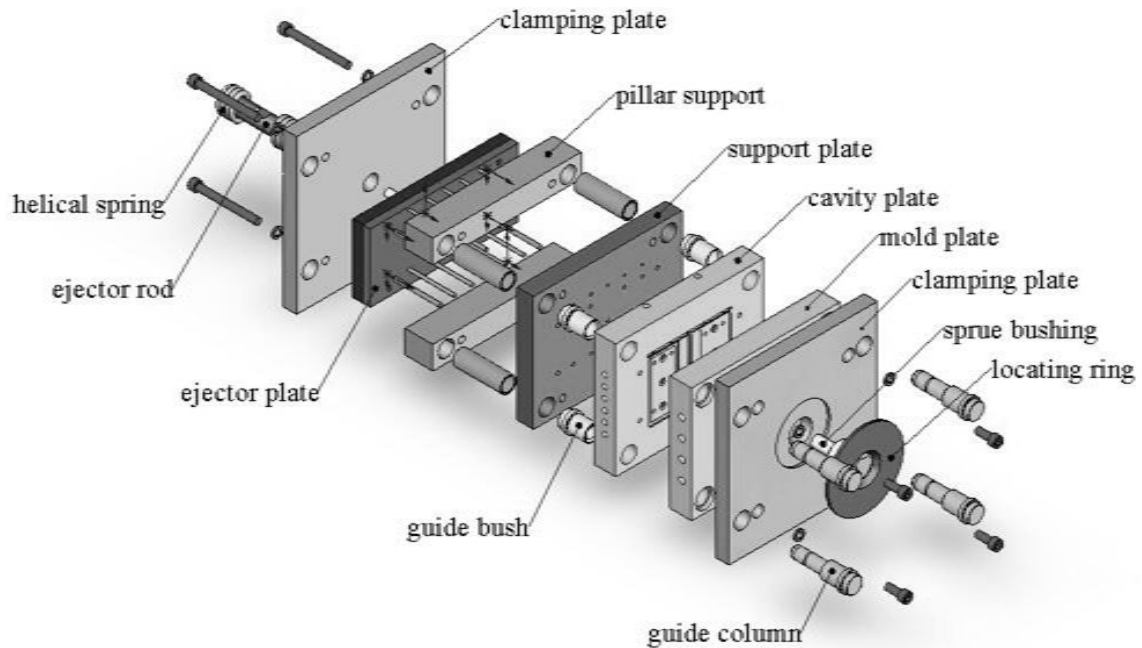

Figure 4.2: Exploded view of the IML mold

4.3 Runner Design

Cold runner with parabolic (or trapezoidal) cross-section (Fig. 4.3) is employed in the IML mold according to its advantages e.g. best approximation of circular cross-section and simpler machining in one mold half only (usually movable side for reasons of ejection).
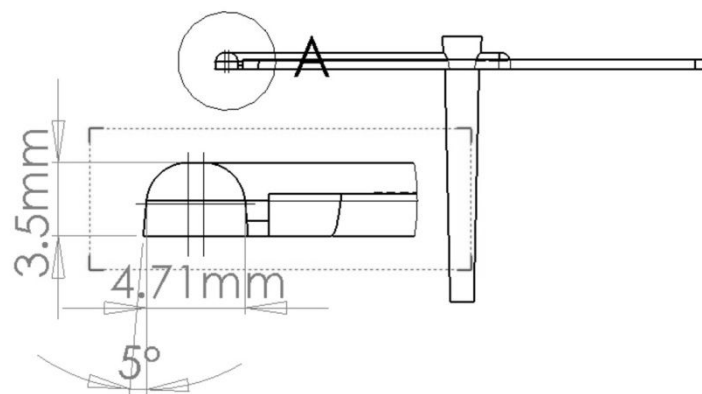

Figure 4.3: Runner cross-section

Since the thickness of the molded part is 2 mm, the diameter of the circle which fits the parabolic cross-section of the runner should be the thickness plus 1.5 mm which, in this case, is 3.5 mm. The side walls of the runner slope down to the bottom. The degree of slope can be set between 5° and 10°.

4.4   Gating

The polymer melt is fed, via conical sprue in the sprue bushing and via runners located in the parting plane, to the film gates at the top of the two cavities (Fig. 4.4).
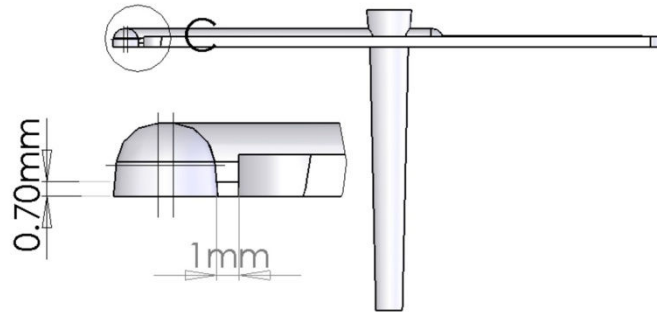

Figure 4.4: Film gate of the IML part

To obtain flat molded parts with few molded-in stresses and little tendency to warp, a film gate over the entire width of the molded part is useful in providing a uniform flow front. A certain tendency of the melt to advance faster in the vicinity of the sprue or inner corner can be offset by correcting the cross-section of the gate. According to Figure 4.1 and 4.3, the film gates are located only on one side (top) of the part. This eccentric location of the gate can lead to opening of the mold on one side, with subsequent formation of flash. However, no flash on the molded part owing to opening of the mold can be detected since the clamping force overcomes the cavity pressure. The film gate must be trimmed off the part after ejection, but this does not impair automatic operation.

4.5   Mold Cooling

To cool the cavities, cooling channels must be incorporated into the cavity plate and the mold plate. In the cavity plate (Fig. 4.5), two symmetrical cooling channel layouts of diameter 8 mm are bored at the distance 16 mm beneath the cavity surface. The water flows into the channel at the top of the part near the runner where most heat exists and is drained out of the mold through the water outlet at the end of the cavity. By this manner, heat will be regularly withdrawn from the melt most efficiently.

The cooling channel layout in the mold plate is similar to that in the cavity plate (Fig. 4.6). The only deviation is that the cooling channel in this plate is larger in diameter and hence the distance between the channels and between the channels and the cavity wall must be automatically greater in order that the cooling remains regular throughout the part. With the smaller cooling channel diameter and smaller distance between the channels machined horizontally, the higher cooling efficiency of the cavity plate can be achieved. This technique is useful for the back injection of a label, in that the label acts as a thermal insulator. Without a reasonable cooling compensation, the IML part is prone to warpage after demolding.
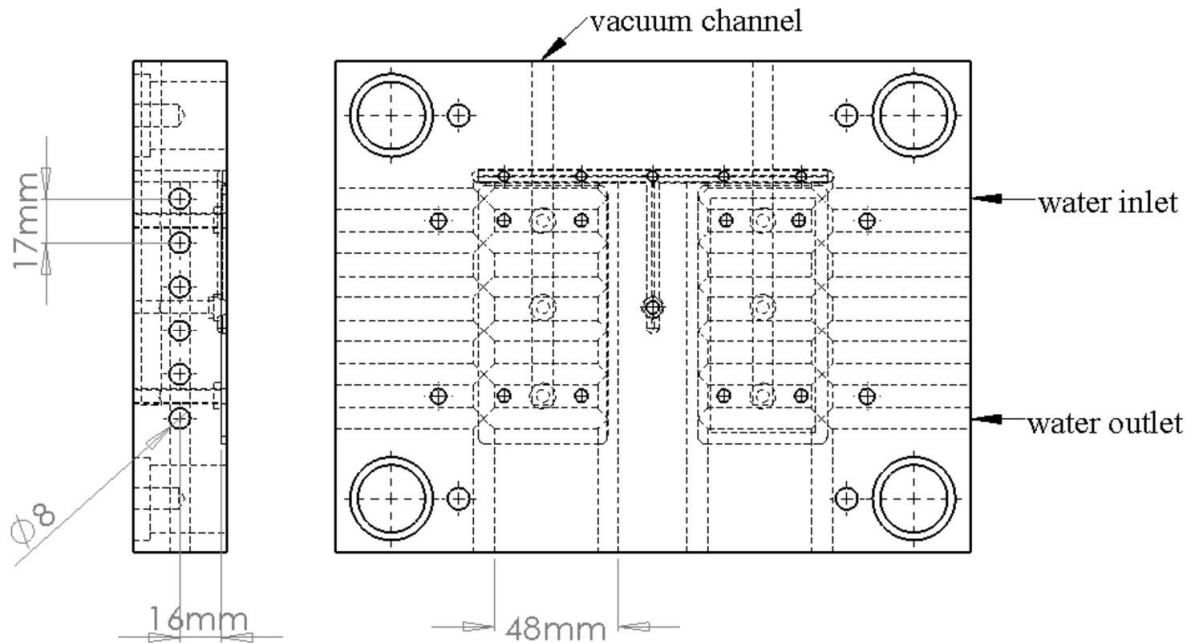
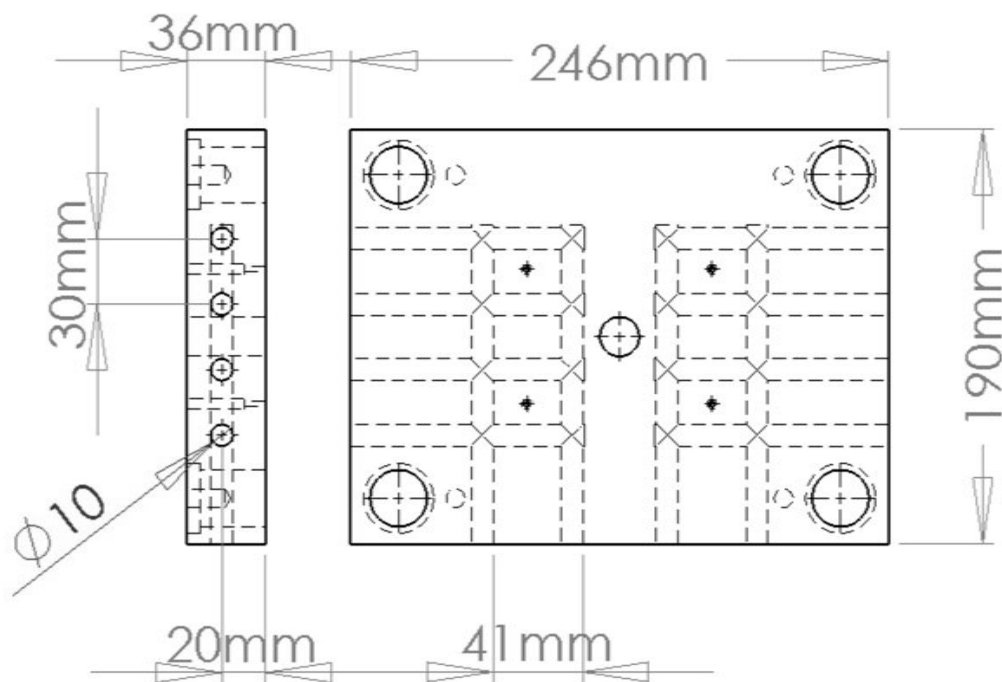**Figure 4.5**: Cavity plate with the cooling channel layout

Figure 4.6: Mold plate with the cooling channel layout

4.6 Part Release/Ejection

Figure 4.7 illustrates the cavity plate of the IML mold. Each cavity is equipped with three vacuum nozzles, each of which is occupied by a sintered metal for holding the label during the mold filling. In addition, four ejector pins in the cavity and other six in the runner are required to strip the molded part off the mold. The part is ejected by means of the machine's ejector system. During mold closing, the return pins press the ejector plates back so that the mold cavity is absolutely cleared and the ejector pins are not damaged by the melt stream.

Without the return pins, marks on the part surface caused by the ejector pins arise, if the ejector pins are incompletely retracted.
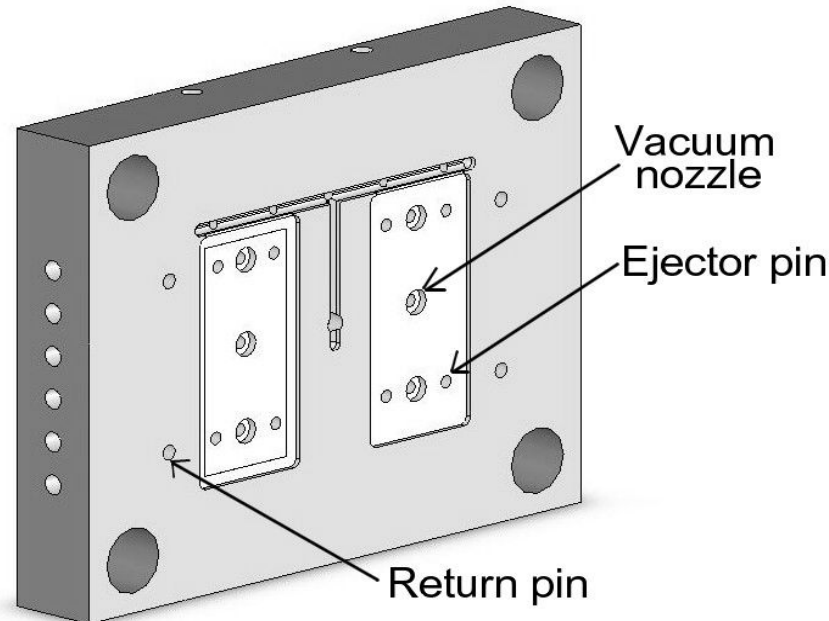

Figure 4.7: Cavity plate of the IML mold with vacuum nozzles and ejector pins defined

4.7   Mold Venting

This IML mold does not require any vent gaps, vent channels, or special design features for venting because air has sufficient possibilities to escape along ejector pins and at the parting line. This is called passive venting. With the passive venting, the air can escape mainly through the parting line during mold filling. This method was proved to be sufficient, since no burning residue due to diesel effect can be observed particularly at the end of the part.

4.8   Label Insertion

A linear pneumatic robot is employed for inserting the in-mold labels into the mold cavities. Firstly, the labels are taken out of the label magazine by the robot end-of-arm tool equipped with small vacuum suction cups. Then the robot transfers the labels to the mold cavity and places them onto the cavity walls at the desired positions. As the vacuum at the robot arm is released, the vacuum in the mold cavity is simultaneously built up so that the labels are hold in the position. At this time, the prepared mold is ready to be injected. To avoid the robot damage, molding must be made with caution. As long as the robot is still found between the two mold halves, mold closing cannot be initiated. In this case, a digital pressure switch is integrated into the molding automation system in order that mold closing is directly controlled by the signal given from the digital pressure switch. If the cavity missed the label, inadequate level of vacuum is generated and the digital pressure switch notifies the molding machine that mold closing cannot definitely be started.

5 Simulation and Experimental Study on the Injection In-Mold Labeling Process

5.1 Simulation on the Injection In-Mold Labeling

5.1.1 Mesh Generation

One of the key steps of the finite element method for numerical computation is mesh generation. Once the part model (usually 3D-CAD model) and the optimum surface mesh were successfully created, 3D-mesh can be generated based on the created surface mesh. In this study, the generation of the part and mesh model was performed using Rhinoceros®, a plug-in for Moldex3D®. Firstly, the IML part model along with the labels as well as the sprue and runners were meshed with prism and tetrahedral elements, respectively (Fig. 5.1).

Two sensor nodes are placed onto the mesh model at corresponding positions where the sensors are mounted in the injection mold, namely on the side without label. It is a so-called combined pressure and temperature sensor used in the injection molding process. In the injected mold half, the first sensor can be found at approximately 20 % of the part length away from the film gate. The second one was placed at approximately 20 % of the part length measured from the end of the cavity. Subsequently, the cooling channels and the mold base were discretized using rod elements and tetrahedral elements, respectively. Before the mesh models can be exported to Moldex3D®, the injection point and the necessary boundary conditions e.g. melt injection point must be defined. Finally, 3D non-isothermal based simulation can be conducted with Moldex3D®.

Figure 5.1: Mesh model of the IML part and mold

The number of the part element is 73,594, whereas the total number of the two label elements is 4,084 prism elements. Mold base was meshed with 386,794 tetrahedral elements.

5.1.2 Viscosity Model

As injected material, polypropylene type Novolen 3200 MC supplied by BASF was applied. The viscosity function and the pVT-diagram of the used material derived from Moldex3D®'s material databank are shown in Figure 3.2. Simulations on the IML were carried out based on the parameter listed in Table 5.1. In addition to polypropylene, polystyrene 158 K supplied from BASF was also used in some experiments in order to make the comparison between two materials regarding the part warpage of the injected IML parts.

5.2   Experimental Study on the Injection In-Mold Labeling

5.2.1 IML Part Geometry

As already discussed in the Chapter 3, IML part is schematically illustrated in Figure 5.2.
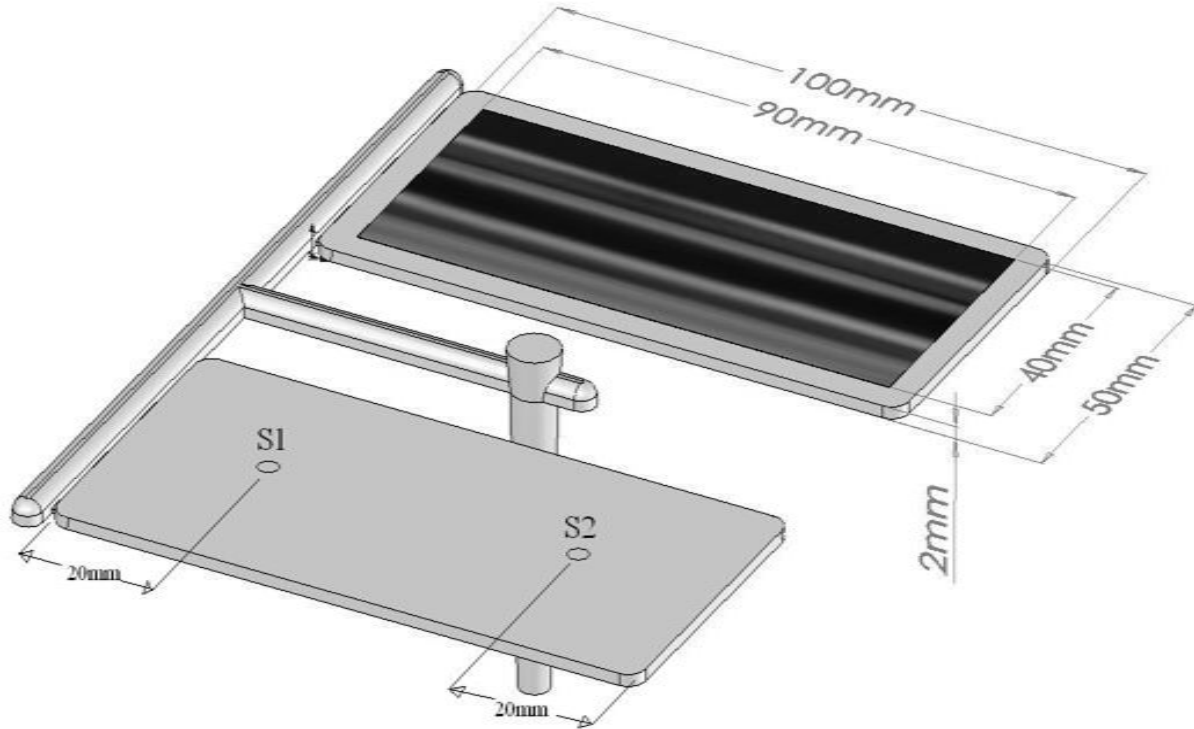

Figure 5.2: Schematic view of the IML part with the label defined

To utilize the holding of the label in the mold cavity, vacuum channels and nozzles (Fig. 4.7) were machined into the mold plate. By inserting the sintered metals onto the vacuum nozzles, label can be hold in the right position without slipping.

To determine the pressure and temperature gradients during the injection molding process, two combined pressure and temperature sensors, supplied from the company FOS measuring technique Co., Ltd., Germany (Fig. 3.3), were mounted into the stationary mold half. The first sensor (S1) is approximately 20 mm away from the film gate. The second sensor (S2) is positioned at 20 mm from the end of the cavity. The IR thermometer can measure the actual melt temperature in a temperature range between 30 $^{\circ}$C and 400 $^{\circ}$C. The pressure sensor can measure the melt pressure during molding within a range between 0 and 2000 bars.

5.2.2 In-mold Label Properties

As in-mold labels, two punched label types with the thickness of 75 μm and 50 μm, supplied by Inotec barcode security Co., Ltd., Germany, were employed. The thick label is a porous type, which comprises the substrates of polyolefin polymers and silica, whereas the thin type consists of only polyolefin polymers. To guarantee the UV-resistance to the printed layer, both labels were coated with an unknown special substance.

Figure 5.3 and 5.4 illustrate the thermal properties of the thick and thin in-mold labels, respectively.
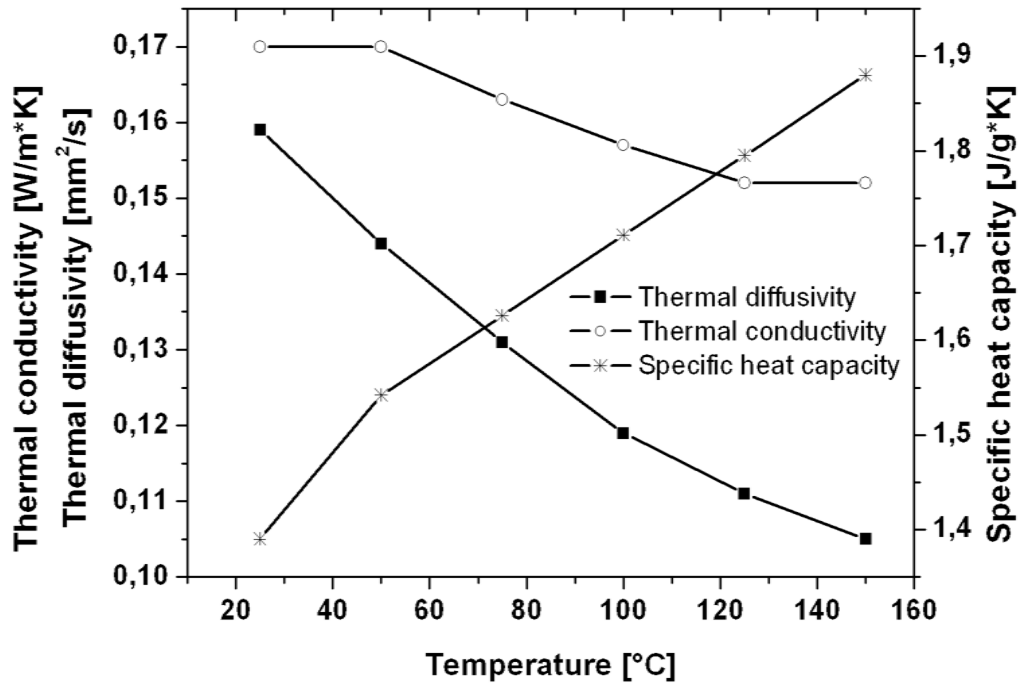
Figure 5.3: Thermal properties of the thick in-mold label
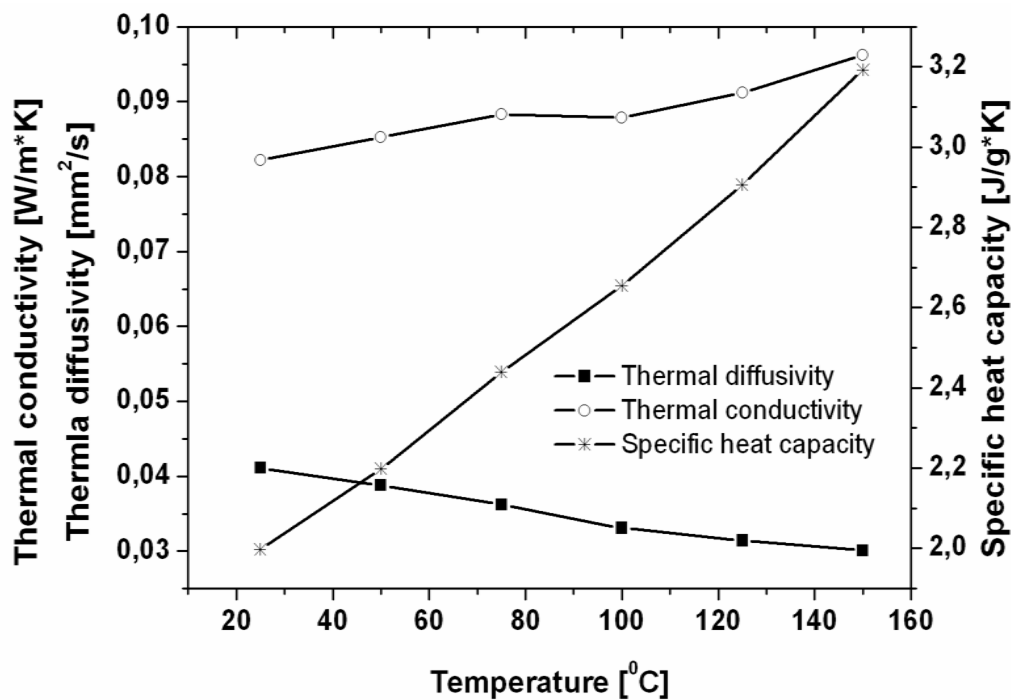
Figure 5.4: Thermal properties of the thin in-mold label

The thermal conductivity is measured by the method of a linear heat source [80]. Thermal conductivity of the label is an important parameter in conducting the simulation of the injection IML process. In this study, label material which must be defined in the simulation as an insert was selected from the Moldex3D® data bank. Many tests had been done in order to acquire the most suitable label material from the Moldex3D® data bank. Eventually, PP Novolen 1040 K was designated to be defined as a suitable label material with the measured thermal conductivity substituted.

5.2.3 Design of Experiments

Usually, in injection molding process there are many different machine and process parameters responsible for the properties of the injection molded parts. Changes in parameters such as melt temperature, mold temperature, and injection velocity affect the orientation, mechanical properties or even the surface roughness of the molded part. Thus the injection molding technique forms a nonlinear, complex, multi-variable process, in which the influences of the parameters superimpose on the quality criteria. During the optimization of the injection molding process, the task consists of analyzing the magnitude of the influence of the individual parameters on the quality criteria and determining the connection between single parameters and the quality criteria. Experiences from the earlier studies have shown that the following parameters are important: injection velocity, holding pressure, cylinder temperature, holding switch, and mold temperature.

According to this knowledge, following parameters were selected in order to carry out systematic experiments. As the normal setting (IML1), the experiment was carried out with the following parameters:

- Holding pressure: 500 bar

- Injection velocity: 50 %

- Cylinder temperature: 195 $^{\circ}$C

- Mold temperature: 40 $^{\circ}$C on the two mold halves, and

- Holding switch: 98 % filled volume

In addition, holding time and cooling time were entirely set at the constant values of 8 and 9 seconds, respectively.

Table 5.1 shows the list of the IML experimental studies. Compared to the normal setting (IML1) holding pressure was varied by the IML2 and IML3 experiments. In IML4 and IML5, injection velocity was changed, whereas the holding switch was differently set in IML6 and IML7. Cylinder temperature was also varied in IML8 and IML9 experiments. Mold temperature variation was performed by IML10 to IML13 experiments.

Experiment	Parameter setting	Detail	Remark
IML1	Normal setting	40 $^\circ$C/40 $^\circ$C	stationary/moving plate
IML2	Holding pressure variation	400 bar	
IML3	Holding pressure variation	600 bar	
IML4	Injection velocity variation	30 %	
IML5	Injection velocity variation	70 %	
IML6	Holding switch variation	90 %	
IML7	Holding switch variation	95 %	
IML8	Cylinder temperature variation	180 $^\circ$C	
IML9	Cylinder temperature variation	210 $^\circ$C	
IML10	Mold temperature variation	35 $^\circ$C/60 $^\circ$C	stationary/moving plate
IML11	Mold temperature variation	60 $^\circ$C/35 $^\circ$C	stationary/moving plate
IML12	Mold temperature variation	35 $^\circ$C/70 $^\circ$C	stationary/moving plate
IML13	Mold temperature variation	70 $^\circ$C/35 $^\circ$C	stationary/moving plate

Table 5.1: List of the IML experimental studies

6 IML-Simulation and Experimental Results

6.1 Melt Front Advancement

Figure 6.1 shows the melt front advancement from the short-shot study conducted with IML1 molding parameters but without holding pressure compared with that from 3D simulation.

30 % filled

40 % filled

80 % filled

90 % filled

100 % filled
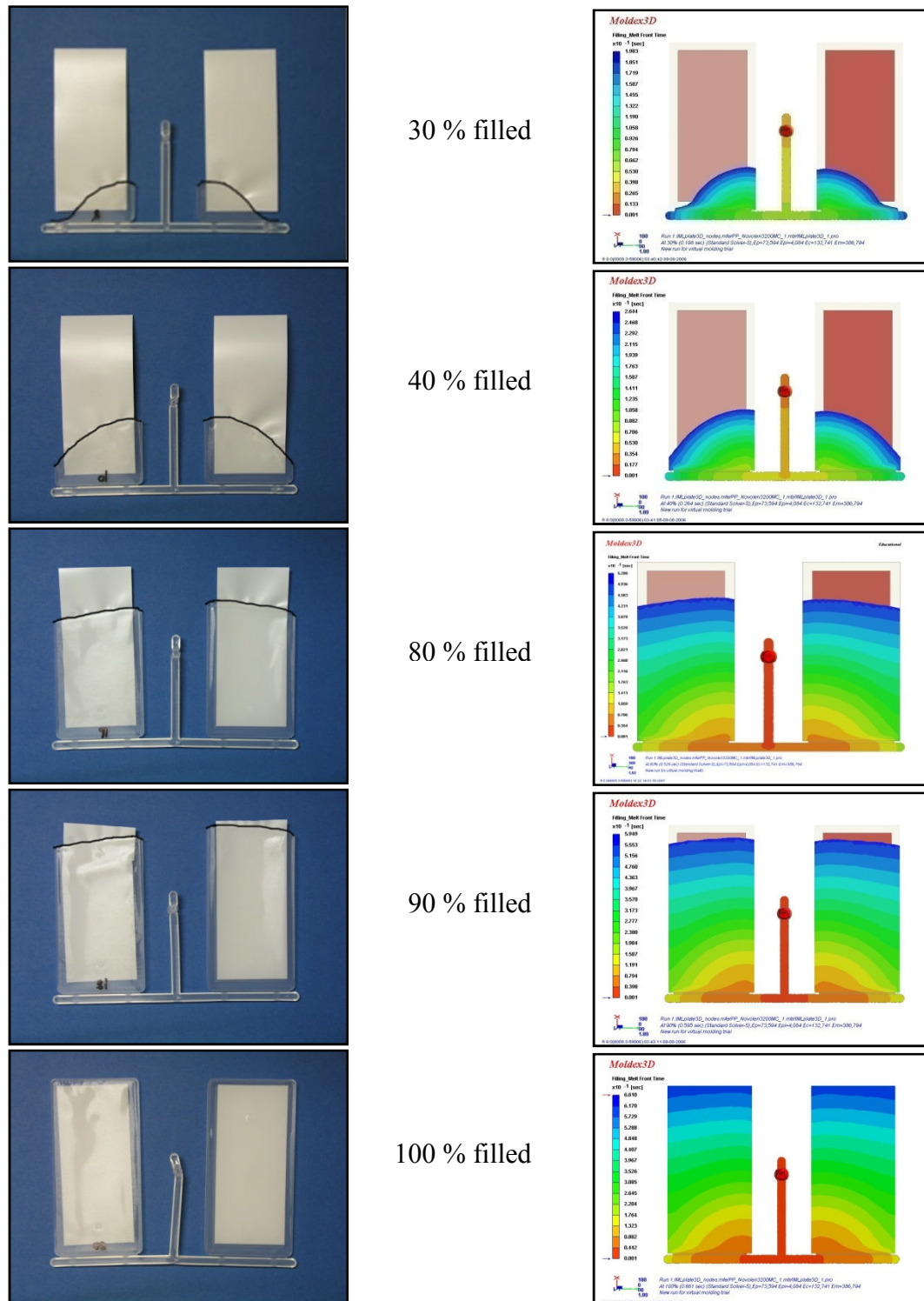
Figure 6.1: Short-shot study from the real process and simulation

From the short-shot study, it is obvious that the melt front advancement at each filling step of simulation agrees well with the advancement from the real molding process. At the beginning the melt flows symmetrically into both cavities through the film gate. Despite the film gates, both cavities were filled first from the inner corners of the part at the beginning of the filling phase. This resulted from the failure to optimize the cross-section of the film gates and from the shear heating of the melt occurring especially at the runner wall and at the corner of the cold runner. In course of filling, the flow fronts at the outer edges advance faster, so that the cavities were filled nearly parallel to the film gate. In addition, it can be seen that starting from an 80 % filled volume the melt front in the right cavity slightly outruns the left cavity. This is due to the shallow window, electrically discharged onto the right cavity which helps fixing the label during molding, which causes the slightly reduced flow resistance in the right cavity. Therefore the right cavity was completely filled with extremely small time difference before the left cavity. In this case, the right cavity which was already filled had experienced the excessive holding pressure, which caused the unnecessary stress to the molded part. In the simulation, however, such difference of the melt front advancement in the cavities is not noticeable.

6.2   Course of the Pressure
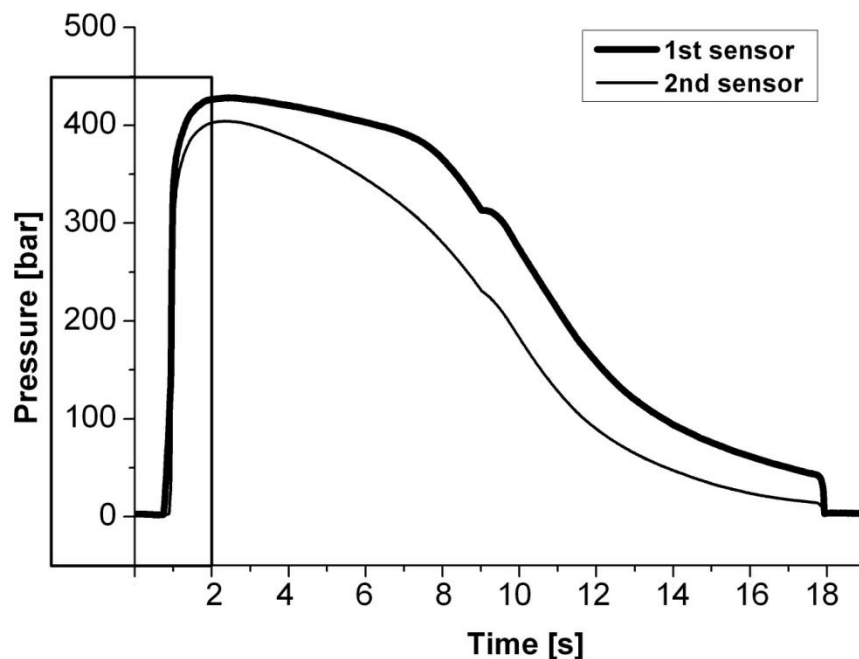
Figure 6.2: Pressure profiles during the injection IML

Figure 6.2 to 6.4 show pressure profiles during filling phase from the experiment and 3D simulation conducted with IML1 molding parameters.

The maximum pressures at the end of filling phase, determined using two sensor nodes placed at the comparable positions where the IR temperature sensors are mounted in the mold, were defined by 91 (S1) and 26 (S2) bars, respectively, while the measured pressure peaks from the 1st and the 2nd sensors lied with approximately 150 and 50 bars. Comparing the values from the 1st sensors, it can be stated that despite the underestimated pressure from

3D simulation, the pressure values from the experiment and simulation lay relatively near together. From the experiment, there is a small kink on the 1st sensor pressure curve. This results from the excessive holding pressure and the compressibility of the polymer melt. At the end of holding phase, the compressed melt becomes more relaxed and expanded with the volume constraint from the cavity against the front of the sensor. By this way the pressure values increase. Concerning the excessive holding pressure, holding was performed during molding with the hydraulic pressure which was entirely set at 500 bars. This constant pressure is apparently too high, not for holding switch itself but for the whole holding period. Parts that have experienced the excessive holding pressure during molding usually contain high residual stresses and hence are prone to warpage. To cope with this, profiled holding pressure with gradually reduced values should be set instead.
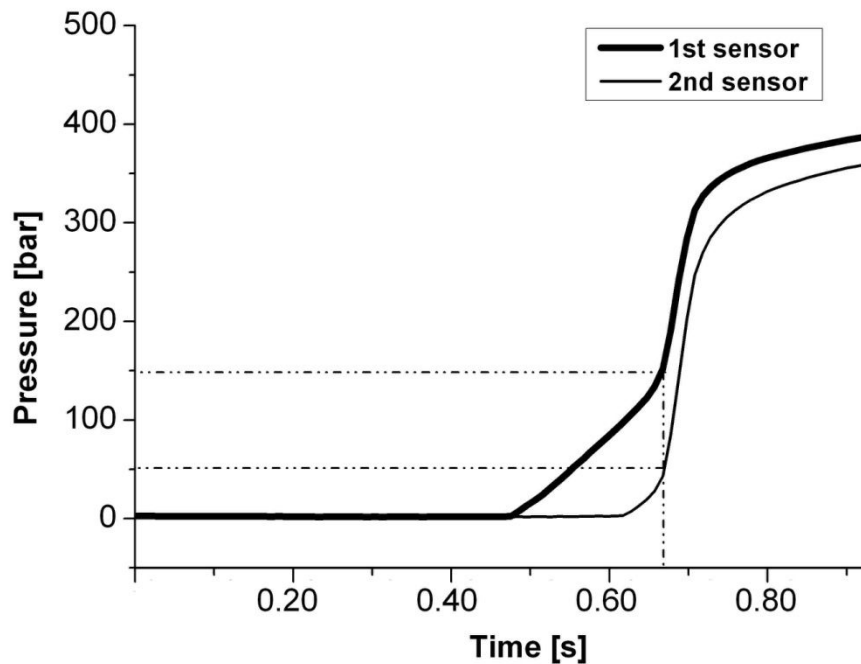
Figure 6.3: Expanded pressure profiles of filling phase (filling time 0.66 s)
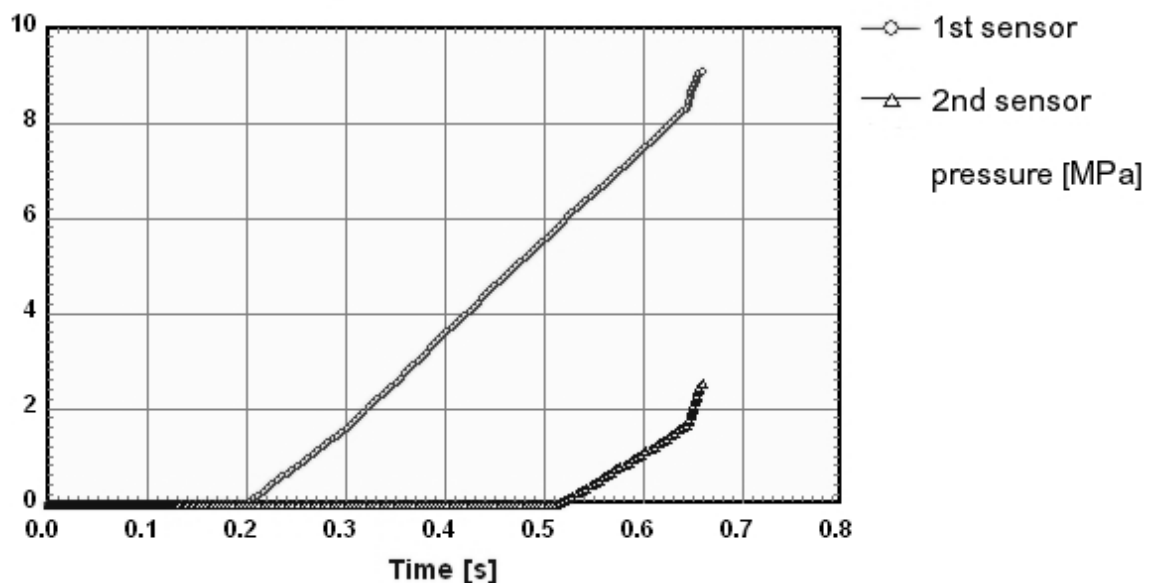
Figure 6.4: Pressure profiles from 3D simulation

6.3   Temperature Profiles and Distributions

The computed temperature gradient over the part thickness of the injected IML part (with IML1 parameter setting) during filling, holding and cooling phase is shown in Figure 6.5. From this figure, the maximum temperature in the part at the end of filling phase is approximately 195°C. At the end of the cooling phase, the melt temperature of approximately 68°C was computed. As an interesting result of 3D simulation, an asymmetrical temperature gradient over the part thickness can be detected. This phenomenon is expected to happen particularly in the back injection of a film, in that the film acts as thermal insulator. In filling phase the temperature distribution was almost symmetrical over the part thickness, whereas in holding and cooling phase unbalances in the temperature distribution become evident. The green to red colors in Figure 6.5 bottom right (End of cooling) point on the fact that the part surfaces covered with labels are still much warmer than the rest of the part uncovered by the label, which already cooled down to the mold temperature level at this time.

Temperature profiles T(t) of the molding was measured by two IR temperature sensors. Commercial IR temperature sensors for plastics processing exhibit response times within the millisecond range and permit measurements without heat conduction errors with high resolution. In practice, the broad employment of this kind of sensor is at present affected by difficulties in the range of the linearity and calibration of such sensors, by the self-radiation of the sensors, as well as by the unknown depth of measurement. Plastics as selective emitters are partly permeable for electromagnetic radiation, with the consequence that the radiant heat from the inside of the plastic part attains the outer region of the plastic part and thus some quantities of the radiant heat can also reach the sensor. Thus the measured temperature represents a weighted average value over an unknown measuring volume.

a)
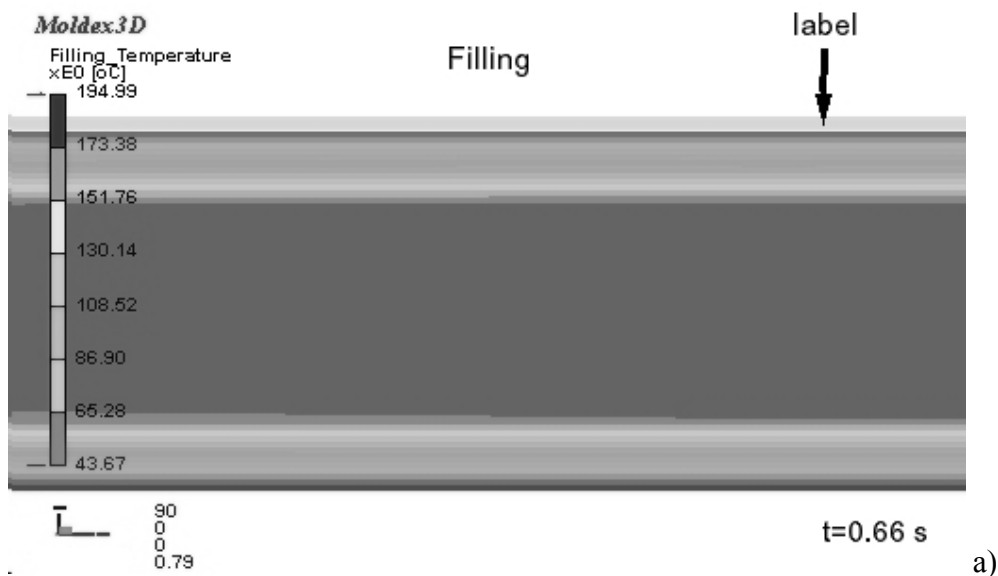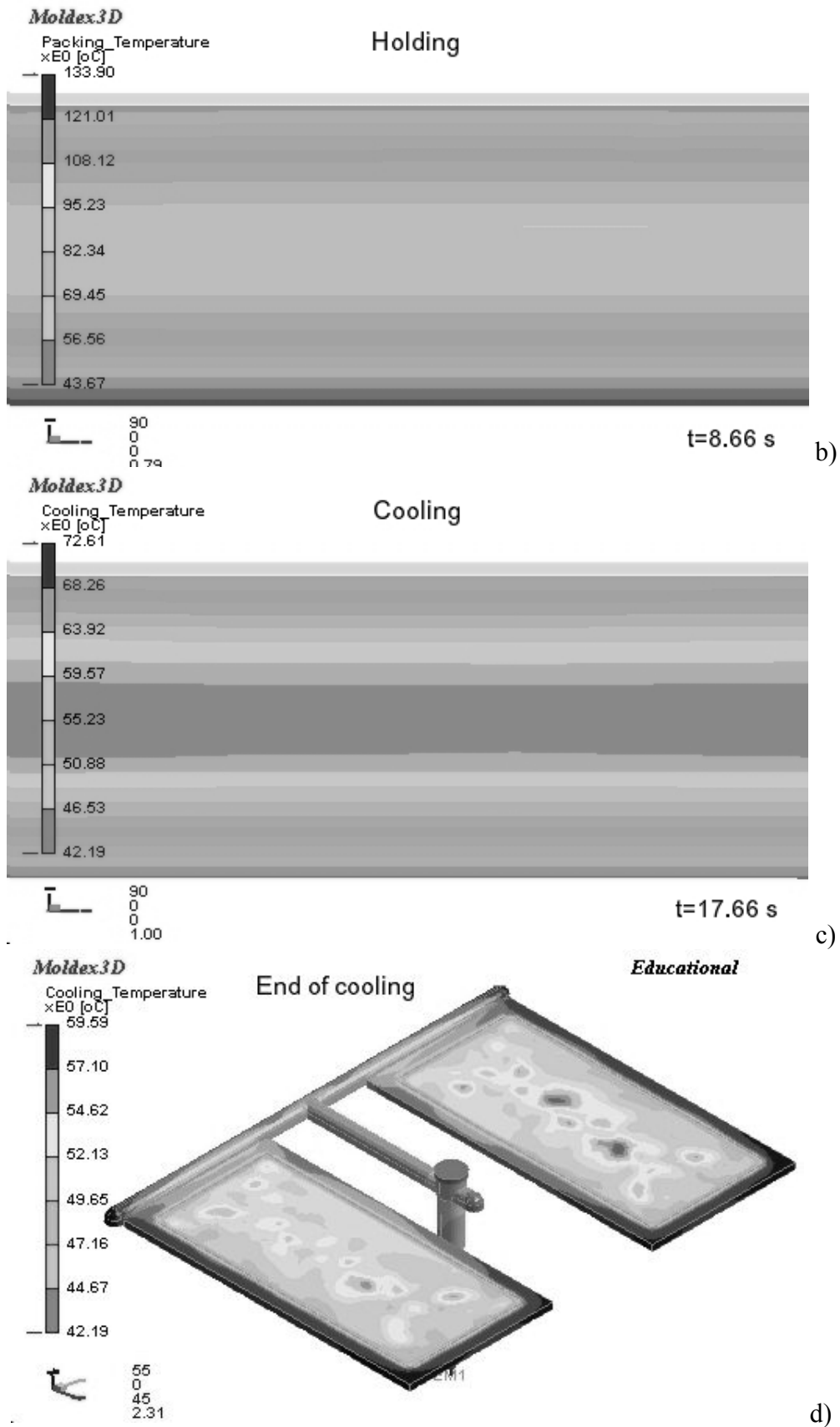
Figure 6.5: Temperature profiles and distributions over the part thickness of the injected IML part at the end of a): filling, b): holding, and c)-d): cooling phase
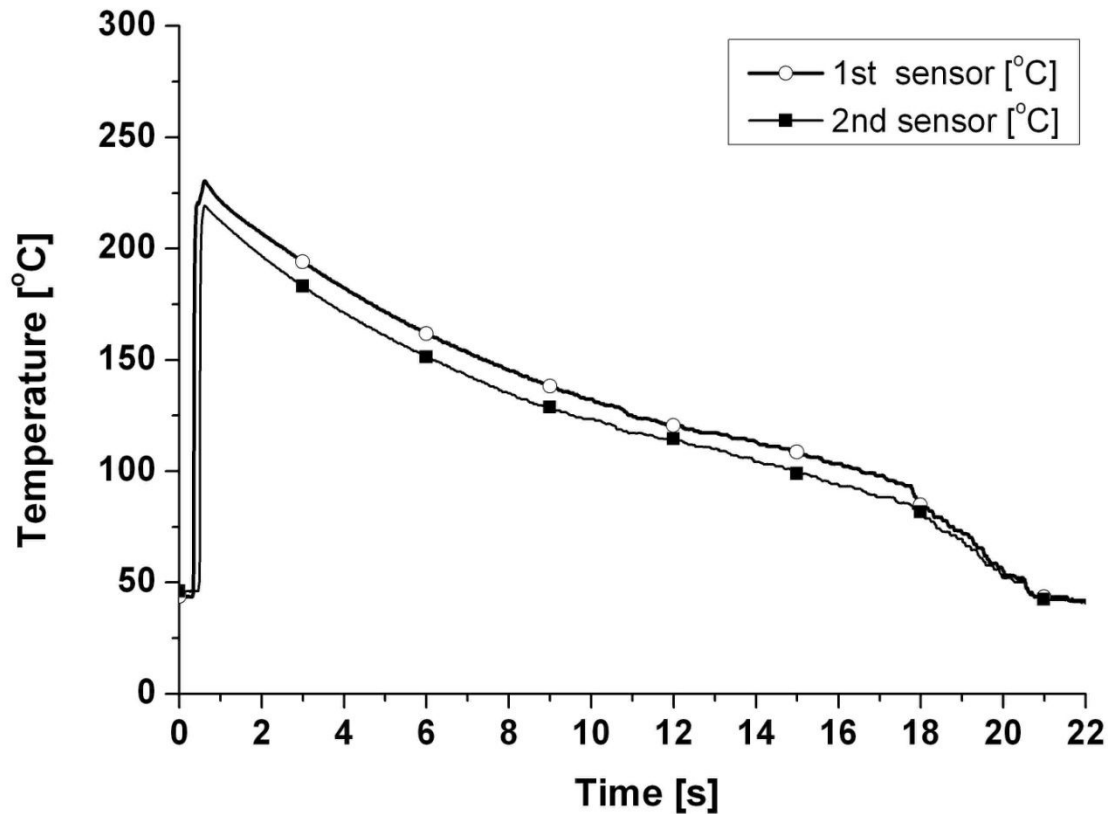
Figure 6.6: Temperature profiles during the injection IML

Figure 6.6 shows temperature profiles during the injection molding of the part molded with IML1 molding parameters. From Figure 6.6, the maximum melt temperature, detected near the gate (1st sensor) is approximately 230 °C, whereas the temperature peak measured away from the gate (2nd sensor) is 220 °C. Compared with those determined from 3D simulation, the maximum temperatures lay relative near together. Because of the unknown depth of measurement of the IR sensors, a comparison of the temperature gradients from experiment and simulation is foregone at this state.

6.4   Structure of an Injected IML Part

In-mold labeling as one of the film insert molding techniques offers many benefits in terms of production time and cost savings as well as esthetics of the products. However, this molding technique has one main drawback, in that the molded parts prone to warpage as a result of an asymmetric cooling process. And because the morphology differentiation over the part thickness of the injection molded part has a tremendous influence on the mechanical behavior of the part, it is necessary to investigate the structure of the IML part closely.

Figure 6.7 illustrates crystalline structures as well as amorphous layer of the IML part. Under the light microscope, four different zones in the IML part can be distinguished. On the label side, porous label structure as well as fine and crystalline structures can be seen, respectively. In the middle of the IML part, crystalline structure (spherulites) can only be found, whereas the amorphous layer in addition to the fine and course crystalline structures can be detected on the opposite side.
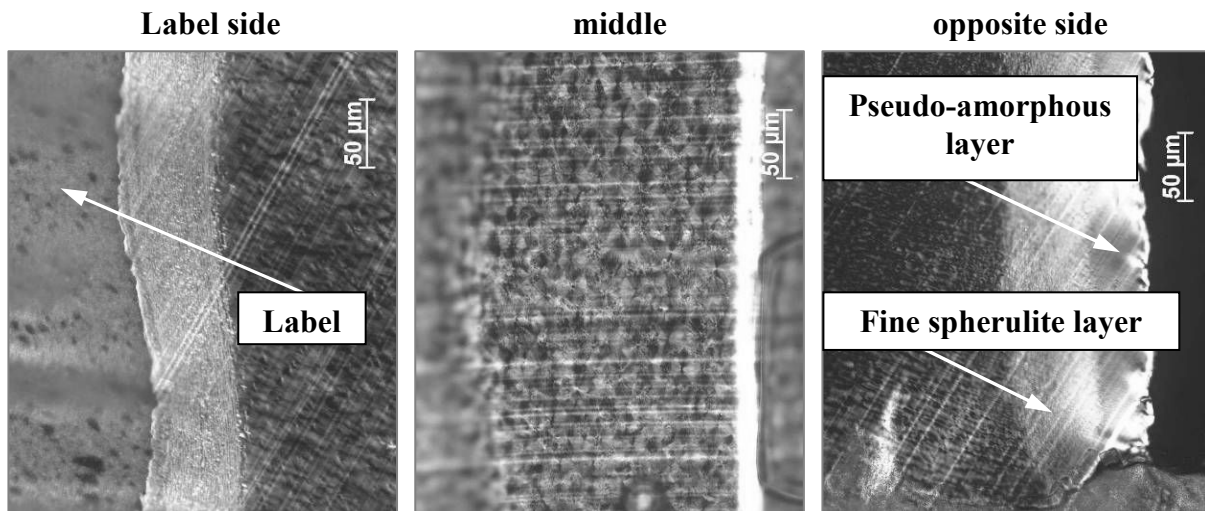
Figure 6.7: Crystal structure and amorphous layer of the PP injected IML part

The crystallization is first determined merely by thermal conditions, whereas the cooling rate primarily affects the degree of crystallization. This mechanism applies with a condition of the steady flow melt. But this condition alone can no longer be assumed especially in an injection molding step, since the crystallization in an injected part results mainly from shear and elongation stress, rather than from the thermal boundary conditions. One speaks in this connection also about shear or flow induced crystallization. At low temperatures and flow rates these crystallization processes are the most important parameters affecting the morphology of technical plastic parts.

Analogous to molecule orientation, two different deformation mechanisms are important to the development of the different zones. The elongation deformations at the flow front cause a flow induced crystallization in the outer zones of an injected part. By contact with the cold mold wall the melt cools down immediately and an extremely fine spherulite structure emerges at the part surface. The influence of the high cooling rate at the outer zone, which would suppress the crystallization there, is partly compensated to some extent by shearing. Under the light microscope the structure near the surface seems to be amorphous (pseudo-amorphous) because of the insufficient resolution of the light microscope. However, it is actually semi-crystalline.

Apart from the deformation processes at the flow front, the crystallization is also affected by the shear deformation in the subsequent flow (shear-induced crystallization). Through shearing a visible fine spherulite structure arises underneath the pseudo-amorphous layer. This structure is the so-called Shish-Kebab structure [81, 82]. However, shearing also causes an increase in temperature, which works against. Thus, the thickness of the fine spherulite layer varies as a function of the melt flow rate. In addition, the shear-induced crystallization is highly influenced by the type of polymer and its molecular structure. The number of spherical nuclei is affected by the local magnitude of the cooling rate [82, 83].

In the middle of the molded part, there is a coarse crystalline structure which occurs as a result of cooling of the steady flow melt. This coarse structure is caused by a smaller number of nuclei induced in the cooling melt and the wider distance between them [84].
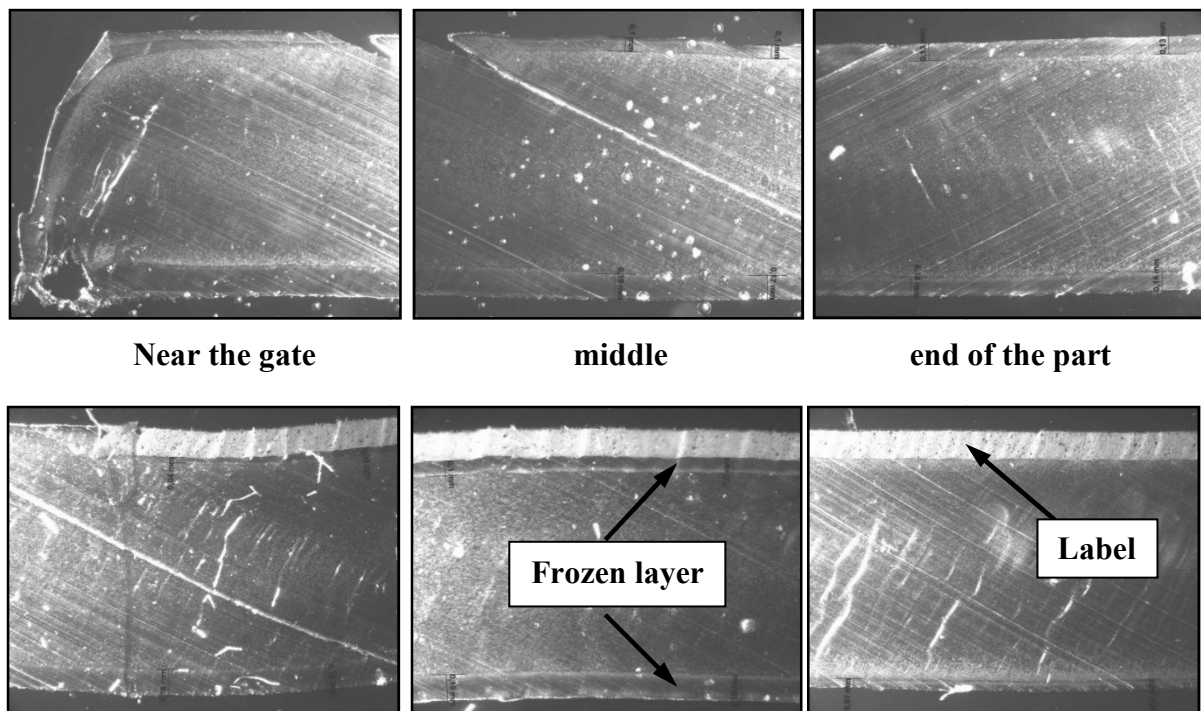
Figure 6.8: Frozen layers in the IML part (top: without label; bottom: with label)

The frozen layers in the IML part are shown in Figure 6.8. These frozen layers actually consist of the amorphous layer and the fine spherulite layer, which are transparent under the light microscope. From the figure, the frozen layer near the gate of the molded part is much thicker than away from the gate. It arises on both sides of the molded part. On the label side this frozen layer is much thinner over the entire part length than on the opposite side. Because the heat conductivity of the label is much lower than that of the metal mold wall, and when the melt contacts the label, it is not quenched. According to this, the crystallization of the melt on the label side can further develop contrary to the opposite side of the molded part. By the different cooling rates, the flow fronts no longer advance symmetrically. In addition, the holding pressure cannot work evenly over the part thickness, which could bring about stresses in the molded part and even to the warpage of the molded part after demolding.

For the molded part without label (Fig. 6.8, top), the two frozen layers are not equal in thickness as expected. This is because of the different cooling efficiency of the mold halves. Moreover, the film gate was not positioned right in the middle of the part thickness and this leads to asymmetrical flow front of the polymer melt over the part thickness, especially at the beginning of filling. The difference in frozen layer thickness, however, decreases with an increase in the degree of the cavity filling.

For the IML part (Fig. 6.8, bottom), the frozen layer on the label side is right from the beginning much thinner than on the opposite side. At the end of the IML part, no obvious frozen layer juxtapose to the label structure can be seen, whereas the layer on the opposite side can still be clearly detected. This can be described again on a basis of the crystallization of the polymer melt, since the crystallization temperature of the polymer melt (Tc) becomes higher with an increase in the cooling rate. According to this, the frozen layer becomes thinner at the distance away from the gate, as the melt cooling rate decreases. With an existence of the label as a thermal insulator during molding, the melt cooling rate at the end of the molded part was once more reduced.
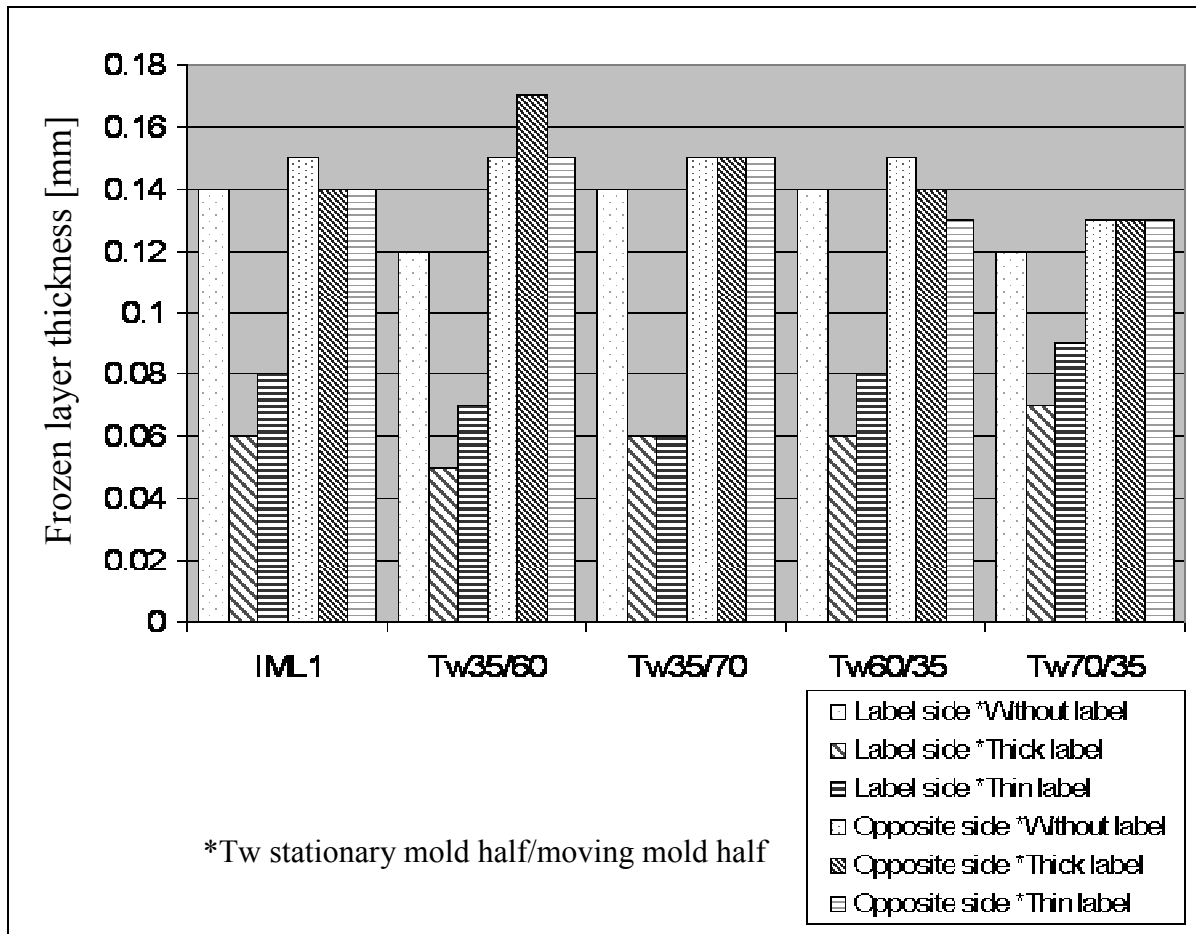
Figure 6.9: Frozen layer thickness of the IML parts

Figure 6.9 shows the frozen layer thickness of the IML part injected with different mold temperature settings. There are three types of samples namely parts injected without label, parts molded with thick and thin labels, respectively. For each type of samples, thicknesses of the two frozen layers, one on the label side (moving mold half) and another on the opposite side (stationary mold half) were measured at comparable distance from the gate. As can be seen from Figure 6.9, in general, the frozen layers on the opposite side of the label are explicitly thicker than on the label side. This resulted from the high temperature difference between the polymer melt and the cold mold wall. In addition, the frozen layer on the moving mold half of the part molded without label is much thicker than parts molded with thin and thick label, since the label acts as a thermal insulator. Despite the higher thermal conductivity of the thick labels (Fig. 5.4 and 5.5), the frozen layer on the label side of the part molded with thick label is somewhat thinner than that of the IML part with thin label. This is because of the thickness of the label itself that also affects, to a large extent, the cooling of the polymer melt. Rule of thumb is, the thicker the label, the better it is to be a thermal insulator.

With the mold wall temperature combinations (different mold half temperature settings), the frozen layer thickness can be considerably influenced with the expectation to cope with the warpage of the IML part. The experimental results show that with the lower mold temperature on the label side (Tw60/35 and Tw70/35) the frozen layer on this side is somewhat thicker than that generated by the IML1 setting. As expected, the frozen layer on the opposite side is thinner. To the contrary, with the higher mold temperature on the label side (Tw35/60 and Tw35/70), the frozen layer is thinner on this side and thicker on the

opposite side. The effect of the mold wall temperature combination on the IML part warpage will be descriptively discussed in Chapter 6.5.
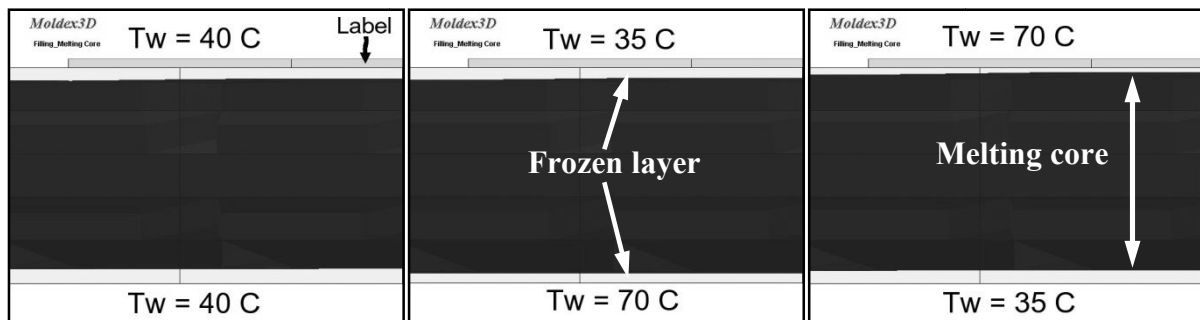
Figure 6.10: Frozen layers and melting core from the simulation

Figure 6.10 shows the numerical simulated frozen layers and the melting core occurring during filling phase at different mold temperature combination settings. 3D simulations were accomplished for three different mold temperature combinations. Firstly, filling phase was simulated at a mold temperature of 40 ^{o}C on both mold halves. Then the molding with the mold temperature combination of 35 ^{o}C/70 ^{o}C and 70 ^{o}C/35 ^{o}C (label side/opposite side) was conducted. All other molding parameters were kept constant. According to the simulation results shown in Figure 6.10, different thicknesses of the frozen layers can be computed. At a mold temperature of 40 ^{o}C on both mold halves, the frozen layer on the label side is somewhat thinner than on the other side. In the real molding situation, the frozen layer thickness near the gate on the label side is much thinner than on the other side. However, this simulation result agrees qualitatively well with the real molding situation. With temperatures of 70 ^{o}C on the label side and 35 ^{o}C on the opposite side, the frozen layer on the label side exhibits a smaller thickness compared to that at the mold temperature of 40 ^{o}C, whereas the frozen layer thickness on the label side increases, if this mold half is kept colder than the other side. This indicates that 3D simulation program is able to consider such asymmetries in the thermal boundary conditions qualitatively correct.
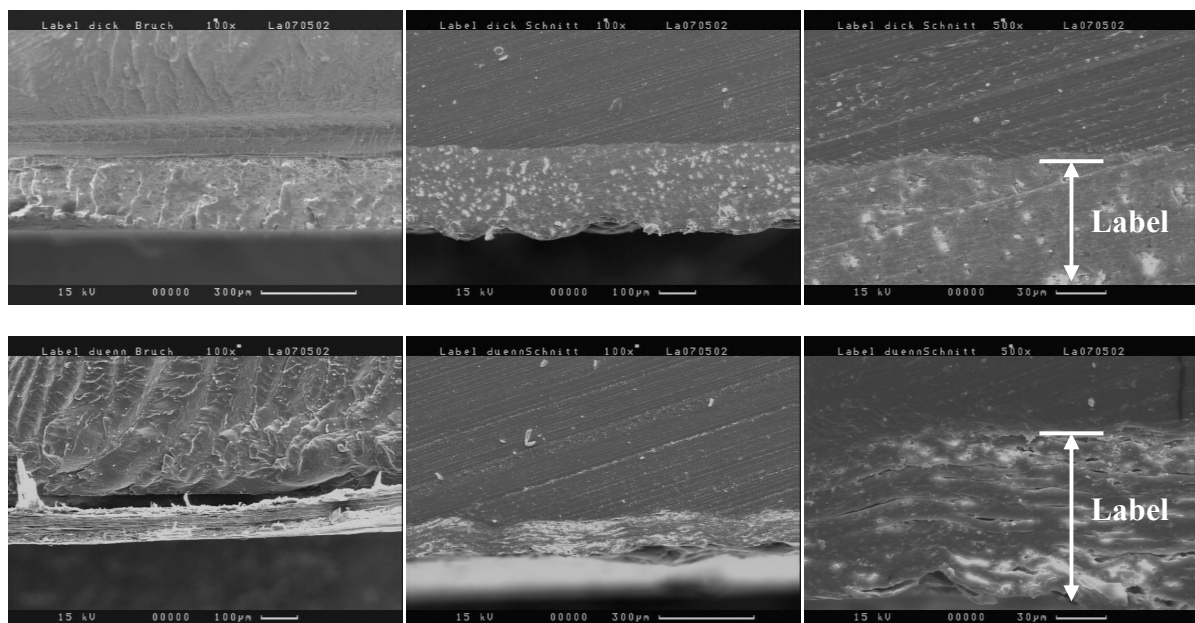
Figure 6.11: SEM micrographs of IML parts (top: with thick label; bottom: with thin label)

Figure 6.11 shows the SEM micrographs of the IML parts molded with thick and thin labels. The figures on the left are the IML parts prepared by immersing the samples into liquid nitrogen and then breaking into two pieces. On the right, the IML parts were prepared by cutting. As can be seen, thick IML label remains adhere to the part surface even if the part has experienced the sudden mechanical load (breaking) whereas the thin label has been detached from the substrate around the broken area. By cutting, both the thick and thin labels still tightly cling to the part. This realization will be discussed later in association with the strength of the IML part in the section 6.6 Modulus of elasticity.

6.5   Warpage of an Injected IML Part

Warpage in association with the injection molding develops as a result of residual stresses or locally shrinkage differentials in the flow and transverse direction, to the flow or over the part thickness [85]. The processing and the post-shrinkage are caused by the crystallization, by volume relaxation and orientation relaxation of the molding material as well as by the thermal contraction. Many dimensional errors result from the part warpage. By warpage one speaks also from the three dimensional deviations from the cavity, which is developed during the part shrinkage. It is not easy to predict the degree of part warpage, since the warpage itself depends on many parameters and environment. Besides the molding parameters such as temperature, pressure and properties of the polymer resin, stiffness and part thickness also affect the shrinkage and warpage of the molded part in a great value.

During the part shrinkage, additional mechanisms which lead to a decrease in the thermal contraction in relation to the pure thermal expansion are also involved. These are for example inherent stress and crystallization. The interaction of these parameters is very complex. Some parameters interact with each other and are, at the same time, dependent on each other. Therefore, the effect between the molding parameters would not be elaborated on the details.
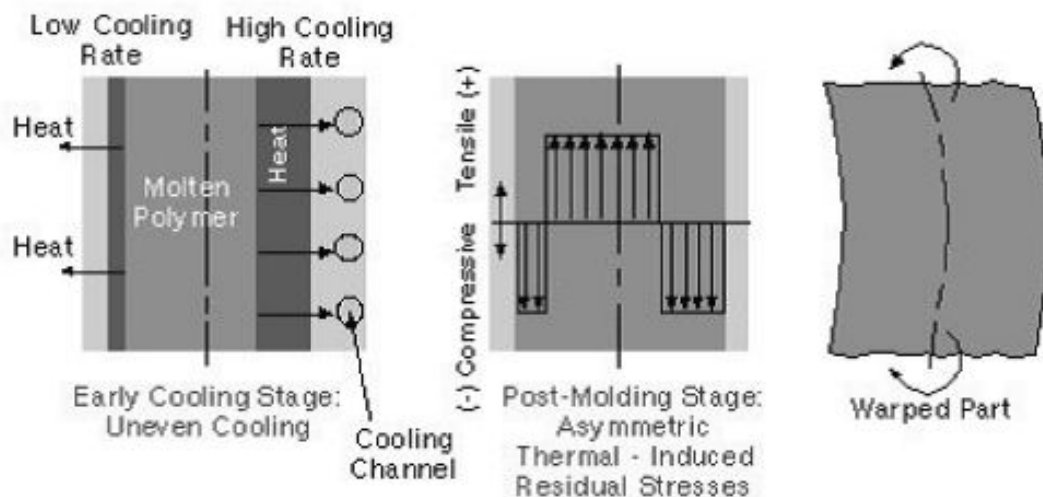
Figure 6.12: Asymmetrical thermal-induced residual stress caused by unbalanced cooling across the molded part thickness introduces part warpage

The internal stress can be mainly evoked by the cooling, expansion and flow effect [85]. The thermally induced stress is raised by a difference of mold wall temperature and polymer melt temperature in cooling process, and caused by a non-uniform cooling of the melt polymer (Fig. 6.12). The flow induced stress, shear stress or wall shear stress, on the other hand, is caused by shearing between melt front and mold wall during filling phase which brings about

orientations of macromolecules. The thermally induced stress is a dominant inherent stress with respect to the stress magnitude [86]. The thermally induced stress leads to the deformation of parts, whereas the flow induced stress causes anisotropy and optical properties, affecting surface molding state of the parts. Figure 6.12 shows how a flat part becomes deformed through different cavity temperatures existing on the left and right sides. Shrinkage is suppressed on the mold side with lower temperature, and the side with higher temperature undergoes more pronounced shrinkage. A type of bi-metal effect occurs [87].

The development of the inherent (internal) cooling stress which is described in a highly comprehensible manner by Stitz's solidification model [89] is shown in Figure 6.13, right hand side. The pronounced temperature profile that prevails in the solidifying melt during cooling (a) gives rise to a dissimilar thermal contraction potential in the different layers (b). The mechanical link that exists between the individual layers prevents them from sliding freely over each other and gives rise to a mean contraction (c). The impeded thermal expansion leads to the development of internal strains over the cross-section of the molded part.

$$\sigma = -\frac{2}{3}\,\alpha E\,(\vartheta_E - \vartheta_A)\left(\frac{6x^2}{s^2} - \frac{1}{2}\right)$$

σ = Stress

α = Coefficient of expansion

E = Young's modulus

ϑ_E = Freezing temperature

ϑ_A = Quenching temperature
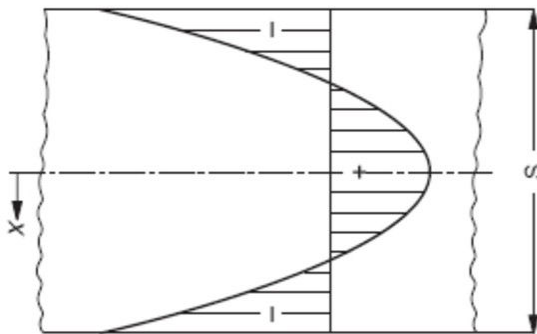
a) Temperature profile of the solidifying melt
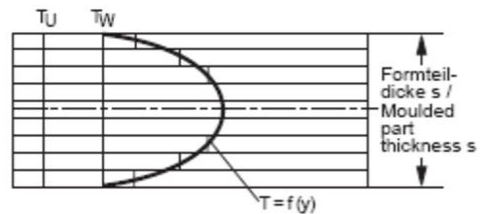
b) Without a mechanical link between the layers
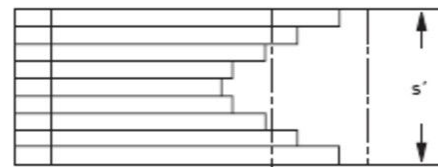
c) True profile (mechanically linked)
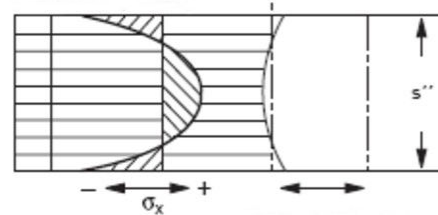
T_W : Wall temperature

T_U : Ambient temperature s : Wall thickness

T : Temperature σ : Stress

Figure 6.13: Cooling stresses according to Knappe [88], thermal contraction and the development of inherent stresses according to Stitz [89]

It is possible to specify an approximation equation for the cooling strain, according to Knappe, which shows a parabolic strain profile over the molding cross-section (Fig. 6.13, left hand side). The tensile phase of the cooling strain is located in the core of the molded part,

whilst the compression phase, which maintains the equilibrium, is located in the outer layers. The inherent cooling stresses can also have flow-conditioned inherent stresses superimposed on them which originate in stretching flow effects at the flow front, as well as internal stresses which result from an overpacking with subsequent demolding under residual pressure (stresses due to expansion).

By inserting a label into the injection mold, the warpage of the molded part is changed due to the decrease in the thickness of the substrate at the constant part thickness as well as the asymmetrical heat dissipation in the injection mold. Furthermore, the different thermal expansion coefficients as well as the different contraction potential affect the part warpage due to the different temperature levels of the insert material and the substrate during the cooling [90].

Figure 6.14 shows the measurement method of the part warpage. This figure shows the in-mold label which is attached to the molded part on the upper side. As can be seen, the IML part warps toward the opposite side of the label.
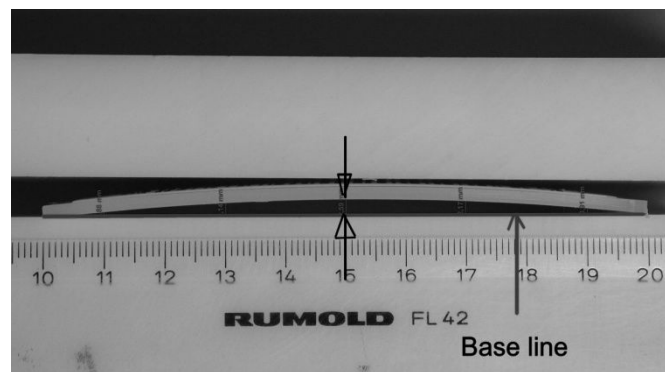
Figure 6.14: Measurement of the part warpage

Figure 6.15 exhibits the schematic diagram of the degree of warpage of the IML parts molded with thick and thin label, compared to the warpage of the parts molded without label. The degree of part warpage was measured 72 hours after being kept in a dry place at room temperature. From Figure 6.15, it is obvious that all the IML parts, independent of the label thickness and the different processing parameters, posses much higher degree of warpage than the parts molded without a label insert. They bend toward the opposite side of the label. The reason for this is the label itself, which caused an asymmetrical cooling over the part thickness and hence is responsible for the shrinkage or contraction differentials of the molded part. An asymmetrical or non-uniform internal stress distribution, as a result of the part shrinkage differential, leads then again to the warpage of the molded part [91]. Moreover, the contraction differential between the substrate and the label is so dominant that with the less contraction of the label owing to low temperature level during molding, the IML part warp toward the substrate side.

Usually, the asymmetrical inherent stress can be divided into contraction and bending stresses. After demolding, the part substrate comes to a contraction in the flow direction due to an existing inherent stress under the mold constraint. This contraction occurs until the force equilibrium in the flow direction comes about. The force equilibrium, then again, consists of tensile and compressive stresses, which can be considered as the bending stress. Therefore, the contraction stress resulted from the difference between an existing inherent stress under the mold constraint and the bending stress.
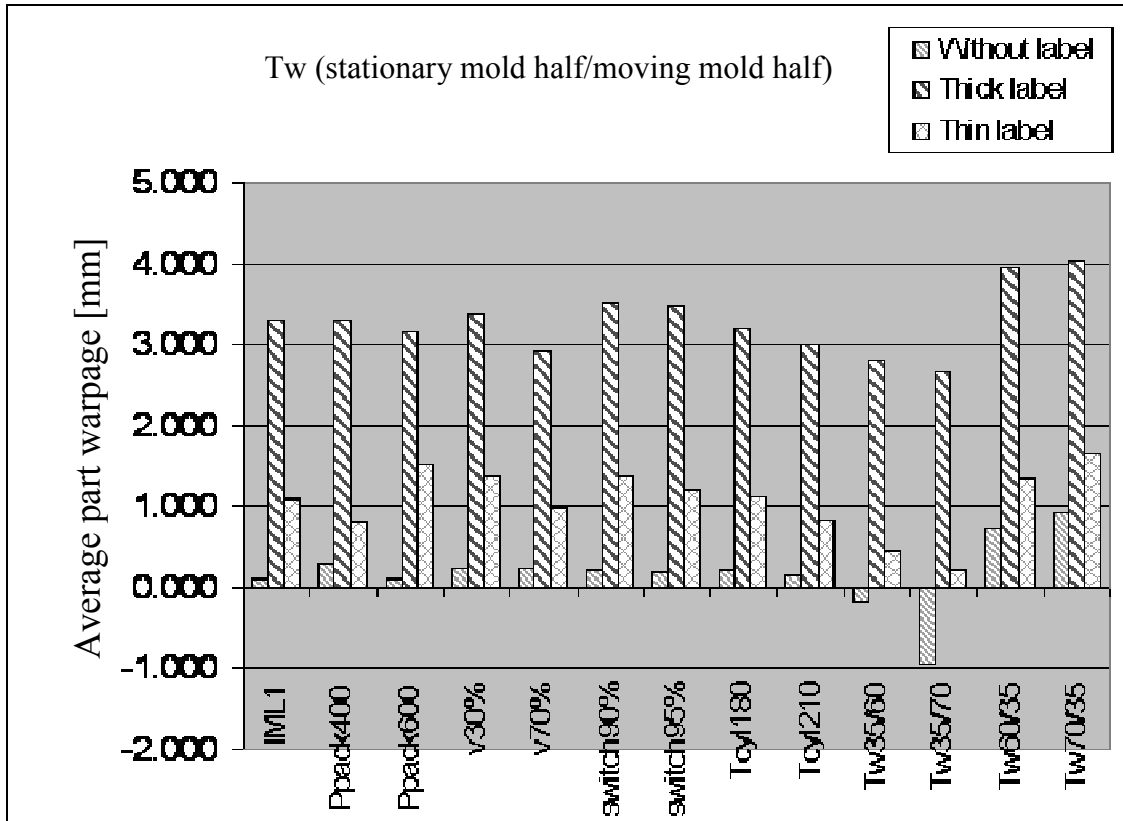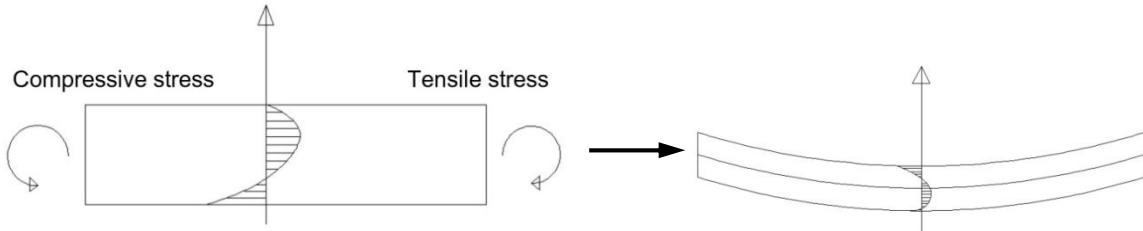
Figure 6.15: Warpage of the IML parts

Figure 6.16: Thermal induced warpage of the substrate due to bending stress
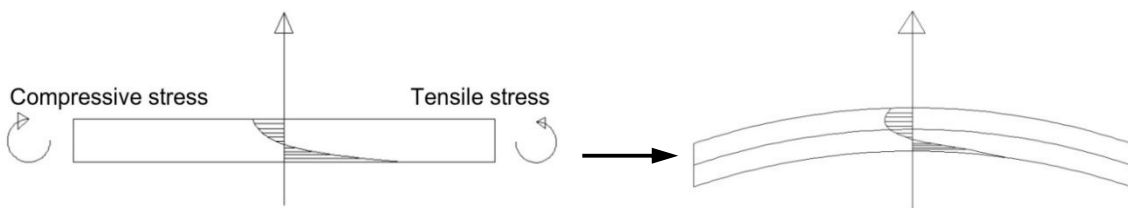

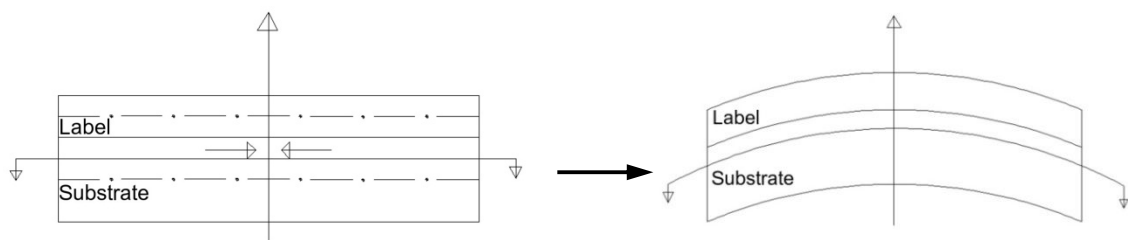**Figure 6.17**: Thermal induced warpage of the label owing to the bending stress

Figure 6.18: Total warpage of the IML molded part

If only the pure contraction stress is considered, a decrease in the length of the substrate in the flow direction after demolding will only be seen. To the contrary, if only the pure bending stress is considered, the substrate will warp toward the warmer side after demolding (Fig. 6.16) by the bending moment which equals to the multiplication of the bending stress, surface area, and the distance between the surface and the middle plane of the substrate.

Due to the heat transport phenomena in injection mold, the in-mold label also subjects to an asymmetrical temperature profile. Without the mold constraint, the label will commonly warp toward the warmer side, which is side to be connected to the substrate (Fig. 6.17). Considering the total deformation of the composite construction (IML part), these effects can no longer be separately taken into account and hence must be joined together due to the mechanical coupling between the substrate and the label.

Because of much smaller thickness and hence less stiffness of the label compared to those of the substrate and the higher expansion coefficient of the substrate, the higher contraction during the rest cooling of the substrate especially near the transition to the label owing to higher temperature field during molding can be implied. Consequently, as a composite construction, the label is forced to warp toward the substrate, whereas the substrate at the transition must be stretched (Fig. 6.18). There were tensile and compressive stresses resulting from these individual length alterations, which take effect on the respective surfaces of the label and the substrate. These stresses bring about the bending moment, which finally leads to the IML part warpage. It can be said that the degree of the part warpage is as a consequence of the relationship between bending stress, surface area, and the distance from the surface to the middle plane of the whole IML part. For the compact decorating materials, the rigidity as well as the coefficient of linear expansion of the substrate and the decorating material has a larger influence on the warpage of composite part.

For the parts molded without label as an insert, despite the equal mold temperature settings on the two mold halves, they bend toward the stationary mold half (Fig. 6.19, middle), which has lower cooling efficiency than on the other mold half (Chapter 3). This occurrence can be easily described by Stitz's solidification model (Fig. 6.13). An asymmetrical temperature profile over the part thickness during cooling evoked by the different cooling efficiencies of the mold halves causes a thermal contraction differential. With the higher melt temperature near the stationary mold half, the higher contraction of the melt develops during cooling and hence brings the part to warp toward this side.

The experimental results also exhibit that IML parts molded with thick labels have higher degrees of warpage than parts molded with thin labels. This is because of the thermal conductivity of the labels as well as the displacement of the middle axis of the substrate compared with the middle axis of the IML part. Thick label has a higher thermal conductivity than thin label (Fig. 5.3-5.4). If two label types are of the same thickness, the temperature maximum in the substrate connected to the label with higher conductivity appears further away from the transition between label and substrate. Consequently, the IML part with higher thermal conductivity tends to warp with higher degree toward the substrate side. Nevertheless, the effect of the volume contraction difference between label and substrate far outweighs the effect of the asymmetrical temperature distribution because much higher temperature of the substrate leads to the higher volume contraction compared to the label. The increase in the average contraction level of the substrate in relation to the average contraction level of the label leads to a warpage of the IML part toward the substrate side after the settlement of the thermal induced inherent stress. In addition, with an increase in the thickness of the same label type, the middle axis of the substrate is shifted compared with the

middle axis of the whole IML part to the substrate side. By this effect, the degree of warpage is intensified along with the increase in label thickness.

Besides the label thickness, the degree of part warpage is affected to a considerable extent by the mold temperature. The experimental study conducted by Wielpütz [90] has shown that the degree of part warpage of the IMD (in-mold decoration) part with compact decorating material can be influenced by heating the decorating material prior to inserting it into the mold cavity. This procedure, however, is not suitable for the injection in-mold labeling. Firstly, the temperature of the tempered IML label is hardly to be maintained uniformly throughout the production. Secondly, the tempering of the label contributes to the development of static charges, which consequently causes an attraction of an individual label within the label stack. A blocking of labels occurs. This complicates the handling of the label and also the whole production of the IML products. All of these speaks against the tempering of the in-mold label. Therefore, in this study, the effect of the mold temperature variation on both mold halves was concentrated instead.

An attempt to rectify the part warpage was carried out in this study. By setting the mold temperature on the moving mold half higher than on the other (Tw35/60 and Tw35/70), the degree of part warpage of the IML parts was reduced to some different extents. For molded parts without label, the part warpage was, to the contrary, intensified by these settings. Thereby, the warpage direction was reversed so that the parts warp toward the moving mold side. This indicates that the excessive temperature difference in both mold halves involved in the molding of the part without label insert.

From Figure 6.15, the last four experimental variants are interesting, with which different mold temperature combination settings for both mold halves were given, namely the combinations of $T_w=35^oC/60^oC$ (stationary half/moving half) and vice versa and $T_w=35^oC/70^oC$ and vice versa. The experimental results show that the degree of warpage of the molded part is greatly affected by the mold temperature combination. As mentioned above, if the mold temperature on the label side is chosen higher than on the opposite side, a smaller degree of warpage is to be realized, except for the parts molded without label. The temperature difference between the two mold halves is decisive to the degree of part warpage. An increase in the mold temperature on the label side resulted in the decrease of the heat flow through the label. On the other hand, the temperature field within the label becomes more homogeneous. The asymmetrical temperature profile turns to be more symmetrical over the thickness of the label. In addition, the temperature level in the label is increased with an increase in the mold temperature on the label side and thereby the contraction differential between the label and the substrate becomes smaller, less warpage occurs. To the contrary, by decreasing the mold temperature on the label side, strong asymmetrical temperature profile is induced, which leads to extreme temperature difference between the average label and substrate temperatures and ,of course, higher degree of warpage.

By tempering the IML parts molded with these conditions (Tw35/60, Tw35/70, Tw60/35, and Tw70/35), it can be manifested that all these parts exhibit higher degree of part warpage after being stored in an oven at the temperature of 80 ^oC for 24 hours. The reason for this is the higher contraction of the substrate as a result of the relaxation encouraged by tempering. While the tempering of both thick and thin labels at the same condition shows no effect to the contraction (shrinkage of label), the warpage of the tempered IML parts are then aggravated merely by the contraction in the flow direction of the substrate. Parts molded without label differentiate themselves from the IML parts. Tempering part without label molded with the mold temperature of 40 ^oC on both mold halves shows a little warpage alteration relative to

the IML parts. Because its temperature distribution over that part thickness is nearly symmetrical, the contraction arises also nearly symmetrically and the warpage has increased by a small amount. As soon as this temperature symmetry was interfered during molding process, for example by the mold wall temperature combination, the part warpage will be strongly influenced by the tempering.

As already mentioned, the effect of the volume contraction difference between label and substrate dominates the effect of the asymmetrical temperature distribution on the part warpage. In this study, besides the injected IML part with polypropylene substrate, IML parts with polystyrene substrate were also molded in order to study the effect of the substrate material and mold temperature combination which provoke the contraction differentials and hence warpage of the IML part. The experimental results have revealed that little to no warpage of the IML part molded with PS as substrate can be detected. This is because the volume contraction of PS is much lower than that of PP, the effect of the contraction difference is hence negligible. Despite the asymmetrical temperature distribution over the PS part thickness, the stiffness of PS substrate remains invincible so that the mold temperature combination shows no effect on the warpage of the referred part (compare Fig. 6.19 with 6.20).

The amount of the temperature difference which can be set between the mold halves depends on the composite part thickness as well as the polymer resin used. How and on which scale this temperature difference between the mold halves affect the IML part property will be discussed in Chapter 6.6.

Figures 6.19 and 6.20 illustrate the computed degree of part warpage from 3D simulations. As mentioned above, mold temperature combination settings have little to no effect on the degree of the part warpage of the IML part molded with PS as the substrate.
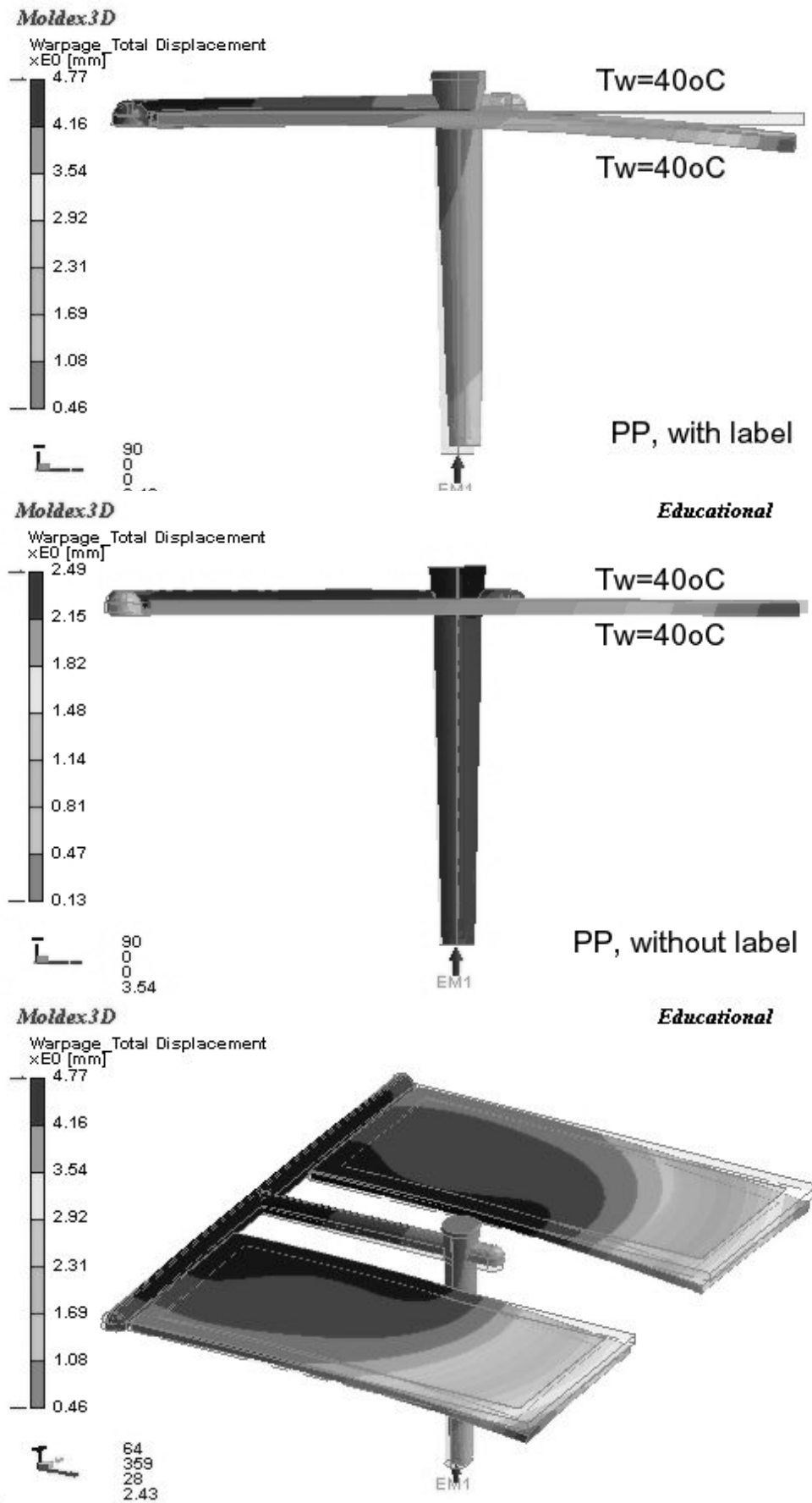
Figure 6.19: Part warpage from 3D simulations (IML1 setting; Tw = 40 ^{o}C)
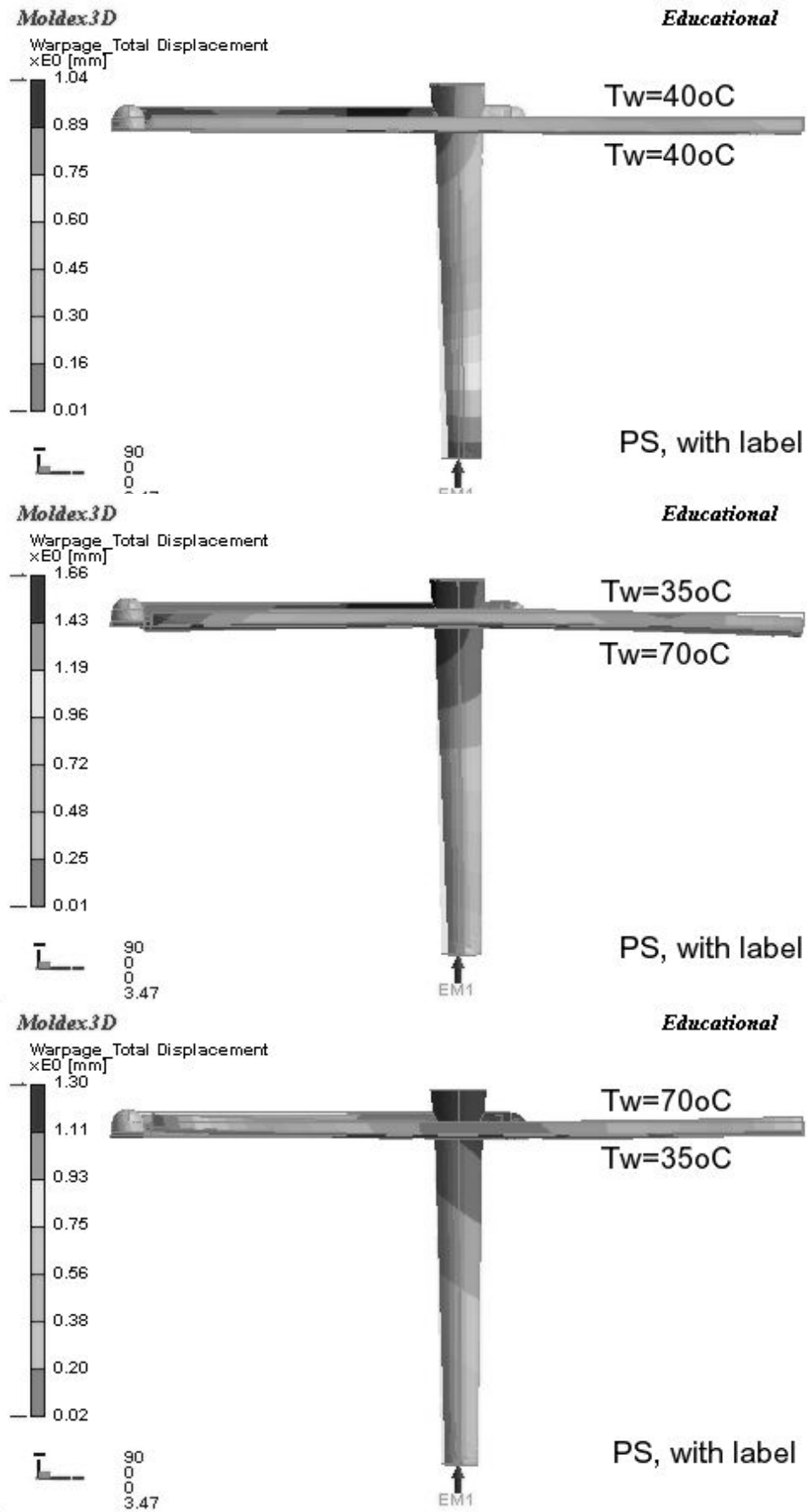
Figure 6.20: Part warpage from 3D simulations

104

Differential shrinkage, frozen-in stresses, and residual thermal stresses contribute to warpage. The degree of warpage is also affected by the overall rigidity or inherent mechanical constraints due to the part geometry. Shrinkage/warpage modules in Moldex3D are extensions to filling, holding, and cooling analyses that predict the final shape of the part. They are in fact a strain analysis, where the stresses have been determined during the previous analyses. In addition to the simulation on the total warpage displacement, it is also possible to predict the degree and direction of part warpage developed by some different effects separately such as by the thermal effect, in-mold constraint effect and moldbase thermal effect (Fig. 6.21). This prevents the mold engineer and part designer to evaluate the warpage tendency of the part to be molded prior to the actual mold making and molding. By comparing the amount of the displacement resulted from an individual effect, the most crucial effect will cause the most displacement. If, for example, the thermal effect accounts for the most displacement or warpage, the cooling layout of the whole mold should be redesign in order to avoid the undesirable and uncontrollable displacement. If, on the other hand, the moldbase thermal deformation is mainly responsible for the part warpage, the mechanical strength or the moldbase material selection should be concerned.

a)

b)
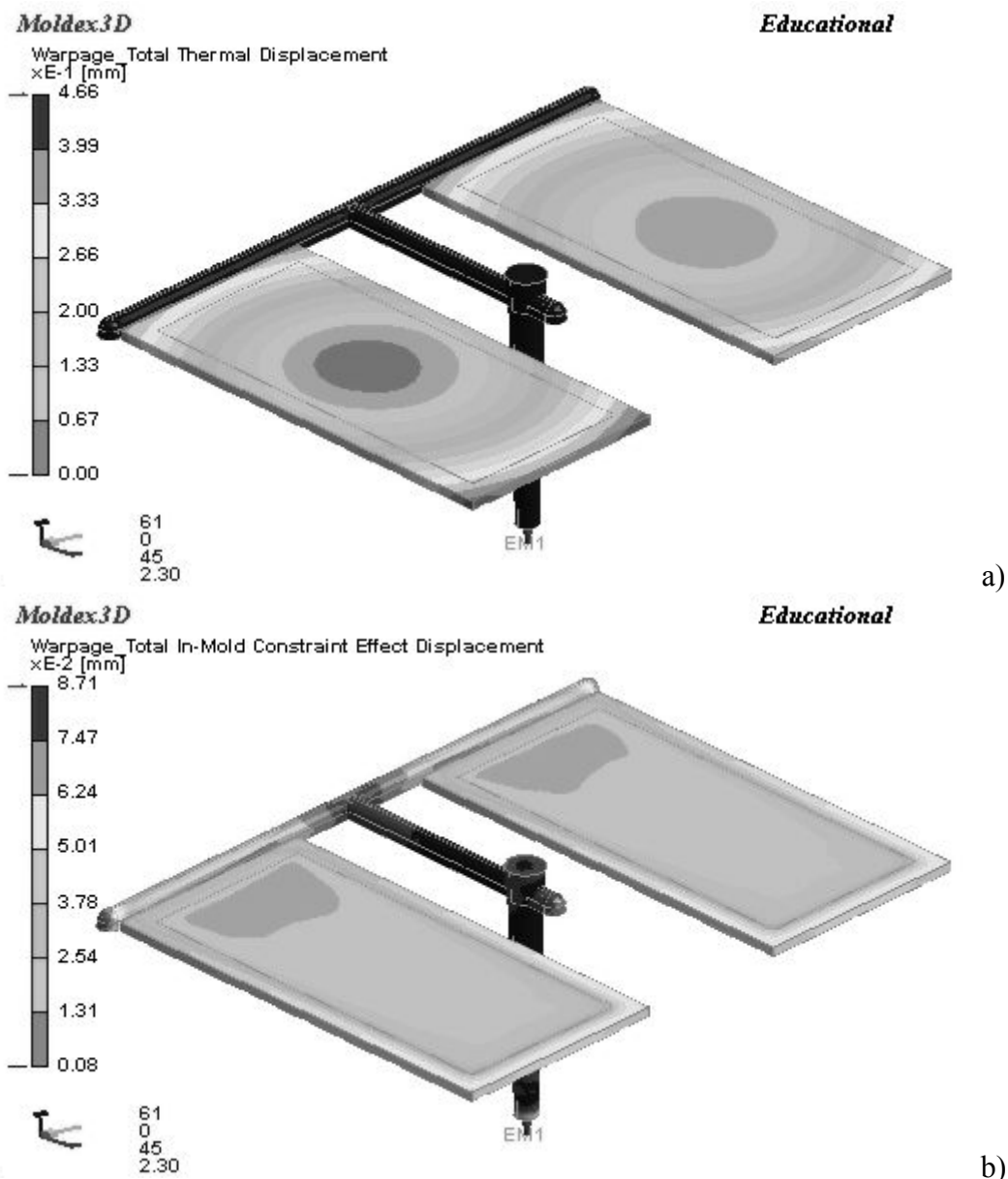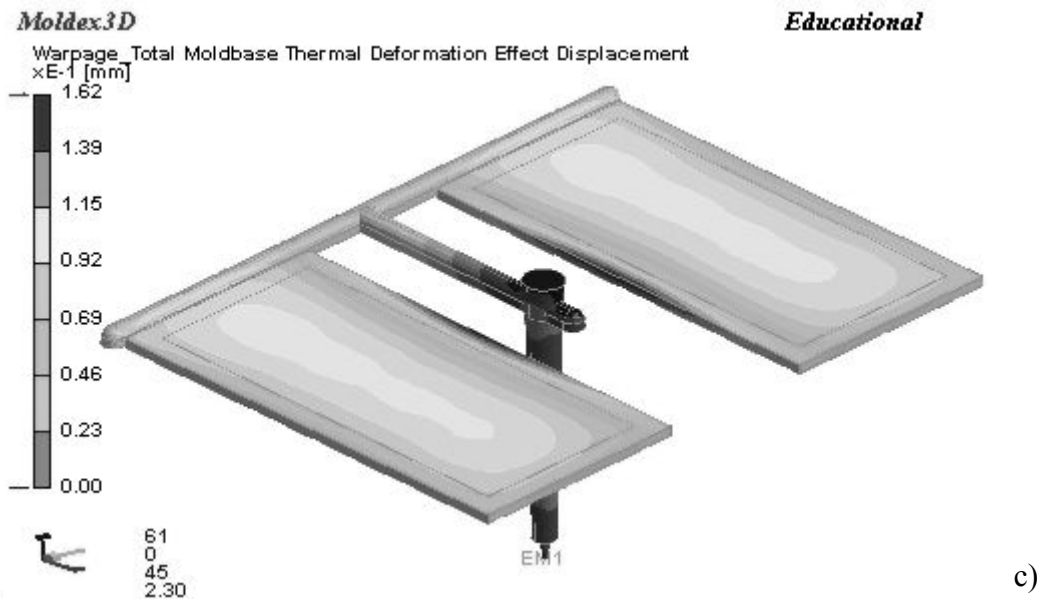
Figure 6.21: Warpage as a result of different molding effects [a): total thermal displacement, b): total in-mold constraint effect displacement, c): total moldbase thermal deformation effect displacement]
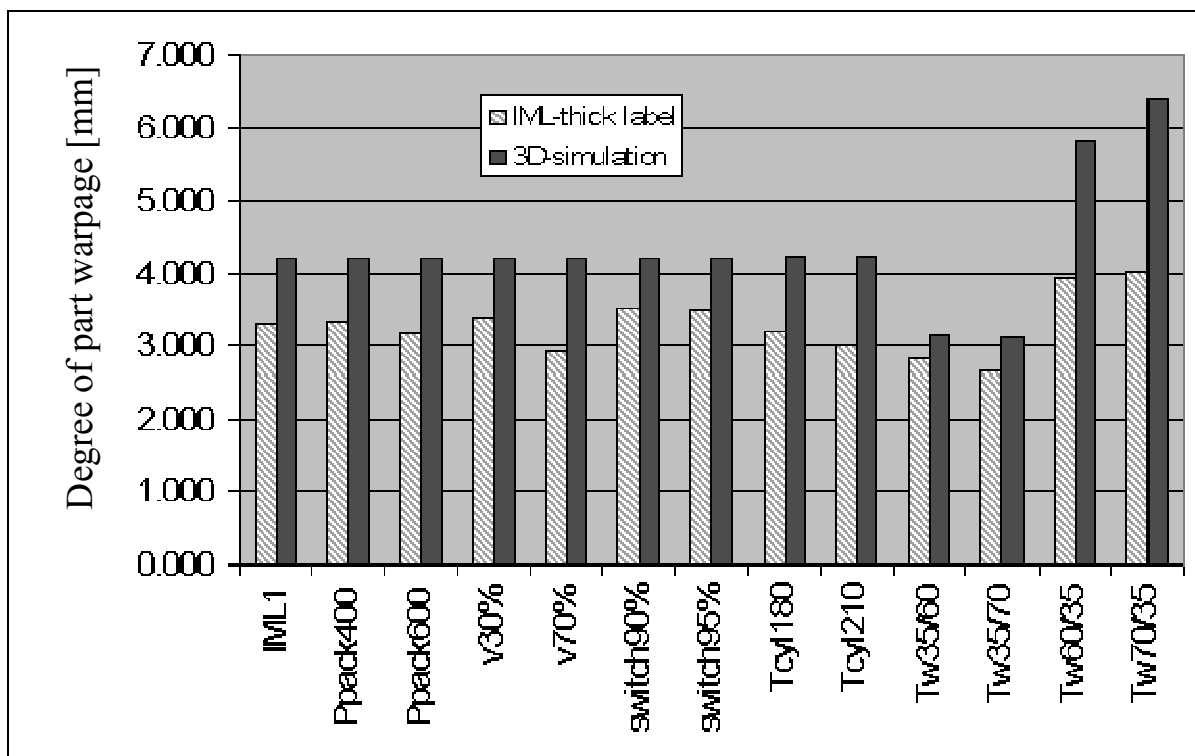
Figure 6.22: Comparison of the warpage between experiment and 3D simulation

As can be seen from Figures 6.19 and 6.22, 3D simulation program can predict the direction and the degree of warpage of the IML parts tendentiously correctly. However the results agree, in some cases, only qualitatively with those of the real molding process and should be taken into account considerably.

6.6 Modulus of Elasticity

The most important mechanical property of a polymeric material is its stress-strain curve. This curve is obtained by stretching a sample in a tensile testing machine and measuring the sample's extension and the load required to reach this extension. Since polymeric materials show viscoelastic behavior (a combination of elastic and viscous behavior) that is highly sensitive to temperature and, in some materials, relative humidity variations, it is important to use samples of standard shapes, preconditioned at a constant and standard temperature and relative humidity before testing. Also, they must be stretched at a constant speed if the results are to be comparable to other tests. The stress-strain curve provides information about the modulus of elasticity (Young's modulus), which is related to the material's stiffness or rigidity. This curve also provides information about the yield point, tensile strength, and elongation at break. The curve defines toughness (the area under the curve), which is the energy per unit volume required to cause the sample to fail. Thus, the stress-strain curve reveals much about a material's mechanical behavior. The information obtained includes the material's elastic property, yield strength, and toughness based on the stress-strain data. Modulus of elasticity is actually the slope of the curve within the elastic area of the specimen. The greater the modulus of elasticity, the stiffer the material or the smaller the elastic strain will be. The modulus of elasticity, E, is the ratio of normal stress to corresponding strain (straight line) for stresses below the proportional limit of the material (Hooke's law); it is the ratio of stress to strain in a test specimen (tensile, compression, etc.) that is elastically deformed.

For the execution of the tensile testing with polymers, the DIN EN ISO 527 represents the preferential standard, which covers the examination of molding materials, films and boards as well as glass-reinforced polymeric materials. A substantial experimental basic condition for the execution of this test is the use of suitable test sample. In this study, test specimens of type 1BA which is a proportional reduction of the type 1B on a scale of 1:2 are employed.

Figure 6.23 illustrates the modulus of elasticity of the part molded without label compared with the IML part molded with thick and thin label, respectively. From this figure, it can be seen that labels have strengthened the molded part to some different extent dependent on type of the label used and the molding parameter. Furthermore, IML parts molded with thin label mostly shows higher modulus than the parts molded with thick label. The modulus of elasticity of the IML part is mainly affected by the structure of the labels rather than by their thickness. This resulted particularly from the stretching of the label film, by which the strength of the film increases. As already mentioned in Section 5.2.2, the thick label is a porous type, which comprises the substrates of polyolefin polymers and silica. And this structure imparts the better adhesion between the label and the substrate. The thin label, on the other hand, composed of many layers of polyolefin polymers (Fig. 6.11), which are biaxially stretched. Despite higher thickness of the thick label compared to thin label and although the thick label film also underwent the stretching to some degrees, highly oriented structure of the thin label as can be seen in the Figure 6.11 dominates and this is responsible for the elevated modulus of elasticity of these IML parts.

The melt temperature also affects the modulus of elasticity of the molded part. Usually, with the relatively high melt temperature, the polymer macromolecules may be shortened or damaged, and hence the strength decreases. In this study, however, the melt temperature was set at the range between 180 $^{\circ}$C and 210 $^{\circ}$C during molding which is not excessively high, so

that only the slight reduction in the modulus of all the molded parts is ascertained at the higher settings.
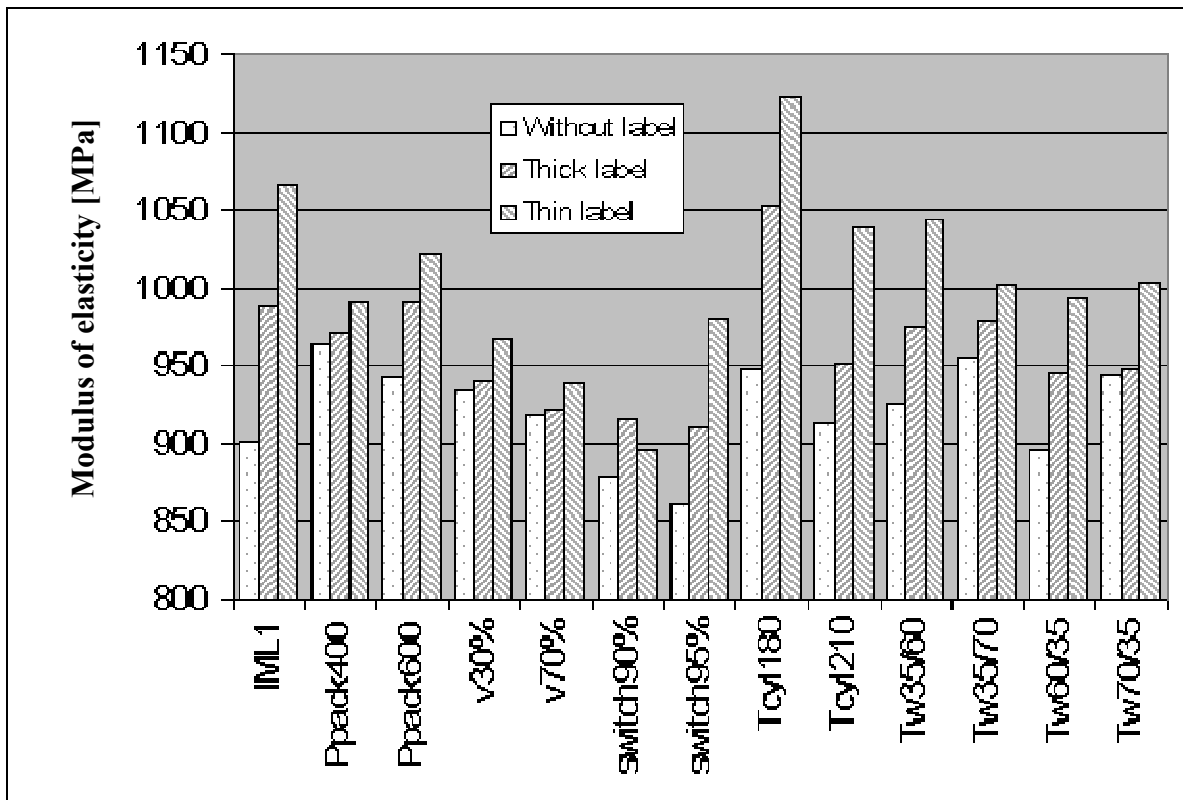

Figure 6.23: Modulus of elasticity of molded part without label compared with injected IML parts molded with thick and thin label

Holding pressure affects the modulus of the molded part in different manners. For parts molded without label, the optimal holding pressure is 400 bars. For parts molded with thick label, holding pressure can be set higher in order to acquire high modulus of elasticity. While holding pressure of 500 bars gives the highest modulus of elasticity to the IML parts with thin label. Normally parts that have exposed the exceeding holding pressure during molding are more at risk of having high internal stress, which contributes to the reduction of strength and modulus.

Injection velocity of 50 % has been proved to be the most optimal for all the IML parts but not for the part molded without label, whereas holding switch at 98 % of filled volume is the best condition for all the molded part.

From Figure 6.23, it can be seen that the mold temperature combination settings affect the modulus of elasticity in an interesting way. The modulus of elasticity of the IML part with thick label has declined with the mold temperature combination settings. In the same way, modulus of elasticity of IML part molded with thin label decreases when the mold temperature in one mold half differentiates from the other. However, this reduction occurs merely to a small extent so that it can be concluded that to rectify the warpage of the IML part by varying the mold temperature in the two mold halves differently, the modulus of elasticity of the part is only influenced in an unharmed way, compared to the modulus of elasticity of the part molded without label using the IML1 molding parameters.

108
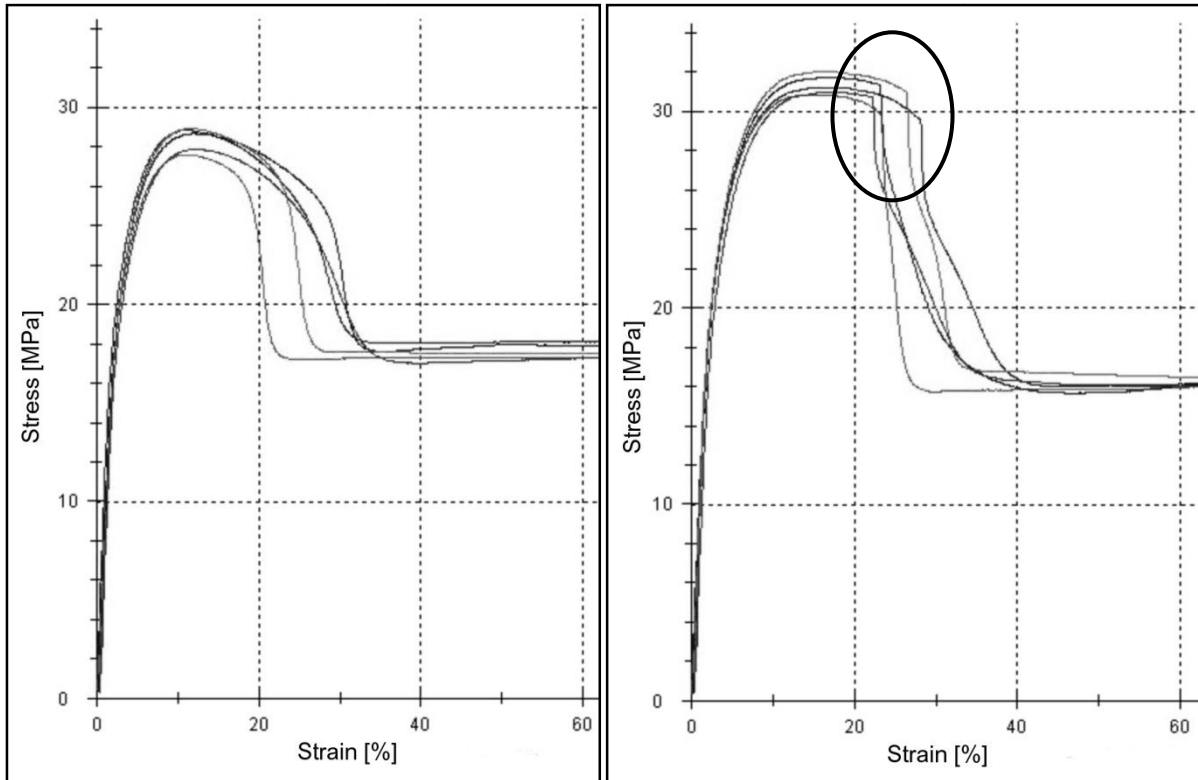
Figure 6.24: Stress-strain graph of IML part (left: with thick label; right: with thin label)

An interesting phenomenon was detected during the execution of the tensile testing of the molded part with thin label. As can be seen from Figure 6.24, stress-strain curves of molded parts with thin labels show a buckling on each curve which is defined with an oval. Whereas the stress-strain diagram of the molded part with thick label manifests only the smooth curves. During the tensile testing of the IML part with thin label, a rupture of the label occurred after the part had undergone the ultimate stress and then the necking followed. This leads to the sudden fall of the employed stress. Some part of the thin label was also detached from the substrate thereafter. IML part with thick label, to the contrary, has overcome the tensile testing without a break and disengaging of the label from the substrate. Due to the porous substrate of the thick label, a better adhesion between the thick label and the substrate of the IML part is promoted. This is already proved to be true by the tensile testing and also by Figure 6.11. It can be said that the thin label is somewhat brittle, due to stretching and orientation procedure compared to the thick label which is more elastic.

The curves in Figure 6.24 show necking and an extensive period of cold drawing, which are characteristic features of the stress-strain behavior of a semi-crystalline polymer above its glass transition temperature (T_g). In this case testing was carried out at the temperature above the glass transition temperature of polypropylene. At the yield point there is a local decrease in cross-sectional area at a point along the length of the specimen. Necking involves a balance between work hardening and softening. As the stress-strain curve shows, the stress falls after yield, before setting at a relatively constant value as the neck extends along the specimen.
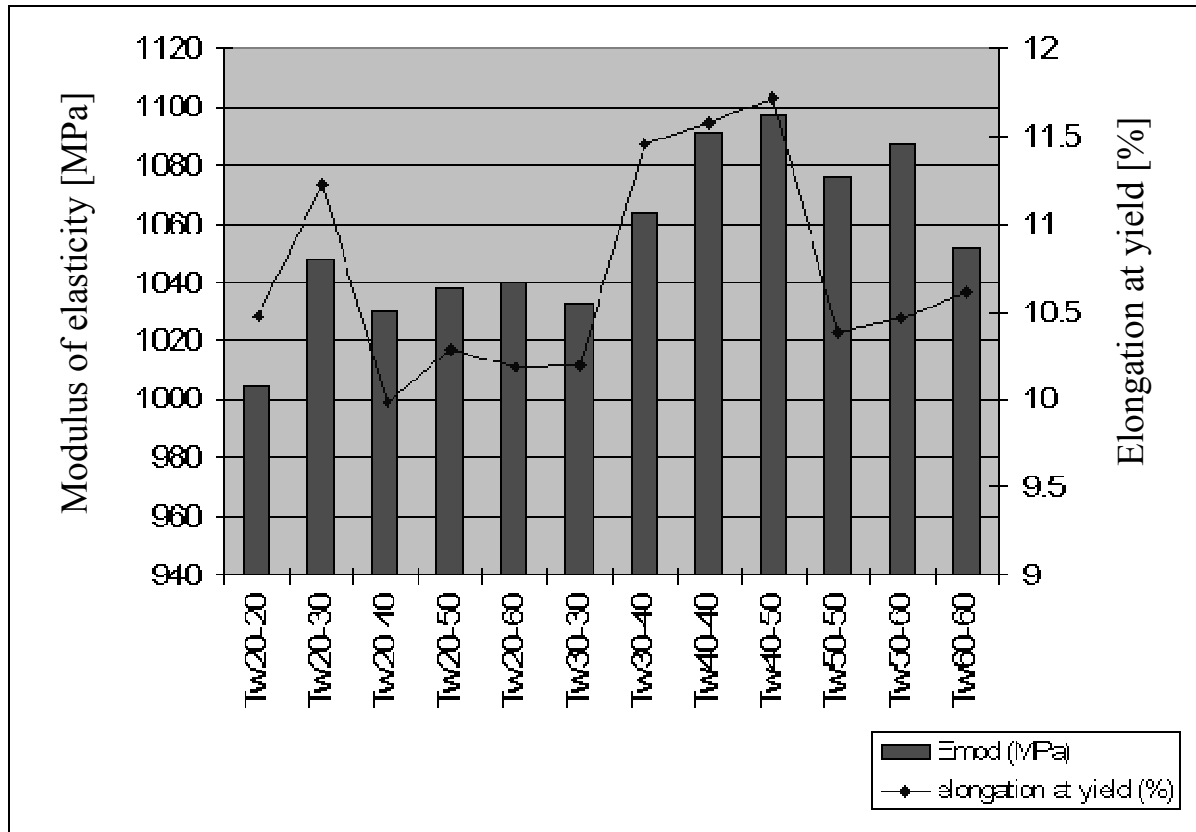
Figure 6.25: Effect of the mold temperature combination settings on the two mold halves on the modulus of elasticity of parts molded with PP Novolen 3200 MC

Figure 6.25 shows the effect of the mold temperature combinations on the modulus of elasticity of the polypropylene part molded without label. This set of experiments was carried out in order to study the effect of the mold temperature combination settings on the modulus of elasticity as well as the elongation at yield of the molded part. The experiments were performed with polypropylene as the injected material and without label as an insert. The mold temperature settings are starting at 20 °C up to 60 °C without taking the side mold halves into consideration, since no label involves in the molding. The temperature difference is defined by 10 degree intervals.

The experimental results display that not the difference between the mold temperatures does greatly affect on the modulus of elasticity or elongation at yield of the molded parts. The optimal mold temperature range, to the contrary, influences much on the modulus of the part. For the molding of polypropylene, the mold temperature range from 25 °C to 50 °C is suggested. Anyway, all the molded parts possess the satisfactory level of modulus of elasticity.

7   Summary

Within this thesis, 2.5D injection molding simulation based on the generalized Hele-Shaw model and 3D simulation were introductory performed with a double-plated part with non-uniform thickness in order to evaluate the efficiency and accuracy of the simulation program Moldex3D. The 2.5D simulations were carried out based on two different surface mesh types and by varying the number of mesh layers that can be freely defined during the simulation parameter setting. The 3D simulations, in the same way, were conducted with three different volume mesh types and by varying the number of element layer counts over the part thickness.

The results gained from 2.5D and 3D simulations have shown that the number of mesh layer over the part thickness has little to no effect on the accuracy of the simulation results in terms of predicting the melt front advancement in the cavity. On the other hand, noticeable deviation in the temperature distribution between the mesh types and the number of mesh layers can be acquired. In case of 3D simulation, tetrahedral meshing compared to prism and voxel meshing is proved to be the worst meshing method concerning the melt front advancement prediction and calculation time. Unexpectedly, 3D non-isothermal based simulation results deviated much from the actual molding situation, while 2.5D simulation can better predict the filling pattern of this part. This results mainly from the numerical instability of the 3D filling simulation of Moldex3D when a highly complex molding situation is involved. In addition, the computed pressure levels in the two cavities were irregularly predicted. The pressure-S2 curve lies over the pressure-S1 one which is clearly incorrect compared to the real pressure profiles. This is mainly responsible for an error in predicting the melt front advancement of the double-plated part with non-uniform part thickness by 3D simulation.

For 2.5D mold filling simulation, higher number of the mesh count over the part thickness dedicates mainly to the computation of the temperature distribution within the molded part rather than to the prediction of the melt front advancement. The advantage of the higher regularity of the voxel derivative mesh over the tetrahedral derivative mesh cannot be observed.

If, instead of 3D simulation based on non-isothermal computation, 3D simulation based on isothermal computation was performed, obvious improvement in predicting the melt front advancement and the proximity of the results to the actual process were provided. This is also due to the instability of non-isothermal numerical computation.

When molding the plates with non-uniform thickness separately, no decisive accuracy deviation in predicting the melt front progression between 3D and 2.5D simulation was manifested because the complexity of the flow and unbalancing of pressure between the two cavities as a system are eliminated.

Despite slightly underestimated, course of the melt temperature during filling and holding phase from 2.5D simulation lies relatively close to that of the real molding process (experiment). To the contrary, course of the melt temperature derived from 3D simulation was not really meaningful since the sensor nodes used in the simulation are not comparable with the real IR-temperature sensor and thus course of the temperature cannot be reasonably reported based on these sensor nodes used in 3D simulation. Generally, a comparison between the measured and the computed melt temperature must be made with caution

because the depth of penetration of the IR-temperature sensor is unknown and this can be problematic when the melt temperature in a relatively thick cavity should be measured.

Contrary to the complex double-plated part with non-uniform part thickness, with the IML part that is relatively simple in the form, Moldex3D can predict the flow pattern, course of the pressure and temperature trouble-freely and correctly. In addition, an asymmetrical temperature gradient over the part thickness can be distinctly detected. This phenomenon is expected to occur particularly in the back injection of a film, because the film acts as a thermal insulator. In filling phase the temperature distribution was almost symmetrical over the part thickness, whereas in holding and cooling phase unbalances in the temperature distribution became evident. Different frozen layer thicknesses can also be computed by 3D simulation. This indicates that this 3D simulation program is able to consider asymmetries in the thermal boundary conditions qualitatively correctly when molding the IML part.

Structure of the IML part was also examined. Four different zones in the IML part can be distinguished under the light microscope. On the label side, porous label structure as well as fine and coarse crystalline structures can be seen whereas the coarse crystalline structure (spherulites) and the amorphous layer can be seen in the middle and the side without label of the IML part, respectively. The frozen layers can also be seen under the light microscope. They arise as a result of the quenching of the melt as it contacts the cold mold wall. On the label side this frozen layer is much thinner over the entire part length than on the opposite side since the crystallization of the melt on the label side can further develop contrary to the opposite side of the molded part.

IML parts usually warp toward the opposite side of the label. This is because of much smaller thickness and less stiffness of the label compared to the substrate as well as the higher expansion coefficient of the substrate. With the existence of a label as an insert, the warpage of a molded part is changed due to the decrease in the thickness of the substrate at the constant part thickness as well as the asymmetrical heat dissipation in the injection mold. The different temperature fields between the insert material and the substrate during mold cooling, together with the different thermal expansion coefficient as well as the different contraction potential play an important role to the occurrence of this part warpage. Higher contraction of the substrate especially near the transition to the label occurs during the rest cooling phase owing to higher temperature field during molding process. The effect of the volume contraction difference between label and substrate, however, far outweighs the effect of the asymmetrical temperature distribution because much higher temperature of the substrate leads to the higher volume contraction compared to the label.

Besides the label thickness, the degree of part warpage is influenced by the mold temperature. By setting the mold temperature on the label side higher than on the other, the degree of part warpage of the IML parts can be reduced, since the temperature field within the molded part became more homogeneous and hence the contraction differential between the label and the substrate became smaller.

Contrary to the PP substrate, little to no warpage of the IML part molded with amorphous PS as the substrate can be detected. This is because the volume contraction of PS is much smaller than that of PP, the effect of the contraction difference is thus negligible. Despite the asymmetrical temperature distribution over the PS part thickness, the stiffness of PS remains invincible so that the mold temperature combination settings show no effect on the warpage of the referred part. This supports the statement that the effect of the volume contraction

difference between label and substrate dominates the effect of the asymmetrical temperature distribution on part warpage.

3D simulation program can predict the direction and the degree of warpage of the IML parts tendentiously correctly. However the results agree, in some cases, only qualitatively with those of the real molding process. This should be taken into account.

Tensile testing has shown that IML parts have higher modulus of elasticity than parts molded without label. This is because label has strengthened the IML molded parts to some degree dependent on type of the labels used and the molding conditions. In addition, the modulus of elasticity of the IML part is mainly affected by the structure of the labels rather than by their thickness, since the IML parts molded with thin labels show higher modulus than the parts molded with thick labels. This results particularly from the stretching of the label film. The experimental results have also manifested that modulus of elasticity of the IML parts molded with thin and thick labels decreases when the mold temperature in one mold half differentiates from the other. However, this reduction occurs merely to a small extent so that it can be concluded that to reduce the warpage of the IML part by varying the mold temperature in the two mold halves differently, the modulus of elasticity of the part is only influenced in an unharmed way.

References

[1] C. A. Hieber, S. F. SHEN, *A Finite-element and finite-difference simulation of the injection molding filling process*, Journal of Non-Newt Fluid Mech, Volume 7, 1980

[2] J. H. ERIK, P. L. HANS, *A unified finite element model for the injection molding process*, Computational Methods Appl. Mech, 178, 1999

[3] E. Pichelin, T. COUPEZ, *Finite element solution of the 3D filling problem for viscous incompressible fluid*, Comput Methods Appl. Mech. 163, 1998

[4] K. Talwar, F. Costa, V. Rajupalem, L. Antanovski and C. Friedl, *Three dimensional simulation of plastic injection molding*, SPE ANTEC Proceedings, 1, 563- 566, 1998

[5] Z. Fan, B. Lin, F. Costa, X. Jin, R. Zheng, P. Kennedy, *Three-dimensional warpage simulation for injection molding*, SPE Annual Technical Conference, 2004

[6] P. Kennedy, *Flow Analysis of Injection Molds,* Hanser, New York, 1995

[7] Z. Fan, R. Zheng, P. Kennedy, H.Yu, A. Bakharev, *Warpage analysis of solid geometry*, SPE Annual Technical Conference, 2000

[8] P. Unger, E. Lindner, *Gastrow Injection Molds 130 Proven Designs*, 3rd Edition, Carl Hanser Verlag, 2002

[9] P. Unger, *Gastrow Injection Molds 130 Proven Designs*, 4th Edition, Carl Hanser Verlag, 2006

[10] H. Rees, *Understanding injection mold design*, Carl Hanser Verlag, 2001

[11] F. Beitl, 1000 Tips zum Spritzgießen Band 4: Anschnitt-Technologie- Grundlagen mit Praxisanleitungen, Hüthig Verlag Heidelberg, 2006

[12] www.scudc.scu.edu/cmdoc/dg_doc/develop/books/dg/index_sp.htm

[13] F. Beitl, Grundlagen zur Angusskanaltechnik mit Leistungsberechnung, Deutsches Industrieforum für Technologie, 2006

[14] R.G.E. Pye, *Injection Mould Design (for Thermoplastics)*, Ilitte Books Ltd., 1968

[15] *Kunststoff-Verarbeitung im Gespräch, 1*: Spritzgießen, BASF, Ludwigshafen, 1979

[16] C. A. Hieber and H. H. Chiang, Rheological Acta 28, 321-332, 1989

[17] Kegelanguß, Schirmanguß, Bandanguß. Technical Information, BASF, 1985

[18] F. Beitl, *1000 Tips zum Spritzgießen Band 3: Angusskanaltechnik- Grundlagen mit Praxisanleitungen*, Hüthig Verlag Heidelberg, 2006

[19] H.-D. Stank, *Anforderungen an den Anguß, seine Aufgaben, Anordnung am Spritzgußteil. Anguß- und Anschnittprobleme beim Spritzgießen*, Ingenieurwissen, VDI-Verlag, Düsseldorf, 1975

[20]   E. Schürmann, *Abschätzmethoden für die Auslegung von Spritzgießwerkzeugen. Dissertation*, Tech. University, Aachen, 1979

[21]   G. Menges, W. Michaeli, P. Mohren, *How to Make Injection Molds*, 3rd Edition, Carl Hanser Verlag, 2001

[22]   O. Kretzschmar, *Rechnerunterstiitzte Auslegung von Spritzgießwerkzeugen mit segmentbezogenen Berechnungsverfahren*. Dissertation, Tech. University, Aachen, 1985

[23]   Dominick. V. Rosato, Donald V. Rosato, M. G. Rosato, *Injection Molding Handbook*, 3rd Edition, Kluwer Academic Publishers, 2000

[24]   N. Rott, *Note on the History of the Reynolds Number*, Annual Review of Fluid Mechanics, Vol. 22, 1990

[25]   *Entformungseinrichtungen*. Technical Information, 4.4, BASF, Ludwigshafen/Rh., 1969

[26]   H. Bangert, *Systematische Konstruktion von Spritzgießwerkzeugen und Rechnereinsatz*, Dissertation, Techn. Univ., Aachen, 1981

[27]   H. Bangert, E. Doring, E, U. Lichius, W. Kemper, W, E. Schumann, *Bessere Wirtschaftlichkeit beim Spritzgießen durch optimale Werkzeugauslegung*, Paper block VII at the 10th Tech. Conference on Plastics, IKV, Aachen, March 12-14, 1980

[28]   S. E. Giragosian, *Continous mold venting*. Mod. Plast, 44 (1966), 11

[29]   W. Hartmann, *Entlüften des Formhohlraums*, Paper at the VDI Conference, Nürnberg, December 6-7, 1978

[30]   A. Rogalla, *Analyse des Spritzgießens mikrostrukturierter Bauteile aus Thermoplasten*, Dissertation, RWTH, Aachen, 1997

[31]   U. Meiertoberens, C. Herschbach, R. Maaß, *Verbesserte Technologien für die Elastomerverarbeitung*, Gummi, Fasern, Kunststoffe, 47 (1994), 10, pp. 642-649

[32]   K. Notz, *Entlüftung von Spritzgießwerkzeugen*, Plastverarbeiter, 45 (1994), 11

[33]   N. S. Rao, G. Schumacher, *Design formulas for plastics engineers*, 2nd Edition, Carl Hanser Verlag, 2004

[34]   N. S. Rao, K. O'Brien, Design data for plastics engineers, Carl Hanser Verlag, 1998

[35]   A. R. Calhoun, J. Golmanavich, Fundamental skills and polymer science, Society of plastics engineers, 2004

[36]   W. B. Hoven-Nievelstein, *Die Verarbeitungsschwindung thermoplastischer Formmassen*, Dissertation, Tech. University, Aachen, 1984

[37]   German Standard: DIN 16901: *Kunststoff-Formteile Toleranzen und Abnahmebedingungen für Längenmaße*

[38]   M. G. Potsch, *Prozessimulation zur Abschätzung von Schwindung und Verzug thermoplastischer Spritzgussteile*, Dissertation, RWTM, Aachen, 1991

[39]   P. Gelardi, *In Mold Decorating and In Mold Labeling & The Future*, Plastics Technology Magazine's Paint-Free Color Conference 2004

[40]   Top 50 Innovations: *In-Mold Decorating & Labeling*, Plastics Technology's Online Article, www. Ptonline.com

[41]   D. Cook, *Advances in IML for Thin Wall Packaging*, 13th International In-Mold Labeling Conference, 2005

[42]   B. König, *Verfahren zum Herstellen von mit bedruckten Etiketten versehenen Formkörpern nach dem so genannten In-Mould-Labelling (IML)-Verfahren sowie Etikett für ein In-Mould-Labelling (IML)- Verfahren*, Deutsches Patentamt, Patentschrift DE 196 19 462 C1, 1997

[43]   N. N., Exxon Mobil Chemical Films Europe

[44]   D. Sinigaglia, *IML Labels and the Environment*, 13th International In-Mold Labeling Conference, 2005

[45]   S. E. Shelton, *Feature Article In-Mold Labeling: Electrostatics Are the Way to Go*, Plastics Technology's Online Article, www. Ptonline.com

[46]   Simco electrostatic control

[47]   S. E. Shelton, *Use of Electrostatics for In-mold label applications*

[48]   W. Cao, C. Shen, *Two Solutions for Three-Dimensional Flow Simulation of Injection Molding*, Antec 2005

[49]   Moldex CAE software handbook

[50]   R. B. Bird, R.C. Armstrong, and O. Hassager, *Dynamics of Polymeric Liquids*, Vol. 1, John Wily & Sons, 1987

[51]   J.D. Ferry, *Viscoelastic Properties of Polymers*, John Wily & Sons, 1980

[52]   W. Michaeli, *Extrusion Dies for Plastics and Rubbers*, Oxford University Press, 1992

[53]   P. Zoller. A study of the pressure-volume-temperature relationships of four related amorphous polymers: Polycarbonate, polyarylate, phenoxy, and polysulfone. *Journal of Polymer Science*, 20:1453–1464, 1982

[54]   R.S. Spencer and G.D. Gilmore. Equation of state for polystyrene. *Journal of Applied Physics*, 20:502–506, 1949.

[55]   R.Y. Chang, C.H. Chen, and K.S. Su. Modifying the tait equation with cooling rate effects to predict the pressure-volume-temperature bahaviors of amorphous polymers: Modelling and experiments. *Polymer Engineering and Science*, 36(13):1789–1795, 1996.

[56] P. Zoller. Pressure-volume-temperature relationship of solid and molton polypropylene and poly(butene-1). *Journal of Applied Polymer Science*, 23:1057–1061, 1979.

[57] W. F. Ames, *Numerical Method for Partial Differential Equations*, Section 1.6. Academic Press, New York, 1977

[58] F. B. Hildebrand, *Finite-Difference Equations and Simulations*, Section 2.2. Prentice-Hall, Englewood Cliffs, New Jersey, 1968

[59] G. Boole, *A Treatise On The Calculus of Finite Differences*, 2nd Ed., Macmillan and Company, 1872

[60] H. Freeman, *Finite Differences for Actuarial Students*, 1967

[61] www.feadomain.com

[62] www.solid.ikp.liu.se

[63] www.math.nist.gov

[64] R. W. Clough, W. L. Edward L, *Early Finite Element Research at Berkeley*, Retrieved on 2007-10-25

[65] W. C. Gibson, *The Method of Moments in Electromagnetics*. Chapman & Hall, 2008

[66] P. K. Banerjee, *The Boundary Element Methods in Engineering*, McGraw-Hill College, 1994

[67] L. C. Wrobel, M. H. Aliabadi, *The Boundary Element Method*. Wiley, 2002

[68] www.boundary-element-method.com

[69] www.conceptanalyst.com

[70] www.imtek.uni-freiburg.de/simulation

[71] www.iam.uni-stuttgart.de/bem/home_bem_introduc.html

[72] www.fos-messtechnik.de

[73] F. Obendrauf, G. Langecker, W. Friesenbichler, Int. Polym. Proc. 13:1 71-77, 1998

[74] C. Maier, Polym. Eng. Sci. 36:11 1502-1512, 1996

[75] A. L. Kelly, E. C. Brown and P. D. Coates, *Infrared Melt Temperature Measurement: Effect of Filler Content on Penetration Depth*, IRC in Polymer Science & Technology, School of Engineering, Design and Technology, University of Bradford, Bradford, BD7 1DP, UK

[76] D. O. Kazmer, P. Knepper, S. Johnston, *A review of in-mold pressure and temperature instrumentation*, University of Massachusetts Lowell

[77]   K. Kobayashi, H. Shimizu and M. Kaiho, *Numerical simulation of unsteady turbulent flow by voxel method*, JSME International journal Series B, Volume 47 No.3, 2004

[78]   J. Zachert, *Analyse und Simulation Dreidimensionaler Strömungsvorgänge beim Spritzgießen*, Rheinisch-Westfälische Technische Hochschule Aachen, Dissertation 1998

[79]   F. Johannaber, *Injection Molding Machines*, Hanser Publishers, Munich, 1994

[80]   T. Wiegmann, F. Oehmke, *Dichte, Wärmeleitfähigkeit und Wärmekapazität automatisiert Messen*, Kunststoffe 80 (1990) 11, p. 1255-1258

[81]   K. Janeschitz-Kriegl, *Polymer solidification by crystallisation under heat transfer and flow conditions*, Process in Colloid & Polymer Science 87: 117-127, 1993

[82]   S. Vleeshouwers, H. Meijer, *A rheological study of shear induced crystallization*, Rheological Acta 35, 1996

[83]   S. Hoffmann, *Berechnungen von Kristallisationsvorgängen in Kunststoffformteilen*, PhD study at Aachen University, 2002

[84]   W. Michaeli, M. Bussmann, *Shear-Induced Morphology Prediction in Injection Molded Semi-Crystalline Thermoplastics*, ANTEC 2005

[85]   H. G. Pötsch, *Prozeßsimulation zur Abschätzung von Schwindung und Verzug thermoplastischer Spritzgussteile.* Rheinisch-Westfälische Technische Hochschule Aachen, Dissertation, 1991

[86]   S. Galuschka, *Hinterspritztechnik-Herstellung von textil-kaschierten Spritzgießteilen*, Rheinisch-Westfälische Technische Hochschule Aachen, Dissertation, 1994

[87]   O. Zöllner, *Optimised Mould Temperature Control*, Bayer

[88]   W. Knappe, *Die Festigkeit thermoplastischer Kunststoffe in Abhängigkeit von den Verarbeitungsbedingungen*, Kunststoffe Bd. 51, 1961

[89]   S. Stitz, *Analyse der Formteilbildung beim Spritzgießen von Plastomeren als Grundlage für die Prozeßsteuerung*, Rheinisch-Westfälische Technische Hochschule Aachen, Dissertation, 1973

[90]   M. Wielpütz, *Analyse der Hinterspritztechnik kompakter Dekormaterialien*, Rheinisch-Westfälische Technische Hochschule Aachen, Dissertation, 2003

[91]   P. Larpsuriyakul, *Injection –IML and its effects on the injected part properties*, Proceeding 20th Stuttgarter Kunststoff-kolloquium, 2007

Appendix 1   Standard Components of an Injection Mold

Pos.*	Designation	standard
1	Clamping plate	-
2	Cavity plate	-
3	Backing plate	-
4	Riser	-
5	Ejector retainer plate	-
6	Ejector base plate	-
7	Locating guide pillar	ISO 8017
8	Locating guide bush	ISO 8018
9	Centering sleeve	ISO9449
10	Guide pillar, angle pin	ISO/CD 8404
11	Ejector pin, cylindrical head	ISO 6751
12	Ejector sleeve	ISO 8405
13	Shouldered ejector pin, cylindrical head	ISO 8694
14	Ejector pin, conical head	-
15	Sprue bushing	ISO 10072
16	Sprue puller insert	ISO/CD 16915
17	Socket head cap screw	ISO 4762
18	Dowel pin	ISO 8734
19	Locating unit, round	ISO 8406
20	Locating ring	ISO 10907-1
21	Coupling	-
22	Connecting nipple	-
23	Hose clip	-
24	Lifting eye bolt	-
25	Support pillar	ISO 10073
26	Thermal insulating sheet	ISO 15600
-	Plain plate	ISO 6753-2
-	Designation and symbols	ISO 12165
-	Specification sheets for injection molds	ISO 16916

Standard components as per ISO

Appendix 2   Description of the Simulation program Moldex3D®

Moldex3D gives a comprehensive CAE tool in injection molding with three major modules: Moldex3D/Solid, Moldex3D/Shell, and Moldex3D/Voxel modules, respectively. Basically, the difference between Moldex3D/Solid and Moldex3D/Shell is clear. Moldex3D/Shell applies the Hele-Shaw approximation approach to deal with the injection system. Moldex3D/Solid utilizes the true 3D geometrical model to catch the full phenomena in injection system. In addition, Moldex3D/Voxel module also applies the true 3D model to simulate injection system. The main difference is that, from the pre-processing point of view, Moldex3D/Voxel module only supports the voxel type of element but Moldex3D/Solid supports various types of element.

Moldex3D-Project: Moldex3D-Project is a project-managing interface in Moldex3D. By providing an environment with Pre-Processing, Analysis and Post-Processing integrated, it compiles all necessary data for the simulation of the injection molding, and enables users to launch all Moldex3D analyses. The flowchart is shown as below.
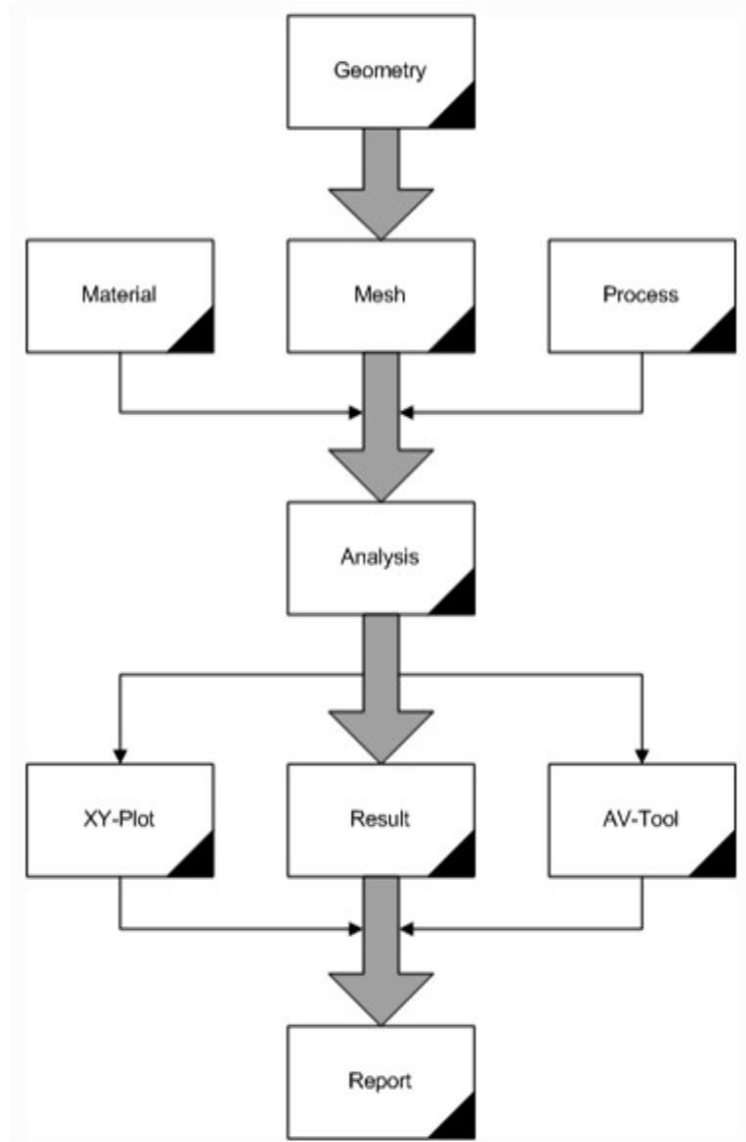
Flowchart for the Moldex3D software system

<u>Pre-processing:</u>

Generally, Pre-Processing takes three categories of data: geometrical model with good mesh quality, proper and feasible process conditions, and suitable material properties with corresponding thermal, mechanical and rheological properties. To help users in Pre-Processing, Moldex3D offers the following tools: Material Wizard, Process Wizard, MeshKit, and Mesh.
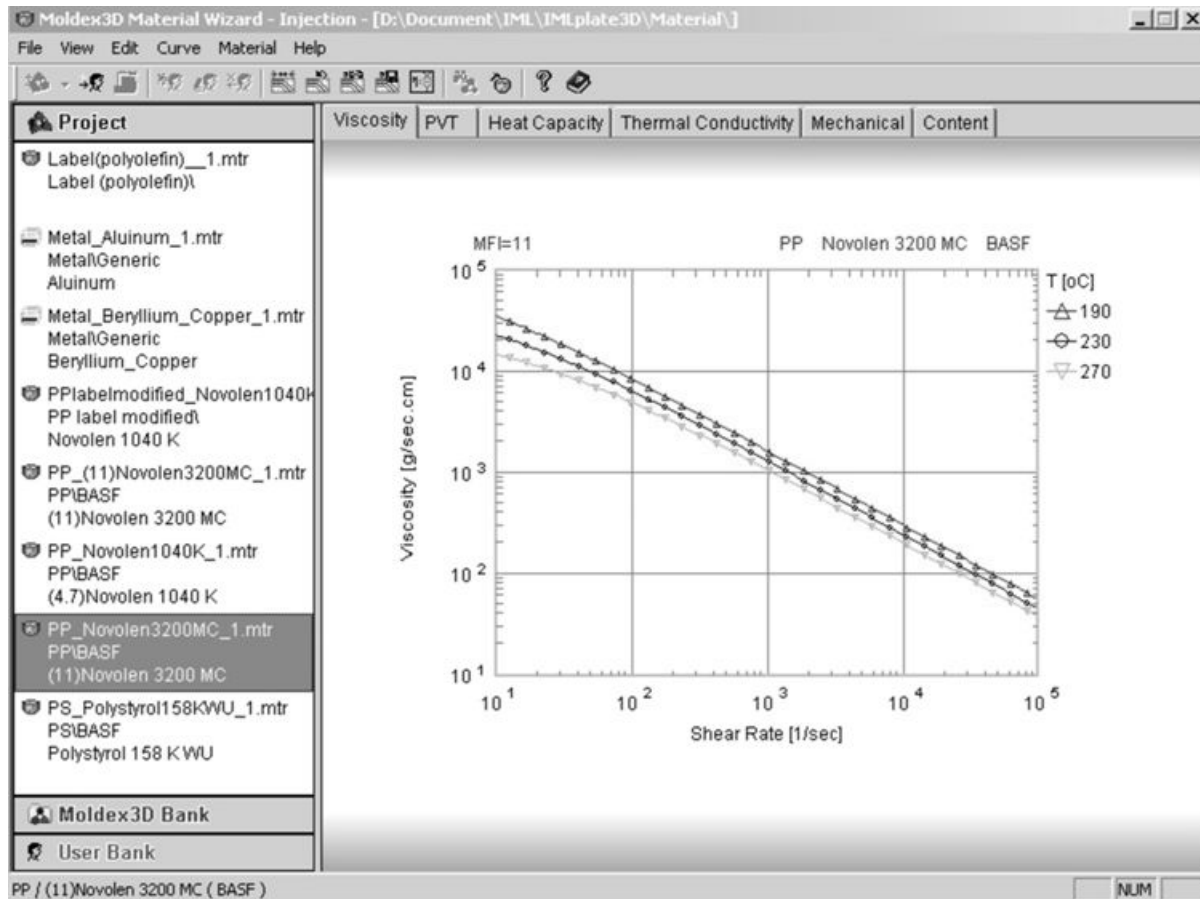
Material selection from Moldex3D databank

To get better simulation, the selection of suitable material is one of the most crucial issues. Polymer material behaviors are very complicated during a cycle of injection molding and differentiate much from those of low molecular weight materials. The situation is further exacerbated by the existing versatility of the different polymer materials available in the market. As a result, an accurate and comprehensive material database is necessary.
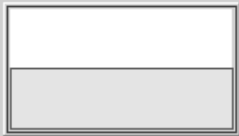
Moldex3D provides users a material database to tailor the analysis to fit numerous materials, by selecting the material from database and linking it to the run of the project for analysis. Besides, Moldex3D also enables users to add a new material into this material database by entering some basic information of material properties.
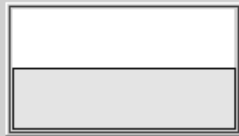
Process condition setting is one of the most important steps in obtaining reliable analysis results. Moldex3D supports two types of interfaces: CAE analysis interface and Machine interface. CAE analysis interface is easier to use but with a weaker link with the injection molding machine characteristics. Machine interface is, however, much more linked to the
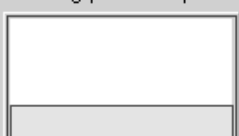
machine characteristics and also more complicated. It's recommended to use the CAE interface to start an analysis quickly. Use the Machine interface only when it's necessary to compare the analysis results with experiments.

Machine setting (CAE analysis interface)

Within computational parameter setting, users can choose between standard analysis, fast analysis, and customize for filling and holding simulation freely. In warpage tab under the solver parameters, user can set the convergence tolerance as well as the maximum number of iterations freely.

Analysis:

When the required data are fully prepared, the simulation can be executed by selecting the Analysis on the tab menu of the Moldex3D-Project Window to start the analysis. At this moment, the role of Moldex3D-Project is the communication bridge between the solver and user interface for analysis. While a number of analyses are waiting to run, the Batch option of Moldex3D-Project will allow users to define a number of analyses to run sequentially on the background. Essentially, analysis is a non-interactive process. It can be run on the background or as a window.

The analysis performed in the console mode

Post-processing:
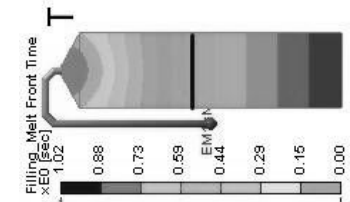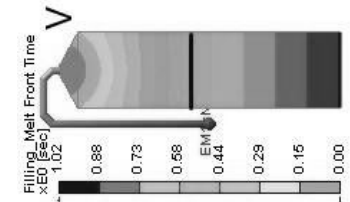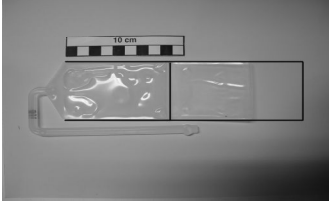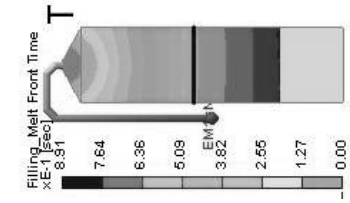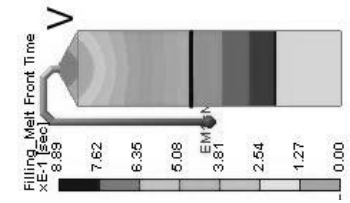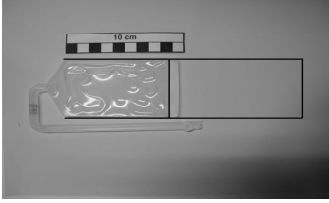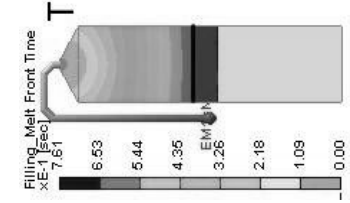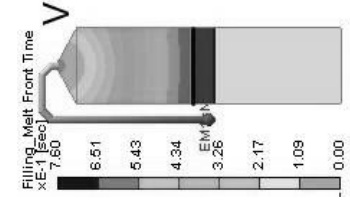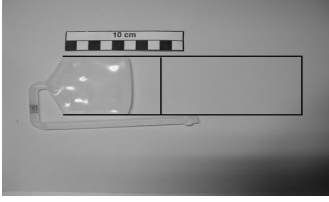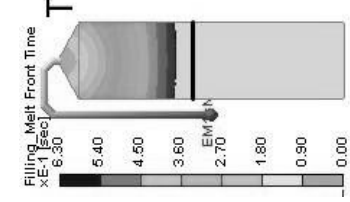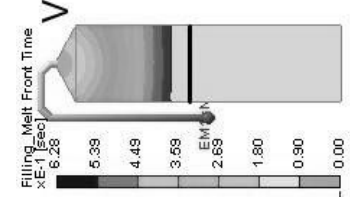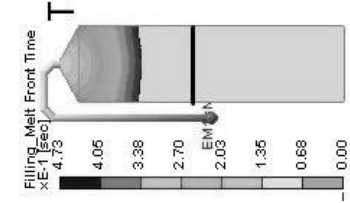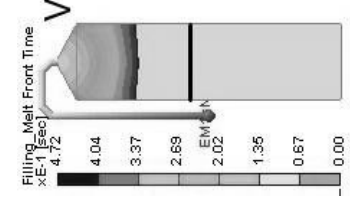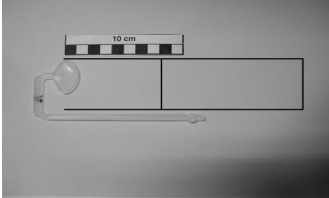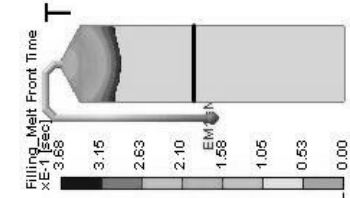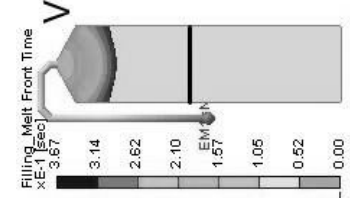
The Post-Processor are essentially the tools to examine the analyzed results in a graphical format. Moldex3D provides three different display types to demonstrate the analyzed results; field plot, x-y plot, animation.

With the field plot, the color illustrations of the simulation results such as melt front time, pressure, temperature, velocity, etc. will be shown.

By applying a sensor node onto the mesh model at the required position, the x-y plot between the simulation results and time for example course of the pressure or course of the temperature at that position can be created.
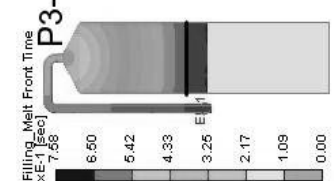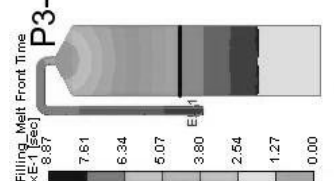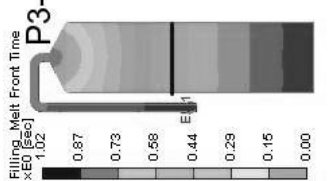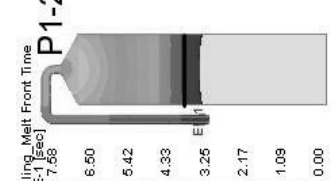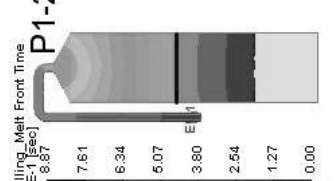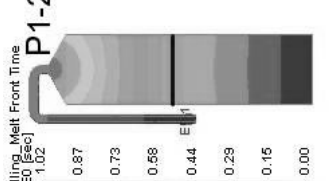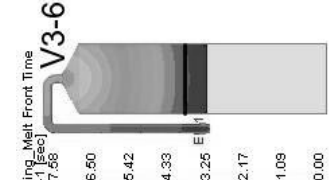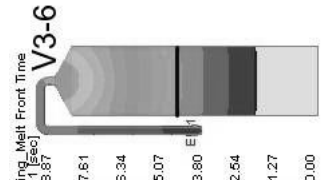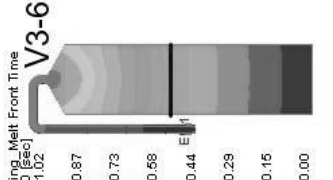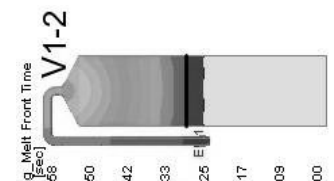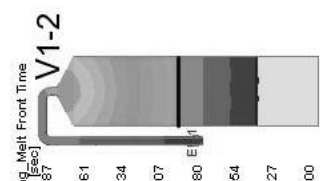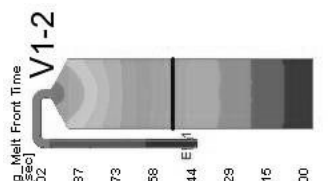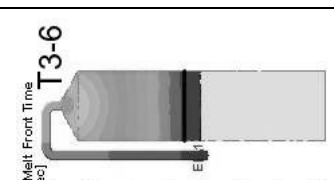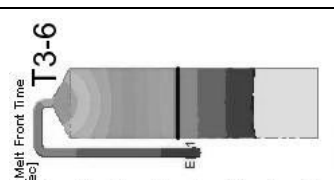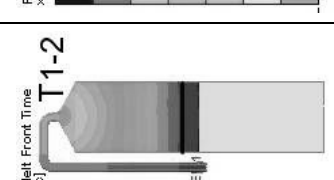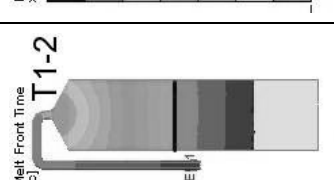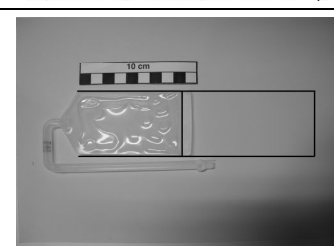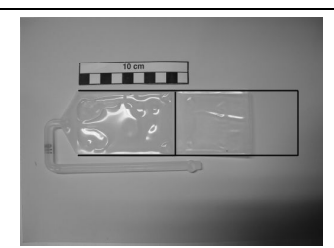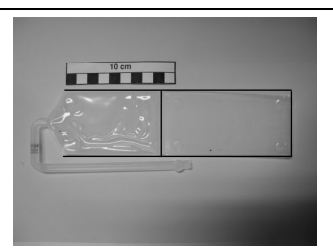
In addition to the field plot and the x-y plot, animation of some simulation results can be made.

Appendix 3 Comparison of the melt front progression of the right cavity between the experimental study and 2.5D simulations
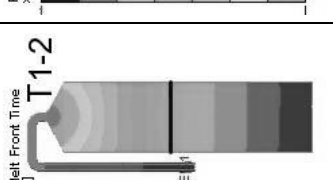
	Short-shot study	Tetrahedral derivative mesh	Voxel derivative mesh
100 % filled			
87 % filled			
74 % filled			
62 % filled			
46 % filled			
36 % filled			

Appendix 4   Comparison of the melt front progression of the right cavity between the experimental study and 3D simulations

	36 % filled	46 % filled	62 % filled
Prism mesh 3-6 layers			
Prism mesh 1-2 layers			
Voxel mesh 3-6 layers			
Voxel mesh 1-2 layers			
Tetrahedral mesh 3-6 layers			
Tetrahedral mesh 1-2 layers			
Short-shot study			

	74 % filled	87 % filled	100 % filled
Prism mesh 3-6 layers			
Prism mesh 1-2 layers			
Voxel mesh 3-6 layers			
Voxel mesh 1-2 layers			
Tetrahedral mesh 3-6 layers			
Tetrahedral mesh 1-2 layers			
Short-shot study			

Appendix 5 2.5D simulation results of the double-plated part with non- uniform part thickness based on the tetrahedral derivative mesh with 10, 20 and 30 layers defined

	10 layers	20 layers	30 layers
38 % filled			
49 % filled			
56 % filled			
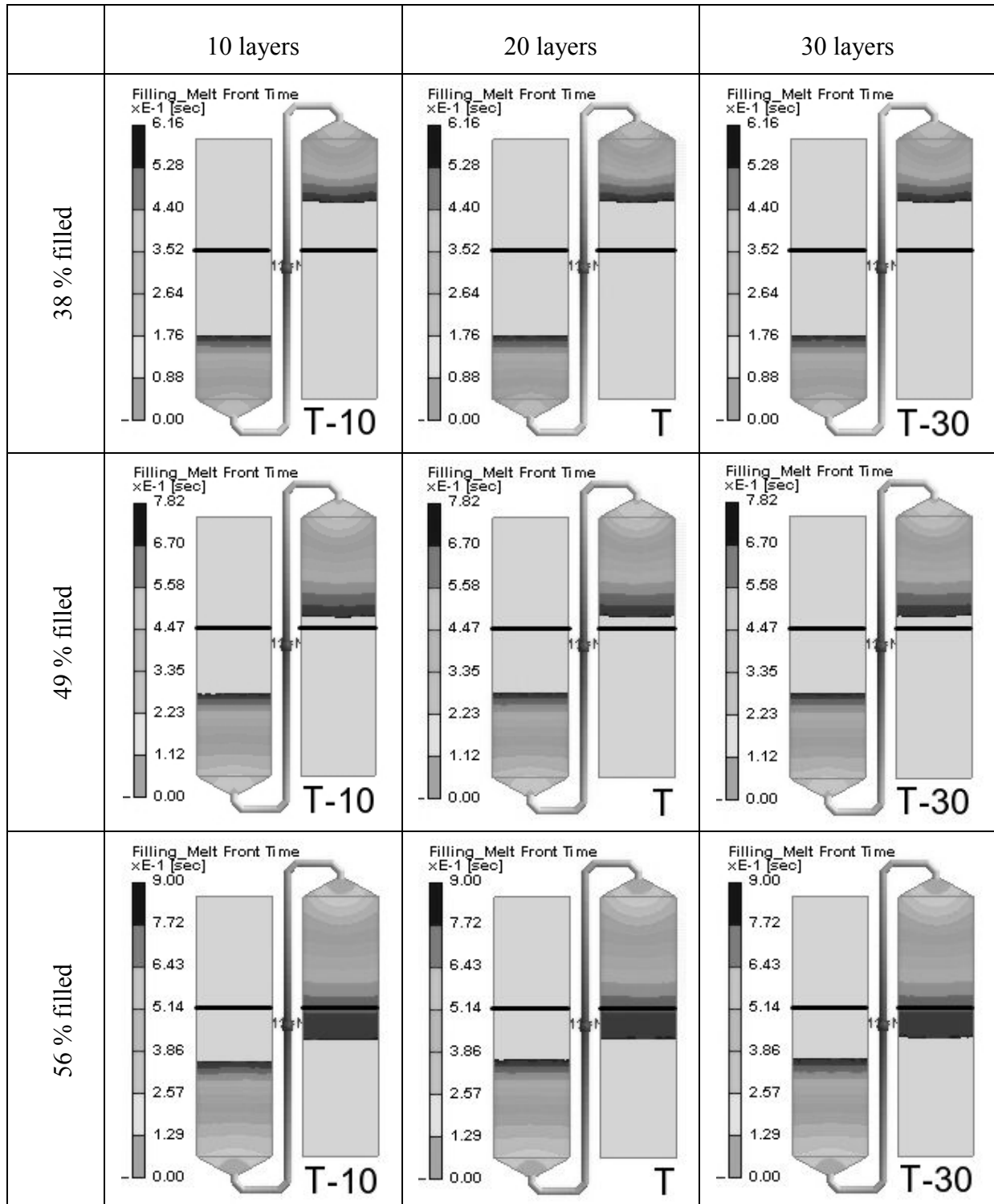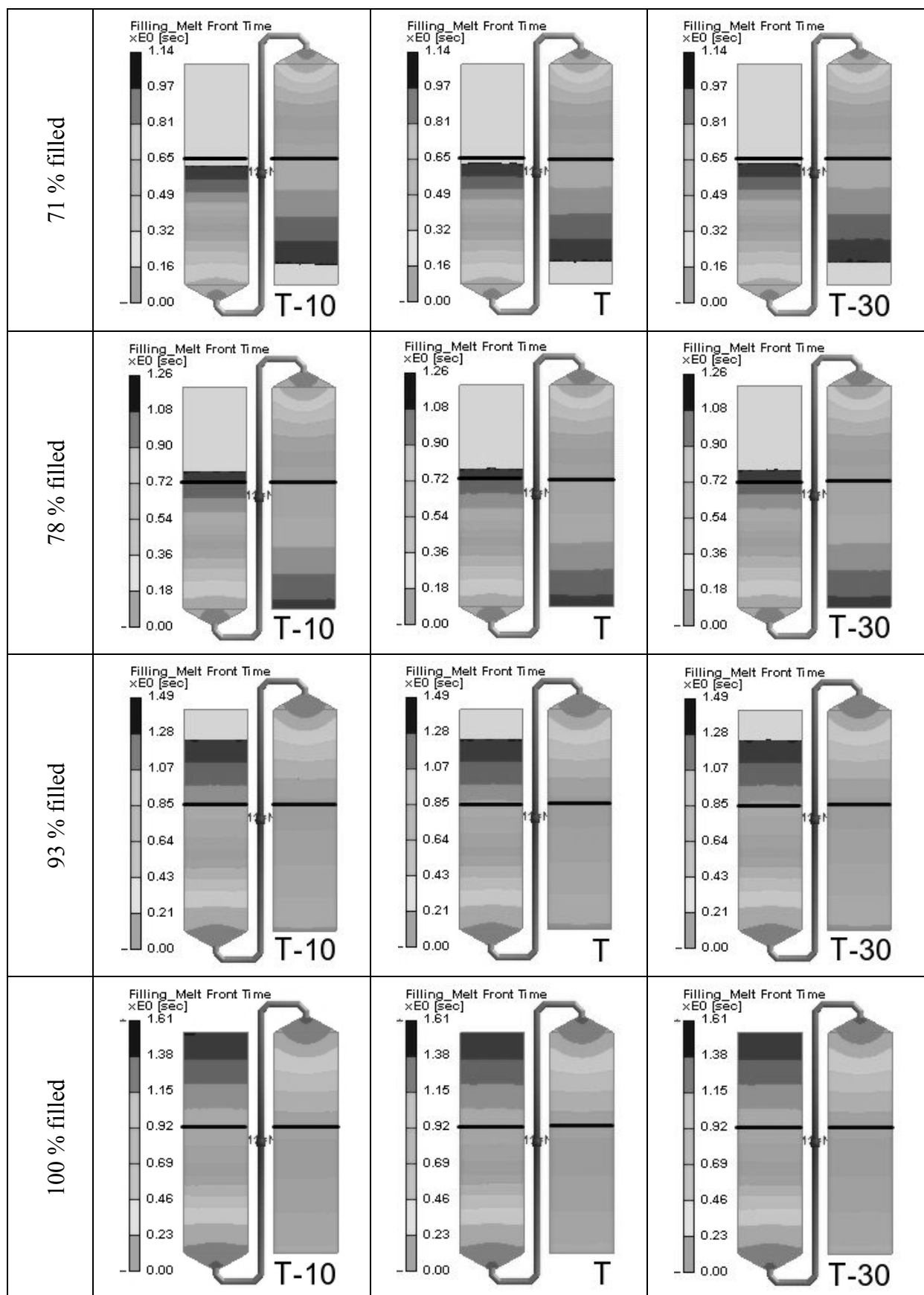
Short-shot study from 2.5D simulations based on tetrahedral derivative mesh as a function of the number of layer counts defined
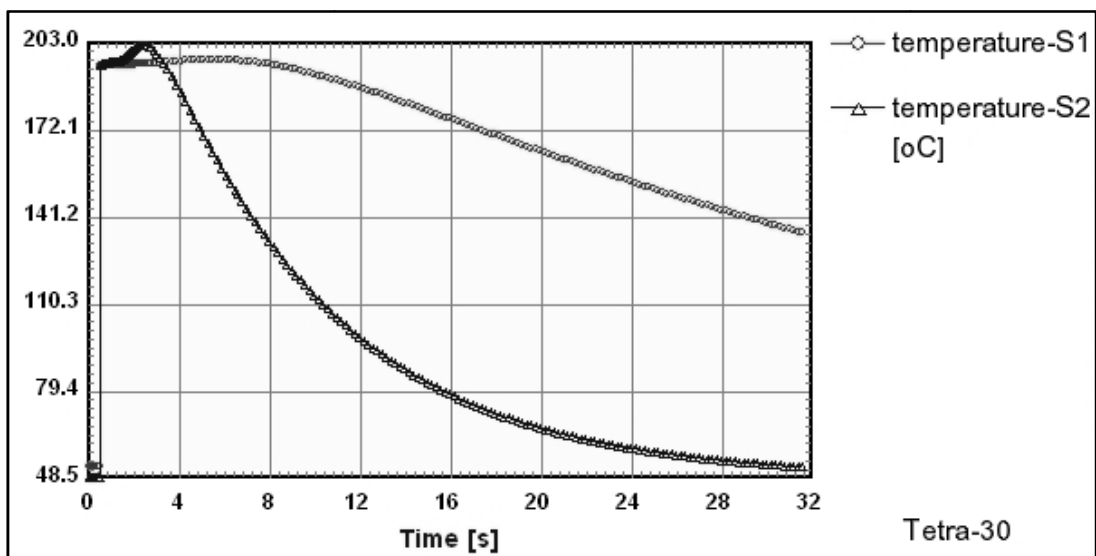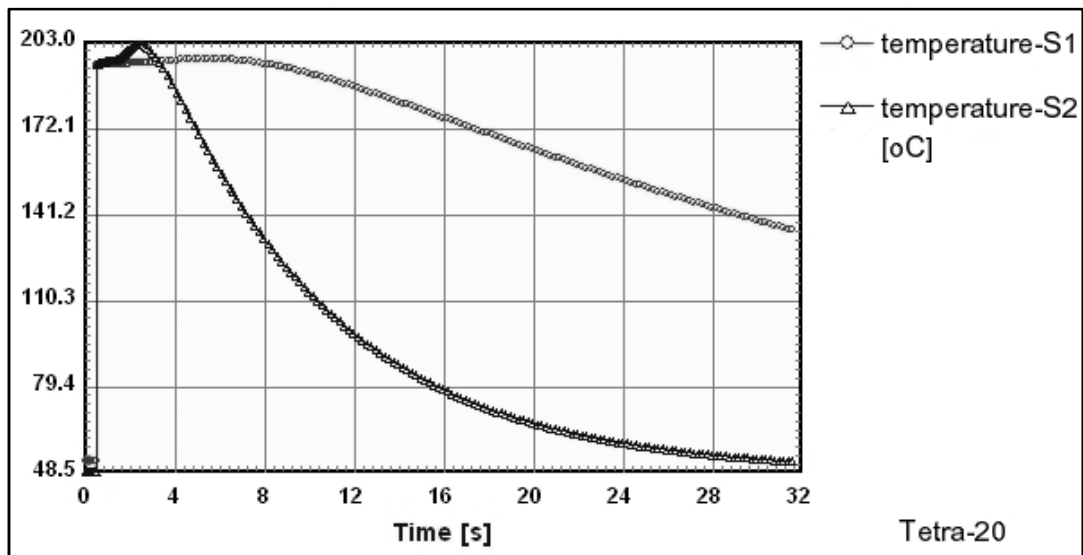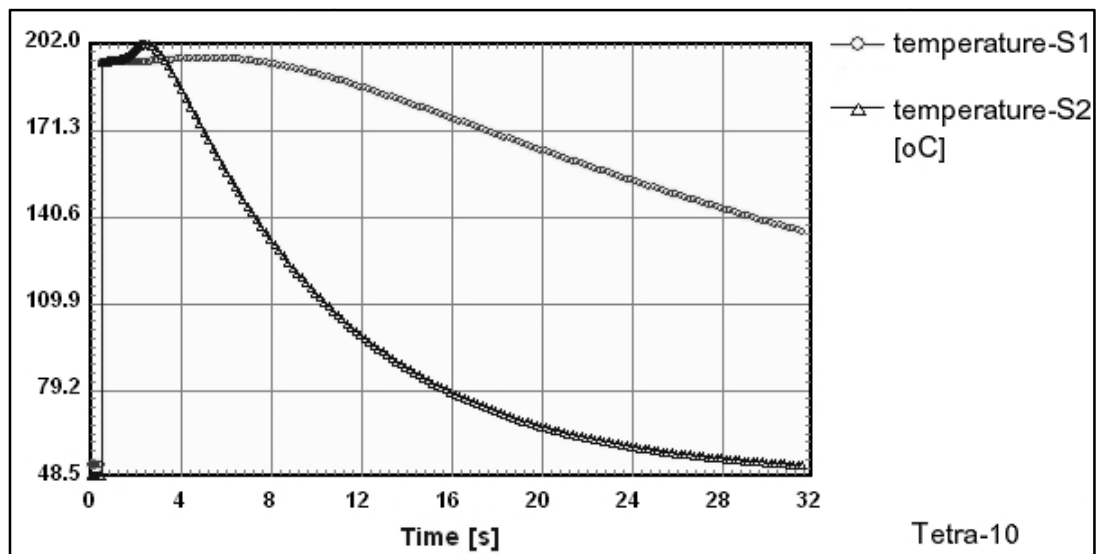
2.5D computed course of the temperature during filling and holding phase based on tetrahedral derivative mesh as a function of the number of mesh layer counts defined

2.5D computed average (left) and center (right) temperature distribution during filling phase based on tetrahedral derivative mesh as a function of the number of mesh layers defined

Appendix 6   2.5D simulation results of the double-plated part with non- uniform part thickness based on the voxel derivative mesh with 10, 20 and 30 layers defined

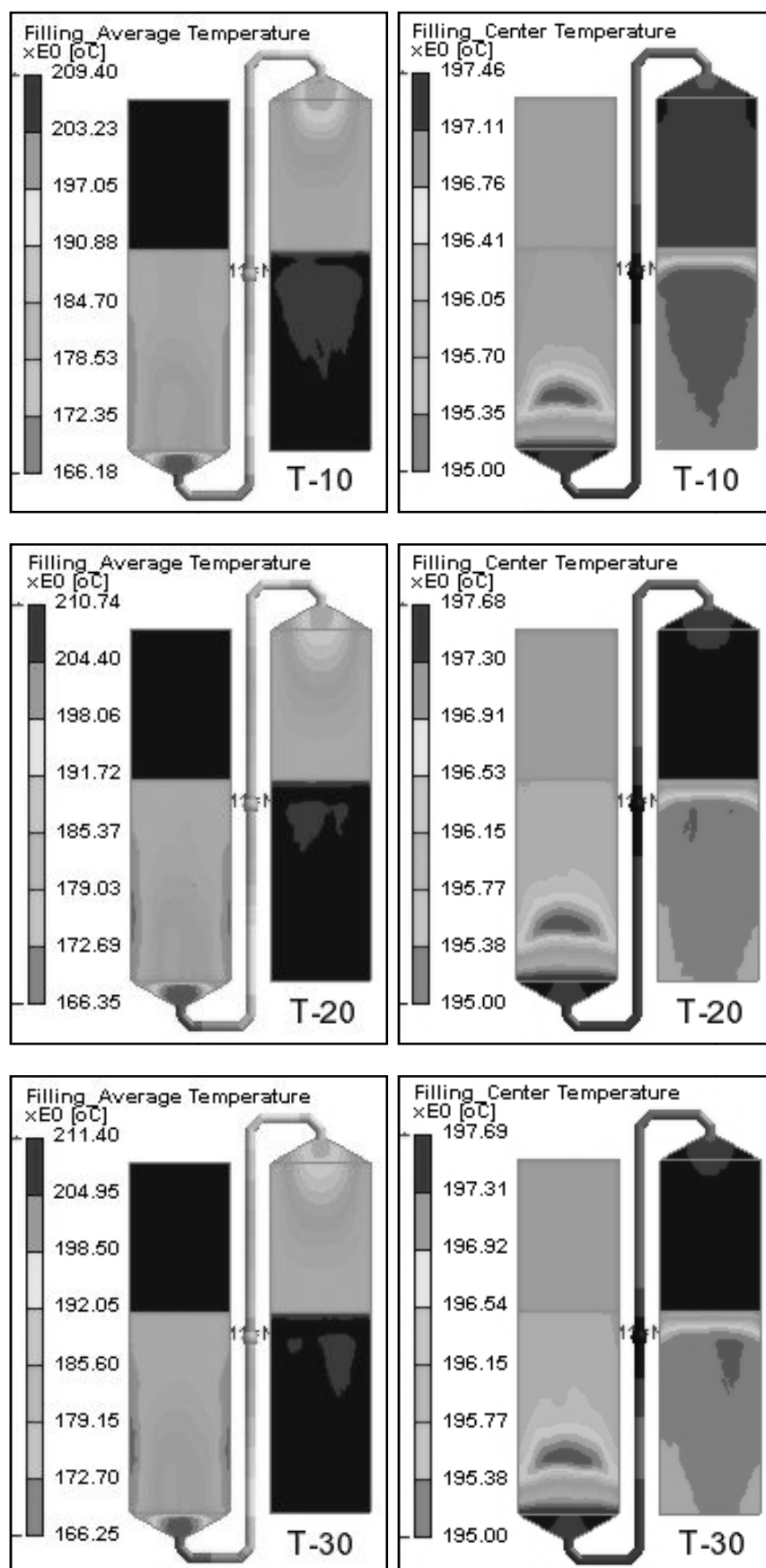|	10 layers	20 layers	30 layers
38 % filled			
49 % filled			
56 % filled			

Short-shot study from 2.5D simulation based on voxel derivative mesh as a function of the number of layers defined

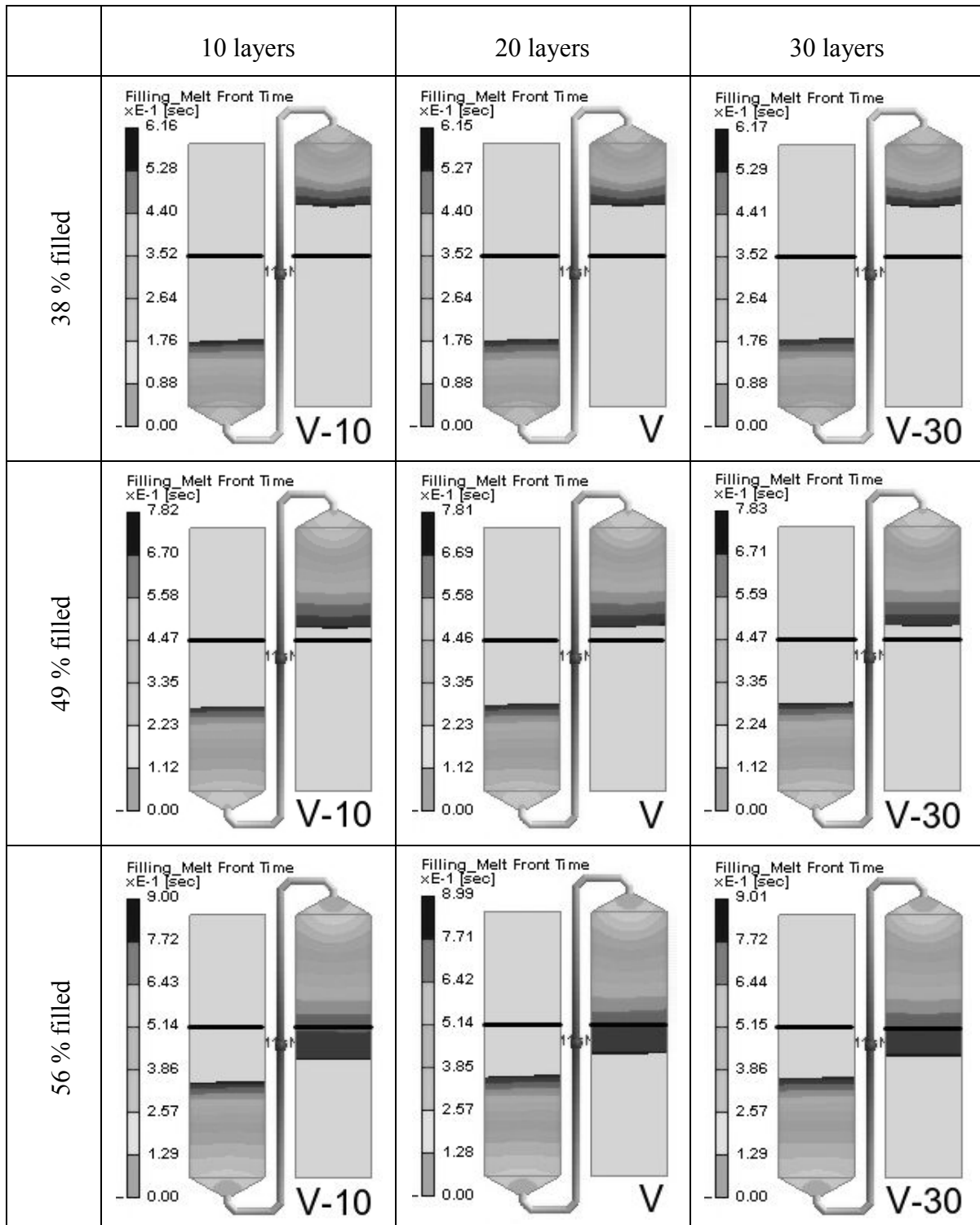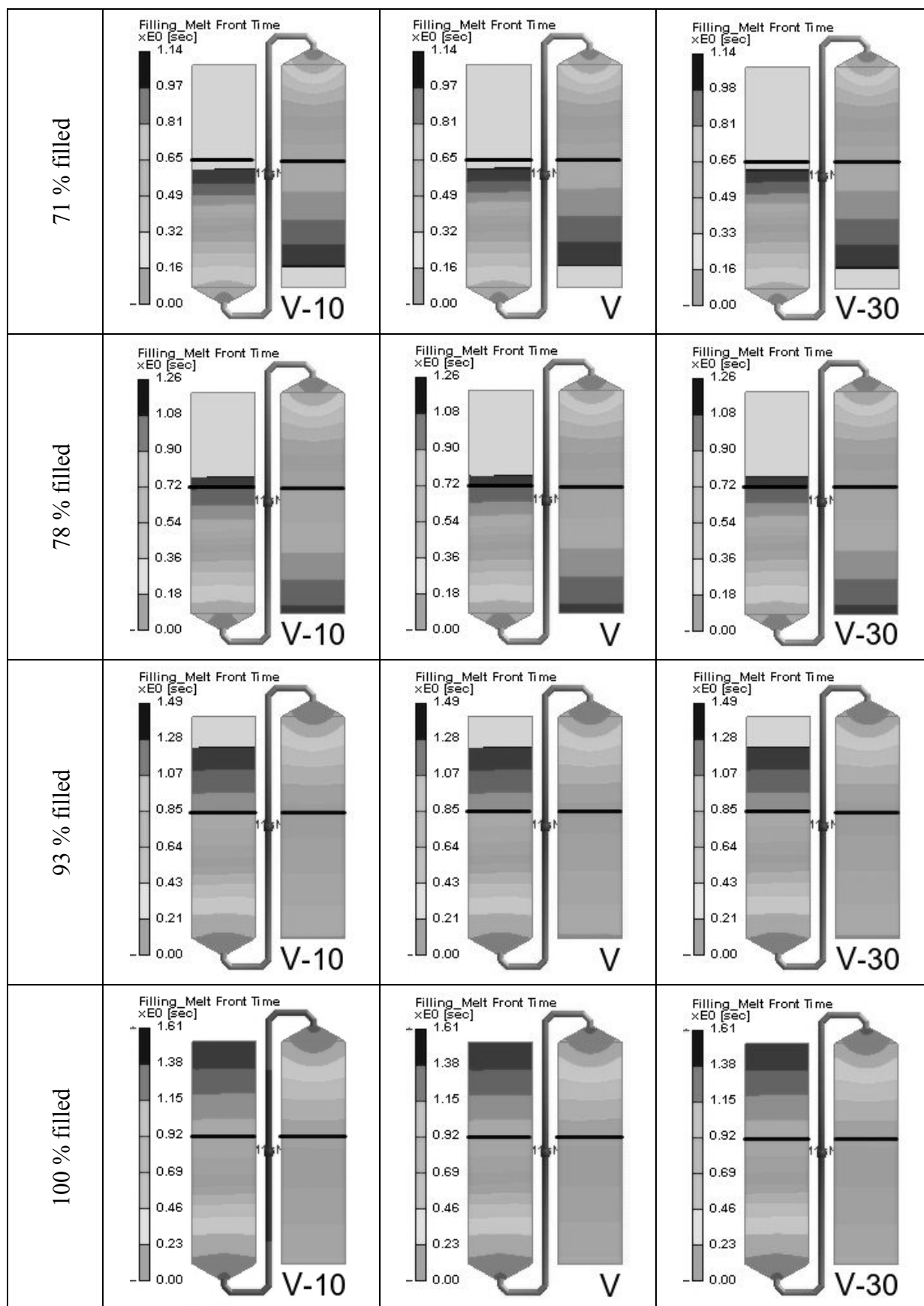2.5D computed course of the temperature during filling and holding phase based on voxel derivative mesh as a function of the number of mesh layers defined
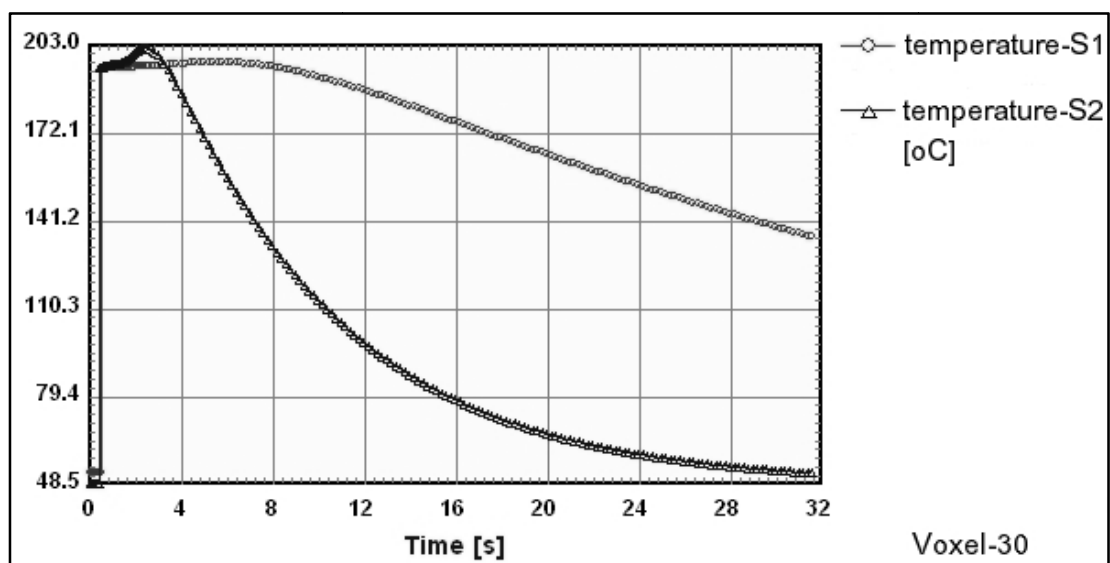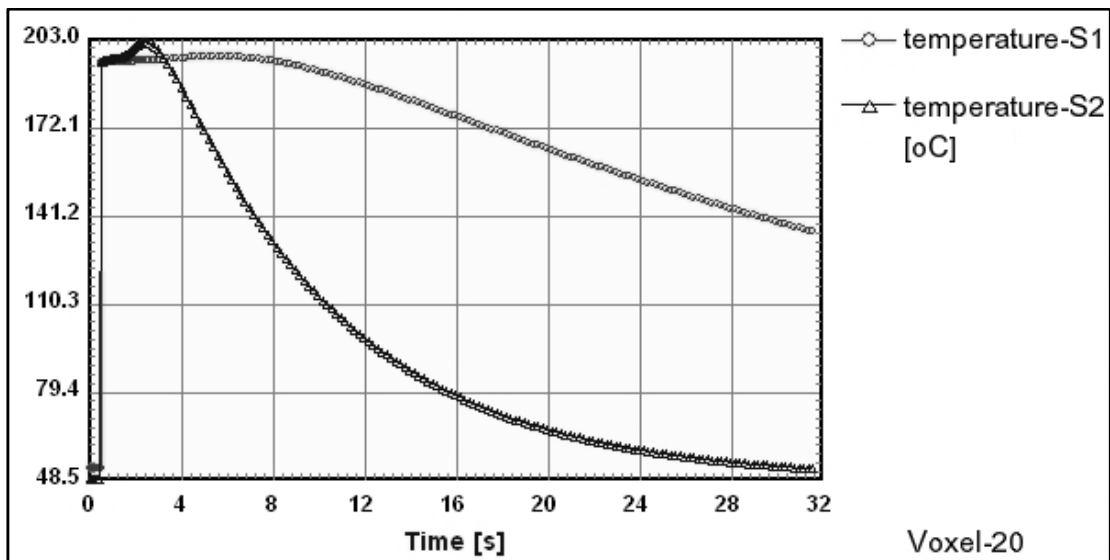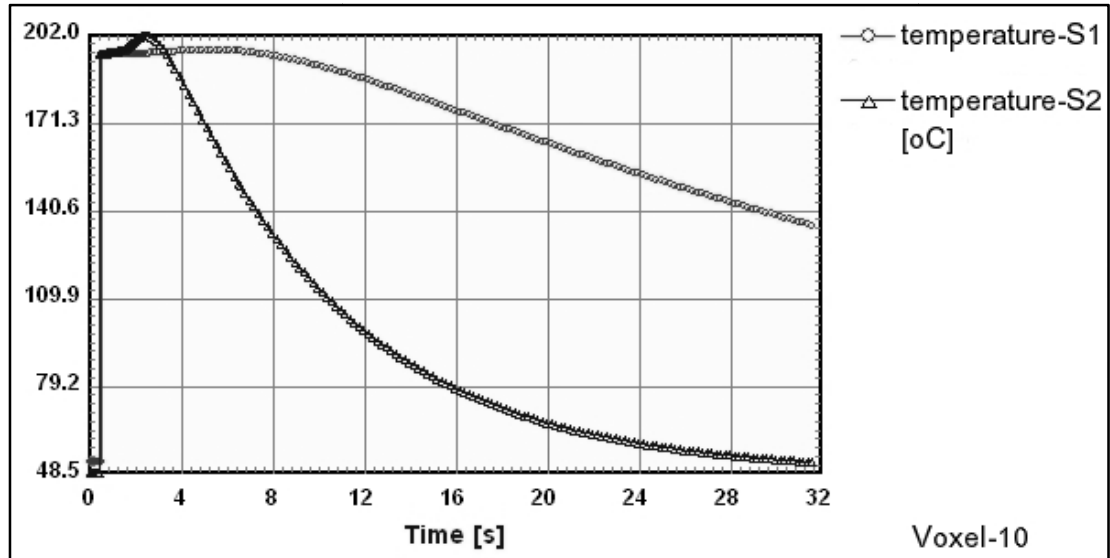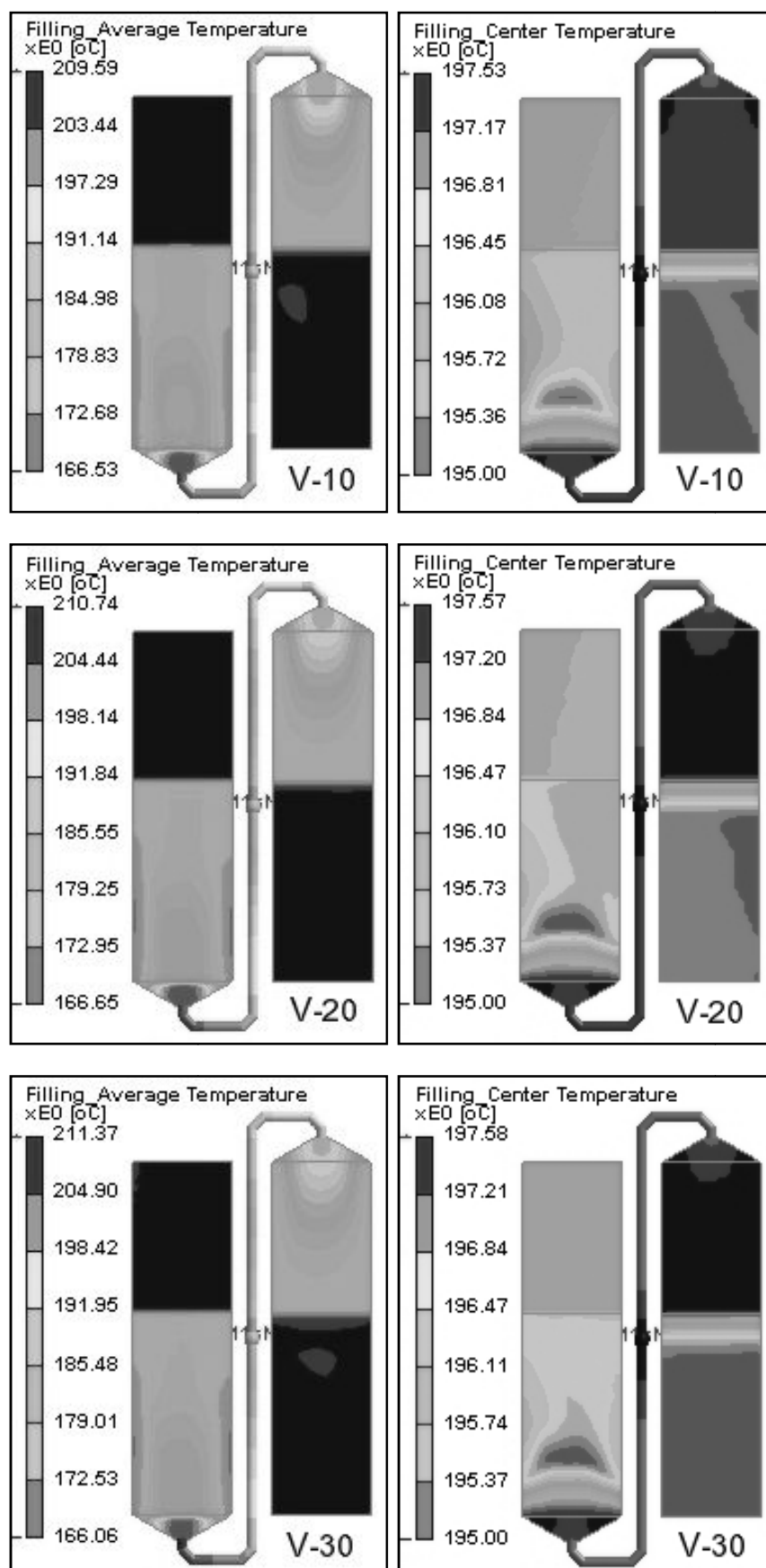
2.5D computed average (left) and center (right) temperature distribution during filling phase based on tetrahedral derivative mesh as a function of the number of mesh layers defined

Appendix 7   Types of Labels used in Packaging

There are numerous types of the label used in packaging. Each type is manufactured differently from each other but they have some of the same characteristics.

In-mold labels (IML): In-mold labels for blow molding have a heat activated adhesive applied to them that is activated during the application process. For injection molding, no adhesive is necessary because of higher temperature involved during molding. The label material can be printed using several different printing processes, such as flexography, offset, screen and hot stamping. In-mold labels are water, grease, weather, and scuff resistant. The label appears as part of the container and has great shelf appeal. They are used for labeling health and personal care products, toys, motor oil, beverages, chemicals and cleaning products.

Thermal labels: There are two different types of thermal labels, thermal transfer and direct thermal labels. Each uses a heat process when imprinted.

* Thermal Transfer Labels

In thermal transfer printing, a ribbon runs over the top of the label material and together they pass between a metal plate and a print head. The print head, which is heated, comes down on the ribbon, causing the coating from the ribbon to be transferred to the label material to create the image. Thermal transfer labels are manufactured on rolls or as continuous fan folded labels. The label stock is not a special paper but must meet the weight, finish and size requirements of the thermal printer.

* Direct Thermal Labels

In direct thermal printing, no ribbon is necessary to create an image. The label material is heat sensitive. The print head is heated as in thermal transfer and when it comes in contact with the special direct thermal label stock, it causes a chemical reaction which creates the image. Direct thermal labels are manufactured on rolls or as continuous fan folded labels. The label is printed on a thermal label printer. Special direct thermal label stock is required.

Linerless labels: Linerless labels are pressure sensitive labels that do not have a liner. The labels are wound on a roll that has had a release coating applied to the front of the facestock to prevent the adhesive from sticking on the label below. The available facestocks include standard paper, film and direct thermal. Linerless labels are available with permanent, removable and repositionable adhesives. Using linerless labels eliminates the waste of the liner material and allows more labels per roll. This increases efficiencies by reducing the number of roll changes, eliminating time used to separate the label from the liner and eliminates time and cost of disposing of the liner waste.

Glue applied labels: A glue applied labels does not have an adhesive layer. It is adhered to the product by glue being applied to the label or to the container during the application process. A cold glue or hot glue adhesive is used to apply the label. The label can be printed on most any type of paper. It can also be printed on metallized paper or film. Once the label is printed, you have the option of adding off-line features to the label, such as foil stamping, die cutting and embossing. Glue applied labels generally cost less than other types of container labels. The material cost is generally less and the labels can be applied at high speeds. Glue applied labels are also more environmentally friendly because there is less waste and the waste is easier to recycle.

Shrink labels: Shrink labels are non-adhesive sleeves constructed from film material that shrinks when heat is applied. Film material such as PVC, PETG, OPP and PP are used in the manufacturing of these labels. Shrink labels allow 360 degrees of print area and will conform to the shape of the container when heat is applied. This allows the packaging company to use some uniquely shape containers that have extreme contours without compromising the copy or graphics. Using shrink labels provides an opportunity to decorate the container with some very eye catching designs. It also provides more printing space for product information since the label can be printed the entire 360 degrees versus a pressure sensitive label that would only allow a certain area of the container to be labeled. There are many product areas in which shrink labels are used, such as food and beverage products, pharmaceuticals, consumer products, cosmetics, personal care products and pesticides.

Stretch labels: Stretch labels are used to label and decorate products such as beverages, food, personal care products, chemicals and cleaning products. They are similar to shrink labels in that they allow 360 degrees of print area on the label around the container. The label is constructed of a stretch film material that has elasticity to it. The label is stretched over the container and released when it is in the proper location. Once released, it will fit snug and form to the contours of the container. The stretch sleeve label does not need any glue or heat to enable it to stay in place. The labels are available on clear or opaque film and can be reverse printed. They are supplied on rolls and a perforation can be added between labels if desired. The stretch labels can be supplied for manual, semi-automatic or automatic labeling applications.

The application process does not cause any fumes and it does not contaminate the container with glue. The application of the label is a very clean process and very environmental friendly. The stretch label is moisture proof and is easy to remove from the container at the time of recycling due to the absence of glue.

Smart labels: Smart labels contain electronic devices that have read/write memory used to store and access information. The electronic device is a radio frequency identification (RFID) transponder or tag. The RFID technology, like bar codes, is used to automatically capture data. It is different from a bar code in that it can hold much more data, it can be reprogrammed, and its data is accessed by a reader but it does not need optical contact with the reader to be read. Some common applications where smart labels would be used are supply chain management, production control, work-in-process, baggage identification and tracking, express delivery services, reusable container tracking and security systems. The industry acceptance of smart labels has been slow. The RFID technology can improve performance and efficiency but is expensive to start up. As more companies commit to the use of this new technology it will become more widely accepted and many will benefit from its capabilities.

Security labels: There are many different options for adding security to the labels. The type of security used on the labels will depend on the label use, the desired level of security and what the user is trying to protect against, such as counterfeiting or product fraud. To provide the proper level of security, many times several security features are used.

Appendix 8   Temperature Measurement with IR Thermometers

Most industrial processes require the measurement of temperature. A radiation thermometer can measure the temperature of an object without physical contact. Such a system does not contaminate, damage, or interfere with the object being monitored and has many advantages over other measurement devices. The radiation thermometer can be mounted remotely from the hot target enabling it to operate for long periods of time with minimal maintenance.

Types of Radiation Thermometers

The most commonly used thermosensors tend to fall into one of four possible classes.

1. Broad Waveband: Often referred to as general purpose low temperature thermometers which have a spectral response of 8 to 14 μm and will be used on temperature ranges typically of 0 to 250 ^{o}C.

2. Selected Waveband: Usually application specific thermometers which have been designed to overcome special application problems.

3. Short Wavelength: These are usually thermometers which operate below 2.5 μm. A typical example of this is a l μm thermometer which is used at high temperatures such as 600 ^{o}C to 1300 ^{o}C. These thermometers are good at minimizing the effect of variable emissivity and are found throughout the steel and other high temperature industries.

4. Ratio Thermometers: The Ratio Thermometer is a dual wavelength device and is often used where the target does not fill the field of view or where there are obstructions in the sight path. Cement Kiln burning zones and wire rod mills are examples of this.

Electromagnetic spectrum
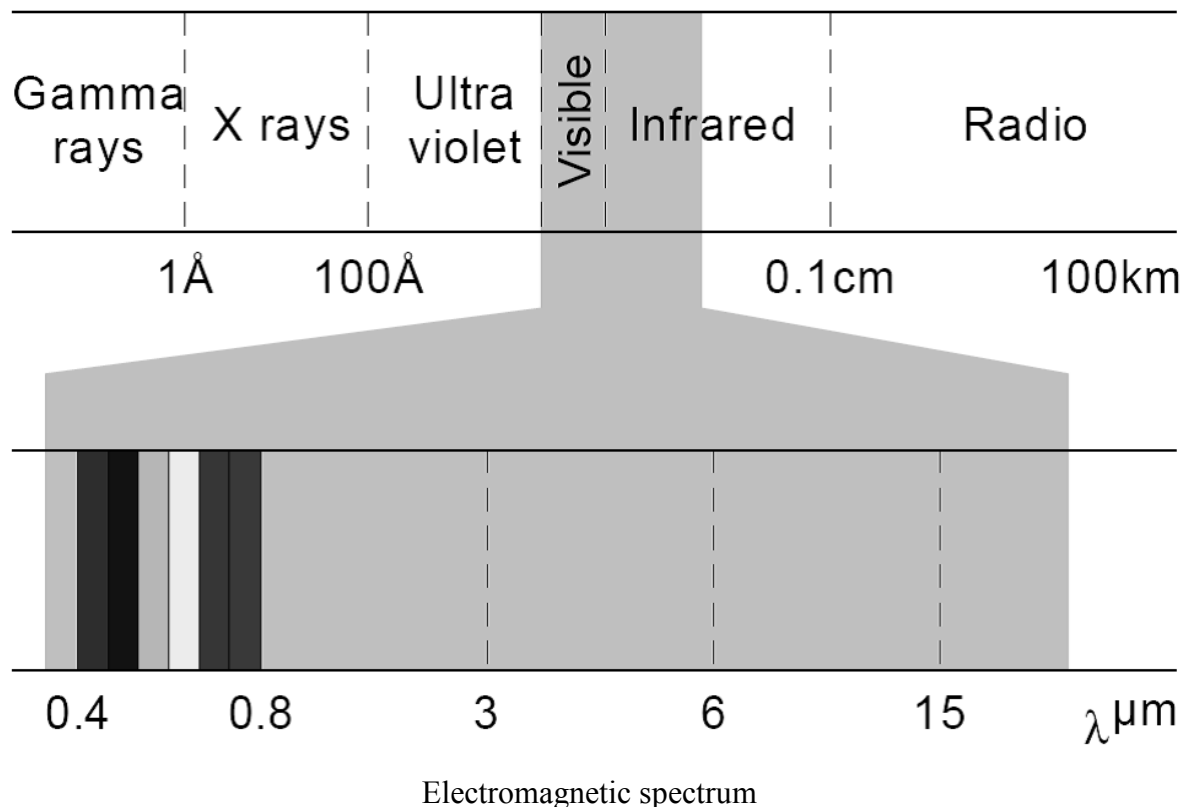
A radiation thermometer determines the temperature of an object by measuring the electromagnetic energy it emits. Any object whose temperature is above absolute zero is capable of radiating electromagnetic energy which is propagated through space at the speed of light. The electromagnetic spectrum contains many different forms of electromagnetic emissions, including infrared, light, X-rays, radio waves, and several others. The only difference between these emissions is their wavelength which is related to frequency. Radiation thermometers are designed to respond to wavelengths within the infrared portion of the spectrum. In practice temperature measurement is made using thermometers operational over many different ranges of wavelength, which generally reside somewhere between 0.2 to 20 μm.

Absorption, Transmission, and Reflection

When the infrared radiated by an object reaches another body, a portion of the energy received will be absorbed, a portion will be reflected and if the body is not opaque a portion will be transmitted through. The sum total of the three individual parts must always add up to the initial value of radiation which left the source.

A perfect absorber and hence emitter of infrared energy is referred to as a black body. A black body would not necessary appear to be black in color as the words black body are a technical term to describe an object capable of absorbing all radiation falling on it and emitting maximum infrared energy for a given temperature. In practice surfaces of materials are not perfect absorbers and tend to emit and reflect infrared energy. A non black body would absorb less energy than a black body under similar conditions and hence would radiate less infrared energy even though it was at the same temperature. The knowledge of a surfaces ability to radiate infrared is important when using an infrared thermometer.

Emissivity

An object's ability to radiate infrared energy depends upon several factors including type of material, surface condition and wavelength. The value of emissivity for an object is an expression of its ability to radiate infrared energy. Emissivity is really a comparison between the energy emitted by the target object and an ideal emitter or black body at the same temperature. Hence emissivity may be expressed as follows:

$$\text{Emissivity} \quad \varepsilon = \frac{\text{Radiation Emitted by target object at Temperature (T)}}{\text{Radiation Emitted by a Black Body at Temperature (T)}}$$

Semi-transparent Targets

In applications where it is necessary to measure the temperature of a semi-transparent target such as glass or plastic film, careful consideration of the materials, transmission, absorption, and reflection should be made. The infrared energy received by the thermometer from a heated target is the sum of three quantities:

- The emitted radiation due to the temperature of the target.

- The background radiation which is reflected from the target.

- Radiation transmitted through the target.

If a, r, and t are the objects fractional absorption, reflection and transmission respectively then: a + r + t = 1.0. The output signal of the thermometer measuring a semi-transparent target is as follows:

$$S = + a.f(T) + r.f(Tb) + t.f(Tf)$$

Where:

T = Target temperature, Tb = Background temperature, Tf = Foreground temperature

It is helpful to visualize the measurement situation where it is imagined that the thermometer detector is hot and the resulting emitted radiation tracked to the point where it is absorbed.
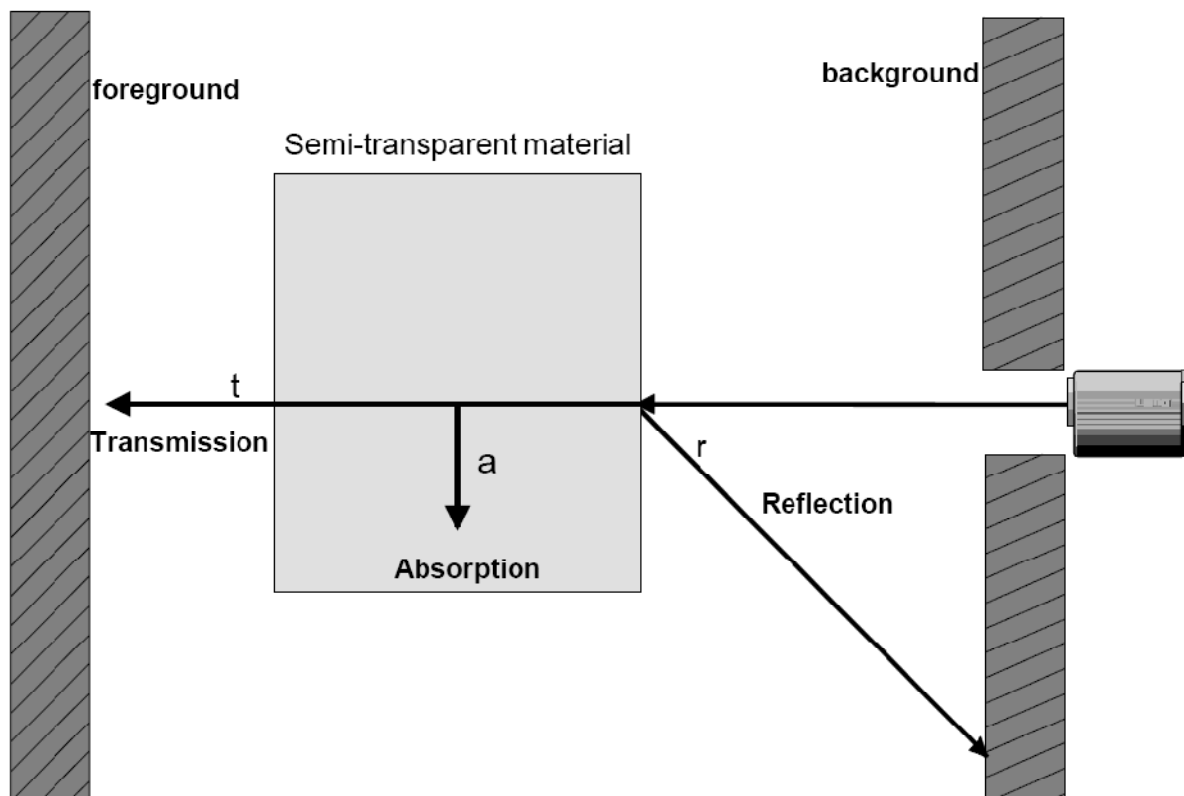
Absorption, Reflection and Transmission of semi-transparent materials

As can be seen in the above diagram there will be a reflection loss at the front surface of the material and a portion of the remaining energy will be absorbed. The energy which is not absorbed or reflected will be transmitted through the material and will end up in the foreground. The absorption and transmission of a semi-transparent material is dependent on material thickness. The transmission of a partially transparent material decreases with increasing thickness. If the reflectivity remains constant the absorption and hence emissivity must increase as the transmission decreases. When selecting a suitable thermometer to measure a semitransparent target one must be sure of two things:

- The target must be measured at a wavelength where the transmission is low to prevent the thermometer from seeing through the target.

- The target must be of sufficient thickness to ensure that transmission is reduced to a very low value.

Plastics

Most plastics are processed at relatively low temperatures as they rapidly decompose at temperatures above a few hundred degrees Celsius. Many types of plastic include filler materials to give color and modify mechanical properties etc. In even moderate thickness these are often opaque over large parts of the infrared spectrum and are therefore easily measured using traditional low temperature wide band thermometers.

Plastic Films:

Thin plastic films have a transmission and hence emissivity which is strongly wavelength dependent.
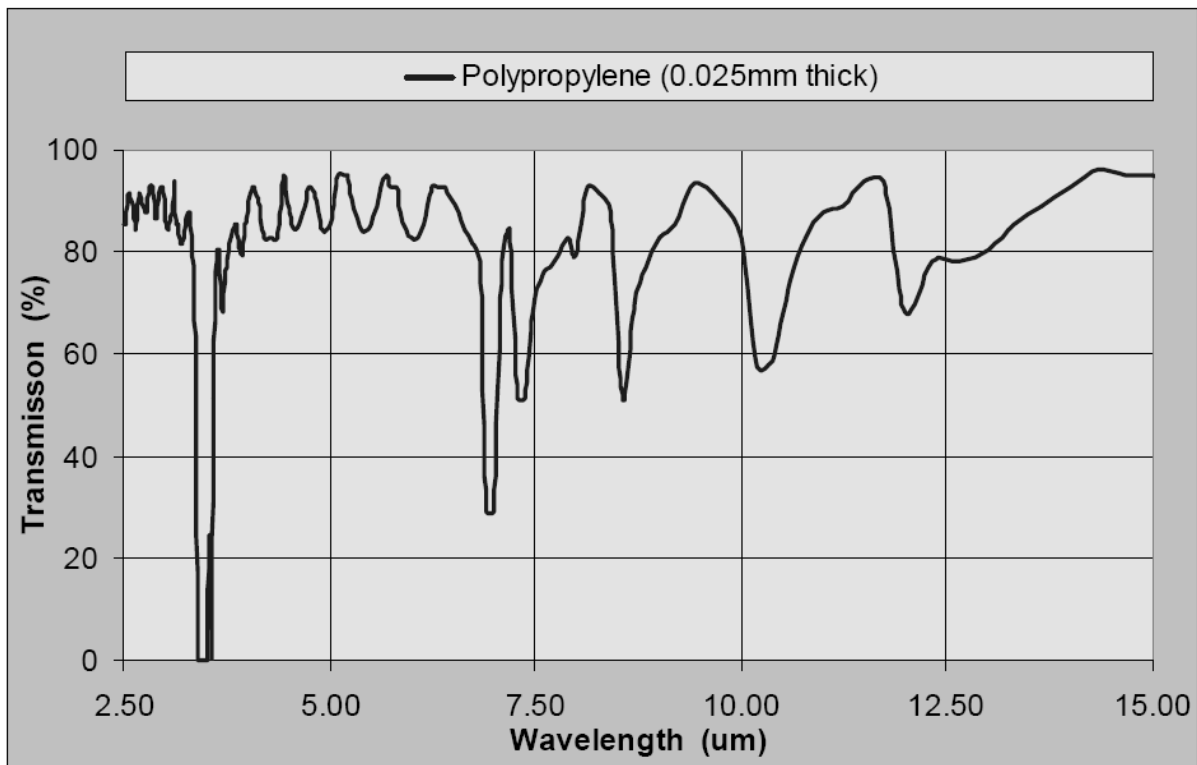
Transmission of Infrared through Polypropylene

The figure above clearly shows how a thin sample of plastic is highly transparent over much of the infrared spectrum. In this case a broad band thermometer will "see" through the sample and will tend to measure whatever is behind it. The figure also clearly shows a region around 3.4 μm where the sample is suddenly quite opaque. In the infrared part of the spectrum this opaque region is associated with particular molecular resonances within the structure of the material. Many common plastics contain saturated hydrogen to carbon molecular bonds (C-H bond) and it is these bonds which are responsible for the effects seen at wavelengths close to 3.4 μm. Measurement of temperature of these types of plastic film is often possible if the thermometer is operational at a wavelength where the plastic film is opaque. It should be noted however that plastic materials have many different compositions and not all include the C-H bond. Some plastic films such as polyurethane, acrylic and some fluorocarbons are not so opaque at 3.43 μm and a better result is obtained at 7.9 μm (C-O bond).

Emissivity:

The transmission and the reflections from the surface of the target limit the emissivity of any semi-transparent target. For most hydrocarbon plastics the reflection coefficient is 0.04 per surface, and this sets an upper limit of 0.96 for the emissivity even when it is totally opaque. The emissivity value will fall with reducing thickness of the plastic film, leading to an increase in transmission from the behind the target. It is useful to specify a minimum thickness for a particular plastic material to ensure reliable temperature measurement results.

Minimum Thickness:

When specifying material minimum thickness, an acceptable transmission value must first be defined. The acceptable transmission at a very low value of 2 % is defined, resulting in emissivity values of >0.94. This definition gives minimum thickness figures which are conservative and which will prove reliable for the vast majority of applications. Minimum thickness to meet this criterion for various plastics is shown in the table below. This Minimum thickness specification should be used with caution as the amount of transmission, which can be tolerated, may vary enormously from one application to the next.

Material	Min Thickness (for E ≥ 0.94)
Polypropylene	20 μm
Polyethylene	20 μm
Polyamide (Nylon)	40 μm
Acrylic	80 μm
Polystyrene	80 μm
Polyvinyl Chloride (PVC)	100 μm
Polyurethane	100 μm
Cellulose Acetate	100 μm
Polycarbonate	150 μm
Polyester (PET)	300 μm
Polyvinylidene Chloride (PVDC)	300 μm

Minimum thickness of various plastics (Note with 3.43 μm Thermometer)

LEBENSLAUF

Vorname	Patcharee
Nachname	**LARPSURIYAKUL**
Geschlecht	weiblich
Geburtsdatum	12.03.1977
Geburtsort	Bangkok, Thailand

Studium

1995-1999	Studiengang Werkstoffwissenschaft (Polymer Science) Chulalongkorn University, Bangkok, Thailand Abschluss Akademischer Grad Bachelor of Science
1999-2001	Studiengang Werkstoffwissenschaft (Polymer Science) Chulalongkorn University, Bangkok, Thailand Abschluss Akademischer Grad Master of Science
2001	Erhalt des Stipendiums der thailändischen Regierung, um in Deutschland auf dem Gebiet Kunststofftechnik zu promovieren

Sprachkurse

Juli 1998-April 1999	Besuchen eines englischen Sprachkurses in Thailand, die TOEFL-Prüfung wurde danach abgelegt
August 2001-März 2002	Erlernen der deutschen Sprache beim Goethe-Institut in Mannheim, die DSH-Prüfung wurde im März 2002 abgelegt
Juni 2002-März 2003	Besuchen eines deutschen Privatkurses beim CDC-Institut in Berlin

Wissenschaftliche Tätigkeiten

2002-2004	Gastwissenschaftlerin im Bereich Fertigungstechnik am Institut für Werkzeugmaschinen und Fabrikbetrieb der Technischen Universität Berlin
2004-2008	Wissenschaftliche Mitarbeiterin im Bereich Prozessanalyse und Modellbildung am Institut für Kunststofftechnik der Universität Stuttgart
Seit 2009	Wissenschaftliche Mitarbeiterin, National Metal and Materials Technology Center (MTEC), Pathumthani, Thailand